Dissertation
zur Erlangung der Doktorwürde
an der

Gesamtfakultät für Mathematik,
Ingenieur- und Naturwissenschaften
der
Ruprecht-Karls-Universität Heidelberg

Thema:

Effects and Devices to Generate Dynamic Fields and Forces with Ultrasound

vorgelegt von:
Rahul Goyal
(M.Sc.)

Gutachter: **Professor Dr. Peer Fischer**
Dr. Kai Melde

Contents

List of Tables

List of Figures

Abstract

Dynamic fields and forces from ultrasound can enable clinical and contactless acoustic energy transfer applications. This thesis examines the generation and control of ultrasound wavefronts, as well as the use of sound to manipulate microbubbles and cm-scaled objects for assembly.

For the latter, this dissertation investigates the dynamics of insonified microbubbles and their long-range interactions associated with the Bjerknes force. It is shown that arrays of microbubbles can be used to amplify the secondary Bjerknes force to permit the manipulation and positioning of cm-sized objects via bubble arrays. The geometry of the bubble arrays can be used to either achieve continuous rotation of an object on the water surface or its relative positioning with 15 µm accuracy, even though the sound wave has a wavelength of 50 cm.

The second part of the thesis presents two new ways to dynamically form ultrasound fields. Complex ultrasound fields are useful in a number of applications, and they play a particularly important role in ultrasound-based therapy. Traditionally, phased array transducers (PATs) are used to achieve dynamic shaping of ultrasound wavefronts. However, the number of elements is limited as all the transducers require a power amplifier. In addition, only the limited (discrete) phase control can at present be realized. This thesis therefore proposes and experimentally demonstrates a light-based scheme to control the phases in a transducer array. Termed the "Optically Programmable Array of Transducers" (OPATs), an analog circuit consisting of a dual-cascaded network of resistors and capacitors, including photoresistors, is realized that can be used to achieve phase shifts of up to 2π of 121 transducer elements with a single power amplifier. A light intensity pattern from a projector determines the phase of the transducer array. Various dynamic wavefronts including a vortex beam are demonstrated using the OPAT technology, as well as the dynamic updating (up to 100 Hz) of wavefronts.

Finally, this thesis explores material systems that could be used to realize a mod-

ulator for ultrasound. Different materials are discussed and a phase change material that shows a solid-to-liquid phase change upon a modest temperature increase is identified as a promising candidate to modulate the speed of an ultrasound wave. A reflective acoustic metasurface and a one-dimensional stack containing the phase change material are experimentally realized. A modulator will require a two-dimensional array of heater elements to drive the spatially-controlled phase change, and this thesis therefore also describes the fabrication of a microheater array for this purpose. Its design and operation are characterized.

In summary, this thesis describes several novel developments in physical acoustics that are expected to find application in systems and devices that use ultrasound for manipulation, or that require the control of ultrasound wavefronts. The designs presented in the thesis show promise, as they achieve relatively large forces and high precision for manipulation, and as they can be used to achieve complex ultrasound fields with affordable, flexible architectures. The thesis paves the way for a first realization of a robust, large-scale ultrasound modulator.

Zusammenfassung

Ultraschall generierte dynamische Felder und Kräfte können kontaktlose, klinische Anwendungen ermöglichen, bei denen Energie in Form von akustischen Wellen übertragen wird. Diese Arbeit untersucht die Erzeugung und Steuerung von Ultraschallwellenfronten, sowie die Verwendung von Schall zur Manipulation und Anordnung von Mikrobläschen und Objekten im Zentimetermaßstab. Für Letzteres untersucht diese Dissertation die Dynamik beschallter Mikrobläschen und ihre Wechselwirkungen im Zusammenhang mit der Bjerknes-Kraft. Es wird gezeigt, dass Arrays von Mikrobläschen verwendet werden können, um die sekundäre Bjerknes-Kraft zu verstärken und so die Manipulation und Positionierung von Objekten über Blasen-Arrays zu ermöglichen. Die Geometrie der Blasenanordnungen kann genutzt werden, um entweder eine kontinuierliche Rotation eines Objekts auf der Wasseroberfläche oder seine relative Positionierung mit einer Genauigkeit von 15 µm zu erreichen, obwohl die Schallwelle eine Wellenlänge von 50 cm hat.

Im zweiten Teil der Arbeit werden zwei neue Möglichkeiten zur dynamischen Formung von Ultraschallfeldern vorgestellt. Komplexe Ultraschallfelder sind in einer Reihe von Anwendungen nützlich und spielen insbesondere in der ultraschallbasierten Therapie eine wichtige Rolle. Traditionell werden hierbei Phased-Array-Wandler (PATs) verwendet. Die Anzahl der Elemente ist jedoch begrenzt, da alle Wandler einen Leistungsverstärker benötigen. Darüber hinaus kann derzeit nur die begrenzte (diskrete) Phasensteuerung realisiert werden. In dieser Arbeit wird daher ein lichtbasiertes Konzept zur Steuerung d er Phasen in einem Wandlerarray vorgeschlagen und experimentell demonstriert. Unter der Bezeichnung „Optisch programmierbares Wandlerarray“ (OPATs) wird eine analoge Schaltung realisiert, die aus einem doppelt in Kaskade geschalteten Netzwerk aus Widerständen und Kondensatoren, einschließlich Fotowiderständen, besteht. Die Schaltung erzielt Phasenverschiebungen von bis zu 2π in 121 Wandlerelementen die mit einem einzigen Leistungsverstärker erreicht werden können. Ein Lichtintensitätsmuster von einem Projektor bestimmt die

Phase des Wandlerarrays. Mit der OPAT-Technologie können verschiedene dynamische Wellenfronten, einschließlich einem Vortex-Strahl, sowie die dynamische Aktualisierung (bis zu 100 Hz) von Wellenfronten demonstriert werden.

Abschließend werden in dieser Arbeit Materialsysteme untersucht, die zur Realisierung eines Modulators für Ultraschall verwendet werden könnten. Es werden verschiedene Materialien diskutiert und ein Phasenwechselmaterial, das bei einer geringen Temperaturerhöhung einen Phasenwechsel (fest-flüssig) zeigt, wird als vielversprechender Kandidat zur Modulation der Geschwindigkeit einer Ultraschallwelle identifiziert. Eine reflektierende akustische Metaoberfläche und ein eindimensionales Schichtsystem, die das Phasenwechselmaterial enthält, werden experimentell realisiert. Ein Modulator benötigt eine zweidimensionale Anordnung von Heizelementen, um den räumlich kontrollierten Phasenwechsel zu steuern. In dieser Arbeit wird daher auch die Herstellung einer Anordnung von Mikroheizelementen für diesen Zweck beschrieben. Das Design und ihre Funktionsweise werden charakterisiert.

Zusammenfassend beschreibt diese Arbeit mehrere neuartige Entwicklungen in der physikalischen Akustik, die voraussichtlich in Systemen und Geräten Anwendung finden werden, die Ultraschall zur Manipulation verwenden oder die Steuerung von Ultraschallwellenfronten erfordern. Die in der Arbeit vorgestellten vorgestellten Systeme sind sind vielversprechend, da sie relativ große Kräfte und eine hohe Präzision für die Manipulation erreichen und da sie zur Erzeugung komplexer Ultraschallfelder mit kostengünstigen, flexiblen Bauweisen verwendet werden können. Die Arbeit ist wegweisend für die erste Realisierung eines robusten, skalierbaren Ultraschallmodulators.

Preface

The primary difference between the propagation of light waves and acoustic waves is the dependency on the medium . The presence of a medium is essential for the acoustic waves to travel from one point to another whereas; light waves can traverse in vacuum . The periodic vibrations of particles in a medium allows the propagation of acoustic waves, hence the physical properties of a medium characterize the parameters of traveling acoustic waves [9]. The research field of ultrasound has been of particular interest from past 100 years due to its biocompatibility and contactless transfer of energy in a medium . The acoustic waves offer higher penetration depth in biological samples in comparison with light waves or radio frequency waves . The technology of ultrasound imaging is the evidence of applications that acoustic waves have provided to the biomedical research community . The application of acoustic waves is not just limited to imaging but it also provides an efficient way of particle manipulation and assembly . Acoustic radiation forces govern the assembly and manipulation of particles in the acoustic field . The classical acoustic principles have proven to be extremely useful in quantitative and qualitative description of the radiation forces that has led to the development of high power acoustic systems . The advantage of acoustic waves over light for particle manipulation is the larger wavelength, which provides the flexibility to navigate particles in broad range of dimensions . However, it is extremely difficult to break the constraint imposed on the particle size by the acoustic wavelength in the medium. Further, the acoustic radiation forces are generally in the range of nN to µN. Thus, it becomes challenging to apply the acoustic radiation forces on structures with an order of magnitude size larger than the wavelength. The work in this thesis is divided into two categories. In the first part, the thesis answers the problem of macrostructure assembly through the amplification of acoustic radiation forces. The second part of this thesis introduces novel approaches for dynamic control of ultrasound wavefront in spatial and temporal domain simultaneously. The first part of this thesis introduces a novel method to assemble structures using sec-

ondary Bjerknes forces between resonant scatterers in a sound field. Bjerknes forces have been used to manipulate individual bubbles and are generally fall in the range of 10 nN which has been considered weak for manipulation of macrostructures. Therefore, it has been shown experimentally that the array of microbubbles can be used to amplify Bjerknes forces. Microbubbles provide many advantages such as efficient scattering of sound and most importantly, the size of microbubbles are much smaller than the resonance wavelength. This thesis shows how a novel amplification scheme can be used to benefit from the small bubble size, and at the same time increase the force between objects. The second part of this thesis answer the questions of how complex ultrasound wavefronts can be generated in a dynamic manner. This thesis demonstrates two methods for the generation of dynamic ultrasound wavefront, where phased array transducers make the foundation of first method with a novel controlling architecture. A phased transducer array is in principle capable of generating acoustic waves with tunable wavefronts, but the digital variation in the phase of electrical signal provides less fidelity to generate different ultrasound wavefronts. Moreover, the complexity of its electrical driving circuitry and unfavorable scaling of power requirements poses several challenges and limits the number of elements that can be operated in an array and thus the complexity of the sound field that can be attained. The first method presents an optically programmable approach to potentially realize very large phased transducer arrays by harnessing the excellent control of optics. Light is used to shift the phase of electrical signals locally, and hence a light-controlled 121 elements transducer array is constructed and generation of various ultrasound wavefronts is experimentally demonstrated. The second method introduces an approach where the medium of sound propagation is manipulated using materials with reconfigurable physical properties. A low temperature phase change material has been considered as a potential candidate for the practical realization of an ultrasound modulator. The phase change material modulates the sound speed through thermal input and hence indirectly affects the propagation path length of acoustic waves. A first large scale multiplexed microheater array is designed and fabricated that has more elements that are also smaller than what has been reported previously. The microheater array is constructed to generate spatial distribution of thermal pattern, which would then modulate the phase change material and hence ultrasound. The work provides a pathway for fabricating an integrated on-chip device for ultrasound modulation. The Chapter 1 of this thesis introduces the basic equations describing sound waves and their propagation through space and describes the angular spectrum method employed to calculate the excitation phase of elements in transducer array. The electrical parameters for piezoelectric transducer is presented as a function of material constants which is subsequently followed by the description of transmitted and reflected acoustic waves across a boundary between two different media. Further, the Chapter 2 intro-

duces secondary Bjerknes forces, starting with the analytical expression of bubble resonances. The fabrication procedure employed to construct a microbubble array is described in a sequential manner. Next, the chapter presents experimental measurements of bubble oscillations and variation of fundamental resonance frequency as a function of radial distance between the microbubbles. The next chapter of this thesis Chapter 3 further extend the work presented in Chapter2 and provides experimental validation for the amplification of secondary Bjerknes forces. The chapter describes the mechanism that causes the amplification of secondary Bjerknes forces and how it can be applied for acoustofluidic manipulation and assembly. A comparative analysis with magnetic force is provided to highlight the favorable scaling of secondary Bjerknes forces. A numerical model validates the experimental results obtained for the secondary Bjerknes force measurements. Finally, this chapter experimentally demonstrates the acoustic assembly and controlled manipulation of centimeter-scale objects. The next chapters of this thesis constitute the second part of the work. The Chapter 4 starts with a brief description of phased array technologies and how it has been utilized to create dynamic ultrasound wavefronts. The limitations of the current architecture of phased array technology are discussed and then, a completely different concept is presented that uses light intensity to precisely control the phase-shift in the electrical signal driving the ultrasound transducers. The chapter further discusses the large-scale implementation of the technology enabled through optical control in an analog architecture. The Chapter 5 builds on the previous chapter and introduces a realization of an "Optically Programmable Array of Transducers" (OPATs). The chapter presents several different experimental demonstrations to dynamically shape ultrasound wavefronts, including multifocal beam formation, and a vortex beam. The last chapter of this thesis, Chapter 6 presents yet another approach to modulate ultrasound wavefronts. The chapter is divided into two sections; the first section focuses on a discussion of different material classes that have been explored for their potential to modify ultrasound wavefronts. The second section presents interesting properties of a low temperature phase change material. Further, an in-depth analysis of a low-temperature solid-liquid transition is presented which is then described as a potential means to modulate the sound speed. The chapter further demonstrates the functioning of phase change material as a reflective metasurface element and then presents a proof-of-concept for dynamic functionality of ultrasound. A system of 1D metamaterial consisting of periodic stacks of different materials is selected as an example for proof-of-concept demonstration. The phase change material acts as one of the constituents of the constructed metamaterial. A dynamic tuning of stop-band and pass-band in the transmission of ultrasound. Lastly, the chapter presents a large scale integrated and multiplexed operation of microheater array fabricated to generate spatial distribution of thermal pattern. The chapter describes the microfabrication

of microheater array in great detail along with the multiplexed operation of electrical architecture. The chapter ends with several different measurements performed to characterize the thermal signature of microheater array. The final chapter of this thesis, Chapter 7 contains a concluding assessment as well as an outlook of how the work presented in the last chapter paves the way for an integrated on-chip dynamic ultrasound modulator.

List of Publications

The work presented in this thesis has in part been published, patented, and presented at conferences or is being prepared for publication or patenting.

Publications

[1] R. Goyal, A. G. Athanassiadis, Z. Ma, and P. Fischer, Amplification of acoustic forces using microbubble arrays enables manipulation of centimeter-scale objects, Phys. Rev. Lett. **128**, 254502 (2022).

[2] A. G. Athanassiadis, Z. Ma, N. Moreno-Gomez, K. Melde, E. Choi, R. Goyal, and P. Fischer, "Ultrasound-responsive systems as components for smart materials," Chemical Reviews, vol. **122**, pp. 5165–5208, 5 Mar. 2022.

[3] R. Goyal, O. Demeulenaere, M. Fournelle, A. G. Athanassiadis, P. Fischer, All-Optically Controlled Phased-Array for Ultrasonics, 2024 (Manuscript Under Review).

[4] Integrated Ultrasound Modulator Mediated by Gallium-Based Liquid Metal (Manuscript under Preparation).

Patents

[1] R. Goyal, A. G. Athanassiadis, Peer Fischer, Optical Control of Phase and Amplitude in an Array of Actuators, 2023 (Patent Pending).

[2] A. G. Athanassiadis, R. Goyal, O. Demeulenaere, and Peer Fischer, Thermal Spatial Sound Modulator, 2023 (Patent Pending).

PRESENTATIONS

[1] Magnetic Actuation of Structures for Cell Penetration, Satellite workshop on "Remote Manipulation of Cellular Functions: Special Focus on Neurodegenerative Diseases" March 2019.

[2] Amplification of Secondary Bjerknes Forces using Microbubble Arrays for Precise Acoustofluidic Manipulation, Acoustofluidics, July 2022.

[3] Optically Controllable Phased Array for Programmable Ultrasound Wavefronts, Institute of Physics (Optics + Ultrasound VII, September 2024).

[4] Secondary Radiation Forces for Manipulation and Assembly, European Summer School on Physical Acoustics, October 2024.

Additionally, the author has during his PhD contributed to work which is not included in the thesis:

[1] X. Guo, Z. Ma, **R. Goyal**; M. Jeong, W. Pang, and P. Fischer, "Acoustofluidic tweezers for the 3D manipulation of microparticles," in 2020 IEEE International Conference on Robotics and Automation (ICRA), IEEE, May 2020, pp. 11 392–11 397.

[2] S. Schnichels, **R. Goyal**, F. Hurst, F. Ziemsen, T. Qiu, and P. Fischer, "Evaluation of nanorobots for targeted delivery into the retina," in Investigative Ophthalmology and Visual Science, 61, The Association for Research in Vision and Ophthalmology, Jun. 2020, pp. 1355–1355.

[3] E. Choi, F. Waldbillig, M. Jeong, D. Li, **R. Goyal**, P. Weber, A. Miernik, B. Grüne, S. Hein, R. Suarez-Ibarrola, M. C. Kriegmair, and T. Qiu, "Soft urinary bladder phantom for endoscopic training," Annals of Biomedical Engineering, vol. 49, pp. 2412–2420, 9 Sep. 2021.

[4] V. M. Kadiri, J. P. Gunther, S. N. Kottapalli, **R. Goyal**, F. Peter, M. Alarcón-Correa, K. Son, H. Barad, M. Börsch, and P. Fischer, "Light- and magnetically actuated FePt microswimmers," The European Physical Journal E, vol. 44, p. 74, 6 Jun. 2021.

[5] T. Qiu, M. Jeong, **R. Goyal**, V. M. Kadiri, J. Sachs, and P. Fischer, "Magnetic micro- /nanopropellers for biomedicine," in Springer International Publishing, 2022, pp. 389–411.

[6] H. Kwon, O. Kamboj, A. Song, M. Alarcón-Correa, J. Remke, F. Moafian, B. Miksch, **R. Goyal**, D. Y. Kim, F. A. Hamprecht, and P. Fischer, "Scalable

optical nose realized with a chemiresistively modulated light-emitter array," Advanced Materials, vol. 36, 29 Jul. 2024.

[7] F. Peter, V. M. Kadiri, **R. Goyal**, J. Hurst, S. Schnichels, A. Avital, M. Sela, P. Mora-Raimundo, A. Schroeder, M. Alarcón-Correa, and P. Fischer, "Degradable and biocompatible magnesium zinc structures for nanomedicine: Magnetically actuated liposome microcarriers with tunable release," Advanced Functional Materials, vol. 34, 23 Jun. 2024.

[8] A. Song, S. N. Murty, **R. Goyal**, B. Schölkopf, and P. Fischer. Low-power scalable multilayer optoelectronic neural networks enabled with incoherent light. Nat Commun 15, 10692 (2024).

1 Introduction

1.1 Generation and Detection of Ultrasound

The generation of ultrasound involves creating a mechanical oscillation at a specific frequency. The effectiveness of ultrasound wave propagation at this frequency relies on the interaction between these oscillations and the medium they enter, facilitating displacements within that medium. A prevalent method for producing ultrasound is the use of piezoelectric materials. By applying an electric voltage across such materials, mechanical deformations occur, thus transforming electrical energy into mechanical energy. Furthermore, an alternating electrical signal induces oscillatory geometric deformations in the piezoelectric material at the corresponding frequency. When there is efficient coupling of the material's surface to the medium, this leads to the generation of acoustic waves that propagate at that frequency. It is important to recognize that the piezoelectric material exhibits a resonance frequency, which is influenced by its geometric and elastic properties. Consequently, the greatest amplitude of acoustic waves is achieved when the piezoelectric material is operated close to its resonance frequency, or, to a lesser extent, at its harmonic frequencies. The work presented in Chapter 2 - Chapter 6 of this thesis utilizes piezoelectric transducer as the source to generate ultrasound waves. The piezoelectric material and resonance frequency of the transducer varies from chapter to chapter based upon the field of applications.

An interesting but less practical way of generating acoustic waves is through magnetostrictive materials. Magnetostriction has been considered in this thesis in the context of dynamic modulation of ultrasound and is discussed in Chapter 6. The principle of magnetostriction is the deformation of ferromagnetic material when subjected to a magnetic field. An oscillating magnetic field can thereby generate an oscillating displacement, and hence an acoustic wave can be produced in the medium. However, one drawback of magnetostrictive materials comes from the fact that the phenomenon is generally efficient only at frequencies below 30 kHz. The operational frequency is limited by the losses in the magnetostrictive material which translates to

heat generation in the system.

1.2 Electrical Properties of Piezoelectric Transducers

Piezoelectricity is a complex electrical phenomenon that combined with the mechanical resonance of the transducer geometry makes it challenging to solve the characteristics of transducer elements. The theoretical background presented in this section is based on a discussion in the book of Physical Acoustics [23] and a research article [24] and shall serve as a general reference for this chapter and the understanding of piezoelectric mechanisms and the inter-dependency between material constants and electrical parameters of piezoelectricity. The operation of piezoelectric transducers is approximated as a thickness resonator with a geometry of a plate or a disc. The resonator's impedance in the thickness extensional mode, depending on the actuation frequency ω, is typically referred to as [24],

$$Z(\omega) = \frac{t}{jA\omega\epsilon_{33}^{S}}\left[1 - \frac{k_t^2 \tan[\omega/(4f_p)]}{\omega/(4f_p)}\right] \tag{1.1}$$

where A is the surface area of the transducer perpendicular to the thickness t, ϵ_{33}^{S} is the electrical permittivity under clamped operation, and k_t is the electromechanical coupling constant. The electromechanical coupling constant describes the capacity of a material to accumulate mechanical energy in response to an electrical input which can be defined as [23, 24],

$$k_t^2 = \frac{h_{33}^2 \times \epsilon_{33}^{S}}{c_{33}^{D}} \tag{1.2}$$

where h_{33} is the piezoelectric field constant and c_{33}^{D} is the elastic stiffness at constant displacement. The term f_p in the Eq. 1.1 is the parallel resonance frequency. The parallel resonance frequency can be defined in terms of the density ρ and elastic stiffness as follows [24],

$$f_p = \left[\frac{c_{33}^{D}}{4\rho t^2}\right]^{1/2} \tag{1.3}$$

The meaning of parallel resonance frequency (f_p) can be interpreted from the Fig. 1.1. It can be observed from the Fig. 1.1 that the frequency which provides the maximum in the impedance of the piezoelectric transducer is defined as f_p. The impedance of a piezoelectric transducer varies as a function of frequency due to the reactive components (inductor or capacitor) such the the maxima of the impedance curve provides the numerical value of f_p as denoted by long red dotted line in Fig. 1.1. The equation for the impedance defined by Eq. 1.1 does not change significantly for typical material constants (ϵ_{33}^{S}, c_{33}^{D}, and h_{33}). It should be noted that a complex material constant causes the parallel resonance frequency f_p to be complex in nature.

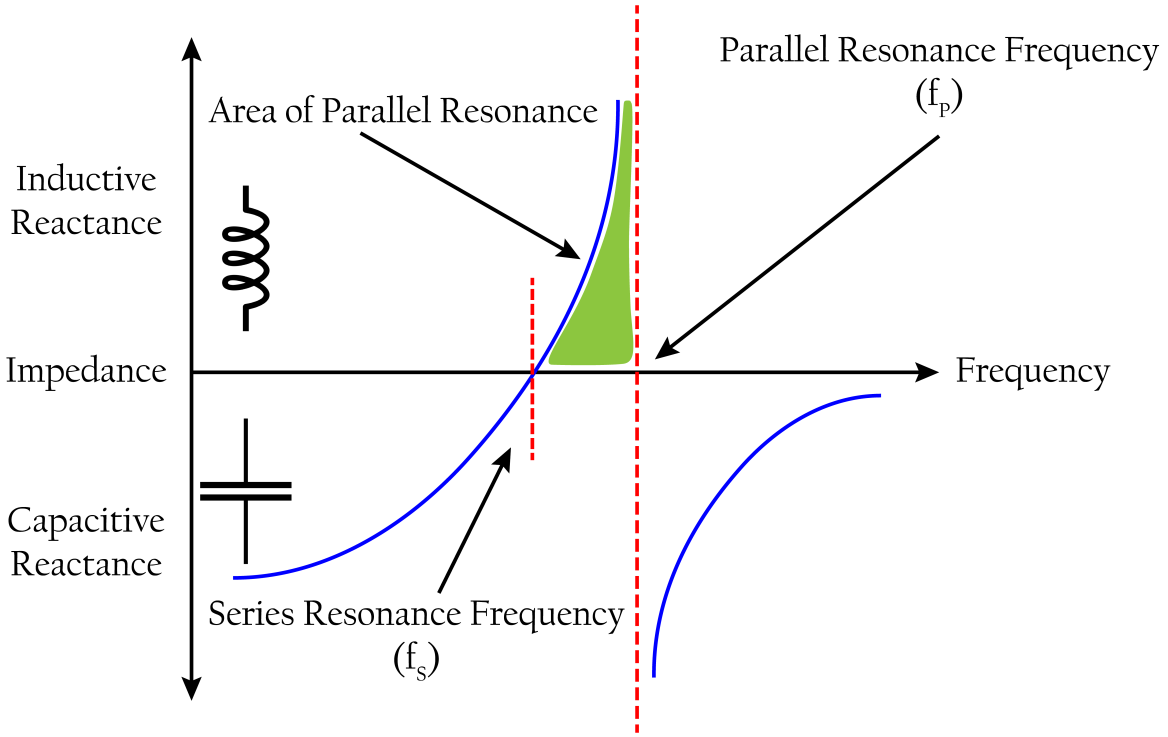

Figure 1.1: Schematics of the generalized impedance curve of a piezoelectric transducer. The curve is drawn schematically and inspired from a Technical Article of Analog Devices.

Therefore, it is important to understand the physical interpretation of real and imaginary components of complex f_p. The real component of f_p indicates the parallel resonance frequency ($f = \omega/2\pi$), whereas, the imaginary component of f_p pertains to the resonance width. [24].

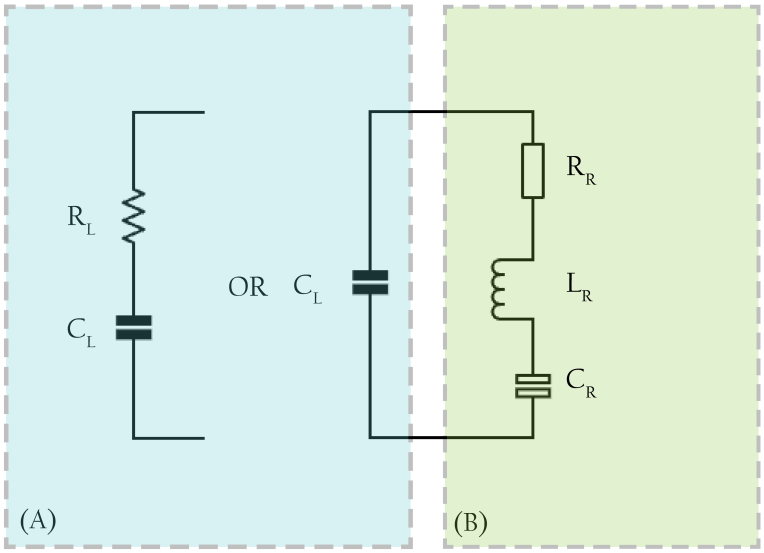

Figure 1.2: Equivalent circuit for the operational piezoelectric transducer. (A) Lumped element equivalent of piezoelectric element. (B) Electrical resonance in a RLC circuit analogous to the mechanical response of the transducer.

The IEEE standard on piezoelectricity [25] recommends the Van Dyke circuit model which has been widely used for representing the equivalent circuit of a piezoelectric resonator. The Van Dyke model is shown in Fig. 1.2 which uses five real circuit parameters, R_L, C_L, R_R, L_R, and C_R, to represent the operation of piezoelectric transducer near its resonance. The modified Van Dyke model [24] considers a piezoelectric ceramic as a capacitor (C_L) and the losses of the capacitor by a frequency-independent resistor (R_L) added in series as shown in Fig. 1.2 (A). The parallel resonance frequency of the piezoelectric resonator is defined by f_p, similarly there exists another parameter f_s which gives the series resonance frequency. The series resonance frequency f_s for a piezoelectric transducer is represented schematically in Fig. 1.1. The resonance frequencies, f_s and f_p determine the impedance shape of the piezoelectric resonance curve. The series resonance frequency is generally defined in the form of transcendental equation and the solution of the equation gives the numerical value of the series resonance frequency. The transcendental equation is given by the following [23, 24, 26, 27],

$$f_s = \frac{2}{\pi} k_t^2 f_p \cot\left[\frac{\pi}{2}\frac{f_p - f_s}{f_p}\right] \tag{1.4}$$

The series and parallel resonance frequencies are also known as resonance and anti-resonance frequencies, respectively. The complex circuit constants in terms of the material constants can be written in the following way [24, 26],

$$\begin{aligned} C_R &= \frac{\epsilon_{33}^S (A/t)}{1 - k_t^2} \times \frac{f_p^2 - f_s^2}{f_p^2} \\ L_R &= \frac{1}{4\pi^2 f_s^2 C_R^2} \\ C_L &= \frac{\epsilon_{33} A/t}{1 - k_t^2} - C_R. \end{aligned} \tag{1.5}$$

It would be valid to argue that because f_s and f_p are functions of material constants, therefore the complex circuit parameters C_L, L_R, and C_R also depend on material constants. The electrical properties of a transducer is of relevance to the work in the Chapter 3, 4, 5, and 6. The equivalent complex circuit parameters of a piezoelectric transducer are necessary to design electrical circuits to drive the transducers. The phase of the ultrasound waves emitted by the transducer is governed by the impedance characteristics of the piezo element, which is the focus of work mentioned in Chapter 4 and 5. The connection between the sound speed and the conductivity is discussed in Chapter 6 of this thesis.

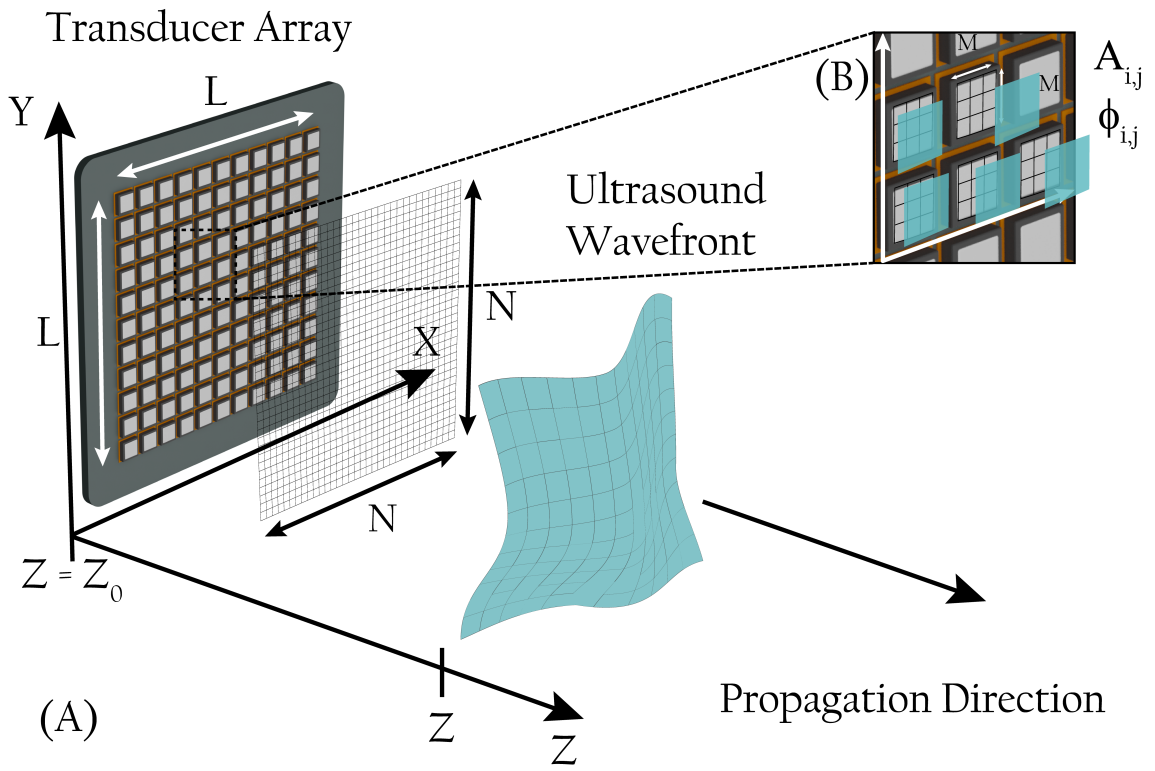

Figure 1.3: The discretized input plane for computation of pressure fields produced by a transducer array. (A) The plane containing the transducer array is discretized in a $N \times N$ grid for the angular spectrum calculations where the input pressure plane of an individual transducer is initialized in a (B) $M \times M$ grid such that $N > M$. The spectral propagation of waves is then evaluated in a $N \times N$ grid for the calculations.

1.3 Characterization of a Transducer Array

The discussion in this section draws from and is largely based on the work referenced as [28]. In an array, the fields produced by the individual transducer elements overlap to generate the pressure wave. There are various methods to compute the pressure fields in parallel planes including the angular spectrum approach which is known for its rapid computation. It is also useful in computing acoustic holograms [29]. The angular spectrum calculation firstly decomposes the propagating wave into the components of plane waves via the two-dimensional (2D) Fourier transform of the time domain signal [30]. Next, the process involves propagating the components of the plane wave within the frequency domain, followed by calculating the pressure field in the spatial domain using the inverse Fourier transform. The initial input is defined as the pressure field in a specified plane, although it can also be replaced with the velocity field derived from the deformation vector of the transducer surface. Ultimately, the output is the pressure evaluated across a series of parallel planes. The primary function of the Fourier transform is to relate the spatial variation of pressure field and angular spectrum at each plane. The schematic representation of

the geometry and variables employed in the angular spectrum approach is shown in Fig. 1.3. The propagation of the acoustic waves in a homogeneous medium can be described in the spatial frequency domain as [28, 31, 32],

$$P(k_x, k_y, z) = P_0(k_x, k_y, z_0) H_P(k_x, k_y, z - z_0)[28] \tag{1.6}$$

or

$$P(k_x, k_y, z) = j\rho c U_0(k_x, k_y, z_0) H_U(k_x, k_y, z - z_0)[28] \tag{1.7}$$

where k_x and k_y are the wavenumbers in the transverse plane such that $k_x^2 + k_y^2 + k_z^2 = k^2$. [28] The 2D Fourier transform of $p_0(x, y, z_0)$ with respect to x and y is represented by $P_0(k_x, k_y, z_0)$ and similarly, the 2D Fourier transform of the normal particle velocity of the transducer surface discretized in a $M \times M$ grid is represented as $U_0(k_x, k_y, z_0)$. [28] The angular spectrum of the pressure in a plane parallel to the source plane given by $z = z_0$, is represented by $P(k_x, k_y, z)$ as shown in Fig. 1.3 (A). Subsequently, the pressure field for each plane at z can be computed by taking the inverse Fourier transform of $P(k_x, k_y, z)$ with respect to k_x and k_y. The propagation function for an input pressure plane is described as follows [28],

$$H_P(k_x, k_y, z - z_0) = \begin{cases} e^{-j(z-z_0)\sqrt{k^2 - k_x^2 - k_y^2}} & \text{if } k_x^2 + k_y^2 \leq k^2 \\ e^{-(z-z_0)\sqrt{k_x^2 + k_y^2 - k^2}} & \text{if } k_x^2 + k_y^2 > k^2 \end{cases} \tag{1.8}$$

The expression defined in the Eq. 1.8 is $H_P(k_x, k_y, z - z_0)$ which describes propagating waves in the angular space where $k_x^2 + k_y^2 \leq k^2$. The functions describing the wave propagation in the Eq. 1.8 can be multiplied by a factor $(S(k_x, k_y, z - z_0))$ for performing calculations in attenuating media. The attenuation factor $S(k_x, k_y, z - z_0)$ can we written as [28],

$$S(k_x, k_y, z - z_0) = e^{-\alpha k (z - z_0)/\sqrt{k^2 - k_x^2 - k_y^2}}, \tag{1.9}$$

where α is the attenuation coefficient for a fixed ultrasound frequency. The inverse Fourier transform of the term $S(k_x, k_y, z - z_0) * H(k_x, k_y, z - z_0)$ provides the equivalent attenuation in the spatial domain.

The angular spectrum approach begins by discretizing the pressure or normal particle velocity field of the source within the spatial domain, as demonstrated in Fig. 1.3 (A). Here, a $L \times L$ plane of the transducer array is divided into a grid comprising $N \times N$ points, with a spatial sampling distance denoted as δ_N. In this grid setup, each individual transducer occupies $M \times M$ grid points, as depicted in Fig. 1.3 (B). It should be noted that the pressure or velocity vector represented as $A_{i,j}$ (Fig. 1.3 (B)) must be governed by the actuation amplitude of transducer element which is spatially occupying the respective $M \times M$ grid points. A similar constraint must be applied to

the actuation phase $\phi_{i,j}$ (Fig. 1.3 (B)) of transducer elements. The variables $A_{i,j}$ and $\phi_{i,j}$ are critical to the work presented in Chapter 4 and Chapter 5 where the mentioned variables are computed to dynamically generate ultrasound wavefront. A Fast Fourier Transform (FFT) algorithm can be used to compute the angular spectrum of the input pressure field. The primary reason for multiple grid points for discretizing the space of single transducer is to increase the resolution in the spatial frequency domain. This increased resolution plays an important role in reducing the spectral aliasing errors and artefacts. The spectral sampling rate is denoted as Δk, which allows us to express the discretized transverse wavenumbers as follows [28],

$$k_x = m\Delta k \text{ and } k_y = n\Delta k \tag{1.10}$$

where m and $n \, \epsilon \, [-N/2+1+\phi, N/2+\phi]$ and ϕ is defined to be $-1/2$ and 0 for odd and even values of N, respectively [28, 33]. The parameter ϕ corrects the offset caused by the odd number of grid points, ensuring that both m and n are integers. In the discussions found in Chapter 4 and Chapter 5 of the thesis, we employ the angular spectrum approach. Here, we calculate the excitation phase for each transducer element to achieve the desired acoustic wavefront, as illustrated in fig. 1.3 (B). Typically, the pressure field generated by a phased array can be described as the sum of the complex pressures that the transducer array produces, which is given by [28],

$$p_0(x,y) = \sum_{i=1}^{N}\sum_{j=1}^{N} A_{ij}(x,y)e^{j\phi_{ij}(x,y)}. \tag{1.11}$$

The pressure field $p_0(x,y)$ mentioned in Eq. 1.11 provides the source pressure at points (x,y) in the input plane $z = z_0$, which then can be multiplied by the appropriate propagation function in frequency domain for the calculations for the wavefront at the parallel planes [28, 30].

The theoretical framework outlined in this chapter serves as a foundation for comprehending the research presented in this thesis. This research explores innovative methods for generating ultrasonic fields. Chapter 4 and Chapter 5 demonstrate how the incorporation of light as a control element can enhance the simplicity of operating transducer arrays. Furthermore, Chapter 6 investigates the modulation of wave characteristics through the passage of acoustic fields within a medium, ultimately presenting a design for a device capable of dynamically modulating ultrasound fields.

2 Secondary Bjerknes Forces and Microbubble Array

The contents of this chapter have been published in Physical Review Letters under an open access license [34]. The author performed the experimentation work and the theoretical analysis was undertaken together with Dr. Athanasios Athanassiadis and Dr. Zhichao Ma.

2.1 Resonance of Air Bubbles in Water

Air bubbles are prominent source of scattering of acoustic waves and thereby are used as contrast agents for ultrasound. The acoustic properties of single air bubbles in water generally depend on the volume of the bubble [35]. There exists a large difference between the acoustic impedances of air and water, therefore the air bubbles can act as a mean to scatter sound effrectively. The oscillation of bubbles in the monopole mode involves a radical movement of the bubble surface, expanding and contracting while maintaining its shape, gives rise to a large scattering cross-section. The mathematical description of a monopole mode of a spherical bubble is given by Minnaert Resonance [36]. It is based on a theoretical bubble, assuming that the process is adiabatic and disregarding any losses caused by water viscosity and thermal damping. This leads to the frequency ω_0 of the monopole resonance given by [36],

$$\frac{\omega_0 a}{c} = k_0 a = \frac{1}{c} \times \sqrt{\frac{3\gamma P_A}{\rho}}, \tag{2.1}$$

where k_0 is the propagation wave number at resonance space,a is the bubble radius, γ is the ratio of the gas specific heats ($\gamma = \frac{C_P}{C_V}$, where C_P and C_V are specific heat capacities of gas at constant pressure and volume respectively),and P_A, ρ, and c are the ambient pressure, density, and sound speed, respectively, of the surrounding liquid. For an air bubble at atmospheric pressure in water ($c = 1483\,\mathrm{m/s}$) the value of $k_0 a$

= 0.0136, the wavelength at resonance is around 100 mm for 250 µm bubble radius which is several hundred times greater than the bubble radius [37]. The presence of multiple air bubbles in water is very different from a single air bubble. The interplay of multiple air bubbles within the scattered acoustic field alters how sound travels, especially in dense bubble clouds compared to a single bubble. Understanding the acoustic interactions between these bubbles is crucial for the experimental studies discussed in this chapter. [38].

The main physical aspect of how sound scatters from a group of interacting bubbles is that the monopole resonance of the bubble cluster differs from that of a single bubble. At the monopole resonance frequency, the acoustic wavelength is significantly larger than the size of an individual bubble and also exceeds the typical distance between adjacent bubbles in the group. It's important to understand that, at this frequency range, the bubbles aren't seen as separate entities by an external sound source. Therefore, imagining sound rays bouncing back and forth between individual bubbles isn't quite accurate. Instead, it's more fitting to consider that the bubbles are collectively responding to a shared external field. Moreover, when an external field is present, the oscillating bubbles are coupled in such a way that they act as a unified source of acoustic scattering. [39].

The interaction between bubbles in water significantly impacts their fundamental properties by altering the collective resonance frequency compared to that of individual bubbles. It's crucial to consider these shifts in resonance frequency for the analyses presented in this chapter to ensure precise calculations [40]. By recombining the equations that describe each bubble's resonances, we can develop a mathematical framework that simplifies the analysis of scattering from multiple bubbles. This allows us to concentrate on the scattering behavior of each normal mode within the ensemble. A model based on coupled oscillators was introduced to effectively capture the acoustic resonance of several bubbles [41]. This model stands out because it offers a clear insight into how frequency shifts within bubble ensembles correlate with various controlled parameters in the system.

2.2 Radiative Coupling in Resonant Bubbles

The physical behavior of a population of resonating bubbles cannot be sufficiently represented by the classical theory of linear acoustic propagation [42]. The classical theory assumes the independent oscillation of bubbles, however it has been shown experimentally in the literature that the bubbles are strongly coupled by acoustic radiation. Therefore, the most accurate way of understanding the sound propagation is through the collective action of the medium. The fundamental theoretical work was performed by C. Feuillade in late 1990s [43–45]. Since then the method developed

by him has been employed to provide adequate description and theoretical characterization of bubble clouds. This section of the thesis briefly presents the theoretical background on the ensemble of interacting bubbles. The formulations [41, 43, 45] presented helps in the understanding of behavior of bubbles interacting through the scattered acoustic field. The equation governing the motion of a monopole resonance within a spherical bubble can be expressed as follows [43, 45, 46],

$$m\ddot{v} + b\dot{v} + \kappa v = -Pe^{\iota\omega t} \tag{2.2}$$

The variable v represents the differential volume, indicating the difference between the bubble's instantaneous volume and its equilibrium volume. The coefficient m is referred to as the inertial mass of the bubble, while κ denotes the adiabatic stiffness of the bubble. These can be calculated using the relationships outlined below [43, 45],

$$m = \frac{\rho}{4\pi a} \tag{2.3}$$

$$\kappa = \frac{3\gamma P_A}{4\pi a^3}. \tag{2.4}$$

The coefficient b characterizes how the bubble's motion is dampened, while P and ω denote the amplitude and frequency of the external pressure field acting on the bubble, respectively. It should be noted that P is preceded by a negative sign since a decrease in pressure results in an increase in the volume of the bubble [43, 44, 47]. A harmonic steady-state solution of the mathematical form $v = \bar{v}e^{\iota\omega t}$ can be assumed for the sinusoidally varying input pressure wave, substitution of the solution gives the resonance response which can be defined as [48],

$$\bar{v} = \frac{-P}{\kappa - \omega^3 m + \iota\omega b} = \frac{-P/m\omega^2}{[\omega_0^2/\omega^2 - 1] + \iota(b/m\omega)} \tag{2.5}$$

where $\omega_0 = \sqrt{\kappa/m}$ is Minnaert's resonance frequency. The expression of Eq. 2.5 describes a Lorentzian response. It should be noted that the imaginary component $b/m\omega$ in the denominator of Eq. 2.5 can be denoted with a damping constant δ_c which reflects radiative, thermal, and viscous terms, which can be written as,

$$b/m\omega = \delta_c = \delta_r + \delta_t + \delta_v \tag{2.6}$$

The radiation damping component is explicitly expressed as $\delta_r = ka$, where $k = \omega/c$. Additionally, the quality factor Q at the resonance frequency of the response can be defined and related to b by the following equation:

$$Q = \omega_0 m/b \tag{2.7}$$

The acoustic field reradiated by the bubble is predominantly monopolar such that the pressure field at the radial distance r from the bubble due to reradiation/scattering is given by [37],

$$p(r) = (\rho e^{-\iota kr}/4\pi r)\ddot{v} \tag{2.8}$$

Therefore, an external pressure field driving an ensemble of N interacting bubbles in

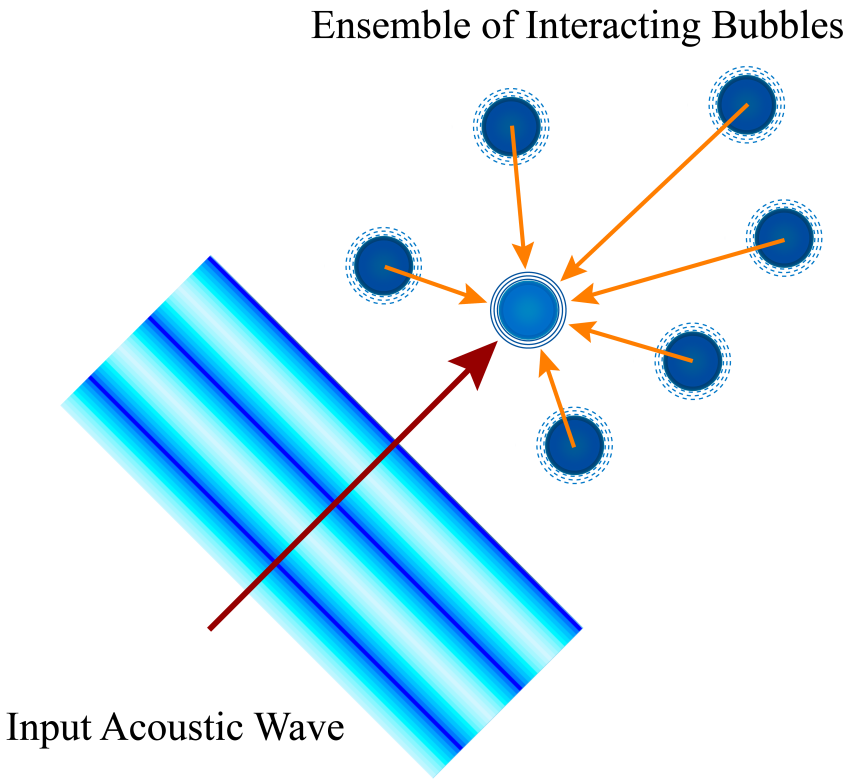

Figure 2.1: The schematic diagram shows that the total field impacting the primary bubble is a combination of the external field (red arrow) and the scattered fields coming from the neighboring bubbles (yellow arrows). The schematic is inspired from [43, 44, 47]

a full space can now be considered to define the total incident field that acts on an individual bubble. The pictorial representation for ensemble of interacting bubbles is shown in Fig. 2.1. The total field acting on any given bubble is composed of the primary external field along with the cumulative scattered fields from the remaining $N-1$ neighboring bubbles. The overall response of the entire bubble ensemble can be

expressed through a series of coupled differential equations, as shown below [44, 47],

$$\begin{aligned}
m_1\ddot{v_1} + b_1\dot{v_1} + \kappa_1 v_1 &= -P_1 e^{(\iota\omega t+\phi_1)} - \sum_{j\neq 1}^{N} \frac{\rho e^{-\iota k r_{j1}}}{4\pi r_{j1}}\ddot{v}_j, \\
&\vdots \\
m_n\ddot{v_n} + b_n\dot{v_n} + \kappa_n v_n &= -P_n e^{(\iota\omega t+\phi_n)} - \sum_{j\neq n}^{N} \frac{\rho e^{-\iota k r_{jn}}}{4\pi r_{jn}}\ddot{v}_j, \\
&\vdots \\
m_N\ddot{v_N} + b_N\dot{v_N} + \kappa_N v_N &= -P_N e^{(\iota\omega t+\phi_N)} - \sum_{j\neq N}^{N} \frac{\rho e^{-\iota k r_{jN}}}{4\pi r_{jN}}\ddot{v}_j,
\end{aligned} \tag{2.9}$$

where P_n represents the amplitude and ϕ_n denotes the phase of the external field acting on the n^{th} bubble, r_{jn} indicates the radial distance from the center of the n^{th} bubble to the center of the j^{th} bubble [43, 44, 47]. The harmonic steady-state solutions are still valid for the set of equations defined in 2.9, therefore by substituting $v_n = \bar{v}_n e^{\iota\omega t}$ in 2.9, a matrix equation can be obtained which may be written as,

$$MV = P, \tag{2.10}$$

where $v = \{\bar{v}_1, ..., \bar{v}_n, ..., \bar{v}_N\}$ and $p = \{-P_1 e^{\iota\phi_1}, ..., -P_n e^{\iota\phi_n}, ... - P_N e^{\iota\phi_N}\}$, are column vectors representing the steady-state volume oscillation amplitudes and the external fields for each bubble, respectively, and M is an $N \times N$ matrix with elements,

$$\begin{aligned}
M_{nn} &= \kappa_n - \omega^2 m_n + \iota\omega b_n, \\
M_{nj} &= \tfrac{-\omega^2 \rho e^{-\iota k r_{jn}}}{4\pi r_{jn}} (n \neq j),
\end{aligned} \tag{2.11}$$

The diagonal elements M_{nn} represent the characteristics of an individual bubble in the ensemble and can incorporate variations in size, damping, and other dependent variables. The radiative coupling between the bubbles is described by the off-diagonal elements M_{nj} which can be physically interpreted through scattered sound fields. The solution to the matrix equation $v = M^{-l}p$ allows us to characterize steady-state scattering from the entire group of bubbles based on the amplitude and frequency of the external field [43, 44, 47].

The case of just two interacting bubbles can be understood by observing two coupled differential equations of the sequence (2.9). The two bubbles are assumed to have identical geometric and physical properties which means that $m_1 = m_2 = m$ and $b_1 = b_2 = b$ and are separated by radial distance r, these equations can be conveniently solved by forming their sum and their difference. It is also assumed that both bubbles experience the same external field amplitude ($P_1 = P_2 = P$) which can be explained by the fact that the dimensions of bubbles are smaller than the acoustic wavelength,

then the equations can be written as [44],

$$\left\{m + \frac{\rho e^{-\iota kr}}{4\pi r}\right\}(\ddot{v_1} + \ddot{v_2}) + b(\dot{v_1} + \dot{v_2}) + \kappa(v_1 + v_2) = -P(e^{\iota\phi_1} + e^{\iota\phi_2})e^{\iota\omega t}, \tag{2.12}$$

$$\left\{m - \frac{\rho e^{-\iota kr}}{4\pi r}\right\}(\ddot{v_1} - \ddot{v_2}) + b(\dot{v_1} - \dot{v_2}) + \kappa(v_1 - v_2) = -P(e^{\iota\phi_1} - e^{\iota\phi_2})e^{\iota\omega t}. \tag{2.13}$$

The combined quantity $v_1 + v_2$ is often represented as v_+, which corresponds to the symmetric oscillation mode of two bubbles. This symmetric resonance mode describes a scenario where the bubbles oscillate together, in phase, and with identical amplitudes. It's important to highlight that when the bubbles are excited by a plane wave that travels perpendicular to the line connecting them, the phase difference between the two bubbles will be negligible, leading to the activation of the symmetric mode in the system. In general, the phase difference in the excited field of the two bubbles remains quite small since, as previously noted [43, 44, 47], the acoustic wavelength at the bubble's resonance frequency is significantly larger than both the distance between the bubbles and their individual sizes. The symmetric mode effectively has an increased mass due to the radiative coupling between the bubbles. Thus, under the assumption of harmonic steady state, we can express the solution to Eq. 2.12 as follows:

$$\bar{v}_+ = \frac{-P(e^{\iota\phi_1} + e^{\iota\phi_2})}{\kappa - \omega^2\left\{m + \frac{\rho e^{-\iota kr}}{4\pi r}\right\} + \iota\omega b} \tag{2.14}$$

$$\bar{v}_+ = \frac{-P(e^{\iota\phi_1} + e^{\iota\phi_2})}{\kappa - \omega^2 m_+ + \iota\omega b_+}, \tag{2.15}$$

where an expansion of $e^{-\iota kr}$ into its real and imaginary components is performed to give the following relations,

$$m_+ = m + \frac{\rho\cos kr}{4\pi r} \tag{2.16}$$

$$b_+ = b + \frac{\omega\rho\sin kr}{4\pi r}. \tag{2.17}$$

The symmetric mode resonates at a frequency different from that of a single bubble and is denoted by ω_{0+} and the corresponding wave number for acoustic wave propagation can be written as $k_{0+} = \omega_{0+}/c$. Application of Minnaert's resonance frequency procedure then gives [41, 44],

$$\omega_{0+} = \sqrt{\frac{\kappa}{m_+}} = \sqrt{\frac{\kappa}{m\left[1 + \frac{\rho\cos k_{0+}r}{4\pi rm}\right]}} = \frac{\omega_0}{\sqrt{\left(1 + \left[\frac{a}{r}\right]\cos\frac{\omega_{0+}r}{c}\right)}} \tag{2.18}$$

It should be noted that the frequency ω_{0+} does not depend upon the damping of

the individual bubbles or the amplitude of the incident field [43, 44, 47], but only upon the value of ω_0 and the radial distance between the bubbles. The conclusive statement of this section is that the resonance frequency of ensemble of interacting bubbles is smaller than the frequency of individual oscillating bubbles. The collective in-phase oscillation of interacting bubbles is called as "symmetric" normal mode and this principal is presented experimentally in the later sections of this chapter.

2.3 Bubbles Trapped in Circular Microcavities

Microfluidics is an exciting scientific tool that's really making waves in the research community thanks to its remarkable precision! At the heart of this technology are microbubbles, which shine brightly when driven by acoustic fields. In the world of lab-on-a-chip applications, microbubbles are absolutely crucial in acoustofluidic devices, as highlighted by numerous studies [49–53]. One of the fascinating phenomena we'll explore in this chapter is the secondary radiation force (SRF), also known as the Secondary Bjerknes force [54–58].

But that's not all! Oscillating bubbles are also being utilized in a plethora of applications such as micropumps [59], microtweezers [60–62], microfilters [63, 64], microrotors [64], biosensors [65], microswimmers [66, 67], and sorting techniques [68–70]. A wealth of literature exists around the theoretical predictions of bubble dynamics and their resonant behaviors, originally explored by M. Minnaert, who is famous for the [71] Minnaert frequency.

The dynamics of spherical bubbles, whether they're free or confined in cavities, have been extensively modeled in the literature, with pioneering contributions from Rayleigh [72] and Plesset [73], among others. Vincent and Marmottant [74] have put together a fantastic overview of cutting-edge technologies arising from fully confined bubbles. However, the situation with partially confined bubbles presents a unique challenge, as they're quite different in terms of parametric dependence.

When comparing free spherical bubbles to those that are trapped, we find that the latter offer enhanced stability and controllability. These intriguing characteristics have been recognized and applied in various experimental microfluidics applications. Nonetheless, there's still a gap in the theoretical studies on this topic, particularly regarding semi-cylindrical bubbles trapped in rectangular cavities [75, 76] and rectangular bubbles situated on a rectangular horse-shoe structure [77]. A key assumption made in this work is that the gas-liquid interface can be modeled as a thin clamped plate, which allows us to leverage existing theories of vibrations for solid plates [78, 79]. The potential here is tremendous, and the journey of discovery is just beginning!

Oscillations of a single free spherical bubble, as noted in previous research [80], are not applicable to a trapped bubble due to the constraints imposed by clamped

boundary conditions. Nevertheless, theories surrounding bubble interactions can be harnessed [81, 82], particularly focusing on scenarios involving pairs of bubbles, which take into account microstreaming effects and secondary radiation forces (SRF). A significant alteration necessary for addressing the experimental framework outlined in this chapter is replacing the Minnaert frequency with that relevant to a partially confined bubble. Previous investigations by Miller [83, 84] and Gelderblom [85] have explored the dynamics of bubbles trapped within circular cavities. The remainder of this chapter aims to analyze the experimental responses of gas-filled cylindrical microcavities when subjected to ultrasound. The analytical model applied in this section is based on the work of Dmitry Goetinski [80], who formulated approximate analytical and semi-analytical solutions. The solution to the problem of obtaining resonance frequency for a fundamental mode of interface oscillations starts by defining the time-dependent interface displacement $[W(r,\theta,t)]$. The interface displacement W can be assumed to have harmonic time dependence because of the sinusoidal variation in the input given to the bubble and therefore can be written in the following way [86–88],

$$W(r,\theta,t) = w(r,\theta)e^{\iota\omega t} \tag{2.19}$$

The interface displacement W exhibits harmonic time dependence, stemming from the sinusoidal input applied to the bubble. In this context, the variables A, κ, and ω denote the amplitude of the oscillations at the interface, the radial wave number, and the frequency of the driving force, respectively [41, 44]. The time-independent bubble displacement $w(r,\theta)$ is articulated by the following equation: [41, 44],

$$\nabla^4 w(r,\theta) - \kappa^4 w(r,\theta) = 0. \tag{2.20}$$

The differential equation mentioned in (2.20) is a fourth-order differential equation with the general solution given by [41, 44]:

$$w(r,\theta) = (J_n(\kappa r) + cI_n(\kappa r)) \times (A\cos(n\theta) + B\sin(n\theta)) \tag{2.21}$$

where $J_n(\cdot)$ and $I_n(\cdot)$ [89] stand for the Bessel and modified Bessel functions of the first kind of order n and A, B, and c are arbitrary constants which can be explicitly calculated from the boundary conditions. We have used MATLAB 2020A to find the solutions for a non-linear multivariate system of equations.

An analytical model [90] has been employed to perform numerical calculations of the fundamental resonance mode of bubbles contained within a cylindrical cavity that is stimulated by an external acoustic field. This model operates under the premise that the air-water interface behaves like a thin clamped circular membrane, oscillating in a vertical direction. The formula for the resonant frequency of a single bubble is

expressed as follows:

$$f_0 = \frac{1}{2\pi}\frac{\sqrt{\kappa^3\sigma J_{-n}(\kappa R_0)(\rho_1+\rho_2)-\kappa^4\eta^2}}{\rho_1+\rho_2} \tag{2.22}$$

where ρ_1 and ρ_2 are the density of water and air respectively, σ is the surface tension of the air-water interface, $J_{-n}(\cdot)$ stands for the Bessel function of the first kind of order $-n$, R_0 is the mean radius of the bubble, and η is the viscosity of water. The radial wave number is denoted by κ ($\kappa \neq 0$) which is the smallest positive root of the equation

$$\frac{J_n(\kappa R_0)}{I_n(\kappa R_0)} = \frac{J_{n-1}(\kappa R_0)-J_{n+1}(\kappa R_0)}{I_{n-1}(\kappa R_0)+I_{n+1}(\kappa R_0)} \tag{2.23}$$

where $J_n(\cdot)$ and $I_n(\cdot)$ [89] stand for the Bessel and modified Bessel function of the first kind of order n. For the lowest order radial mode, $n = 1$. The resonance frequency is calculated by substituting κ from Eq. (2.23) into Eq. (2.22). Using the geometry of our bubbles yields a resonance frequency of $f_0 = 3.98\,\text{kHz}$.

When the bubbles are patterned as an array, we expect their coupling to lower the resonance frequency [91]. The presence of a second array that is in the close vicinity of the first array will shift the resonance frequency of the bubble system to f_{0s}, which can be estimated based on the frequency shift experienced by two bubbles separated by a distance H [90]:

$$f_{0s} = \frac{f_0}{((1+2R_0/H)^2+\zeta^2)^{\frac{1}{4}}} \tag{2.24}$$

where f_0 is the resonant frequency of a single bubble (see Eq. (2.22)), R_0 is the bubble radius, and ζ is the damping coefficient of a single bubble. We have applied the theoretical model outlined in this section to establish the fundamental mode of a single bubble confined within a circular cavity [89]. This model operates on the premise that the gas-liquid interface behaves like a thin, clamped circular membrane, as previously discussed. This approach has also been utilized to forecast the resonance frequency of a coupled bubble pair. Notably, the theoretical coupling of identical bubble pairs produces a controllable frequency shift, which has been experimentally demonstrated in the latter part of the chapter.

2.4 Experimental Methods

2.4.1 Fabrication of Cylindrical Cavity in PDMS

Planar PDMS (Poly Di-Methyl Siloxane) slabs containing cylindrical cavities are fabricated using soft lithography. A 275 µm thick layer of negative photoresist (SU-8 2075, Kayaku Advanced Materials Corporation, Westborough, MA) is spin-coated on a silicon wafer (WS-650 spin coater, Laurel, PA, USA), exposed on a mask aligner

(MJB4, SUSS MicroTec, Garching, Germany) with a photomask, and then the wafer is developed and hard baked to obtain the master mold. The soft photomask that is used to create the master mold consists of an array of 11×11 transparent circular holes. The hole diameters are 300 µm and have a center-to-center spacing of 500 µm. This mask produces cylindrical posts after developing the negative photoresist with the solution MR-DEV 600, which dissolves the non-exposed photoresist. Further, a degassed mixture of PDMS prepolymer and curing agent (Sylgard 184 Silicone Elastomer Kit, Dow Corning Corporation, Freeland, MI) with a weight ratio of 10:1 is poured onto the SU-8 mold on the silicon wafer and cured at 75 °C for 2 hours. Fully cured PDMS replicas are then peeled from the wafer, leaving cylindrical cavities in the PDMS with a height $L = 275$ µm and diameter $d = 300$ µm. When the dried PDMS surface is immersed in water, air bubbles are trapped in the cavities facilitated by the small size of the cavity and the hydrophobicity of PDMS [92].

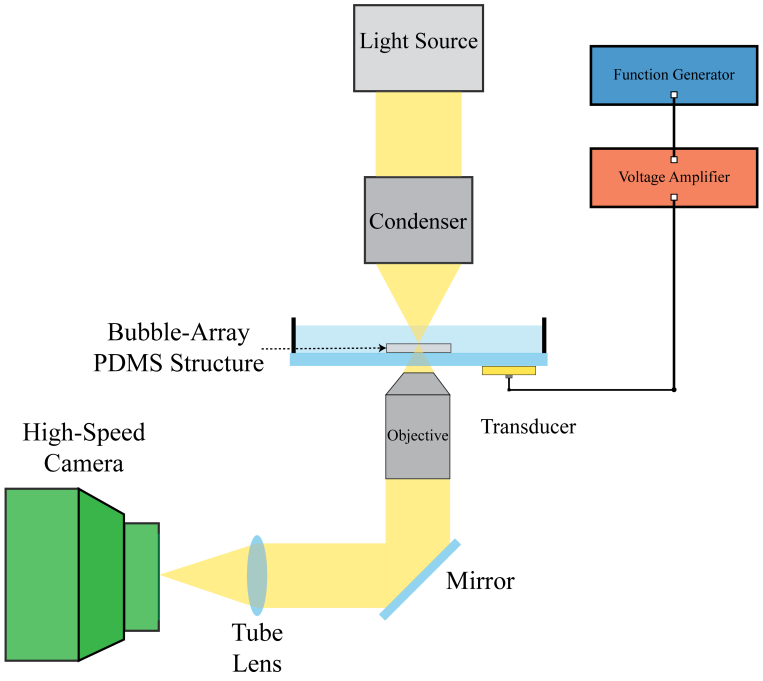

Figure 2.2: Experimental setup used for monitoring and excitation of the microbubble array. Image taken from the Supplementary Information of [34].

2.4.2 Acoustic Excitation

A piezoelectric transducer (Part #724-3162, RS Electronics) is attached to the underside of the petri dish using vacuum grease. The transducer is pushed firmly against the dish, leaving a thin acoustic coupling layer. The disk-shaped buzzer transducer has a diameter of 27 mm and a thickness of 0.52 mm. This transducer was chosen because of its size, availability, and flat response in the audible frequency range, which makes

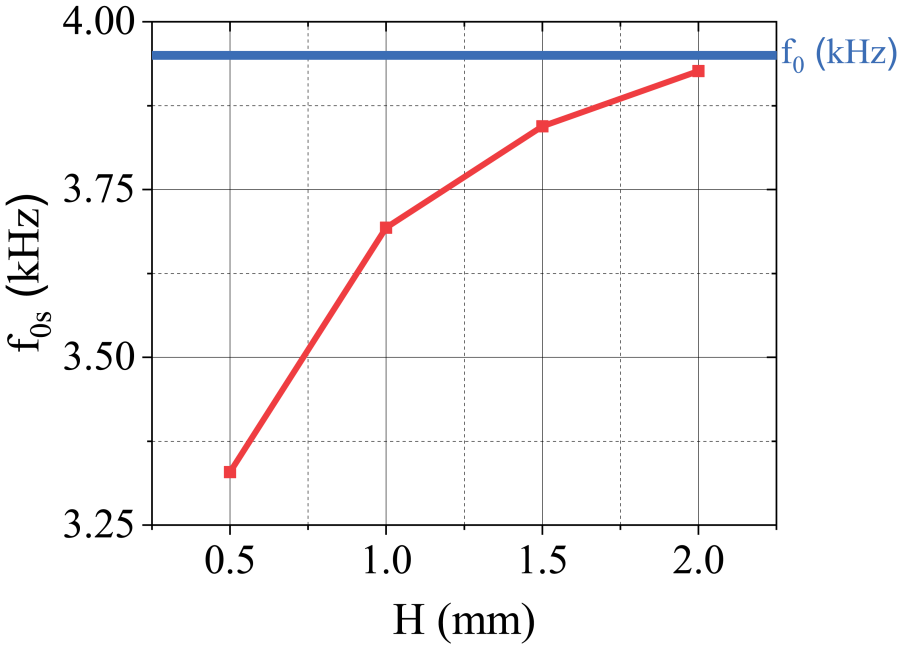

Figure 2.3: Bubble resonance frequency as a function of distance between bubble arrays H. The dark blue solid line represents the resonance frequency of a single isolated bubble of diameter 300 µm. As bubbles are brought closer together, the resonance frequency shifts downward. Image taken from the Supplementary Information of [34].

it well-suited to sweep the frequencies when searching for a bubble resonance. The signal from a function generator (AFG 1062, Tektronix) is fed to a low-impedance 50× voltage amplifier (WMA-300, Falco Systems), which drives the transducer (Fig. 2.2 (b)). The transducer was driven with 15 V signals from the signal generator. The bubble oscillations were observed in an upright microscope with a water layer covering the fixed array. The array was imaged with a 5× objective and a high-speed camera (Photron Nova S16) recording at 100,000 FPS. The resonance frequency of the bubbles determined experimentally by sweeping the frequency in the interval from 1 kHz to 10 kHz, with a resolution of 0.1 kHz, and found to be 3.3 kHz. Because the frequency of maximum oscillation does not correspond to a traditional Minnaert frequency, or a volume resonance, the resonance is instead governed by the air-water interface geometry [41, 44], as has been shown in other experiments with trapped bubbles [86, 93]. For bubbles on the order of $R_0 = 100$ µm driven below 100 kHz, damping is dominated by thermal effects and $\zeta \approx 0.1$ [48]. The bubble resonance as a function of bubble spacing H is plotted in Figure 2.3. For a bubble spacing of $\Delta = 0.5$ mm in the array, we expect a resonance frequency of $f_{0s} = 3.3$ kHz. This is in excellent agreement with our experimentally determined resonance frequencies.

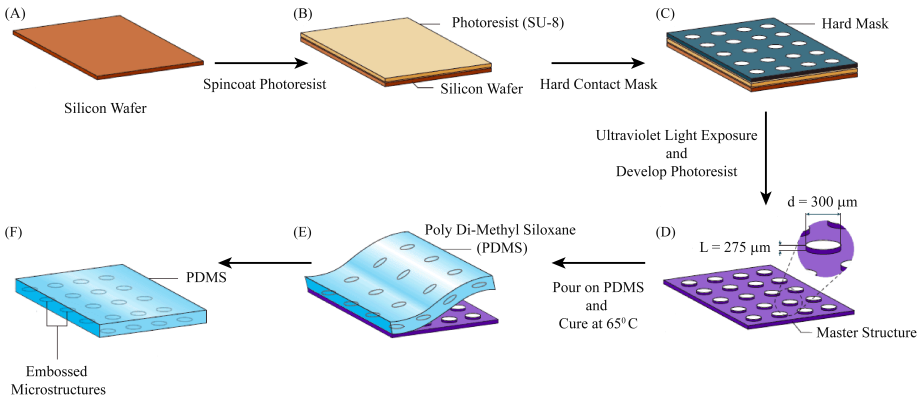

Figure 2.4: Fabrication of a Poly Di-Methyl Siloxane (PDMS) layer incorporating microstructures. The graphics (A) – (D) correspond to the fabrication of a rigid master structure through the process photo lithography whereas (E) and (F) can be considered as the processing steps of soft lithography. The schematics are adapted from the Elveflow microfluidics.

2.4.3 Determination of the Bubble Oscillation Amplitude δ

The oscillation amplitude of bubbles in the PDMS plate is measured by observing the trapped bubbles under the microscope. The microscope is focused on the air-water interface of the bubble, and as the bubble interface oscillates, so does the intensity of the transmitted light, due to an optical lensing effect from the interface. Experimental images of bubbles in the PDMS plate are shown in Figure 2.5 (a) at different points in their oscillation cycle. These images clearly highlight the variation of the transmitted light through the interface as it oscillates with the frequency f_0.

The optical focusing can be modeled using the Fresnel equations [94], so that the geometry of the interface at each time step gives a two-dimensional power distribution of the transmission light which is used to calculate the magnitude of the bubble oscillations. It is assumed that initially at $t = 0$, the interface has a small enough curvature that it can be approximated as a flat surface. The power transmittance of parallel-polarized light (T_P) from a medium of refractive index (n_I) to the medium of refractive index (n_T) is given by [95],

$$T_P = \frac{n_T \cos(\theta_T)}{n_I \cos(\theta_I)} t_P^2 \tag{2.25}$$

where θ_T and θ_I are angles of the transmitted and the incident light wave with respect to the normal of the surface, and t_P is the transmission coefficient [95]:

$$t_P = \frac{2 n_I \cos(\theta_I)}{n_I \cos(\theta_T) + n_T \cos(\theta_I)} \tag{2.26}$$

In cylindrical coordinates, the interface position S_C of the fundamental resonance

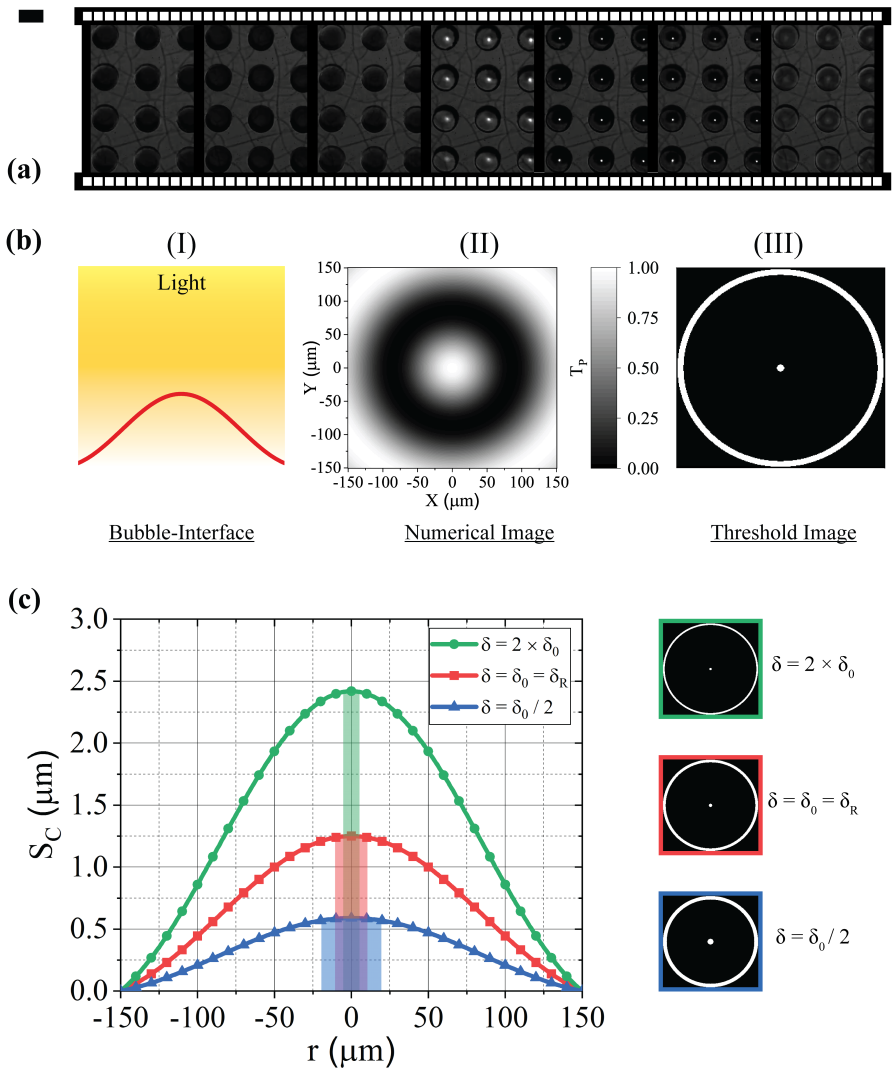

Figure 2.5: Variation in light transmission associated with bubble oscillations can be used to estimate the oscillation amplitude. (A) A series of transmitted light microscopy photographs taken regularly during one bubble oscillation at a frequency of 3.3 kHz. Scale bar: 300 µm. The images are extracted from the Movie S1. (B) (I) Modeled bubble interface shape at time $t = 1/(4f_0)$), and (II) the resultant numerical image. By thresholding the image at 95% of the max intensity, a characteristic spot size can be calculated that depends uniquely on the oscillation amplitude δ. (C) The interface shape is plotted for varying δ. The highlighted regions represent the central bright spot after thresholding (see images right). The spot size clearly depends monotonically on δ, and can therefore be used to calculate δ from experimental images. Image taken from the Supplementary Information of [34].

mode is given as

$$S_C = \delta_0 J_0(\kappa r)\sin(2\pi f_0 t) \tag{2.27}$$

where J_0 denotes the Bessel function of 0^{th} order, δ_0 is the amplitude of the interface, κ is the wavenumber in the radial direction which is substituted from Eq. (2.23), and f_0 is the resonant frequency of bubble (see Eq. (2.22)). The interface shape S_C is plotted in Fig. 2.5 (b)(I), and the corresponding transmittance is plotted in subpanel

(II). The transmittance is calculated using a 1 µm grid.

The oscillation amplitude of the experimental bubbles is identified by comparing the microscope image corresponding to peak transmission with the computed transmittance $T_P(r)$ of the interface at its maximum (time $t = 1/(4f_0)$ where $f_0 = 3.3\,\text{kHz}$). The comparison process is further simplified by isolating the image of a single bubble and then thresholding the image to 95% of the maximum intensity, as shown in Fig. 2.5 (b)(III). The size of the central spot after thresholding varies monotonically with the oscillation amplitude δ. As shown in Fig. 2.5 (c), as δ increases, the thresholded spot size decreases. The numerical results are used to calculate the spot size as a function of δ, which can then be used to directly find the value of δ from the experimental images. The resultant $\delta = 1.25\,\mu\text{m}$ is thus obtained, which corresponds to oscillations of approximately 1% of the bubble radius R_0, in good agreement with linear bubble oscillation amplitudes typically reported in the literature [96]. Because the images used to calculate δ were acquired with only a single PDMS structure, the actual value of δ in our alignment experiments may vary, because of interactions between two bubble arrays. Therefore, to determine the actual values of δ in our experiments, we fit the model trajectories to the experimental trajectories by eye. The resulting values of δ for each height are given in Table 3.2.

2.5 Secondary Bjerknes Force

C. A. Bjerknes and his son V. F. K. Bjerknes uncovered a fascinating scientific phenomenon known as the Secondary Bjerknes force [97]. According to their findings, when bubbles oscillate in sync, they attract one another, while those that oscillate out of sync repel each other. They elucidated this effect by presenting a mathematical model demonstrating that any object immersed in or moving through an accelerating fluid experiences a kinetic buoyancy. This buoyancy is equal to the product of the fluid's acceleration and the mass of the fluid that is displaced by the object. [98, 99]. The force responsible for the attraction and repulsion in the oscillating bubbles is very weak because of the low amplitude of pressure wave radiated by the bubbles oscillation. It was also observed by C.A. Bjerknes that the secondary force increases with increasing the frequency of oscillations. The secondary force between two interacting bubbles is basically based on the law of kinetic buoyancy and is analogous to the Archimedian law, when two bubbles are submitted to an oscillatory pressure field of angular frequency ω,

$$p(t) = P_0 e^{[-\iota\omega t]}$$

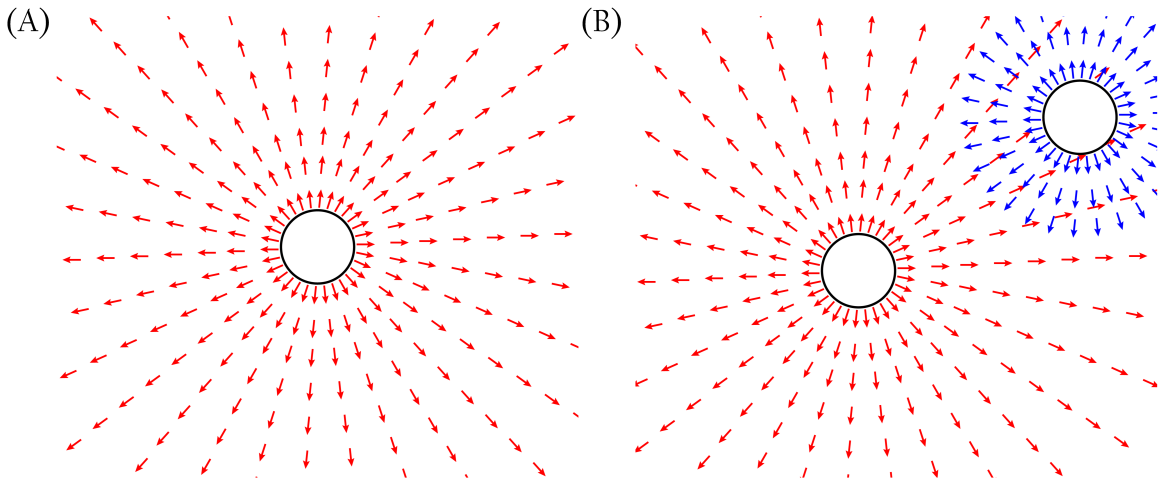

Figure 2.6: (A) Schematic representation of a pulsating bubble. The red arrows represent the velocity field. (B) Schematic representation of the bubble interaction occurring through secondary sound field scattered from the bubbles.

the secondary force between two bubbles of mean radius R_i and R_j, with respective pulsation amplitudes ΔR_i and ΔR_j separated by distance $|\vec{r}_{ij}|$ is expressed as [100],

$$\vec{F}_B = 2\pi\rho\left(R_i R_j \omega\right)^2 \left(\Delta R_i \Delta R_j\right) \frac{\vec{r}_i - \vec{r}_j}{|\vec{r}_i - \vec{r}_j|^3} \cos\left(\phi_i - \phi_j\right)$$

where ρ is the density of the liquid, $\vec{r}_i$ and $\vec{r}_j$ are the position vectors of bubbles i and j respectively which can be written as,

$$\vec{r}_{ij} = \frac{\vec{r}_i - \vec{r}_j}{|\vec{r}_i - \vec{r}_j|}$$

and each bubble is oscillating with an instantaneous radius given by,

$$R_i(t) = R_i + \Delta R_i e^{[-\iota(\omega t - \phi_i)]}$$

$$R_j(t) = R_j + \Delta R_j e^{[-\iota(\omega t - \phi_j)]}$$

For simplicity we assume that the bubbles are of equal mean radius ($R_i = R_j = R_0$) and pulsating amplitudes ($\Delta R_i = \Delta R_j = \Delta R_0$), and disregard attenuation effects ($\phi_i - \phi_j = 0$), which yields the expression for the secondary interaction force as follows [98, 99],

$$\vec{F}_B = 2\pi\rho\left((R_0)^2\omega\right)^2 \left(\Delta R_0\right)^2 \frac{\vec{r}_i - \vec{r}_j}{|\vec{r}_i - \vec{r}_j|^3} \tag{2.28}$$

When two bubbles are coupled, they should not be seen as separate resonators. Rather, they create a two-level system characterized by a symmetric mode that resonates near the Minnaert frequency of the bubbles, where ω represents the resonant frequency of the combined bubble system. The coupled system resonance frequency

can be calculated from Eq. 2.24. Given the dependence of the Bjerknes force on the relative phase of the bubbles, it is natural to obtain an attractive force for in phase excitation ($\phi_i - \phi_j = 0$), and a repulsive force for out of phase excitation ($\phi_i - \phi_j = \pi$). The work presented in this thesis focuses mainly on the attractive nature of secondary Bjerknes forces for acoustically triggered assembly applications.

2.6 Summary

This chapter discusses the frequency characterization of bubble arrays, which are fabricated using soft-lithography. The interaction of oscillating bubbles is described as well as an experimental method to accurately determine the amplitude of oscillation is presented. The concept of the secondary Bjerknes force is introduced which is the result of coupling between the scattered sound field from bubbles. The resonance frequency obtained experimentally is consistent with the theoretical predictions employed for coupled resonant system of microbubble array. We have experimentally measured the pulsation amplitude of bubbles in the acoustic field based on optical measurements and the resultant amplitude corresponds to oscillations of approximately 1% of the bubble radius R_0.

3

Amplification of Secondary Bjerknes Forces Enables Acoustofluidic Manipulation

The chapter is adapted from a paper which first appeared in Physical Review Letters under an open access license [34]. The author performed all the experimentation work and the theoretical analysis was undertaken together with Dr. Athanasios Athanassiadis and Dr. Zhichao Ma.

3.1 Acoustofluidic Manipulation and Assembly

Sound, from a long time has been an interesting candidate to manipulate particles due to its contact-free nature and low attenuation in liquids. The acoustic assembly using primary radiation force on the particles is the topic of majority work that exists in the literature. The pattern of assembly is dependent on the geometrical shape of the acoustic field, and the size of the particles is restricted by the acoustic wavelength. Thus, the spatial complexity together with the necessary electrical power to produce sufficiently large primary radiation force scale unfavourably with the size of the individual components, this poses a great challenge for the primary radiation force to direct the assembly of macrostructures.

Recently, a promising approach for manipulation and directed assembly is through the application of acoustic fields. Acoustic fields can propagate through most media and generally do not require special responsive materials [34, 101–105]. The acoustic assembly techniques that exists are fundamentally restricted by the wavelength of sound [34]. The following constraints entail the acoustic assembly:

- The dimension of the manipulated object must be smaller the wavelength of acoustic field.
- The accuracy of positioning is controlled by the field shape and hence the min-

imum feature size also cannot be smaller than the acoustic wavelength.

Acoustic fields with longer wavelengths tend to perform better in water applications due to the increase in attenuation that occurs with higher operational frequencies. While shorter acoustic wavelengths can provide more precise positioning, they come with the downside of higher attenuation, which leads to less effective acoustic excitation. Consequently, a trade-off arises for larger objects or structures that could greatly benefit from assembly and manipulation techniques utilizing acoustic fields.

It is intriguing to delve into secondary interactions within the realm of acoustic assembly. In this chapter, we explore how air bubbles offer a distinctive method for acoustically guiding the assembly of macrostructures through the interplay of the scattered sound field. We introduce an innovative approach for assembling and manipulating macrostructures facilitated by the secondary acoustic radiation forces that arise between resonant scatterers, as depicted in Fig 3.1. These resonant scatterers are activated by a sound field. Microbubbles, which scatter sound efficiently and are typically subwavelength in size, play a crucial role here. The sound fields scattered by these bubbles create a coupling effect that leads to secondary radiation forces, commonly referred to as secondary Bjerknes forces [97].

Notably, individual bubbles have been effectively controlled using these forces [106], which directly contributes to the clustering behavior observed in bubble ensembles when they are stimulated by an acoustic field [107–110]. Although secondary Bjerknes forces generally operate within the 10 nN range, making them seem inadequate for larger systems, this chapter demonstrates how these secondary radiation forces can be enhanced between approximately ~ 100 µm bubbles. This enhancement allows acoustic assembly and manipulation techniques to be utilized on cm-scale structures, as illustrated in Fig. 3.2. Importantly, we employ acoustic fields with wavelengths significantly larger than the objects and bubbles, effectively overcoming the constraints posed by primary radiation forces.

3.2 Amplification of Secondary Bjerknes Force

The secondary Bjerknes force generally depends on the oscillation amplitude of bubbles and the frequency of acoustic field [100]. The secondary Bjerknes force experiences by a bubble of radius R_0 located at the origin, due to an identical bubble located at position $\vec{r}$, is given by [100]:

$$\vec{F}_B = 2\pi\rho R_0^4\omega^2\delta^2\vec{r}/r^3. \tag{3.1}$$

where the notations are described as follows,

- ρ is the density of the liquid

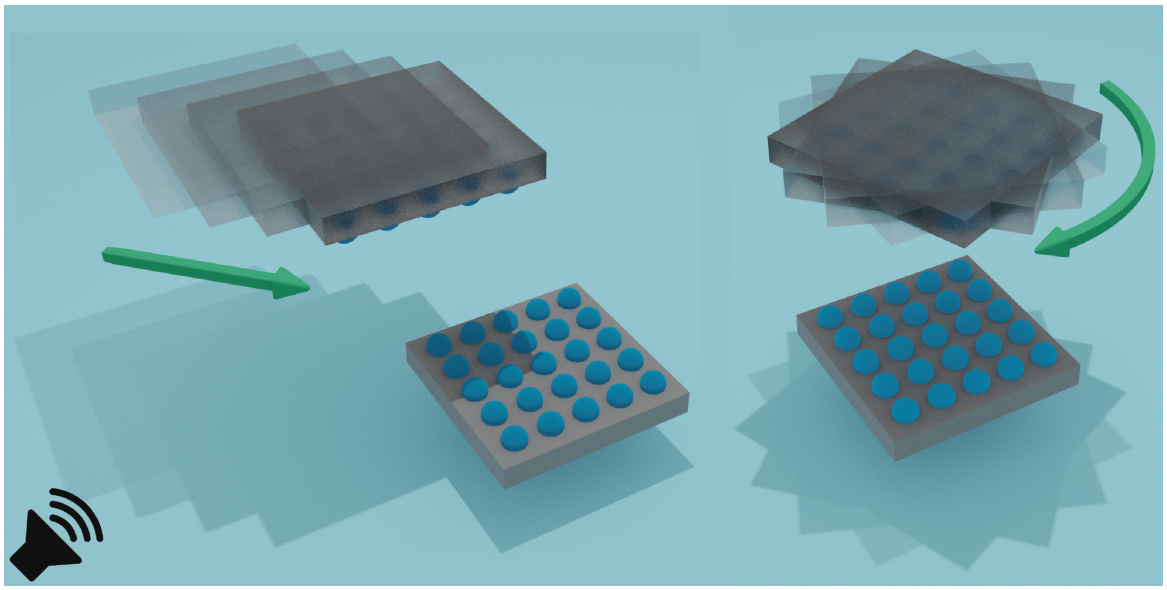

Figure 3.1: Schematic illustration of the direct assembly and handling driven by the secondary Bjerknes force acting between resonant scatterers in an acoustic field. Image is adapted from weltderphysik.

- $\omega = 2\pi f$ is the radial oscillation frequency
- δ is the radial oscillation amplitude of each bubble

We consider that the sizes of the bubbles, denoted as R_0, and the distance between them, r, are both significantly smaller than the acoustic wavelength λ [34]. The force acting between the bubbles is directed along $\vec{r}$ and is attractive, as illustrated in Fig. 3.2 (a). For bubbles with a radius of $R_0 = 150\,\mu\text{m}$ that are $r = 1\,\text{mm}$ apart in water, with a gap of $\delta = 5\,\mu\text{m}$ and a frequency of $f = 3.3\,\text{kHz}$, the resulting attractive force is $F_B = 28\,\text{nN}$. The force acting on a single bubble at the origin by a bubble array with N bubbles is given by the pairwise sum of forces between the lone bubble and each bubble in the array:

$$\vec{F}_{B1} = \sum_{i=1}^{N} 2\pi\rho\, R_0^4 \omega^2\, \delta_0^2\, \frac{\vec{r}_i}{r_i^3} \tag{3.2}$$

where the index i indicates the bubble in the array and $r_i = |\vec{r}_i|$. Extending this to the interaction between two arrays of N and M bubbles, respectively, the force becomes

$$\vec{F}_{B2} = \sum_{j=1}^{M} \sum_{i=1}^{N} 2\pi\rho\, R_0^4 \omega^2\, \delta_0^2\, \frac{\vec{r}_{ij}}{r_{ij}^3} \tag{3.3}$$

where j indicates the bubbles in the second array and $\vec{r}_{ij} = \vec{r}_i - \vec{r}_j$. We ignore interactions between bubbles within the same array due to the physically trapped nature of microbubbles. Therefore, the force responsible for acoustic assembly is secondary Bjerknes force exist between independent microbubble array.

The azimuthal angle θ as shown in Fig. 3.2 (b), denotes the angular deviation of the total interaction force vector ($\vec{F}_{B2}$) relative to the x-axis. The horizontal ($\vec{F}_{B2,xy}$) and vertical ($\vec{F}_{B2,z}$) components are estimated by the equations given by,

$$\begin{aligned} |\vec{F}_{B2,xy}| &= |\vec{F}_{B2}| \cos\theta \\ |\vec{F}_{B2,z}| &= |\vec{F}_{B2}| \sin\theta \end{aligned} \tag{3.4}$$

The total force on the mobile PDMS structure from the fixed array can be computed for any point in space by employing the Eq. (3.3) and thus, it can be used to spatially model the variation of the total force.

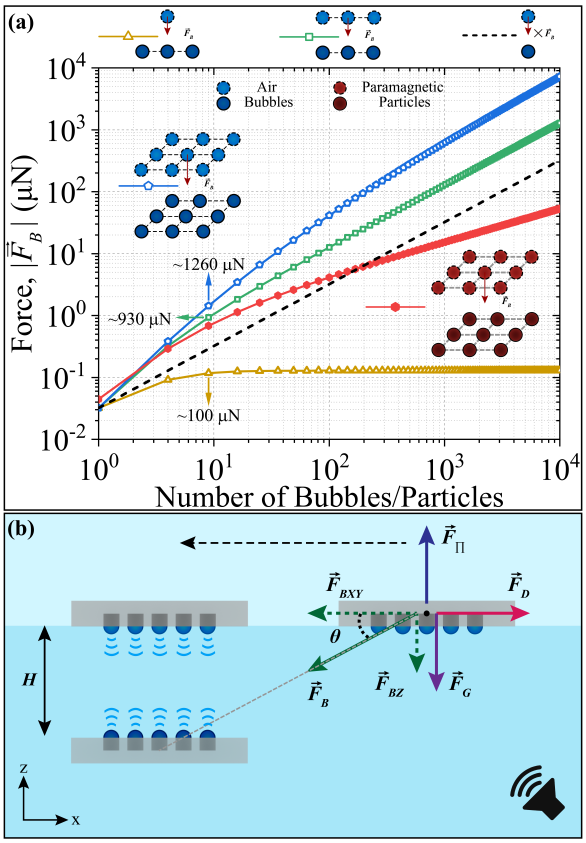

Figure 3.2: The interaction between bubbles significantly increases when they form an array. (a) The graph above illustrates how the force between bubble arrays scales with the size of the arrays in various geometries depicted schematically. The blue pentagons indicate that the forces experienced between two bubble arrays are amplified by a factor of 25 compared to an equivalent number of isolated bubbles, as shown by the black dashed line. Similarly, the force between comparable magnetic arrays, represented by red hexagons, is lower than that of the bubble arrays in a sound field. (b) This section describes the forces at play between two structures with embedded bubble arrays that are activated by a sound field. The lateral component of the secondary Bjerknes force, denoted as $\vec{F}_{B,xy}$, is responsible for the movement of the floating structure. The fluid drag, $\vec{F}_D$, opposes this motion. Meanwhile, buoyancy, $\vec{F}_\Pi$, counteracts gravity, $\vec{F}_G$, while the vertical component of the Bjerknes forces is represented by $\vec{F}_{B,z}$. Image is taken from [34].

The forces are numerically calculated to provide a mathematical foundation for

the understanding of secondary Bjerknes forces. The forces can be scaled up or amplified by patterning microbubbles into an array using soft-lithography as discussed in Chapter 2. The microbubbles create a pattern that significantly increases the overall secondary Bjerknes force, which is illustrated in Fig. 3.2. In this figure, we can see the forces related to different arrangements of microbubbles. The yellow line represents the force acting on a single bubble from an array of bubbles spaced at $\Delta = 500\,\mu m$. To calculate this force between the array and the individual bubble, we sum the vector forces $\vec{F}_B$ exerted on the free bubble by each bubble in the array, indexed by i [34]:

$$\vec{F}_{B1} = \sum_i \vec{F}_B(\vec{r}_i) \tag{3.5}$$

The interactions between bubbles do not lead to rearrangement of bubbles in the array because the bubbles in the array are rigidly fixed in a place. Moreover, scattering from the PDMS structure would be significantly weaker than scattered acoustic field from bubbles because of the weak acoustic contrast between water and PDMS relative to the contrast between water and air. Therefore, it is reasonable to ignore the scattering of acoustic field from PDMS structure. The force between one bubble and a line of 9 bubbles increases to ~ 100 nN as denoted by yellow arrow of Fig. 3.2 (a), but then saturates as more bubbles are added to the 1D arrangement due to the r^{-2} dependence of the secondary Bjerknes force. This saturation of secondary Bjerknes force can however be solved by considering the interaction between two arrays of bubbles. Then, each bubble in one array will always have a neighbouring partner in the other array, leading to a growth of F_B with the number of bubbles in each array. A two 9-bubble arrays separated by a height $H = 1\,mm$ experience an attractive force of 930 nN which is denoted by green arrow in Fig. 3.2 (A).

The amplification in secondary Bjerknes force is more favourable when 2D arrays of bubbles are considered as shown in Fig. 3.2 (A): the secondary Bjerknes force between two 3×3 arrays of bubbles is 1260 nN as pointed out by the blue arrow in Fig. 3.2. The secondary Bjerknes force has so far been considered to be in the range of nN and was not explored for practical applications. The numerical estimates presented herein open therefore opportunity for applications including the switchable assembly of larger objects resulting from secondary radiation force between resonant scatterers in a sound field.

3.3 Scaling of Amplified Secondary Bjerknes Forces

This section explores the dependency and variation of the secondary Bjerknes force on parameters which can be controlled externally. The mathematical equation signifying the secondary Bjerknes force experienced by the two-dimensional arrays of bubble is

given by Eq. 3.3 which can be directly used to predict how the force will scale with different parameters such as the driving pressure (P) or the bubble radius (R_0).

The first externally controlled parameter is the driving pressure P which depends on the power provided to the piezoelectric transducer coupled to generate the acoustic waves, since P determines the bubble oscillation amplitude δ [48]. In a linear oscillation regime, $\delta \sim P$ and increasing the pressure will increase the force $F_{B2} \sim P^2$.

We simplify the understanding by considering arrays of identical bubbles, but the mathematical description could be applied to non-identical bubbles, id required. The second independent variable is the bubble radius R_0. Although the role of the bubble radius R_0 is more complex than the driving pressure. The oscillation amplitude at resonance should grow linearly with bubble size so that $\delta \sim R_0$. At the same time the resonance frequency will drop with increasing bubble size. It can be shown from Eq. (2.22) that the frequency scales as $f_0 \sim \kappa^{1.5}$. Since κR_0 is a constant (Eq. (2.23)), $\kappa \sim R_0^{-1}$ and $\omega \sim R_0^{-1.5}$.

We assume that gap heights and bubble spacing are fixed by the experimental parameters, but r and R_0 are independent, so that $F_{B2} \sim R_0^3$ with bubble size. If instead, the entire system were scaled up proportionally, so that $r \sim R_0$, the total force would scale as $F \sim R_0$, indicating that the force will still grow with bubble size, albeit more slowly.

These scalings should hold for oscillations in the linear regime, and therefore will be valid for low pressures, until a maximum bubble size, which would likely be set by surface tension and the onset of nonlinear oscillations of the bubble interface. Such effects could lead the bubbles to pinch off during oscillations. These effects are beyond the scope of this work but provide an interesting direction for future work.

The secondary Bjerknes force is closely tied to the number of bubbles, showing that as the number of bubbles N in each array increases, the force amplification rises accordingly. What's interesting is that this force does not increase in a linear fashion with N, which might be the initial expectation for N independent bubble pairs, illustrated by the black-dashed line in Fig. 3.2 (A). Instead, the force between bubble arrays exhibits a superlinear growth concerning N. As depicted in Fig. 3.2 (a), the force between these arrays initially scales as approximately $\$F \sim N^{1.6}$ for lower values of N [34], before transitioning to an asymptotic behavior of $F \sim N$ as N becomes large. This superlinear scaling of the secondary Bjerknes force highlights the significance of long-range interactions among bubbles within the arrays, interactions that aren't considered when calculating the force purely on the basis of independent bubble pairs. The experimental parameters have already been established, showing that this long-range coupling allows for a remarkable amplification, reaching up to approximately 25× compared to the force generated by independent bubble pairs when N is very large. It is important to note that extremely large arrays aren't a

necessity for practical applications; thus, the number of bubbles should be determined according to the required force. A two-dimensional array with $N = 100$ already offers a 13× amplification compared to N independent bubble pairs [34], producing nearly 0.1 mN of force.

3.4 Comparative analysis of Bjerknes and magnetic forces

The forces generated by the Bjerknes bubble arrays is compared to a similar array consisting of paramagnetic particles in a magnetic field. For the force estimates, we assume that the bubbles in the PDMS structures are replaced by an equivalent volume of paramagnetic material. We compare the magnitude of both forces and show that, while magnetic forces are stronger at short ranges, the Bjerknes force is two orders of magnitude larger at larger distances, and that the Bjerknes force grow more rapidly with the number of bubbles/particles. The Bjerknes force is calculated as described in the main text.

The magnetic forces are calculated between two square, N-particle arrays consisting of uniformly magnetized paramagnetic particles with dipole moment

$$\vec{m} = m_0 \hat{z}. \tag{3.6}$$

The particles will create their own magnetic fields, which in turn gives rise to a force on the other surrounding dipoles. The force on a dipole in a magnetic field is given by

$$\vec{F} = -\vec{\nabla} U, \tag{3.7}$$

where

$$U = -\vec{m} \cdot \vec{B} \tag{3.8}$$

is the magnetic interaction energy of the dipole in the field.

The magnetic field at a point $\vec{r}$ produced by a single dipole at the origin is given by [111, 112]:

$$\vec{B}_0(\vec{r}) = \frac{\mu_0}{4\pi}\left[\frac{3\,\vec{m}\cdot\vec{r}}{r^5}\vec{r} - \frac{\vec{m}}{r^3}\right], \tag{3.9}$$

where $r = |\vec{r}| > 0$, and μ_0 is the permeability of free space. Combining Eqs. (3.7)–(3.9) gives the force on dipole m_2 due to the dipole m_1, when they are separated by $\vec{r}_{12} = \vec{r}_2 - \vec{r}_1$:

$$\vec{F}(\vec{r}_{12}) = \frac{3\mu_0}{4\pi r_{12}^5}\left[(\vec{m}_1\cdot\vec{r}_{12})\vec{m}_2 + (\vec{m}_2\cdot\vec{r}_{12})\vec{m}_1 + (\vec{m}_1\cdot\vec{m}_2)\vec{r}_{12} + \frac{5(\vec{m}_1\cdot\vec{r}_{12})(\vec{m}_2\cdot\vec{r}_{12})}{r_{12}^2}\vec{r}_{12}\right]. \tag{3.10}$$

We assume parallel and equal magnetic moments as in Eq. (3.6) in the presented

system, which allows Eq. (3.10) to be simplified to

$$\vec{F}(\vec{r}_{12}) = \frac{3\mu_0 m_0^2}{4\pi r_{12}^5}\left[2z_{12}\hat{z} + \vec{r}_{12} - 5\left(\frac{z_{12}}{r_{12}}\right)^2 \vec{r}_{12}\right], \tag{3.11}$$

where z_{12} represents the z-distance between the two dipoles.

In general, the force between two magnetic dipoles is not central, because of the term parallel to $\vec{m}$. However, the magnetic force between particles in the same array, for which $z_{12} = 0$, is central and purely within the x–y plane. Assuming that such forces are countered by the rigidity of the structure, as we assumed for the bubble arrays, we can continue the force calculations ignoring the interactions between particles in the same array.

The force between two arrays of N magnetic particles can then be calculated by adding the pairwise forces between particles in the arrays. If the arrays are separated by a vertical height H, and the particles in the fixed and mobile arrays are indexed by i and j, respectively, then the total force on the mobile array is given by [113]

$$\vec{F}_M = \sum_{i=1}^{N}\sum_{j=1}^{N} \frac{3\mu_0 m_0^2}{4\pi r_{ij}^5}\left[2H\hat{z} + \vec{r}_{ij} + 5\left(\frac{H}{r_{ij}}\right)^2 \vec{r}_{ij}\right]. \tag{3.12}$$

We estimate the actual forces between the arrays by considering Iron (II) Oxide (FeO) as a paramagnetic material, due to its commercial availability and high magnetic susceptibility compared to other paramagnetic materials. The molar magnetic susceptibility (χ_M) is typically reported in CGS units, and is 7.2×10^{-3} for FeO. This can be converted into a volume magnetic susceptibility in the SI system of units by the equation [114]:

$$\chi_V^{SI} = 4\pi \frac{\rho}{M} \chi_M^{CGS} \tag{3.13}$$

where M is the molar mass of FeO and ρ is the density of FeO. The volume magnetic susceptibility can be used to calculate the saturation magnetization m_{SAT} of FeO in the presence of an external magnetic field B [114]:

$$m_{SAT} = \frac{B}{\mu_0}\left(\frac{\chi_V^{SI}}{1 + \chi_V^{SI}}\right) \tag{3.14}$$

where μ_0 denotes the vacuum permeability which is equal to $4\pi \times 10^{-7}$ H m^{-1}. Thus, if V_C denotes the volume of an individual paramagnetic particle, then the total magnetic moment of the particle is given by,

$$|\vec{m}| = m_{SAT} V_C \tag{3.15}$$

Thus, the dipole strength of the Iron (II) Oxide particles is 2.72×10^{-7} Am^2. The phys-

Parameters	Value
$M(\mathrm{g\,mol^{-1}})$	71.84
$\rho(\mathrm{g/cm^3})$	5.74
$\chi_M(\mathrm{cm^3/mol})$	7200×10^{-6}
χ_V(SI units)	0.0072
B(T)	1
$m_{SAT}(\mathrm{A\,m^{-1}})$	5.71×10^3

Table 3.1: Physical properties of iron oxide (FeO) at 20 °C [1, 2].

ical properties of FeO and the derived magnetic properties used for force calculations are tabulated in Table 3.1.

The magnitude of the Bjerknes and magnetic force between the arrays are presented in Figure 3.3, using the parameters given in Table 3.2. It is clear from the results that while magnetism provides competitive forces for the directed-organization of microstructures, the magnetic forces are an order of magnitude weaker than the acoustic counterpart, and decay more quickly with respect to the space (H). Moreover, as the array size is increased, the acoustic forces can be amplified more effectively than the magnetic forces. This is likely because the acoustic forces provide longer-range interactions, decaying as r^{-2} rather than r^{-4}.

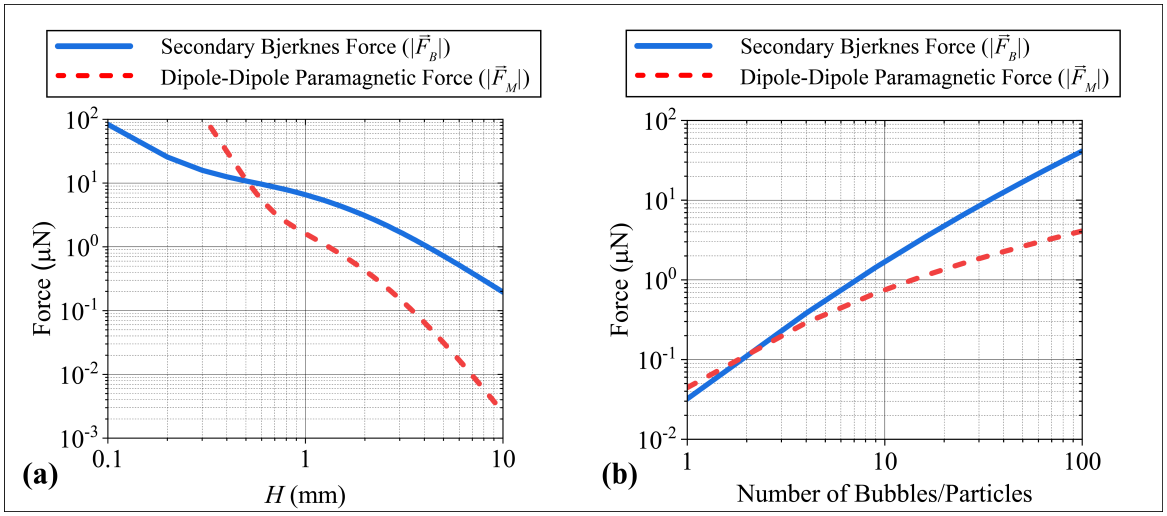

Figure 3.3: Comparison between the Bjerknes force ($|\vec{F}_B|$) and the magnetic force ($|\vec{F}_M|$). The magnitude of secondary Bjerknes force between the microbubble arrays and the magnetic force due to dipole-dipole interaction between the paramagnetic particles (FeO) of the arrays are plotted as a function of the (a) distance (H) between the arrays and the (b) number of particles/bubbles N in the square array. Image is taken from [113].

Magnetic forces are popular for manipulation and assembly applications and therefore we compared them with the acoustic forces between the bubble arrays. We found that the bubble arrays lead to more effective force scaling than the magnetic counterpart. Magnetic forces are typically considered to be much stronger than acoustic forces

between bubbles but surprisingly we find that these benefits are limited to small-range interactions or very large system dimensions. The quantitative comparison between the secondary Bjerknes force and magnetic force is shown in Fig. 3.2 (a), the detailed description of the calculations involved in the magnetic force is presented in the later section of the chapter. It can be observed that while the force between two magnetic particles is stronger than that between two bubbles of the same size, the force produced by bubble arrays increases more efficiently and quickly with N, yielding higher forces when $N > 1$ [34]. The benefits of bubble arrays stand out especially in longer-range interactions, whereas magnetic arrays excel in generating greater forces during close-range interactions—specifically at distances comparable to the particle's size. The enhanced force scaling observed in bubble arrays for longer ranges can be attributed to the secondary Bjerknes forces, which scale as r^{-2}, in contrast to the magnetic dipole forces that scale as r^{-4}. This distinction clearly illustrates why the secondary Bjerknes force prevails over the magnetic force in long-range scenarios.

3.5 Assembly and Alignment of Sound Activated Structures

We experimentally demonstrate the manipulation with the secondary Bjerknes forces by fabricating identical array of patterned bubbles. The bubble arrays are embedded into ~ 1 cm-diameter PDMS structures using soft lithography [115]. An array of 11×11 cylindrical cavities is molded into the center of each structure which is schematically shown in Fig. 3.2 (B). Each cavity has a diameter $2R_0 = 300\,\mu m$ and height $L = 275\,\mu m$. The cavities are uniformly spaced with a pitch $\Delta = 500\,\mu m$. The cavities are only open on one face of the disk, so that when the PDMS structures are placed in a reservoir of water (Fig. 3.2 (b)), air bubbles are trapped. In the presence of an acoustic field, the bubble surfaces vibrate, with a primary resonance (maximum vibration amplitude) at 3.3 kHz. All bubbles in the system are excited in phase which can be justified by the long acoustic wavelength in water (450 mm). It should be noted that in phase excitation of bubble arrays lowers the resonance compared to predictions for a single bubble interface.

The upper structure is designed to float freely at the interface of air and water, while the lower structure remains securely anchored to the bottom of the reservoir through a plasma-bonding process that connects glass and PDMS. The gap between the upper and lower structures is maintained at a vertical distance of H. When the acoustic transducer mounted to the reservoir is activated at the bubble's resonant frequency, the attractive secondary Bjerknes force generated between the bubbles propels the free-floating structure towards its fixed counterpart. The vertical part of this force counteracts buoyancy, while the horizontal component initiates movement

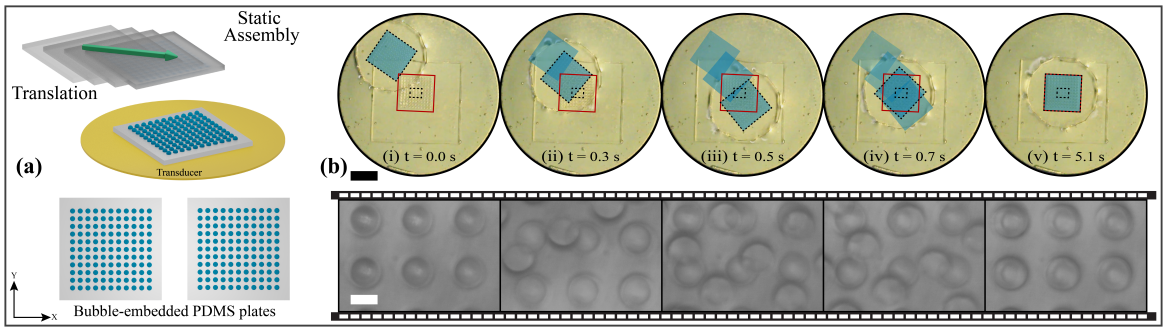

Figure 3.4: Assembly and alignment of bubble-embedded structures. (a) This diagram illustrates the assembly experiment. (b) The experimental findings are shown, with the blue square indicating the position of the floating array and the red square illustrating the location of the fixed array, which are separated by a distance of $H = 1\,\text{mm}$. The microscope images below focus on the central area of the fixed array, highlighting its precise alignment. Scale bars are provided as follows: 5 mm (black) and 300 µm (white). Image is reproduced from [34].

along the surface of the water. Additionally, the motion of the floating structure is influenced by other forces, such as fluid drag and gravity, as illustrated in Fig. 3.2 (b).

The acoustic forces acting on the bubble arrays generate sufficient thrust to facilitate the assembly of centimeter-scale PDMS structures. The assembly of bubble arrays using secondary Bjerknes forces is schematically shown in Fig. 3.4 (a). A 2D graphics of the 11×11 bubble arrays are shown in Fig. 3.4 (a). Experimental images at different time instants of the alignment process are shown in Fig. 3.4 (b) where the bubble arrays are separated by a water layer of height $H = 1\,\text{mm}$. The movement of mobile array towards a stable trap position is revealed by the time-lapse photographs shown in Fig. 3.4 (b). The mobile structure moves at a speed of 10 mm/s to 30 mm/s until it is aligned above the fixed bubble array which is denoted by red square in Fig. 3.4 (b). We conducted the same experiments using a 10× microscope objective to assess the precision of our alignment technique. Our findings showed an alignment accuracy of $14\,\mu\text{m} \pm 4\,\mu\text{m}$ for structures measuring a few centimeters. This translates to an accuracy of 0.1 % when compared to the objects' dimensions and 0.003 % relative to the acoustic wavelength [34].

We performed further experiments to confirm the dominant role of secondary Bjerknes forces in our system of acoustic assembly. The following experiments are performed as control to validate the presence of secondary Bjerknes force:

- The experiment involves replacing the mobile structure with a bubble-free PDMS slab, allowing for the observation of the floating structure's motion when exposed to a sound field.

- The experiment involves the presence of the original mobile structure while the fixed structure is absent, allowing us to observe the effects of the sound field on

the mobile structure.

The floating structure did not respond in both the experiments when the transducer was turned ON. This non-responsive behavior of mobile structure clearly indicates that the acoustic assembly is driven by the secondary Bjerknes forces between the bubble arrays and not by forces or streaming effects from the primary acoustic field.

We further validated the role of secondary Bjerknes force using a numerical model which calculates the position of mobile structure under the influence of secondary Bjerknes force. The bubble-embedded structure undergoes damped oscillatory motion during the process of assembly and at the steady state it aligns with the fixed alignment target according to signature of central trapping force. The dynamics reveal that the attractive Bjerknes force is responsible for the motion, while viscous drag at the water interface acts as the source of damping in the motion. The assembly dynamics can therefore be described by the differential equation:

$$m\frac{\partial^2\vec{x}}{\partial t^2} = \vec{F}_{B2}(\vec{x}) - \beta\frac{\partial\vec{x}}{\partial t}, \tag{3.16}$$

where $\vec{x}$ denotes the center of mass of the free PDMS structure relative to the fixed PDMS structure. The mass of the structure is denoted by m and $\beta \approx 2.5\times10^{-4}\,\mathrm{N\,s\,m^{-1}}$ is a viscous damping coefficient which is estimated experimentally using the conservative properties of secondary Bjerknes force. The spatially-dependent force exerted on the mobile structure from the fixed structure is denoted by $\vec{F}_{B2}(\vec{x})$.

The force between the arrays is calculated by summing the pairwise Bjerknes force (Eq. 3.1) between the bubbles in the two arrays [34]:

$$\vec{F}_{B2}(\vec{x}) = \sum_{i=1}^{N}\sum_{j=1}^{N}\vec{F}_B(\vec{r}_{ij}). \tag{3.17}$$

where $\vec{r}_{ij}$ denotes the displacement vector connecting the position of bubble i in the free array with the position of bubble j in the static array. The $\vec{r}_{ij}$ depends implicitly on the position of mobile array which is denoted by $\vec{x}$ [34]. The total force on the mobile structure is calculated by taking the sums over all N bubbles in each array. The horizontal component of the force between the two arrays is always attractive and exhibits a trapping force field with a stable equilibrium point at the center. The equilibrium point at the center can be observed in Fig. 3.5 (b) (inset). As described in Eq. (3.1), $\vec{F}_B$ depends on the pulsation amplitude δ of bubbles in the acoustic field. The estimation of the bubble oscillation amplitude (δ) yielded approximately 5 µm which is based on optical measurements of the bubble oscillations. The experimental measurement of pulsation amplitude is also consistent [34] with other observations of excited bubbles that are reported in the literature [96]. Given, Eq. 3.16 can be used to estimate Hence, the dynamics of the free-floating structure under the influence of

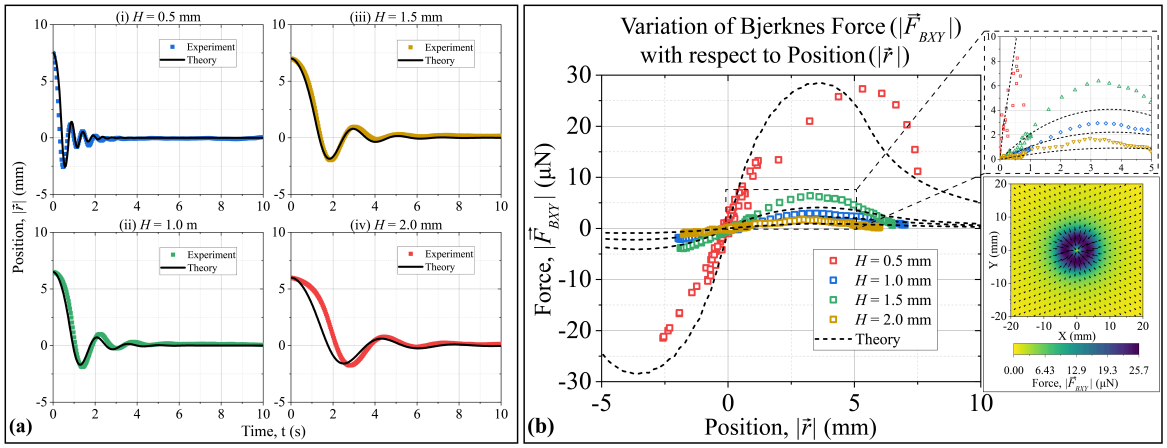

Figure 3.5: Comparison between numerical results and experimental results. (a) The results of the simulation which calculated the motion of the floating array under the influence of secondary Bjerknes forces (black lines) for four different separation between arrays denoted by heights H. The simulation results match very well with the experimental measurements which are denoted by the scattered plot of different colors namely, blue, yellow, green, and red. (b) The analytical prediction (dashed lines) for the lateral component of secondary Bjerknes force between the bubble arrays matches very closely with the experimentally obtained results (symbols) and the analytical prediction. Upper inset: zoomed region around $r = 0$ showing lower forces. Lower inset: 2D lateral force distribution showing a central, attractive trap. Image is adapted from [34].

the secondary Bjerknes forces between the arrays can be estimated through Eq. 3.16, provided that the force field $\vec{F}_{B2}(\vec{x})$, m and β are explicitly known for the experimental system.

3.6 Numerical model of the motion

The system is modelled as an equivalent of damped harmonic oscillator, where damping is governed by the drag force which can be modelled as being proportional to the velocity ($\vec{v}$) of the object ($\vec{F}_D \propto \vec{v}$). In particular, as mentioned previously, we considered that the vertical component of the Bjerknes force is balanced by buoyancy, so that the mobile structure remains at the water-air interface. Therefore, we only model the horizontal motion of the mobile PDMS structure in response to the Bjerknes force given in Eq. (3.4). Accounting for all of the lateral forces, we can write

$$\vec{F}_{B2}(x,y,z) - \vec{F}_D(v) = m\vec{a} = m\left[\frac{d^2x}{dt^2}\hat{x} + \frac{d^2y}{dt^2}\hat{y}\right]. \tag{3.18}$$

where m and a is the mass and acceleration of object, respectively. And F_D represents the velocity-dependent fluid drag on the structure, which we assume to be a Stokes drag

$$\vec{F}_D = -\beta\vec{v} = -\beta\left[\frac{dx}{dt}\hat{x} + \frac{dy}{dt}\hat{y}\right]. \tag{3.19}$$

where β is the viscous damping coefficient and $\vec{v}$ is the velocity vector of object.

The array motion is simulated by solving Eq. 3.18 using an explicit 4_{th}-order Runge-Kutta method from the Ordinary Differential Equation (ODE) library of MATLAB 2020A. The ordinary differential equation is solved by starting from an initial condition, $[x_{j0}\ ,\ y_{j0}\ ,\ 0]$, as well as a period of time over which the answer is to be obtained, $[t_0\ ,\ t_f]$, the solution is obtained by solving the equation iteratively. The final result is a vector of time steps $[t_0\ ,\ t_1\ ,\ t_2\ ,\ \ldots\ ,\ t_f]$ as well as the corresponding solution at each step $x_j = [x_{j0}\ ,\ x_{j1}\ ,\ x_{j2}\ ,\ \ldots\ ,\ x_{jf}]$ and $y_j = [y_{j0}\ ,\ y_{j1}\ ,\ y_{j2}\ ,\ \ldots\ ,\ y_{jf}]$. The pulsation amplitude (δ) and viscous damping coefficient (β) are essential control parameters for the computation of the numerical model. Unidirectional radial oscillations of the bubbles complicate the optical measurement of δ therefore we have approximated the magnitude as $1\% \times R_0$. Similarly, to estimate the magnitude of the damping coefficient (β), the space-dependent Bjerknes force is assumed to be a single-valued function of position and this provides the mathematical value of order $\sim 10^{-4}$ to the viscous damping coefficient (β). The detailed description to calculate β is provided in the later section. The initial position of the floating structures is taken to be in the $x-y$ plane with coordinates set to match experiments. The height is constrained to $z = H$. The fixed structure is centered at the origin. The total simulated time is 10 s with a time step of 3 ms.

3.6.1 Physical parameters for numerical simulations

To simulate the motion of the PDMS structures with embedded bubbles under the influence of the Bjerknes forces, values for the fluid damping coefficient β and the bubble oscillation amplitude δ_0 must be known. We empirically determined these values from experiments, as described in the sections below. Both values were found to depend on the vertical separation between the two structures H. The values extracted from experiments and used for our simulations are given in Table 3.2.

H (m)	β (N s m^{-1})	δ_0 (m)
0.5×10^{-3}	4.25×10^{-4}	4.750×10^{-6}
1.0×10^{-3}	2.50×10^{-4}	2.125×10^{-6}
1.5×10^{-3}	1.75×10^{-4}	1.750×10^{-6}
2.0×10^{-3}	1.25×10^{-4}	1.250×10^{-6}

Table 3.2: Parameters used to simulate the dynamics of PDMS plate driven by Bjerknes forces.

3.6.2 Determination of the damping coefficient β

The damping coefficient was identified based on the measured motion of the PDMS structure under the influence of the attractive Bjerknes forces. The motion of the PDMS structure can be described by Eq. 3.18. Based on this equation, we can calculate $F_{B2,xy}(r)$ given an estimate for β, the raft's mass m, and the trajectory information $\vec{r}(t)$ from experiments, as shown in Fig. 3.5. While the raft's mass can be measured independently, we determine β using other information. We assume that F_{B2} is a conservative force, that is, it does not introduce losses and therefore must be a single-valued function of position $\vec{r}$. Because the PDMS structure undergoes a damped oscillation around the final alignment position, the end of its trajectory revisits the same spatial point multiple times, and can be used to test this assumption for different values of β. As shown in Fig. 3.6, only one value of β is compatible with this assumption (β_0 in the figure). Other values of β produce estimates of $F_{B2,xy}$ that are multi-valued over a large range of positions, as shown by the spiral traces in panels (a) and (c). Therefore, for each height, we use the value of β that is most compatible with the assumption that $F_{B2,xy}$ is conservative. As can be seen in Table 3.2, β decreases with increasing height H, following a roughly linear dependence.

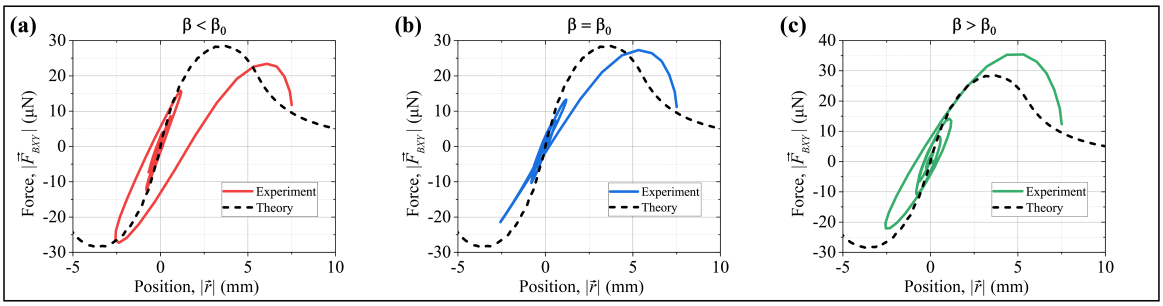

Figure 3.6: Determination of damping coefficient β from the experimentally-measured trajectories of PDMS structures. The secondary Bjerknes force should be conservative and therefore a single-valued function of position $\vec{r}$. When estimating $F_{B,xy}$ from trajectory data, this condition is only satisfied for a single value of damping coefficient $\beta = \beta_0$ (panel (b)) and false when $\beta < \beta_0$ (panel (a)) or $\beta > \beta_0$ (panel (c)), as indicated by the multi-valued spiral trajectories. Image is taken from the Supplementary Information of [34].

The model's performance was evaluated against assembly experiments conducted at various separations between the microbubble arrays, with H ranging from 0.5 mm to 2.0 mm. A comparison of the measured positions of the mobile structure from these experiments with simulation results is presented in Fig. 3.5 (a). It's important to highlight that the model's parameters, δ and β, exhibit only a slight dependence on H, which can be attributed to the fluidic interactions between the two plates. As shown in Fig. 3.5, the theoretically predicted trajectories align remarkably well with the experimental data. The findings consistently indicate that assembly time increases with greater separations H. Additionally, the numerical model precisely

reproduces the observed overshoot and damped oscillations of the mobile structure as it approaches a stable equilibrium position. Additionally, we performed further verification by estimating the spatially-dependent secondary Bjerknes force acting on the mobile structure through the measured trajectories $\vec{x}(t)$ and Eq. 3.16. These estimates agree very well with the analytically calculated forces as shown in Fig. 3.5 (b). It is evident that the secondary Bjerknes forces agree in both trend and magnitude where the peak lateral attractive forces lies in the range of 1 µN and 30 µN for different H. The inset in Fig. 3.5 (b) shows the two-dimensional force on the floating array as a function of position [34]. The results obtained from the simplified model to match the dynamics and force magnitude of the structures in experiments where only the secondary Bjerknes force between the arrays is accounted, demonstrates that the assembly process is dominated by secondary forces and not other effects such as acoustic streaming [34].

3.7 Acoustic Rotor Assembly

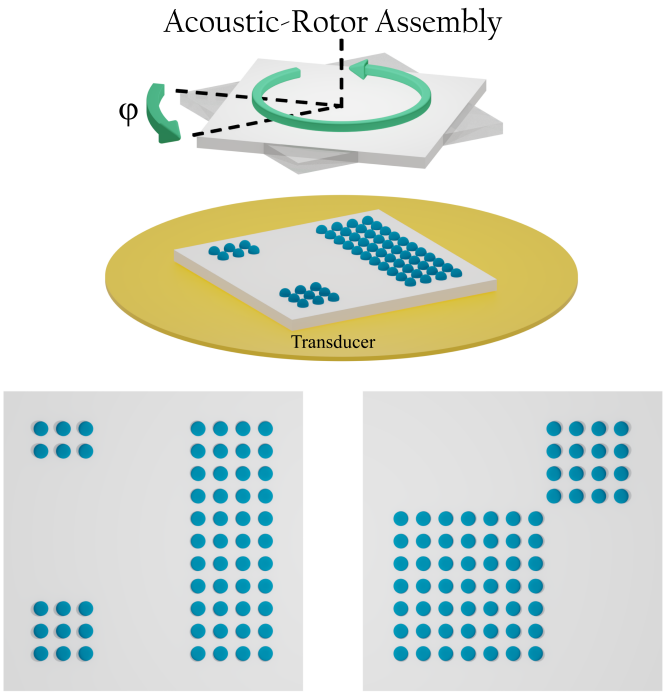

Figure 3.7: Schematic representation of acoustic rotation of structures with the asymmetric bubble arrays. Image is reproduced from [34].

The experimental and numerical description provided previously in the chapter gives the foundation for understanding the interaction between oscillating bubbles. It is clear that the force vector depends directly on the spatial arrangement of patterned bubbles. Therefore, we further explored the acoustic-force mediated assembly

by exercising the possible combinations of interactions between subunits for various interesting applications. We explored an acoustic rotor assembly as shown in Fig. 3.7, which could demonstrate a continuous rotational motion even though the acoustic field imparts no direction preference. This can be accomplished by exploiting both the static and dynamic configuration of the secondary Bjerknes force. The disordered configuration of structures when activated by the acoustic field should autonomously assemble in a coaxial configuration and then subsequently start rotation due to torque generated by a differential interaction force along the tangential direction. The application of an asymmetric force on the mobile subunit can generate a torque which can be harnessed to create a circular motion. We therefore designed an asymmetric pattern of bubble structures such that the fixed and mobile units have a different arrangement of bubbles. The bubble patterns of the structures are shown in Fig. 3.7. The secondary Bjerknes force between the bubble arrays can be calculated by the $\vec{F}_{B2}(\vec{x}) = \sum_{i=1}^{N} \sum_{j=1}^{M} \vec{F}_B(\vec{r}_{ij})$, which can be employed to determine the torque Γ along the axis of the mobile structure.

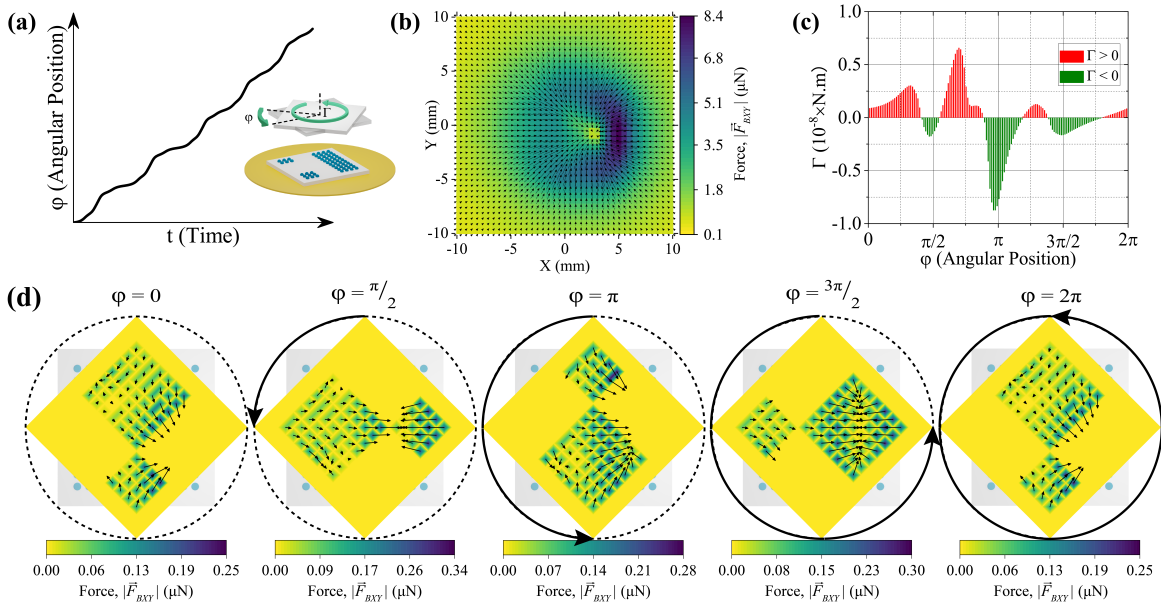

Figure 3.8: Numerical simulation for acoustic rotation of structures. (a) Angular position as a function of time. (b) 2D distribution of the lateral secondary Bjerknes force between the structures shows a central trap along with the tangential gradient of force. (c) Numerically calculated torque applied on mobile structure as a function of relative angular position between the structures. (d) Vector representation of the forces acting on the mobile structure at different angular positions. Image is reproduced from [34].

The rotational motion of the PDMS plate is modelled in an identical manner as the static assembly by solving the following ordinary differential equation,

$$\Gamma - \Gamma_D(\Omega) = I_P \left[\frac{d^2\varphi(t)}{dt^2} \right] \tag{3.20}$$

where Γ is the torque generated by the Bjerknes force along the centre axis of the PDMS plate, Γ_D is the rotational drag on the PDMS plate, I_P is the moment of inertia of the circular PDMS plate and φ is the angular displacement of the PDMS plate. The torque generated by the Bjerknes force is calculated by applying summation to the vector product of Bjerknes force vector of an individual bubble and position vector of the bubble with respect to the centre of the PDMS plate which can be written as follows,

$$\Gamma = \sum_{j=1}^{M} \sum_{i=1}^{N} 2\pi\rho\, R_0^4 \omega^2 \,(\delta_0)^2 \,\frac{\vec{r}_j - \vec{r}_i}{|\vec{r}_j - \vec{r}_i|^3} cos\theta \otimes \vec{r}_{ij} \tag{3.21}$$

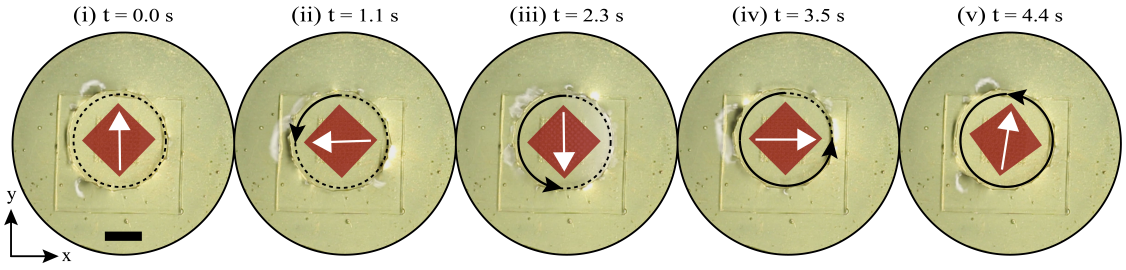

Figure 3.9: Acoustic rotation of structures. Experimental images of acoustically-driven rotation of structure through asymmetric distribution of bubbles. Red colored rectangle and white colored arrow indicate the instantaneous position and orientation of the mobile structure, respectively. Scale bar: 5 mm. Image is reproduced from [34].

The 2D distribution of force between the asymmetric bubble arrays is plotted in Fig. 3.8 (b) which is calculated numerically from Eq. 3.5. The numerically calculated angular position of the mobile structure as a function of time is shown in Fig. 3.8 (a), which clearly suggests that the rotational motion is continuous. The interplay between the positive and negative torque can be witnessed from Fig. 3.8 (c) where the analytically calculated torque at different angular positions is presented. The spatial distribution of the force acting on every individual bubble of the mobile structure along with the direction of force vectors are presented in the Fig. 3.8 (d). The different bubble patterns of the two structures creates a force distribution which varies tangentially and hence generates a torque that varies with the angle. It should be noted that the acoustic rotation of structure has no preferred direction unlike as in an electric motor. The initial position and angular momentum of the rotor determine the rotational direction of the motor. Once it rotates in a specific direction, inertia maintains the rotation direction. The results of the rotation experiments are shown in Fig. 3.9 for a $H = 1$ mm [34]. With the given parameters, our acoustic rotor spins at a rate of $1.4\,\mathrm{rad\,s^{-1}}$, or about 14 RPM. By further designing different bubble patterns into fixed and mobile structures, it is expected that more complex manipulations can be realized [34].

3.8 Angular Assembly and Controlled Rotation

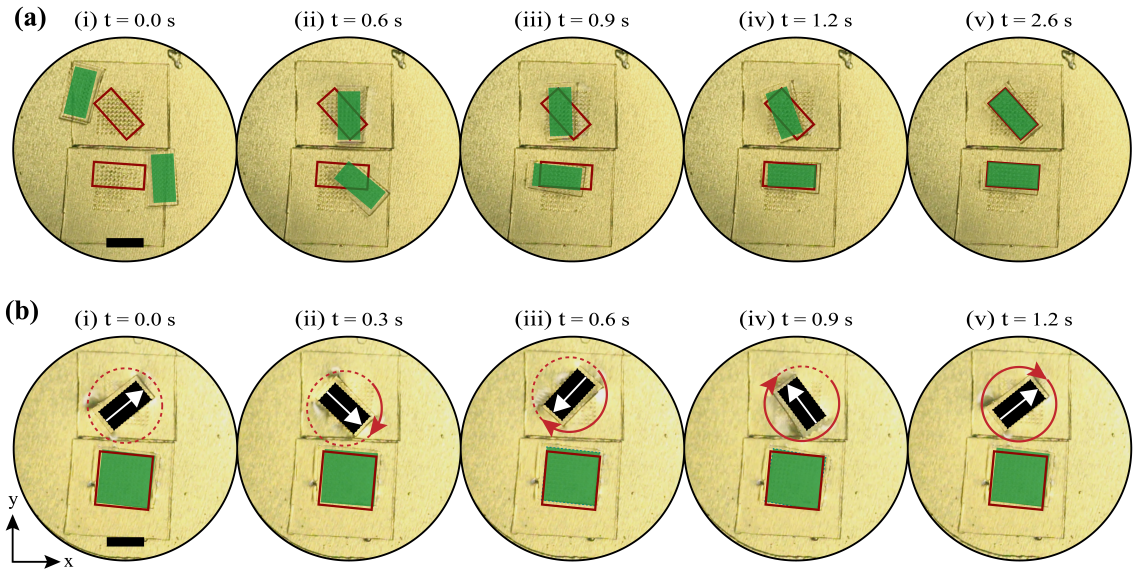

Figure 3.10: Simultaneous demonstration of assembly and manipulation through patterned microbubble arrays. (a) Experimental images of acoustically powered angular oriented assembly. (b) Simultaneous demonstration of acoustic rotatory motion and static assembly assisted by the secondary Bjerknes forces between differently patterned microbubble arrays. The black colored rectangle indicates the mobile structure and white colored array denotes the instantaneous angular position of the mobile structure. The red colored rectangle denotes the position of fixed structure and green colored rectangle indicates the instantaneous position of mobile structure. Scale bar: 5 mm. Image is reproduced from [34].

We performed experiments to demonstrate the assembly with rotation and translation components as shown in Fig. 3.10 (a). The structures autonomously organize into stable defined-patterns where 'red' rectangle denotes the acoustically active bubble surface, whose dynamics depends on the interplay between the angular and the space coordinates of the components. The experimental results clearly show accurate interlocking of the assembly. The digital images presented in the Fig. 3.10 at different time instants are extracted from the experimental recording performed through a Canon DSLR camera. Finally, we present the combination of rotor assembly and static assembly. The experimental images at different time instants are shown in Fig. 3.10 (b). The bubble arrays are patterned differently such that the 'rectangular' bubble-array acquires a 'acoustic rotor assembly' due to the application of an asymmetric force and performs continuous rotation at an average angular speed (Ω) of ~ 5.4 rad.s^{-1} whereas the 'square' bubble-array transitions to an equilibrium interactive state and generates a static assembly of structures. The assemblies form within seconds of the application of an external sound field, and dissolve when the external field is removed, indicating the rapid and switchable nature of the assembly technique presented in the chapter. Application of the demonstrated acoustically actuated self-assembly

technique to three-dimensional components might provide a general approach [115] to create complex structures for a broad range of spatial dimensions. More immediate and practical can be the alignment of planar components.

3.9 Summary

In conclusion, a method for directed assembly powered by acoustic fields has been introduced which is based on the secondary Bjerknes force between arrays of microbubbles. By using bubbles, it has become possible to achieve a precision in assembly far below the wavelength of the acoustic field. Although scattering forces between bubbles have been typically considered to be weak, it has been shown that arrays of bubbles can amplify the interaction forces by up to 25× compared to an equivalent number of individual bubble pairs. The benefits of bubble arrays arise from their long-range interactions associated with the Bjerknes force, which leads to higher forces in macro-scale systems, compared to a comparable arrangement based on magnetic assembly. cmm-scale objects in solution were rotated and translated using the µN-scale forces produced by an 11×11 array. The suggested technique's switchable character is demonstrated by the assemblies that form within seconds after an external sound field is applied and continue to exist for as long as the sound field is applied. Experiments and theoretical predictions of the forces and motion dynamics are in good agreement. Although slower dynamics due to increasing drag are anticipated, the technique should be scalable to larger and heavier systems. The weight and buoyancy of the floating structure should establish size restrictions. The cm-scale objects that are assembled and manipulated from the secondary Bjerknes force between microbubble arrays are experimentally demonstrated for the first time in this work.

Selective and pre-programmed directed assembly may be made possible by this acoustic approach. Although the larger cm-scale structures have been the focus of these demonstrations, mm-scale structures should also be able to be assembled by reducing the bubble and array dimensions. In addition to opening the door for possible uses in manufacturing, soft robotics, and microfluidics, the all-acoustical approach of manipulating and assembling macrostructures utilizing bubble arrays might be coupled with position-sensitive optical observations for contactless manipulation and control.

4

Light-Addressable Phase Shifter (LAPS) For Ultrasonics

The results presented in this chapter are part of an under review manuscript titled as "All-Optically Controlled Phased-Array for Ultrasonics". Some of the results of this chapter have also been submitted as a patent application "Optically Controlled Phase Shifter and Phased Array for Ultrasound Applications" under the inventor names of Rahul Goyal, Athanasios Athanassiadis, and Peer Fischer.

4.1 Introduction to Phased Array Technology

A dynamic ultrasound wavefront can be projected when the amplitude and/or phase are spatially altered over the wave front. A phased array made up of several independently controlled transducer is the conventional method for producing a desired sound field. The complexity of driving electronics, which necessitates a single channel, and the digital control in phase, which is limited by the digital control electronics, are the two main drawbacks, though which restrict the scalability of phased array technology. This chapter presents a completely new concept of optical control for using an ultrasound phased array to produce intricate ultrasonic wave fields.

Electronically controlled phase-arrays provide significant systems advantages and are receiving considerable attention b for airborne-, space-, surface- and ground-based applications and specially for medical imaging and treatment purposes. The arrays are mostly act as a central transmitter or receiver but have to shift the phase at each radiating element or subarray. The input to the radiating element is generally provided by the feeder network which contains a high power amplifier and a control system for phase configuration. FPGA (Field Programmable Gate Array) is the current state of technology which can be used to implement the phased-array configuration on chip based devices. FPGAs also have digital functions in addition to analog features, the most common analog features are quartz-crystal oscillators, on-chip resistance-capacitance oscillators and phase-locked loops with embedded voltage-controlled os-

cillators. They are engineered to have integrated peripheral ADCs (analog-to-digital converters) and DACs (digital-to-analog converters) with analog signal conditioning blocks allowing them to operate as a SoC (system-on-a-chip). The distinct advantage of functionalizing phased-arrays with FPGAs is that they are dynamic and can be reconfigured in real time with controllable phase of individual elements. This simple approach can really revolutionized the generation of electromagnetic waves and ultrasound waves. However, the complexity arrives in implementing elaborate arrays where each radiating element is individually addressable, which typically requires an independent drive input with complex support electronics. Thus, the complexity and cost of phased-array systems increases unfavourably with the number of radiating elements.

The primary application of the phased array was originally conceived by military radar systems. A phase array antenna in broadcast engineering means an array of multiple radiator elements designed to radiate a directional radiation pattern, as opposed to a single radiator element which emits radio-frequency waves in an omni-directional pattern. Generally, a radiated signal arrives at spatially separated antenna elements at different times which is controlled by electrical circuitry. Versatile multiple antenna systems provide a plethora of solutions for communications and radar, such as MIMO (Multiple-Input-Multiple-Output) diversity transceivers and SAR (Synthetic Aperture Radars). The phased array principle can also be used in acoustics, and phased arrays of acoustic transducers are used in medical ultrasound imaging scanners, reflection seismology, and military sonar systems. Electronically configurable phased-array systems are well engineered in shaping electromagnetic fields but are less well know in the ultrasonic acoustic field, but exist in a basic form especially in the sonic (audible) acoustic area. Generally, the electroacoustic transducer can be driven by an analog signal which is fed by a digital power amplifier. The digital power amplifier incorporates a signal input, a clock input, an output clock, which is either internally generated, or externally controlled by clock generator circuits, this constitutes the variable digital signal time-delay element which translates to phase control of the signal. This provides a means to adjust the delays between a given input terminal and each electroacoustic transducer, therefore it can shape a sound field which may comprise of a directed beam, focus beam or a simulated origin.

4.2 Electrically Controlled Phase-Shift

Phase shift is a relative quantity and is generally denoted by the difference in phase between the output and input analog signal. Phase shift in an electrical circuit originates from the presence of reactive components: capacitors and inductors. Capacitors causes a 90° lag of voltage behind current, while an inductor causes a 90° lag of current

behind voltage. This is represented by the $+\iota$ or $-\iota$ in the inductive and capacitive reactance respectively. The basic circuit that provides a phase-shift to an input analog signal is a series RC network. Inductors can also be utilized to design the phase-shift networks such as in LCR series or LR series but inductors generally introduce frequency instability and distorted waveforms in the output. Moreover, they have larger aspect ratio compared to resistors and capacitors which poses a problem in the design of array of phase shift circuits operating in a parallel configuration. Inductors stored the electrical energy in the form of magnetic field and therefore they can easily establish electromagnetic coupling with the adjacent inductors based on the mutual inductance. This further introduces another drawback of electromagnetic interference between the individual elements of array, when inductors are constituted the phase shift networks. It is therefore justified to design a phase shift network based on passive elements which are resistors and capacitors for good frequency stability and undistorted waveform in the output of the circuit.

The other branch of electronic elements that can be utilized for the design of phase-shift networks are active elements such as BJTs (Bipolar Junction Transistors), FETs (Field Effect Transistors), OpAmps (Operation Amplifiers) and so on. Active elements become important in the design of active circuits that use an OpAmp or transistors as the active element in combination with some resistors and capacitors to provide an analogue performance with respect to LCR series circuits. The first problem that one encounters in designing the transistor-based phase shift is that of the relatively low impedance associated with the transistor. Secondly, the transistors mostly operate in the positive voltage regime therefore the AC sinusoidal voltage inputs are generally superimposed on a DC voltage to match the low negative voltage level with the zero level voltage. This means that at the output terminal one has to design a high pass filter circuit to obtain the undistorted waveform without the presence of constant voltage. The requirement of the biasing at constant voltage makes it a non-feasible design for the high power applications which has very high input voltages (100V - 500V). The addition of the high pass filter circuit at the output increased the level of complexity in an array of phase shift circuits operating in parallel based on a single/double input. The design based on the active elements thus makes it difficult to be implemented on a chip scale fabrication which is not the case for the passive elements circuit due to the presence of fundamental electronic components.

4.3 Spatial Light Modulator: Motivation for Acoustic Analogue

The control of optical waves have achieved a major technological advance where a complex optical wavefront can be obtained by the superimposition of secondary wave-

fronts, thereby generating a desired wavefront. A SLM (Spatial Light Modulator) is a state-of-the-art device that modulates intensity or phase of a light beam or both. Most SLMs are based on liquid crystal technology. A microsystem called DMD (Digital Micromirror Device) is another way to shape beams. It consists of mirror actuators arranged in a matrix. The angle of each mirror can be adjusted individually through the application of electrostatic fields. Hence, these devices are generally called a EASLM (Electronically Addressable Spatial Light Modulator). There are also OASLM (Optically Addressable Spatial Light Modulator) which contains liquid crystals or metal oxide nanoparticles which can modulate the wavefront in response to an optical signal by displaying a phase pattern configured by the intensity distribution of write light input. These technologies used to generate phase modulated optical wavefronts suggest that one may employ light as the control for a phased-array system of radiating ultrasound generating elements (transducers).

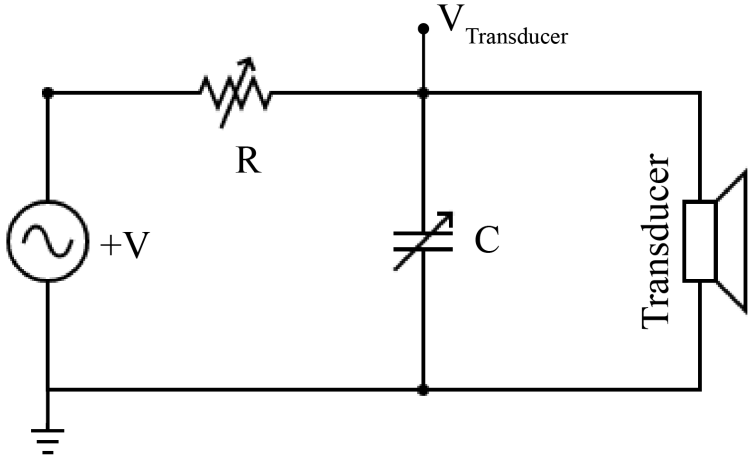

Figure 4.1: Schematics of series resistor-capacitor circuit.

The strategy involves implementing a monolithic optically addressable control circuit in conjunction with the radiation element to adjust the phase of the output waves. This process begins with a basic resistor-capacitor (RC) network that can provide the desired phase shift to an input signal represented by $+V = V_I \sin(\omega t)$ (see Fig. 4.1). In a straightforward RC circuit, the output voltage ($V_{Transducer}$ or V_T) theoretically lags the input voltage by a phase angle of 90°. Generally, the phase angle will be slightly below 90°, because a purely ideal capacitor does not exist and has resistive components. The phase shift of a practical RC network depends on the value of the capacitor, resistor and the operating frequency. Piezoelectric elements used to generate sound waves upon the application of alternating external voltage, behave like capacitive loads and hence can be implemented in a series RC circuit (Eq. 4.1). It is evident from Eq. 4.2 and Eq. 4.3 that a photoactive resistor provides a variable phase shift to the output voltage. The magnitude and phase of the output voltage with respect

to the input supply voltage at the terminal V_T (Fig. 4.2 and Fig. 4.3) clearly present the variation in the phase as a monotonic function of resistance (R). The terminal voltage at V_T is a sinusoidal output voltage which is equal to $V_{CF}\sin(\omega t + \phi_{CF})$.

$$C_F = C + C_T \tag{4.1}$$

$$V_{CF} = \left| \frac{V}{1 + \iota\omega \times RC_F} \right| \tag{4.2}$$

$$\phi_{CF} = \angle \frac{V}{1 + \iota\omega \times RC_F} \tag{4.3}$$

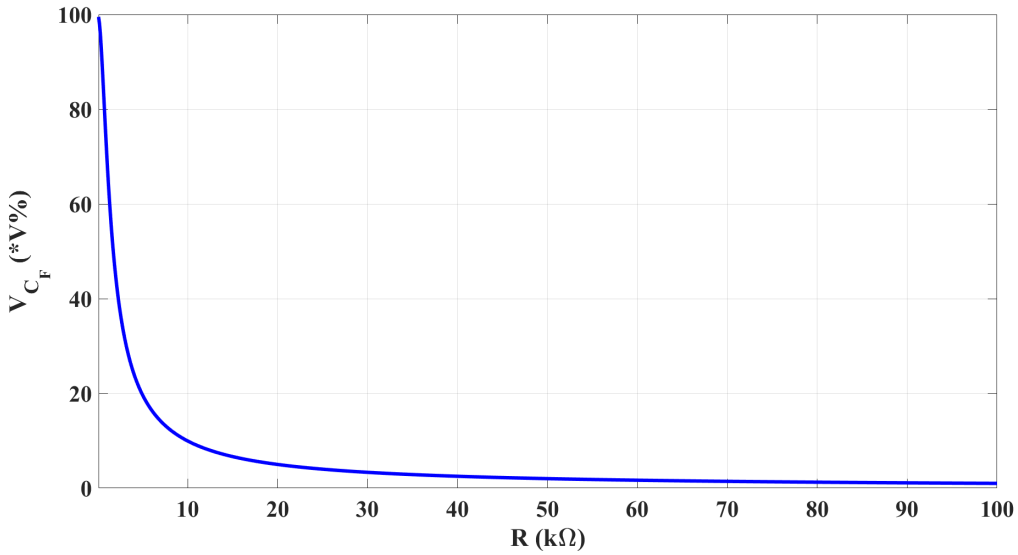

Figure 4.2: Analytical results for the magnitude-response of the output voltage in the series resistor-capacitor circuit.

4.4 Circuits to Generate a Electrical Phase-Shifted Signal

The primary disadvantage of a simple RC circuit for phase modulation is unfavourable scaling in the amplitude of the output voltage. This makes the circuit unreliable and power inefficient for practical applications. Nevertheless, it provides a $\approx 90°$ phase shift control to the output signal based on the value of resistance. Hence, the circuit can acts as a basic building block for designing more efficient phase control circuit. Further improvement is obtained by implementing a two-stage RC circuit (Fig. 4.4) where the resistors vary identically upon the optical excitation. The phase output of two-stage RC circuit is governed by the following set of equations:

$$C_F = C_2 + C_T \tag{4.4}$$

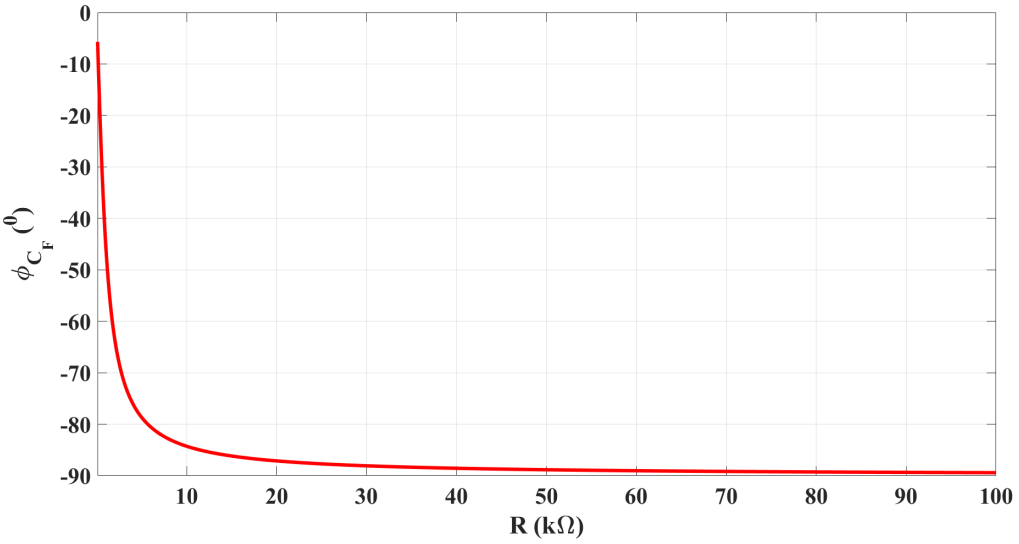

Figure 4.3: Analytical results for the phase-response of the output voltage in the series resistor-capacitor circuit.

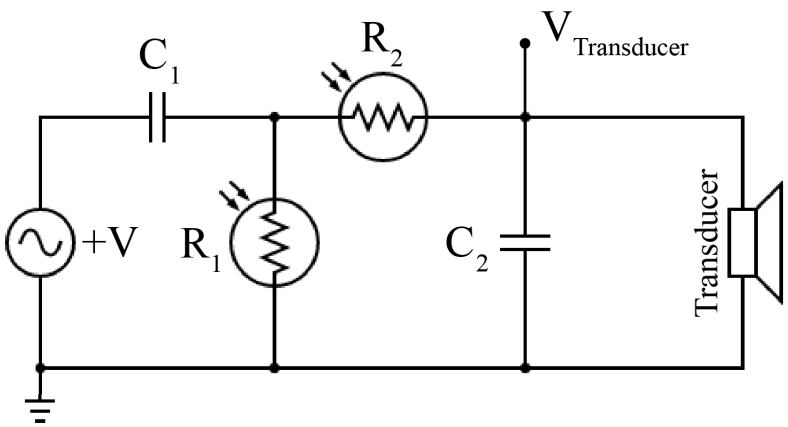

Figure 4.4: Schematics of two-stage resistor-capacitor circuit.

$$V_{CF} = \left| \frac{+\iota\omega R_1 C_1 \times V}{-\omega^2 C_1 C_F R_1 R_2 + 1 + \iota\omega \times (R_1 C_1 + R_2 C_F + R_1 C_F)} \right| \tag{4.5}$$

$$\phi_{CF} = \angle \frac{+\iota\omega R_1 C_1 \times V}{-\omega^2 C_1 C_F R_1 R_2 + 1 + \iota\omega \times (R_1 C_1 + R_2 C_F + R_1 C_F)} \tag{4.6}$$

The analytical variation in the magnitude and phase of the output voltage ($V_{Transducer}$) in the two-stage RC circuit are provided in the Fig. 4.5 and Fig. 4.6 respectively. This circuit provides the phase difference of $\approx 180°$ which approximately ranges from $-\frac{\pi}{2}$ to $+\frac{\pi}{2}$ and therefore gives a better phase-shift output as compared to the conventional RC phase shift circuit. Despite the improvement in the phase response of the two-stage RC circuit, there is a 10% to 50% variation in the output voltage with respect to the input voltage.

To minimize the variation in voltage and maximize the phase change, the following

Elements	Values
C_1	200 pF
C_2	100 pF

Table 4.1: Values of the elements in the two-stage RC circuit.

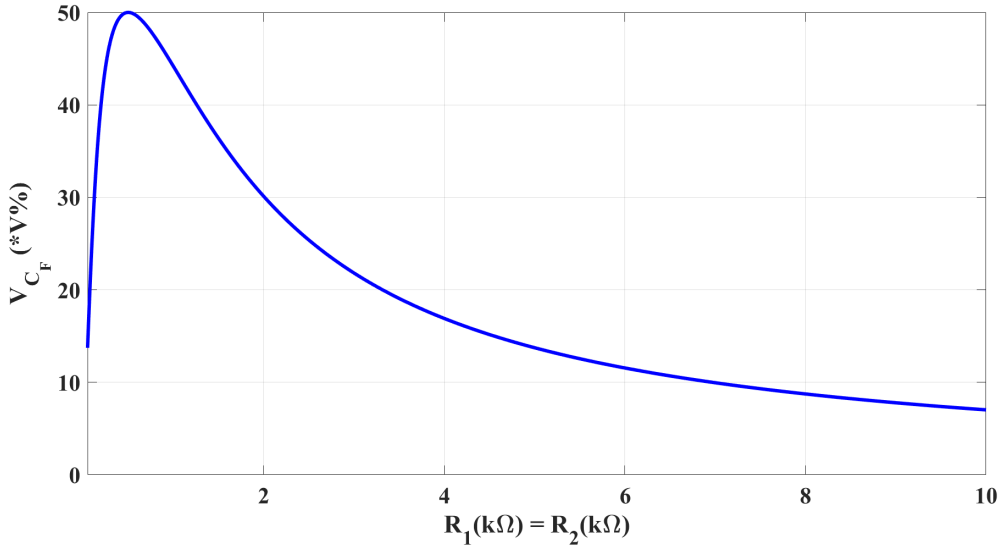

Figure 4.5: Analytical results for the magnitude-response of output voltage in the two-stage resistor-capacitor circuit.

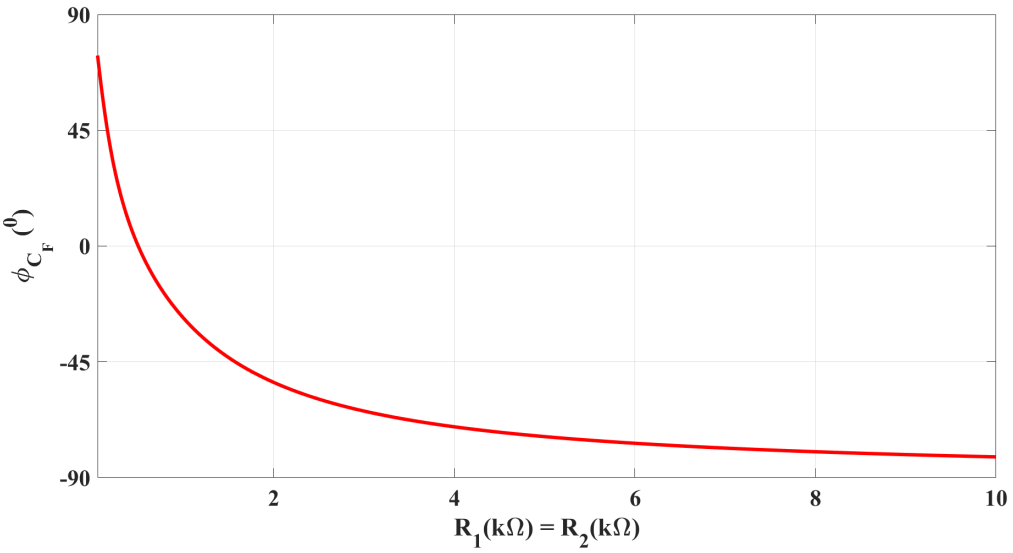

Figure 4.6: Analytical results for the phase-response of output voltage in the two-stage resistor-capacitor circuit.

improvement in the form of a simultaneous application of a π phase-shifted input and a 0 phase-shifted input signal. This change is inspired from the balanced RC filter circuits, where the ground terminal is replaced by the π phase-shifted input to provide a constant output voltage, numerically equivalent to the input supply

voltage. Therefore, the circuit of the two-stage RC phase circuit is further modified by substituting the ground terminal with the π phase-shifted input signal (Fig. 4.7).

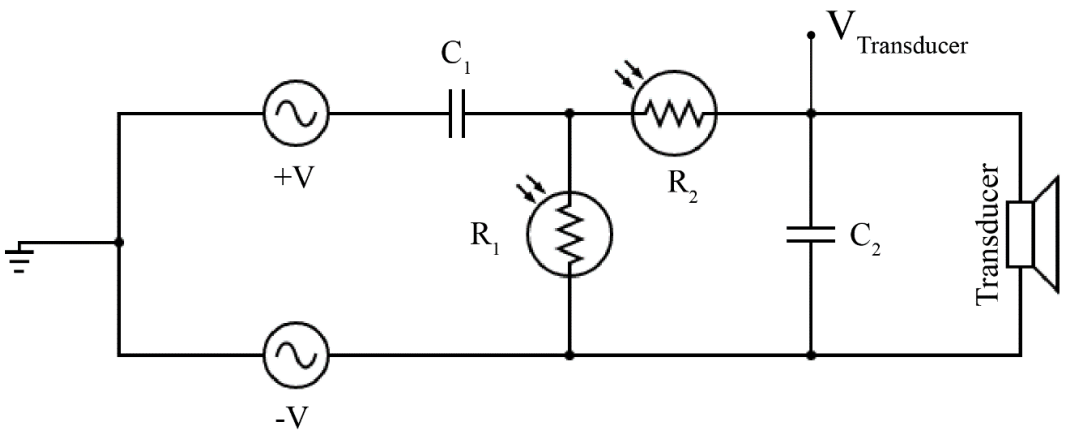

Figure 4.7: Schematics of the two-stage resistor-capacitor circuit with π phase-shifted input signal.

The voltage response (Fig.4.8) is well improved as compared to the two-stage RC circuit and therefore provides a better solution to the problem of obtaining an optically controlled phase shifter circuit. Similarly, the phase response (Fig.4.9) shows an almost complete $-\pi$ to $+\pi$ phase variation. This circuit can be modelled by the following set of equations:

$$C_F = C_2 + C_T \tag{4.7}$$

$$V_{CF} = \left| \frac{V \times (+\omega^2 R_1 R_2 C_1 C_F - 1 + \iota\omega \times (R_1 C_1 - R_2 C_F - R_1 C_F))}{-\omega^2 C_1 C_F R_1 R_2 + 1 + \iota\omega \times (R_1 C_1 + R_2 C_F + R_1 C_F)} \right| \tag{4.8}$$

$$\phi_{CF} = \angle \frac{V \times (+\omega^2 R_1 R_2 C_1 C_F - 1 + \iota\omega \times (R_1 C_1 - R_2 C_F - R_1 C_F))}{-\omega^2 C_1 C_F R_1 R_2 + 1 + \iota\omega \times (R_1 C_1 + R_2 C_F + R_1 C_F)} \tag{4.9}$$

The circuit contains the π phase-shifted input signal to balance the magnitude-response of the output signal (V_T) and hence it should be noted that the voltage across the transducer is not directly given by V_T. The voltage across the transducer is actually equivalent to $V_T - (-V)$ where $V_T = V_{CF}\sin(\omega t + \phi_{CF})$ and $V = V_I \sin(\omega t)$. The output voltage can be simplified to $\sin(\omega t) \times (V_{CF}\cos(\phi) + V_I) + \cos(\omega t) \times (V_{CF}\sin(\phi))$. This clearly shows that the output voltage is a superposition of two-voltage signals with $\pi/2$ phase difference. The superposition results in a non-sinusoidal waveform which depends on the numerical values of V_{CF} and ϕ_{CF} and therefore, it is important to constrain the output voltage across the ground terminal to restrict the superposition of voltage signals. The possible amendment to the circuit is connecting the π phase-shifted input terminal to ground (Fig. 4.10), this solves the problem of superposition and also partially isolates the circuit from the variation in the electrical properties of piezo-capacitance. The mathematical description now only contains in the term for

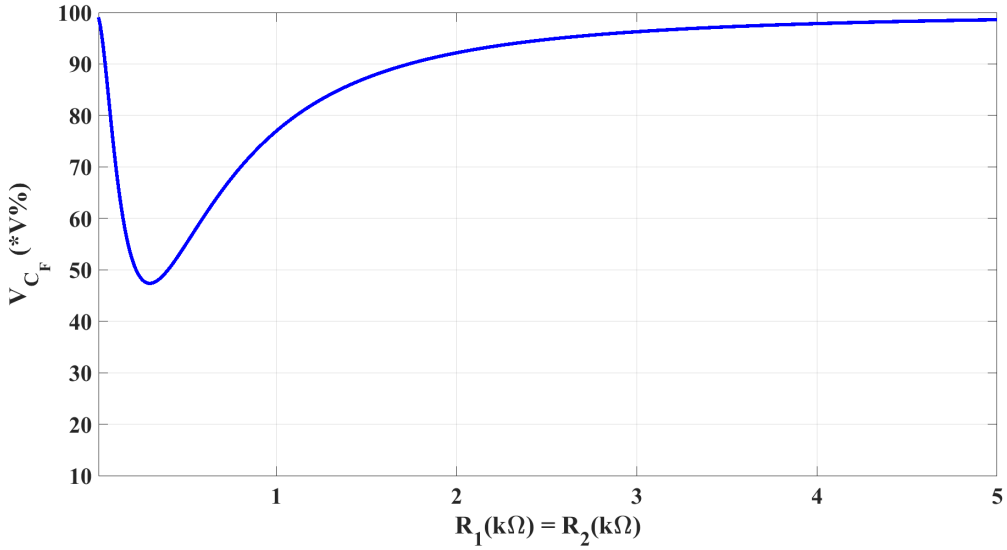

Figure 4.8: Analytical results for the magnitude-response of the output voltage in the two-stage resistor-capacitor circuit with π phase-shifted input signal.

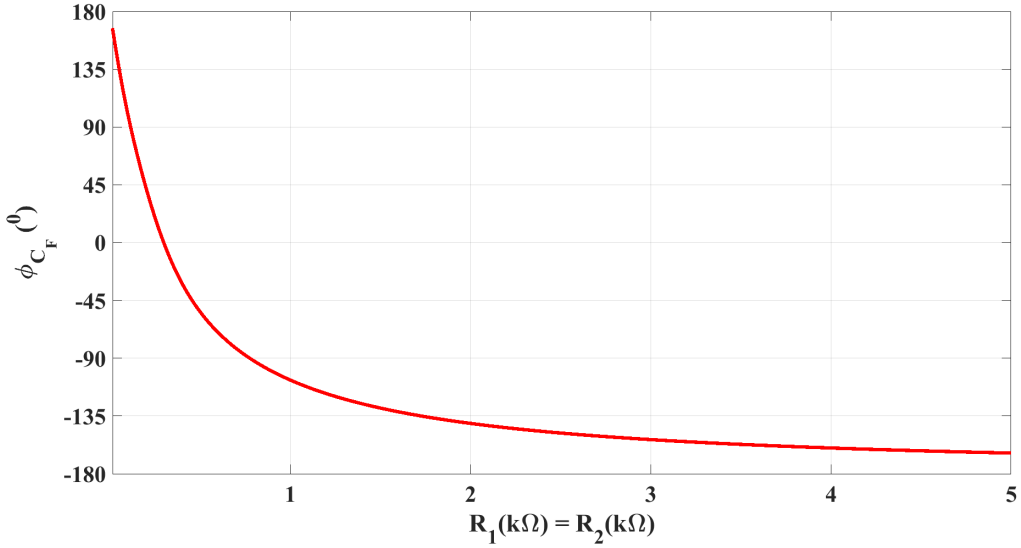

Figure 4.9: Analytical results for the phase-response of the output voltage in the two-stage resistor-capacitor circuit with π phase-shifted input signal.

piezo-capacitance (C_F), in the expression for the voltage and phase:

$$C_F = C_2 + C_T \tag{4.10}$$

$$V_{CF} = \left| \frac{V \times (+\omega^2 R_1 R_2 C_1 C_2 - 1 + \iota\omega \times (R_1 C_1 - R_2 C_2 - R_1 C_2))}{-\omega^2 C_1 C_F R_1 R_2 + 1 + \iota\omega \times (R_1 C_1 + R_2 C_F + R_1 C_F)} \right| \tag{4.11}$$

$$\phi_{CF} = \angle \frac{V \times (+\omega^2 R_1 R_2 C_1 C_2 - 1 + \iota\omega \times (R_1 C_1 - R_2 C_2 - R_1 C_2))}{-\omega^2 C_1 C_F R_1 R_2 + 1 + \iota\omega \times (R_1 C_1 + R_2 C_F + R_1 C_F)} \tag{4.12}$$

The analytically calculated value of the voltage at the terminal V_T varies by 50%

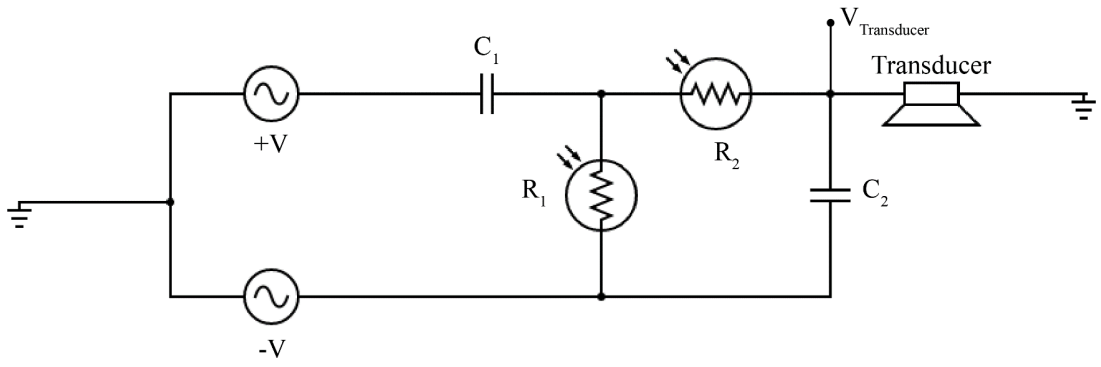

Figure 4.10: Schematics of two-stage resistor-capacitor circuit with π phase-shifted input signal and grounded transducer.

across the phase change with respect to the input voltage (Fig. 4.11). The voltage is neither monotonically increasing nor monotonically decreasing which is the primary drawback of series RC circuits when employed in phase modulating networks. The circuit is capable of generating a full 2π phase shift which is demonstrated by varying the resistors present in the circuit (Fig. 4.12).

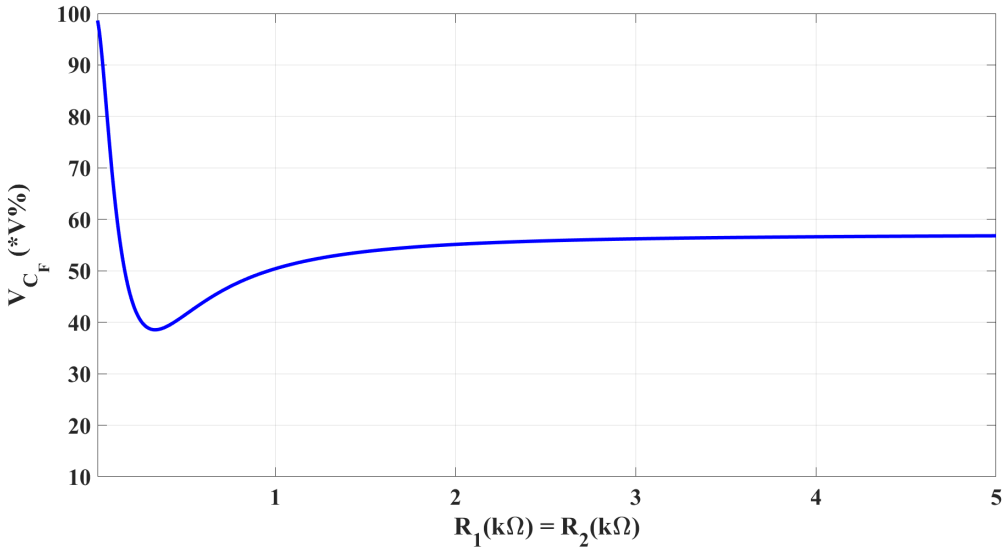

Figure 4.11: Analytical results for the magnitude-response of output voltage in the two-stage resistor-capacitor circuit with π phase-shifted input signal and grounded transducer.

4.5 Optically Controlled Phase-Shift for Electrical Signal

In order to achieve controlled phase-shift in the electrical signal, a variety of tunable/reconfigurable digital phase-shifters have been reported and designed using various technologies based on either semiconductor-based devices [116] (such as field-effect

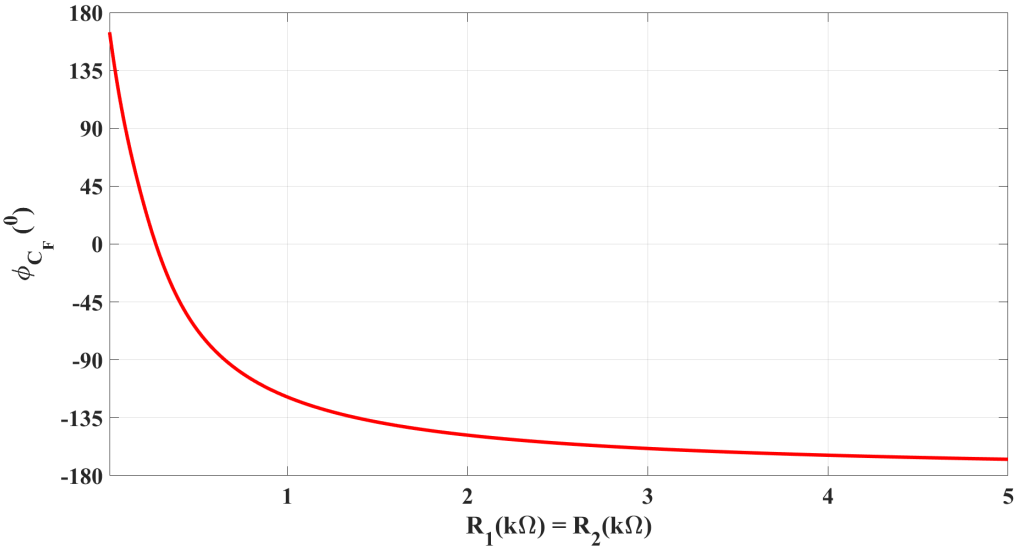

Figure 4.12: Analytical results for the phase-response of output voltage in the two-stage resistor-capacitor circuit with π phase-shifted input signal and grounded transducer.

transistors [FETs], PIN diodes, varactors) [117–119] or micro-electro-mechanical systems (MEMS) devices [120]. The phase-shifter circuits shown in the cited literature use tuning/switching components integrated into individual channels or placed in front of several output transducer channels (switched multiplexer design). However, in order to function, each of the aforementioned technologies needs a sophisticated biasing circuit [117–120]. Due to digital control in the phase from the bias circuitry, performance issues are introduced, which cannot be avoided. Additionally, circuit design and integration become challenging. The resolution of the digital phase control becomes more low as frequencies enter the higher ultrasound domain (5 MHz to 10 MHz). In addition, switching circuits typically exhibit significant performance degradation making them unsuitable for future systems. Although MEMS switches can be applied, their extremely challenging fabrication, and potential reliability issues make them extremely costly and sophisticated to integrate with multifunctional systems [116, 121].

To address these challenges and we propose a completely different approach for achieving high fidelity phase-shift in next-generation ultrasound phased-array systems. A novel optical control technology based on the modulation of conductivity in photoresistors (Fig. 4.13 (A)) has been introduced and explored. To realize our device, it is necessary to choose a photoresistor with low capacitive charge storage and high resistance ratio. These characteristics are necessary to achieve high phase tunability in a wide frequency band. To meet these requirements, we use a NSL-19M51 photoresistors (Advanced Photonix), whose resistance can be tuned from 50 Ω to 20 kΩ with a maximum operating voltage of 100 V. We measured how the photoresistor resistance

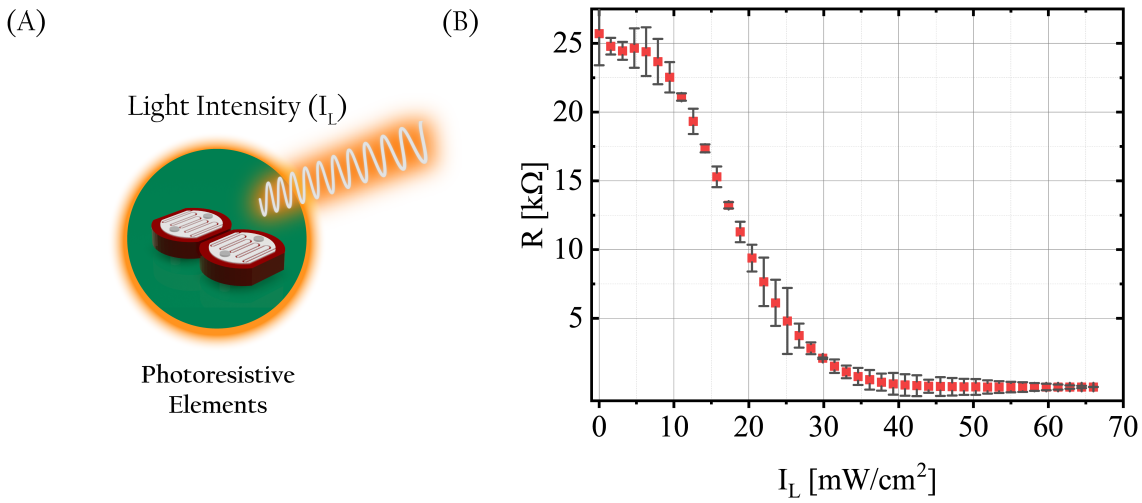

Figure 4.13: (A) Light addressable elements integrated with a Active Network based on photoresistors. (B) Electrical characteristics of the photoresistive element embedded in the pixel unit where the resistance (R) is measured for different values of light intensity (I_L).

depends on the incident light intensity. The measured values of resistor are 24.7 kΩ and 54.5 Ω for a maximum incident light intensity of 65.7 mWcm^{-2}. The experimental results for the variation of resistance as a function of light intensity is shown in Fig. 4.13 (B). This photoresistors-based method reduces circuit complexity and increases frequency bandwidth by doing away with the need for extra biasing circuits to achieve tunability and reconfigurability, especially in the context of phased-array designs at high frequencies (0.1 MHz to 5.0 MHz).

To further harness the simplicity in optical control and in pursuit of achieving a complete 2π phase-shift in the electrical as shown in Fig. 4.12, we substitute both the resistors R_1 and R_2 with the photoresistor such that the photoresistors are coupled together with an identical light intensity. By changing the illumination light, the resistive component of the circuit (Fig. 4.10) can be dynamically reconfigured and continuously tuned. We expect that using the light as an external control signal, a wide range of wirelessly tunable/reconfigurable analog phase-shifter with various frequency responses and multiple functionalities can be achieved. The element is driven with a 10-cycle sinusoidal pulse, amplified to 25 V_{pp}.

4.6 Electrical Characterization of Light-Addressable Phase Unit

The architecture of the light activated phase-shifter is presented in Fig. 4.14 (A). We used piezoelectric disks as the ultrasound transducers which are 3 mm in diameter and have contact electrodes on the top and bottom surfaces. We considered the transducers that are driven at a frequency of 2.25 MHz with peak-to-peak voltage

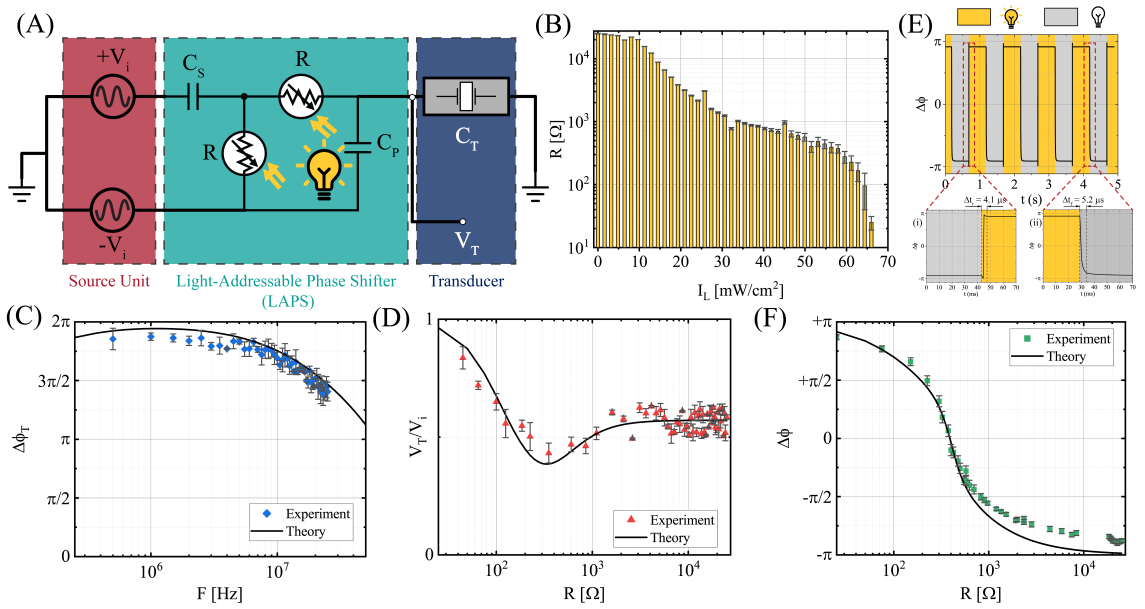

Figure 4.14: Electrical architecture with the measured and calculated performance of light addressable phase unit. (A) Simplified circuit diagram of the programmable pixel unit where the loaded transducer element is modelled as a capacitor with the capacitance C_T. (B) Electrical characteristics of the photoresistive element embedded in the pixel unit where the resistance (R) is measured for different values of light intensity (I_L). (C) and (D) The experimental and theoretical curves of phase-shift ($\Delta\phi$) (C) and relative amplitude (D) in the ultrasound pressure wave presented for several different values of resistance R. The resistance R is controlled by regulating the light intensity I_L. (E) The phase-shift ($\Delta\phi$) of the emitted ultrasound wave under a reversible alternative switching at 1 Hz between 0 and 1 states of light intensity which symbolize power of 0.1 µW cm^{-2} and 65.7 mW cm^{-2} respectively. The insets (i) and (ii) describe the magnified sections of the reversible phase switching to determine the rise-time (Δt_r) and fall-time (Δt_f) respectively. (F) Experimentally measured range of total phase shift presented for several different values of frequency (F).

(V_{PP}) of 82.5 V with a maximum current of approximately 12.7 mA. The transducer under the operation of high frequency voltage signal is modelled as a capacitor, where the capacitance (C_T) is evaluated to be in the range from 75.3 pF to 80.1 pF. We constructed a balanced dual-cascaded RC network which can be interpreted as a second-order (two-pole) type system attributed to the two reactive components in the structure. By adjusting the resistance of the embedded resistors, the driver circuit's effective time constant can be altered with this configuration without changing the ultrasound element's physical dimensions. This causes the excited ultrasound wave to phase change from $-\pi$ to $+\pi$ at a fixed frequency (F). The phase-shift ($\Delta\phi$) with respect to the input electrical signal (V_i) applied at the angular frequency ω ($\omega = 2\pi F$) can be written as:

$$\Delta\phi = \tan^{-1}\left[\frac{\omega \times (R_o C_S - 2R_o C_P)}{\omega^2 R_o^2 C_S C_P - 1}\right] - \tan^{-1}\left[\frac{\omega \times (R_o C_S + 2R_o (C_P + C_T)}{-\omega^2 R_o^2 C_S (C_P + C_T) + 1}\right] \quad (4.13)$$

,

where R_0 is the photo resistance value at a defined optical intensity (I_L).

The substrate of the ultrasonic transducer is composed of the low-loss dielectric material FR4, which has a dielectric constant (ϵ_r) of 4.3 and loss tangent ($\tan\delta$) of 0.025. The transducer elements are cylindrical piezoceramic disks of diameter 3 mm and height 1 mm, which are made of hard ferroelectric piezo material (PIC181, PI Ceramic). The transducer elements have coated silver electrodes and a resonance frequency of 2.25 MHz in the thickness mode of operation. We designed suitably designated circular copper pads analogous to the dimensions of elements on the rigid Printed Circuit Board (PCB). The copper pads are approximately 20 µm thick, which provide sufficient mechanical support to the transducer elements. The signal from a function generator (AFG 1062,Tektronix) is fed to a low-impedance 50× voltage amplifier (WMA-300, Falco Systems), which drives the transducer. The pressure amplitude and phase output by the transducers are recorded using a 0.4 mm diameter hydrophone (HGL0400, Onda Corporation) and a digital storage oscilloscope (Tektronix, TDS2000C). We extracted the equivalent continuous wave pressure field by taking a Fourier transform of the received pulse, and the pressure amplitude and phase are extracted at 2.25 MHz. The error bars are present due to the variation in the light intensity which is around 1.1 mW/cm^2 to 2.0 mW/cm^2. The other reason for the presence of error bars in the phase is the non-identical variation in the photo-resistances upon the excitation with light. The photo-resistances have a 10% variation in the resistance which also contributes towards the generation of errors in the phase of the output signal.

We selected a photoactive element with low capacitive charge storage and high resistance ratio as mentioned previously in the chapter. The detailed measurement results of photoresistors as a function of light intensity are presented in the Fig. 4.14 (B). Then, we monitored the pressure with a hydrophone that is placed approximately 2.5 mm above the surface of transducer while changing the light intensity incident on a photoresistor. The experimental and theoretical results for the relative amplitude (V_T/V_i)and phase-shift ($\Delta\phi$) of the ultrasound wave for distinct resistance values are shown in Fig. 4.14 (D) and (C), respectively. Tuning the light intensity from 0.1 µW cm^{-2} to 65.7 mW cm^{-2}, the phase-shift of the electrical signal is translated into the phase-shifted ultrasound wave emitted from the transducer. The experimental results convincingly validate the device functionality. Its agreement with the theoretical analysis supports the argument that a broadband optically programmable

phased-array of transducer can be constructed experimentally in the complete angular domain of $-\pi$ to $+\pi$.

The refresh rate of the phase reconfiguration is limited by the switching speed of the cascaded network, whose operation depends on the response time of embedded resistors and capacitors. We modulated the light intensity between ON/"1" (high light intensity of 65.7 mW cm^{-2}) and OFF/"0" (low light intensity of 0.1 µW cm^{-2}), which provides an ON/OFF ratio of approximately 58 dB and started the digital light intensity control clock at 1 Hz. We experimentally measured the rise-time (Δt_r) and fall-time (Δt_f), which is the phase reconfiguration time from $-\pi$ to $+\pi$ and $+\pi$ to $-\pi$ respectively, as shown in Fig. 4.14 (E). The measured values of Δt_r and Δt_f are ~4.1 ms and ~5.2 ms described in Fig. 4.14 (E) (i) and (ii) respectively, which clearly suggest that the total cycle time for phase reconfiguration is Δt ($\Delta t_r + \Delta t_f$) ≈ 9.3 ms. This switching time definitely suggests the modulation of the ultrasound wavefront at a maximum rate of ≈ 100 Hz. The optical switching of ultrasound phase at a frequency of 100 Hz is demonstrated experimentally as shown in Fig. 4.15.

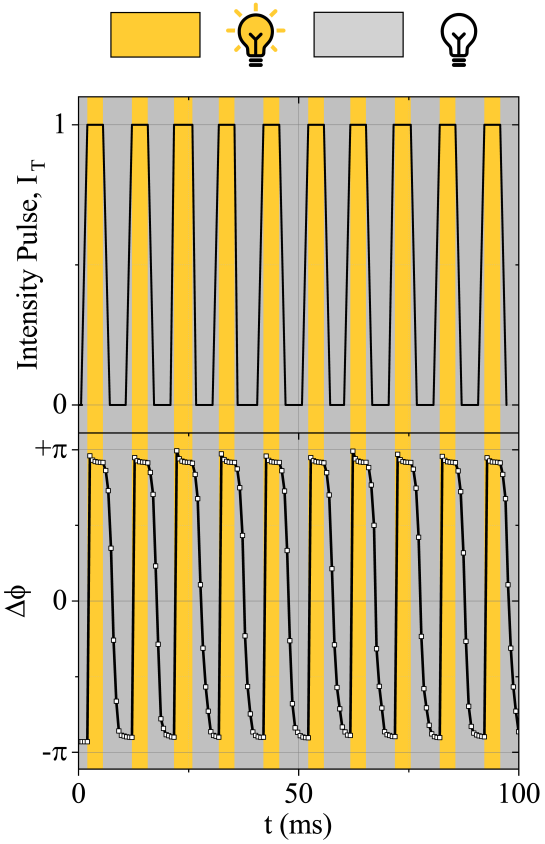

Figure 4.15: Fast switching of ultrasound phase. The phase-shift of the emitted ultrasound wave when the light is switched on (I_L = 65.7 mW cm^{-2}) and off at 100 Hz.

Additionally, we investigated the output electrical characteristics for different capacitor loads and determined that the total phase shift (max($\Delta\phi$) - min($\Delta\phi$)) is

independent on the capacitance of the transducer element. We performed a frequency analysis to measure the bandwidth of the system by substituting the transducer element by an equivalent non-polarized thin film capacitor. The LAPS as discussed in previously in the chapter can produce an approximate total phase-shift of 2π in a wide frequency band ranging from 0.1 MHz to 10 MHz by tuning the light intensity (I_L). The results are demonstrated in Fig. 4.14 (F). Thus, the realized device facilitates controlled implementation of sophisticated phased-devices by simple light illumination with the benefits of gentle change in the phase-shift and large dynamic tuning range from $-\pi$ to $+\pi$.

4.7 Experimental Measurement of Crosstalk Effects

It has been mentioned that in an ultrasound transducer array, the phase output of an individual transducer element could experience electrical crosstalk which could give undesirable distortion in the performance characteristics of the array structure while observing other elements. We therefore investigated the amount of crosstalk effects and measured the performance by individually addressing elements with different intensity of light. We evaluated crosstalk in our architecture by individually addressing individual elements in a 5×5 array of cylindrical piezos with different light intensities projected onto the LAPS. We quantified cross-coupling by measuring phase changes in the remaining inactive transducers.

4.7.1 Independent Operation of Transducer Elements

An important aspect in the circuit design is that there is no or little electrical cross-talk between the operating load of the circuit. The two-stage RC circuit with π phase-shifted input signal and grounded transducer are utilized for the cross-coupling study. The circuit schematics of the bi-piezo experimental system is shown in Fig. 4.16. The pressure measurements are performed upon the excitation with a voltage pulse. The voltage pulse contains 10 cycles at the respective frequency. The system is synchronized by a 10 V positive square voltage pulse whose positive edge provides the trigger to execute the input voltage and start the recording of the generated pressure through the hydrophone. The method is utilized to differentiate the true pressure signal from any Electro-Magnetic Interference (EMI) signals. The differentiation is based on the fact that the EMI signal is recorded in the adjacent time proximity of the positive edge of trigger voltage pulse while the hydrophone receives the true pressure signal after a certain interval of time based upon the sound propagation distance between the hydrophone and piezo surfaces. The current experimental system has the time interval of 2.5 µs to 4.9 µs.

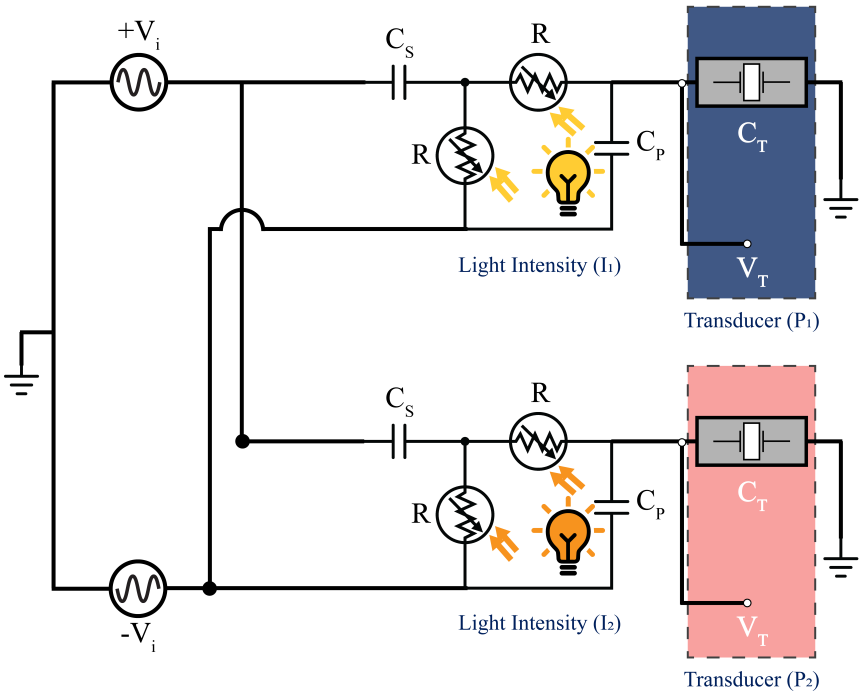

Figure 4.16: Simplified circuit diagram of the programmable pixel unit where the loaded transducer element is modelled as a capacitor with the capacitance C_T

The experimental measurements are performed at 2.25 MHz (Fig. 4.17) and 2.50 MHz (Fig. 4.18), these results corresponds to the two-stage RC circuit and the light-ON mode symbolizes the maximum intensity of $\approx 66\,\mathrm{mW/cm^2}$ whereas the light-OFF mode symbolizes the intensity of $\approx 0\,\mathrm{mW/cm^2}$. It is evident from the pressure waveform of P_1 piezo that the output signal phase varies from $-\pi/2$ to $+\pi/2$ when compared in the light-OFF and light-ON mode. Thus, this provides the phase control of π to the P_1 piezo output pressure which is depicted both numerically and experimentally in the phase of the output voltage. Similarly, the pressure waveform for the P_2 piezo is plotted for the actuation frequency of 2.25 MHz (Fig. 4.17b) and 2.50 MHz ((Fig. 4.18b)). The result shows the independent phase modulation and hence the absence of cross-coupling in the bi-piezo system.

Further experiments on the two-stage RC circuit considered the variation of P_1 piezo and P_2 piezo based light amplitude and examined the output pressure waveform generated by the P_1 piezo through the hydrophone. The measurement is performed at the operating frequency of 2.50 MHz (Fig. 4.19). The term I_O symbolizes the maximum intensity of $\approx 66\,\mathrm{mW/cm^2}$; I_1 and I_2 represents the P_1 piezo and P_2 piezo based light-control amplitude respectively. The results further validate the fact that the output pressure waveform from the P_1 is completely independent of the P_2 based light amplitude (I_2) and therefore the phase of the output pressure from the P_1 is a single-variable function of light amplitude (I_1).

The next stage of experiments considered the two-stage RC circuit with π phase-

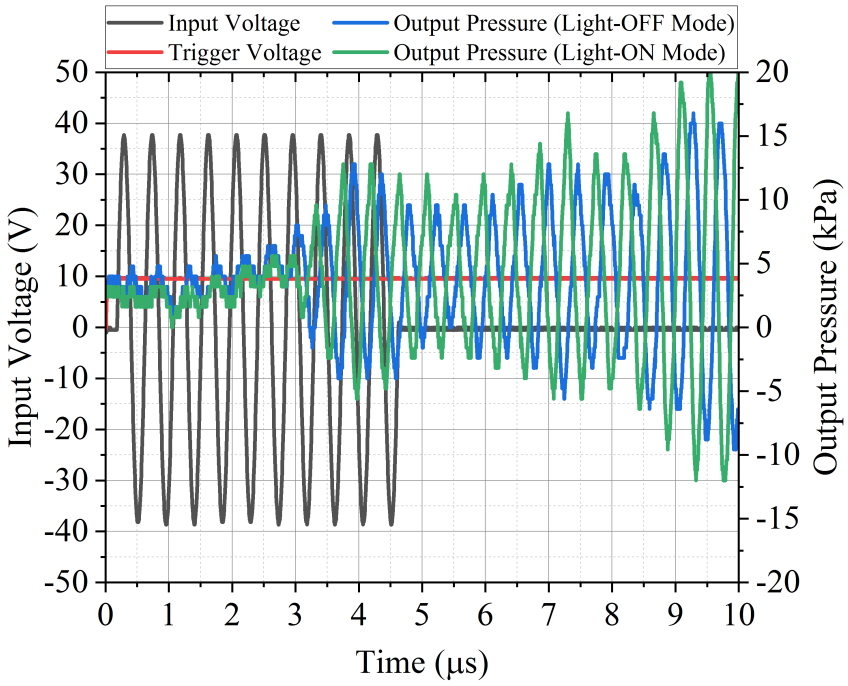

(a) Pressure measurements of P_1 piezo with respect to light-ON and light-OFF mode of P_1.

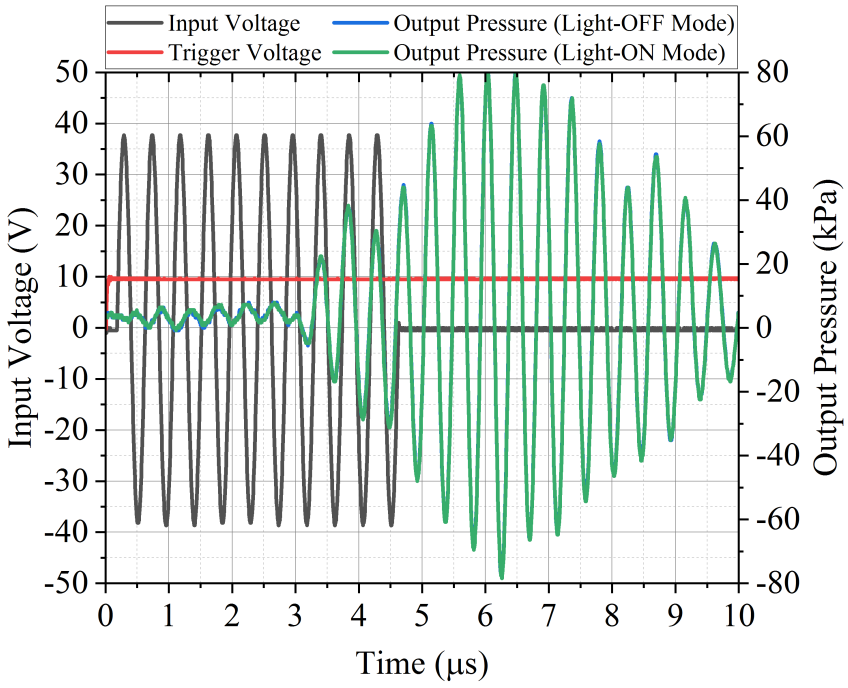

(b) Pressure measurements of P_2 piezo with respect to light-ON and light-OFF mode of P_1.

Figure 4.17: Pressure measurements in a bi-piezo system developed using two-stage RC circuit to examine the effect of P_1 piezo based light-ON and light-OFF mode on the P_2 piezo output pressure at the ultrasound frequency of 2.25 MHz.

shifted input signal and grounded transducer. The pressure measurements are per-

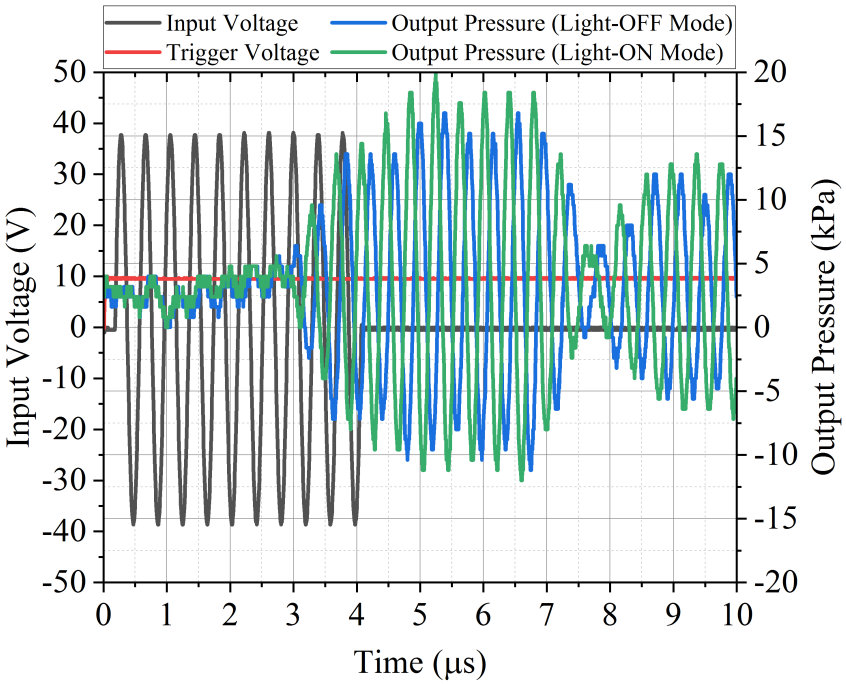

(a) Pressure measurements of P_1 piezo with respect to light-ON and light-OFF mode of P_1.

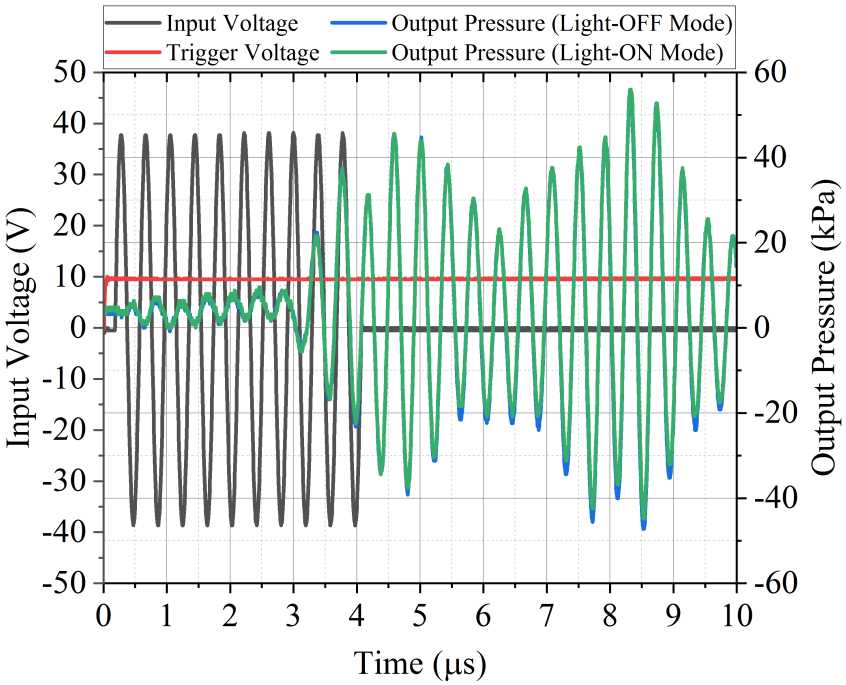

(b) Pressure measurements of P_2 piezo with respect to light-ON and light-OFF mode of P_1.

Figure 4.18: Pressure measurements in a bi-piezo system developed using two-stage RC circuit to examine the effect of P_2 piezo based light-ON and light-OFF mode on the P_2 piezo output pressure at the ultrasound frequency of 2.50 MHz.

formed based on an identical pulsed-input based method and the effect of P_1 piezo

based light amplitude control (I_1) and P_2 piezo based light amplitude control (I_2) on the output pressure from P_1 and P_2 are plotted sequentially at the ultrasound frequency of 1.75 MHz (Fig. 4.20), and 2.25 MHz (Fig. 4.21). It is evident from the results that the phase of output pressure waveform from the P_1 piezo is a function of P_1 piezo based light amplitude (I_1) and is completely independent of P_2 piezo based light amplitude (I_2). The amplitude of the pressure waveform shows a weak dependency on the P_2 piezo based light amplitude (I_2) and this can be explained by the fact that the power source is constraint by the maximum current supplied to the circuit. The circuits have an equivalent impedance which varies depending upon the magnitude of the photo-resistances which thereby affects the current level of the circuit elements of array. Each circuit is the array connected in parallel and the maximum voltage level of the sinusoidal input is kept constant across the end terminals. The variation in the equivalent impedance of each circuit in the array affects the current level provided to the complete circuit architecture but the performance of individual elements is independent of each other in the parallel configuration.

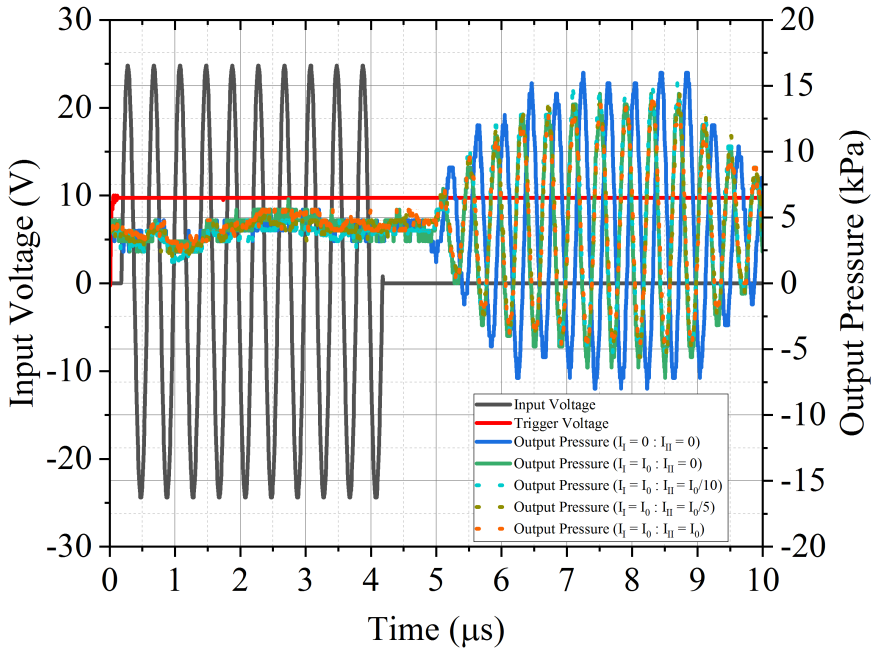

Figure 4.19: Pressure measurements in a bi-piezo system developed using two-stage RC circuit to examine the effect of P_1 and P_2 piezos based light-control mode on the P_1 piezo output pressure at the ultrasound frequency of 2.50 MHz.

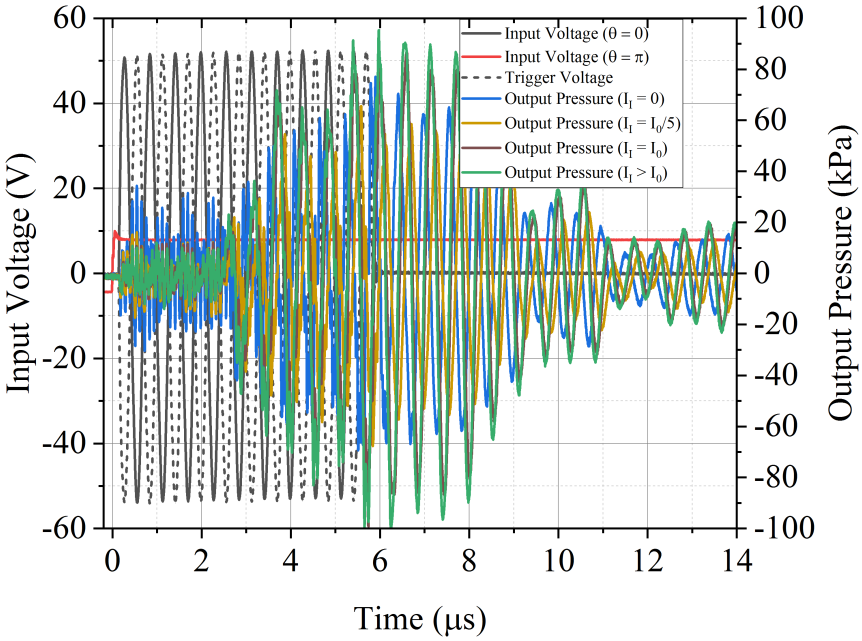

(a) Pressure measurements of P_1 piezo with respect to light amplitude control (I_1).

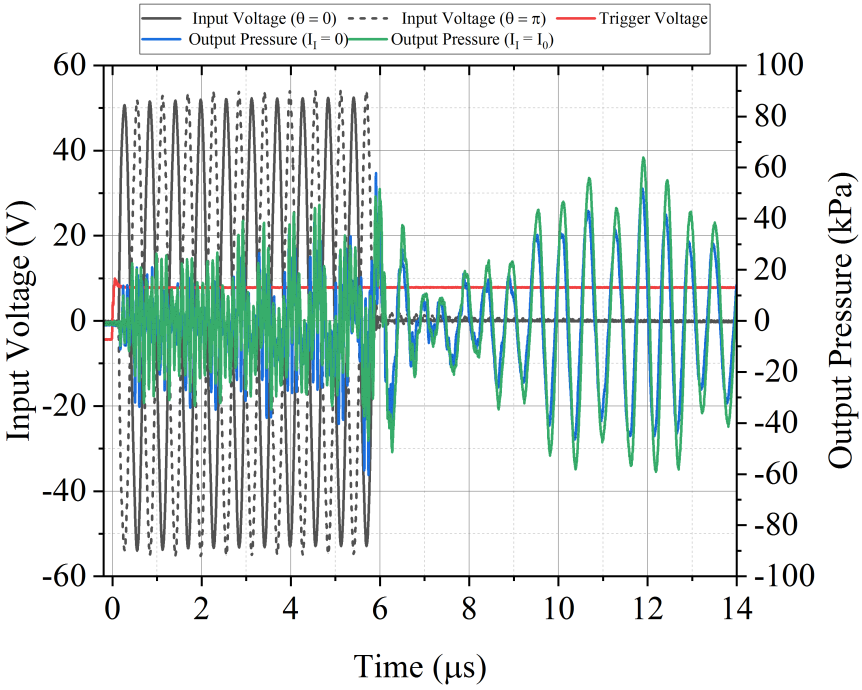

(b) Pressure measurements of P_2 piezo with respect to light amplitude control (I_1).

Figure 4.20: Pressure measurements in a bi-piezo system developed using two-stage RC circuit with π phase-shifted input signal and grounded transducer to examine the effect of P_1 piezo based light amplitude control (I_1) on the P_2 piezo output pressure at the ultrasound frequency of 1.75 MHz.

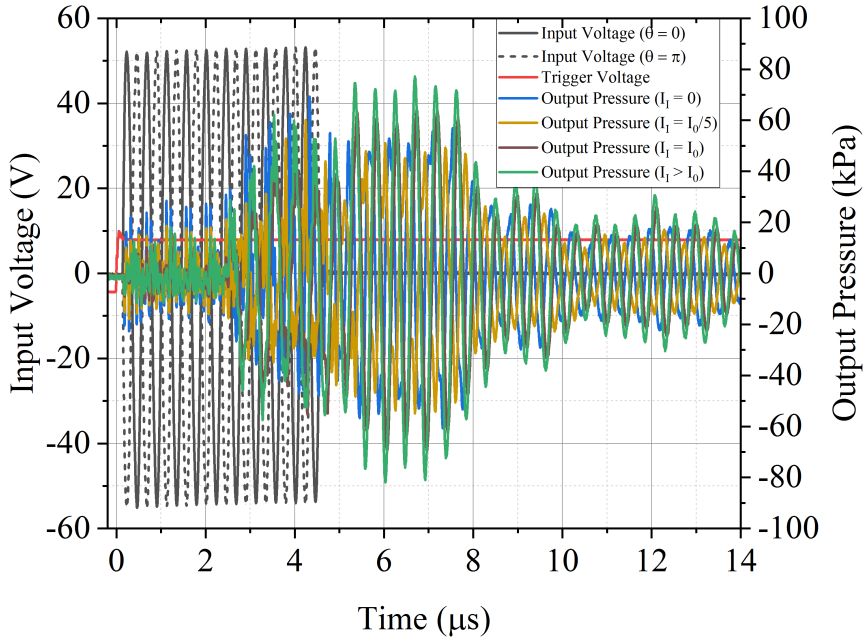

(a) Pressure measurements of P_1 piezo with respect to light amplitude control (I_1).

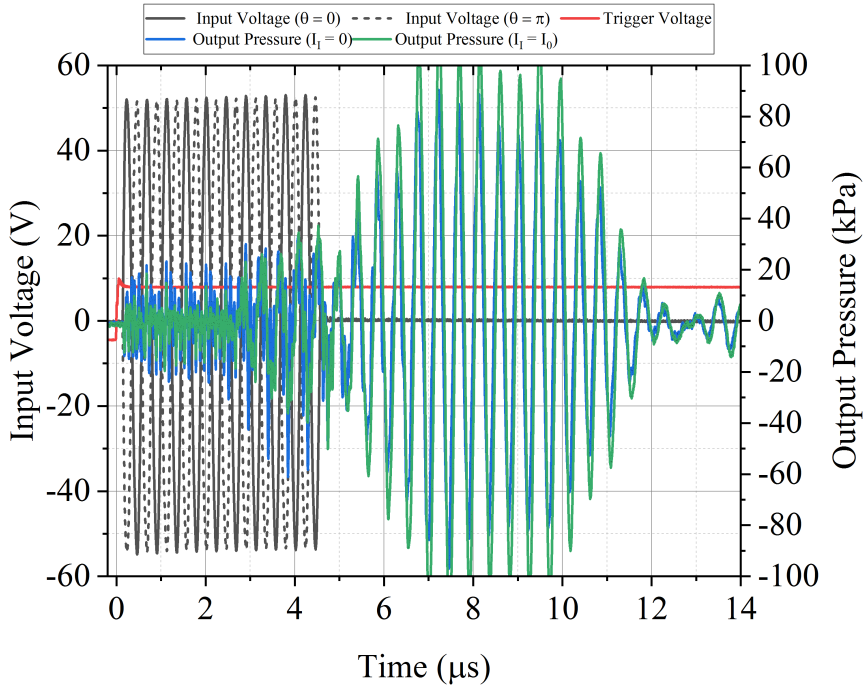

(b) Pressure measurements of P_2 piezo with respect to light amplitude control (I_1).

Figure 4.21: Pressure measurements in a bi-piezo system developed using two-stage RC circuit with π phase-shifted input signal and grounded transducer to examine the effect of P_1 based light amplitude control (I_1) on the P_2 piezo output pressure at the ultrasound frequency of 2.25 MHz.

4.7.2 Design Parameters for Two-Dimensional Array of Ultrasonic Transducers

We constructed the 5×5 array of ultrasonic transducers on a printed circuit board. The substrate of the ultrasonic transducer is composed of the low-loss dielectric material FR4, which has a dielectric constant (ϵ_r) of 4.3 and loss tangent ($\tan\delta$) of 0.025. The radius r of an individual element is 1.5 mm and the thickness t is 1.0 mm. We designed suitably designated circular copper pads analogous to the dimensions of elements on the rigid PCB. The copper pads are approximately 20 µm thick, which provide sufficient mechanical support to the transducer elements. The copper pads are implemented in the system for two major functions, first to provide an alignment for precise positioning of the actuator elements, and second to operate as the terminals for power transfer to the bottom electrode of ultrasonic actuators. In order to facilitate soldering of pads which supply excitation voltages to the electrodes and the ground paths, solder flux is often applied to the part of the surface of electrodes in piezoceramic disks, which does not affect the electro-mechanical parameters of transducers. The array pitch is 5.0 mm. The top electrodes are operated as the ground terminal in order to minimize electromagnetic interference between the actuation voltage and the measurement system. The top electrodes are custom-machined rectangular pads from a bronze sheet of thickness 100 µm. The rectangular-shaped top electrode pad has a length of 2.5 mm and width of 1.0 mm. The width of the bus line is 0.5 mm. The transducer elements are cylindrical piezoceramic disks of diameter 3 mm and height 1 mm, which are made of hard ferroelectric piezo material (PIC181, PI Ceramic). The transducer elements have coated silver electrodes and a resonance frequency of 2.25 MHz in the thickness mode of operation.

4.7.3 Mathematical Description of Crosstalk Matrix

We quantify the crosstalk by a statistical parameter that describes the cross-correlation. We calculate the cross-correlation ϱ_{ij} of the acoustic phases ϕ_{ij} produced at pixel i as a function of the light-controlled phase shift on pixel j. The cross-correlation is taken over a vector of phases measured as a function of different light intensities incident on pixel j of the OPAT. For our 5×5 array, the normalized cross-correlation matrix ϱ is a 25×25 matrix containing the pairwise cross-correlation between all elements, as given by

$$\varrho_{ij} = \frac{\mu[\phi_i \phi_j] - \mu[\phi_i]\mu[\phi_j]}{\sigma_{\phi_i} \times \sigma_{\phi_j}}, \tag{4.14}$$

where ϕ_i and ϕ_j are the output phase vectors of the transducer elements i and j, respectively. The output phase vectors ϕ_i and ϕ_j are recorded with respect to the

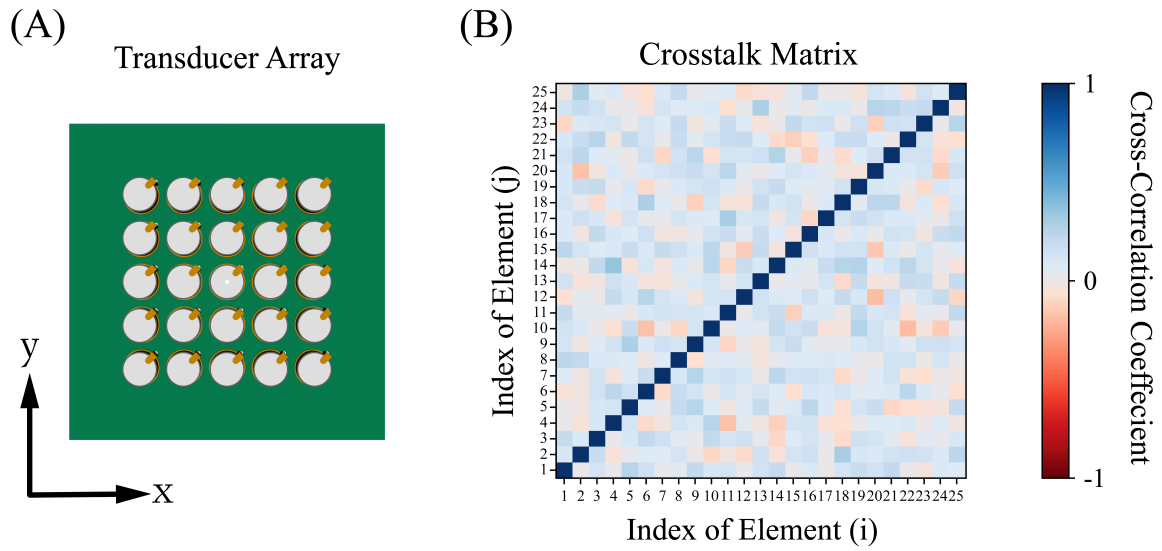

Figure 4.22: Crosstalk measurement in 5×5 transducer array. (A) Schematic of the constructed 5×5 transducer array. (B) The results of the cross-correlation measurements plotted in matrix representation.

input light intensity vector $I_{L|i}$ controlling the active transducer element E_j. μ and σ denote the mean and standard deviation operator, respectively.

The function ϱ_{ij} is defined such that the value must lie in the range $[-1, 1]$, with 1 indicating perfect correlation and -1 indicating perfect anti-correlation. This provides a scale free measure for the strength of the statistical dependence. The magnitude of cross-correlation factor is always less than 1, therefore in a decibel scale it always has to be a negative dB value. The cross-correlation factor in decibels can be defined as,

$$\varrho_{ij}(dB) = 10 \times \log_{10}\left[\frac{|\varrho_{ij}|}{100}\right] \tag{4.15}$$

The results of the crosstalk measurements for our 5×5 array of cylindrical piezo elements are shown in Fig. 4.22 along with the schematic presentation of the constructed 5×5 transducer array (Fig. 4.22 (A)). The results presented in the Fig. 4.22 (B) show that the OPAT introduces minimal crosstalk ($< 10\%$) in the output ultrasound phase. The maximum measured crosstalk level of transducer elements is -28.5 dB which corresponds to less than 10% correlation in ultrasound phase transmitted by the adjacent transducer elements.

5 Optically Programmable Array of Transducers (OPAT)

The results presented in this chapter have been in part submitted as a patent application "Optically Controlled Phase Shifter and Phased Array for Ultrasound Applications" under the inventor names of Rahul Goyal, Athanasios Athanassiadis, and Peer Fischer. Some of the work presented in this chapter forms the basis of a publication titled as "All-Optically Controlled Phased-Array for Ultrasonics" that is under review for publication in a scientific journal.

5.1 Introduction

The discovery of holography in ultrasound [104] made possible the modification of ultrasound fields with very high resolution which considerably increased the complexity of projected ultrasound fields. It enabled the realm of ultrasound wavefront engineering and applications ranging from in single-shot acoustic fabrication [19, 122], cellular assembly into complex patterns [123], manipulation of sub-micron particles [124, 125] and neurostimulation [126]. Phase plates are widely used for complex wavefront shaping as they can be constructed with high fidelity using 3D printing technology. Yet, they come with the limitation of producing only static wavefronts. The ability to dynamically change the phase would allow programmable functionality such as beam steering and focusing. Various control mechanisms have been explored for providing dynamic functionalities to ultrasound wavefront control [127, 128], including electronically or optically controlled microbubble arrays[101, 129] and multiplane diffractive acoustic phase networks [130]. An established approach for creating dynamic wavefronts at ultrasonic frequencies is to employ phased array transducers (PATs), which consist of periodic or quasi-periodic elements with a spacing of the order of a wavelength. They can be used to emit ultrasound waves dynamically by pulsing elements in a programmed manner. However, this comes with a complex drive circuitry to

address the individual elements electrically and requires an amplifier for each transducer that is cascaded with matching circuits. Furthermore, it is challenging to scale and develop to large numbers because the external power supply units or amplifiers need to be physically connected to each transducer element with a synchronized clock [131, 132].

PATs have been used for more than 50 years since the industrial application of ultrasonic phased array systems [133], and recent microfabrication advances have led to better power-saving electrical architectures and surface integrated board electronics [134]. However, there has been no improvement in the multi-channel sequential architecture for individually addressing transducer elements, which determines the scalability of phased array systems. Optical control [135] can be conceptually used to address the transducer elements remotely which could provide a great advantage by providing parallel addressability and thereby scalability to large phased array systems [136, 137]. Thus, optical control is in contrast to the operation of wired electrical control. Moreover, these optically driven networks would have a larger bandwidth, and wireless reconfigurability of ultrasound waves [135]. Hence, an approach based on optical intensity can significantly reduce the size, and cost of electronic systems and is attractive to many diverse applications including therapeutic ultrasound, non-destructive testing [138] and neural modulation [139].

This chapter introduces a novel analog technology that can be programmed optically at ultrasonic frequencies to generate dynamic wavefronts. We implement our Optically Programmable Array of Transducers (OPATs) by integrating an array of transducers with Light Addressable Phase Shifters (LAPSs) that have been introduced in Chapter 4 and which are connected to a single source power unit. Generally, PATs are integrated with independently connected amplifier chips addressing individual transducer elements and a Field Programmable Gate Array (FPGA) for digitizing the phase of transmitted ultrasound waves [103, 132]. The approach of generating a phase-digitized electrical signal is called Direct Digital Synthesis (DDS) where a synchronized clock in operation with phase registers perform time discretization which results in phase-shifted signal [140]. The LAPSs discussed in chapter 4 are high frequency analog circuits based on photoresistive elements coupled with passive electronic devices in a cascaded architecture. The electrical circuits convert an optical intensity into a precisely controlled phase-shifted electrical signal. The phase is controllable in real-time by the externally applied light intensity. which is confirmed by measurements of ultrasound waves through hydrophone. The idea to shape ultrasound wavefront with a light-addressable phase-shifter is schematically shown in Fig. 6.1. Subsequently the components and their operations are explained in detail. The experimental setup is then used to generate a vortex beam and to switch multifocus ultrasound fields.

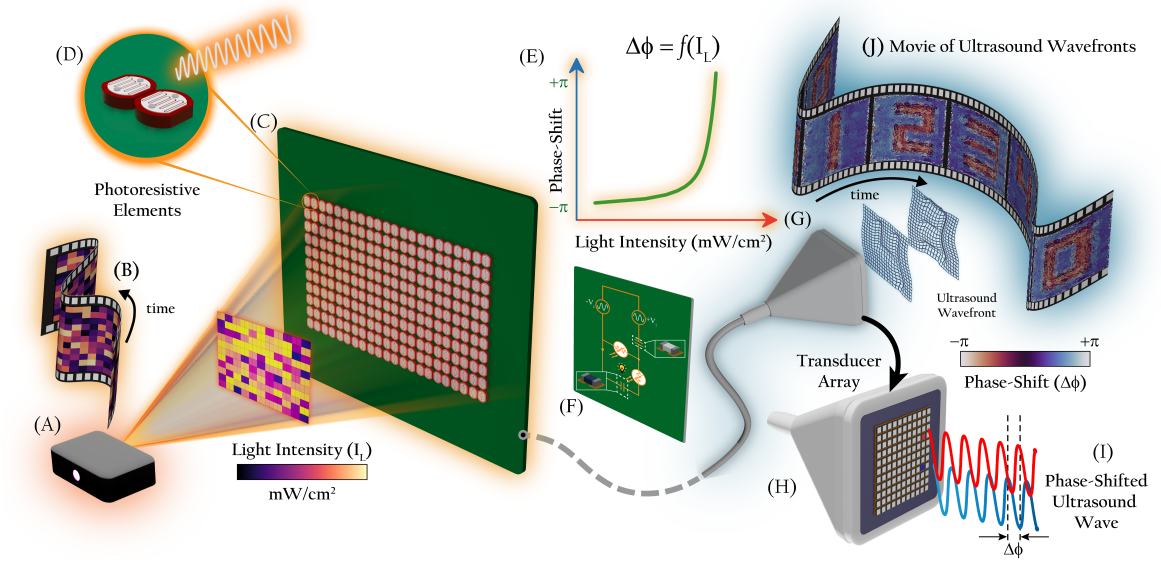

Figure 5.1: Optically Programmable Array of Transducers (OPATs) for implementing ultrasonic functions. The ultra-compact OPATs are programmed by light intensity patterns (I_L) which are illuminated from (A) projector unit in the representation of (B) time-framed motion picture. The pixel unit of OPATs are individually and independently addressed by (C) illuminating light and contains (D) 2 light addressable elements integrated with an Optical Active Network (LAPS) based on photoresistors. The time domain characteristics of the network are analyzed using equivalent circuit model and when the light is projected onto the photoresistive elements, the LAPS will convert the various (E) illumination intensities to phase-shifted ($\Delta\phi$) electrical signal which is then applied to the corresponding transducer element. The optical control provides a great advantage of favourable scalability to (F) large-sized transducer array, (G) which can be simply plugged to the network for generating dynamic phase distributions locally without complex electronic circuits and power amplifiers. The relative phase-shift ($\Delta\phi$) of the ultrasound waves emitted from the individual transducers (H) can be tuned remotely through different light patterns. the programmable OPATs can generate various phase distributions on the transducer array, thus creating complex ultrasonic wavefronts which are dynamically switched analogous to a motion picture (I) of ultrasound wavefronts.

5.2 Principle of the Optically Programmable Array of Transducers

The concept of controlling individual phase of ultrasound actuators in an array using a light projection system is illustrated in Fig. 5.1. The system consists of two electrically connected layers: first layer is photoactive layer which constituted by light-dependent resistors and connected to a single power supply unit, these networks correspond to the LAPSs introduced in chapter 4. The second layer consists of ultrasound actuators which are connected in parallel with the cascaded network of LAPSs to control the emitted ultrasound waves independently. We employed a digital light projector to generate optical patterns in the current work, but in principle this technique could also work with other optical projection methods such as Digital Mirror Device (DMD) or

Light Emitting Diode (LED) matrices. The communication with the system is through the light projection, where the optical intensity individually manipulates the temporal parameters of the networks which thereby manipulates the phase of the electrical signal and thus controls the phase-shifted ($\Delta\phi$) ultrasound waves. Compared with the traditional electrically controlled PATs, which require bulky power supplies, complex wiring and controllers, the presented programmable OPATs are lightweight, compact, scalable, and wirelessly tunable. Most importantly, the integrated LAPSs have broadband operational bandwidth which signifies the compatibility of the network circuits with transducer arrays of diverse frequency operation.

5.3 Experimental Instrumentation and Hardware

5.3.1 Transducer Array

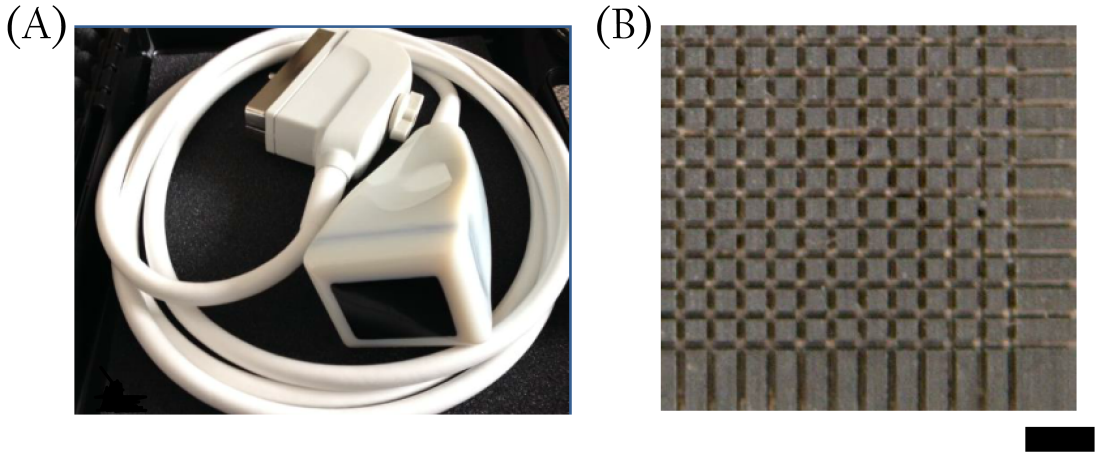

Figure 5.2: 11×11 transducer array with the operational frequency of 700 kHz. (A) A photograph of the transducer array probe where one end is the ITT canon connector and the other end is the array of piezoelectric elements. The probe is generally covered with layer of soft material for best acoustic contact and to protect array. (B) A photograph of the diced composite material which shows matrix-structure of active elements whereas the right and lower edge shows the passive area of the transducer array. The black color scale bar represents a length of 7.5 mm.

The custom 11×11 matrix array transducer was provided by Dr. Marc Fournelle from the Fraunhofer Institute for Biomedical Engineering IBMT, St. Ingbert, Germany. It is shown in Fig. 5.2. The transducer array has been produced as follows: a 1-3 PZT composite material was generated from bulk PZT using a dice and fill technique. The composite plate was then applied to a backing carrier material and the matrix structure was generated with a new dicing step. Dicing was performed with a kerf of 250 µm and a resulting pitch of 2.81 mm. Individual contacting of the elements was generated from the bottom side. The array gaps were filled with an epoxy

material and a common ground electrode was applied using a sputtering process on the top side. A matching layer was then applied for optimization of the transducer bandwidth. After housing integration, a protective coupling layer made of soft silicone was applied. Connection was provided in a multi-micro coaxial cable terminated with an ITT Cannon connector [141], which could be connected to the OPAT for transfer of electrical power. The capacitance C_T of individual elements is measured to be in the range 301.7 pF to 309.2 pF.

The transducers are driven through individually connected LAPS which is supplied with two sets of synchronized RF voltage signals. The first is denoted by $+V_i$ and the other is a π phase shifted signal represented as $-V_i$. The frequency of the driving signal was 0.7 MHz which has been used for the experimental demonstration. The positive and negative source signals were generated separately by a single function generator (AFG 1062, Tektronix) in the experiments, and each amplified by their own low-impedance 50× voltage amplifier (WMA-300, Falco Systems). It would be possible, however, to split a single amplified RF signal and use a phase shifter on one branch of the signal to provide both $\pm V_i$ to the OPAT and then followed by the ultrasound generating transducer elements.

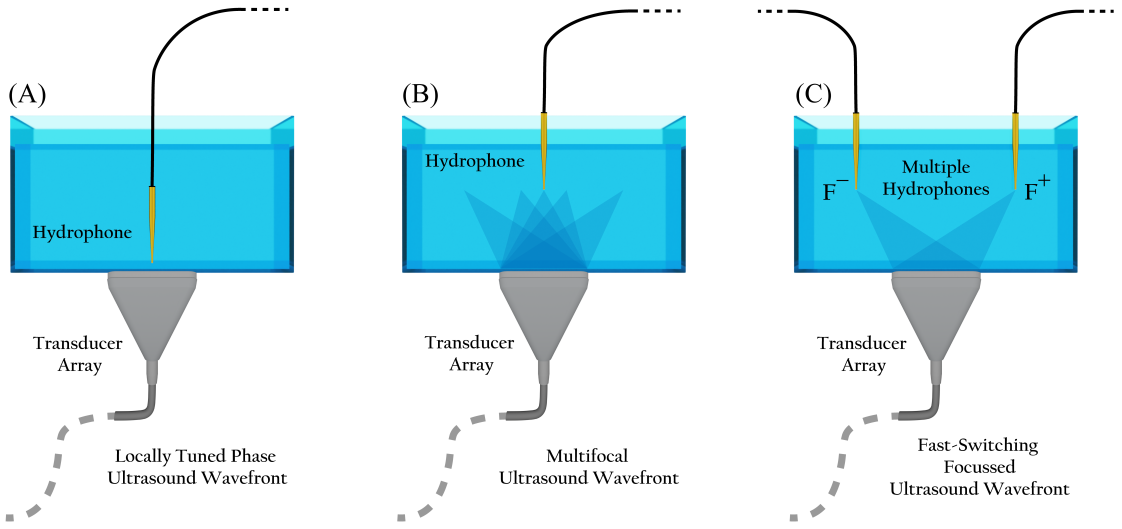

Figure 5.3: Experimental setups for acoustic pressure measurements. (A) To measure the generation of complex phase patterns at the transducer, the hydrophone is scanned in a plane 1.5 mm from the surface of the transducer array. (B) To measure fields generated with multiple focus points, the hydrophone is scanned in a plane 50 mm from the transducer array. (C) To measure the temporal response when switching between two foci F_- and F_+, two hydrophones are positioned at the focal points and their output is recorded simultaneously.

5.3.2 Measurement of Ultrasound Wavefronts

Ultrasonic pressure fields were mapped using a 0.5 mm-diameter needle hydrophone (HNR0500, Onda Corporation) scanning in a water tank. An open 3D printed water

tank (175 mm × 175 mm × 75 mm) made from a UV-cured polymer (VeroClear, Stratasys) was filled with deionized water and the transducer array was placed in acoustic contact with the water. For experiments with the 11 × 11 array, the array was coupled to the outer surface of the water tank using a thin layer of vacuum grease (Dow Corning), projecting through the wall and into the tank. For experiments with the PZT disks, the piezoceramics were mounted onto a printed circuit board, which was waterproofed with a spray coating of dielectric strength 48 kV/mm (RS Components GmbH, Germany) and the water tank was coupled to the piezos using vacuum grease.

Pressure waves from the transducer produce a voltage in the hydrophone, which was digitized using a USB oscilloscope (Picoscope 5000 Series, Pico Technology) and saved on the computer. The time-domain voltage data was converted to a pressure using the manufacturer-provided calibration. For accurate measurements, a 25-cycle sinusoidal pulse was used to drive the OPAT. The hydrophone correspondingly recorded a pulse, which was converted to amplitude and phase data using a Fast Fourier Transform. The spatial variation in pressure field is measured through hydrophone scanning, where the hydrophone was mounted on a computer-controlled three-axis motorized translation stage (MTS25-Z8, Thorlabs GmbH). The scan area in the imaging plane was 20 mm × 20 mm, with a lateral resolution of 0.37 mm. 25 pulse measurements were averaged at each point of the imaging plane to increase the signal to noise ratio. A typical scan took 3 - 4 h which can be reduced if needed by decreasing the lateral resolution of the two-dimensional hydrophone scan.

5.3.3 Computation of Source Phases for Complex Wavefronts

The Iterative Angular Spectrum Approach (IASA) has been employed to compute the relative phase shift for individual transducer elements required in generating the programmed wavefront [104, 142, 143]. The phase distribution of the transducer elements is determined by iteratively propagating a wave from the target plane to the transducer plane and back, with amplitude constraints being applied in each plane. In our adaptation of the IASA algorithm, we applied an amplitude constraint per pixel to match the experimentally measured phase shift-dependent amplitude. The amplitude constraints for every iteration are set separately and explicitly. The algorithm converges in a few tens of iterations to yield the desired phase map. We performed 50 iterations for every wavefront to accurately compare the performance of OPATs for different applications. To set the transducer phases for fields with higher resolutions than the driving array, we subdivided the transducer elements into multiple pixels and assumed a uniform phase output of all pixels corresponding to a single element. The relative phase shift for individual transducer elements is then calculated by averaging the obtained phase shift for all pixels comprising one element. The algorithm provides

good experimental results which are consistent with the theoretically predicted wavefronts. The IASA-computed phase distribution is then converted to a light intensity using a look-up table based on the experimentally measured curves provided by the light addressable phase shift architecture.

5.4 Electronics Board Design

The optically controlled transducer array is implemented by projecting light from a commercially available light projector (ViewSonic PRO8510L-S Light Stream 5200-Lumen Projector) to a 2D array of photoresistors (NSL-19M51, Advanced Photonix). The printed circuit board design of the photoresistor board is shown in Figure 5.4. It can be seen for the Figure 5.4 that a total $2 \times 11 \times 11$ number of photoresistors are mounted in close proximity to decrease the net footprint of the array. The photoresistor board is used for light detection, where the light intensity causes a change in resistance. The board has a Samtec Socket Strip with a pitch of 2.54 mm which allows the connection of pin headers of identical pitch and hole dimensions. The socket strip has the insulator material of black liquid crystal polymer with the contact material and plating (1.27 µm) of Phosphor Bronze and Gold respectively. Board has dimensions of 351 mm × 285 mm with a thickness of 1.55 mm. The photoresistor board is connected separately to measure the AC resistance and capacitance at operation frequencies of up to 1 MHz and is then passed on further electronics operation.

The photoresistor board is connected to a capacitor board which is shown in Fig. 5.5. The capacitor board performs the analog conversion of the light intensity to an electrical phase-shift through a cascaded architecture which has been explained in chapter 4 of the thesis. The capacitor board is mounted with through-hole-pin-header connects directly with the socket strip of the photoresistor board. The terminal material is Phosphor Bronze with a Gold plated contact. The pin headers are rated to be operational below 3.2 A with a high-speed channel bandwidth of 8 Gbps. The 8 Gbps of bandwidth provides 12-bit resolution for an electrical signal at 1 MHz. The PCBs are designed using the computer-aided software KiCad 6.1 with components from standard distributor libraries. The capacitors are surface mounted on the capacitor board as shown in Fig. 5.5 (C). The capacitors are thin film ceramic capacitors with a maximum operational voltage of 250 V.

The capacitor board also consists of the input and output power connectors which are different based on the components. The input power is supplied through vertical shaped BNC Coaxial connector as shown in Fig. 5.5 (D). It should be noted that the input power connectors are central to the individual elements of the transducer array and hence does not scale linearly with the number of elements in the array. which happens in the conventional transducer array devices. The placement of ITT canon

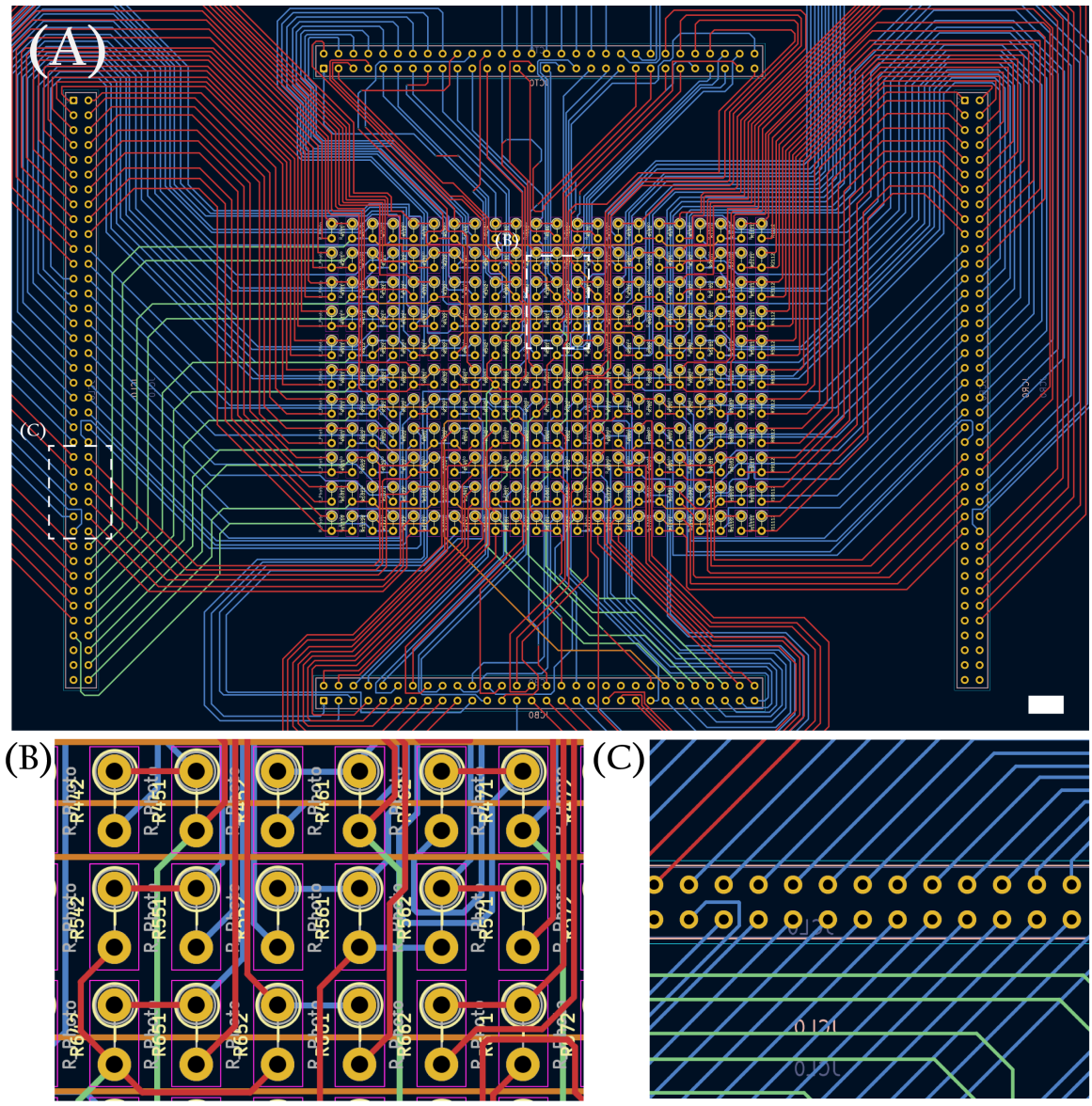

Figure 5.4: Design of the printed circuit board for the photoresistor panel of the OPATs where (A) and (B) shows the magnified areas of the board to mount photoresistors and pin headers, respectively. See text for further details on the electronics design and components. Scale bar in the (A) represents a length of 5 mm.

connector on the capacitor board is shown in Fig. 5.5 (A) with white dotted line and the corresponding magnified version of the footprint is shown in Fig. 5.5 (B). ITT canon connectors are circular mechanical connectors which provides high-performance solutions for electronics component where load is reactive in nature. The capacitor board is designed in a four layer architecture, as indicated by the four different colors of wire tracks shown in Fig. 5.4 and Fig. 5.5. The combination of the board for the photoresistors with the board for the capacitors together generate the phase shift and together provide the following functions: photodetection, phase modulation, and transducer actuation. After the design, the boards were manufactured by Eurocircuits GmbH. The components were then assembled and soldered in the lab.

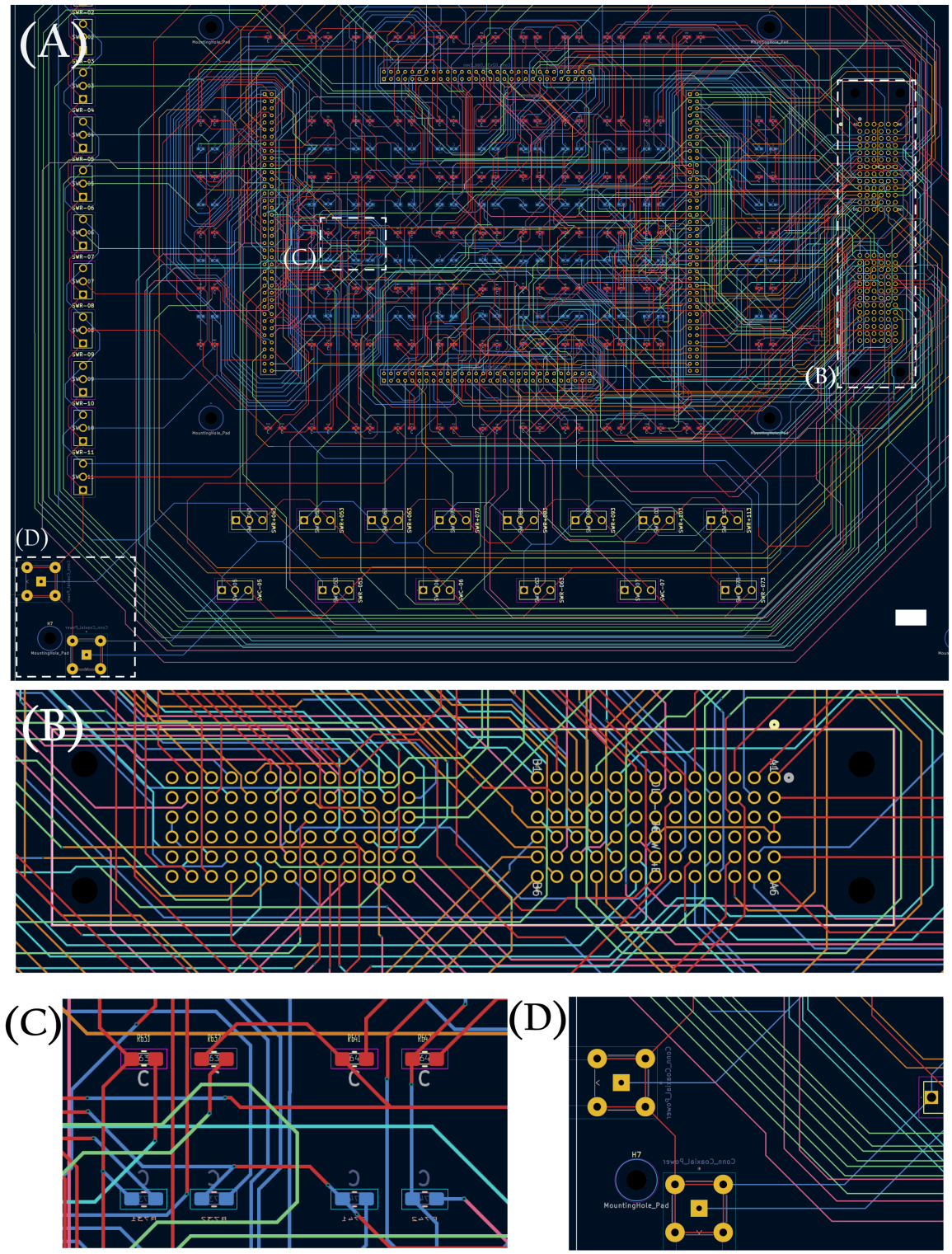

Figure 5.5: Design of the printed circuit board for the capacitor panel of the OPATs where (A), (B), and (C) show the magnified areas of the board to ITT canon connectors, surface mounted capacitors, and power connectors, respectively. See text for further details on the electronics design and components. Scale bar in (A) represents a length of 5 mm.

5.5 Concept Demonstration and Ultrasound Wavefront Generation

The suggested technology works on the basis of adjusting the light's illumination intensity to produce the required phase distributions. The LAPS contains 2 NSL-19M51

photoresistors cascaded with 2 thin film capacitors which convert the optical signals into corresponding phase-shifted voltage signals for energizing the loaded transducer element. We fabricated 11×11 LAPS array to verify experimentally the concept of programmable OPATs. The wired board of LAPSs is printed on the 1.55 mm-thick FR4 dielectric substrate, implemented with a panel mountable connector having zwitter contacts for a custom designed transducer probe of 11×11 elements. The integrated transducer probe is operational at the frequency of 0.70 MHz with the total acoustic aperture of 30.9 mm × 30.9 mm. The pixel unit can dynamically and locally control the ultrasound phase by receiving light of various illumination intensities. A graphical representation of the realized system for the measurements is shown in Fig. 5.6 (A) with the 3 main components depicted : light projector, power unit and transducer array. We connected a centralized power source unit to distribute the power across a large-scale array of transducers. Importantly, the proposed architecture is established on a design approach that constructs an explicit and optically tunable phase relationship between individual transducers and the input signal (V_i). The interference of local phased-shifted ultrasound waves generate an ultrasound wavefront pattern which is presented in the Fig. 5.6 (B).

We projected several different light intensity patterns denoted in Fig. 5.6 (A) (i) onto the LAPSs which resemble to the numerical digits. The contour map of the illumination pattern are plotted in Fig. 5.6 (B) (i), (ii), (iii), (iv), and (v) respectively. The absolute amplitude of the light intensities illuminated for the digits "0", "1", "2", "3", and "4" are 61.1, 64.3, 65.7, 37.4, and 49.2 mW cm^{-2} respectively. It should be noted that the experiments are performed in a dark room to avoid the interference of ambient light. The light intensities are determined to achieve a differential phase-shift ($\delta\phi$) of approximately $\pi/3$ as presented in the Fig. 5.6 (B) (i). A two-dimensional hydrophone scan is performed to gather information about the ultrasound wavefront at the monitoring plane which is approximately 1.5 mm from the surface of transducer array. The graphical representation of the close-proximity scanning of the ultrasound wavefront is presented in the Fig. 5.3 (A) which simultaneously shows the experimental system for the results presented in Fig. 5.6. It is obvious from the amplitude and phase distributions of ultrasound wavefronts presented in Fig. 5.6 (C) and (D) that there is, indeed local tuning in the phase of pressure wave at the pixel unit level. The amplitude distributions presented in the Fig. 5.6 (C) (i)-(v) corresponding to the illumination pattern of Fig. 5.6 (B) (i)-(v) respectively. This clearly indicates that the magnitude of the emitted pressure wave is changed slightly during the optical tuning of phase. However, the variation in the pressure magnitude has small effect on the performance of OPATs and most importantly, would be compensated in the iterative calculations to optimize the parameters for desired ultrasound wavefront.

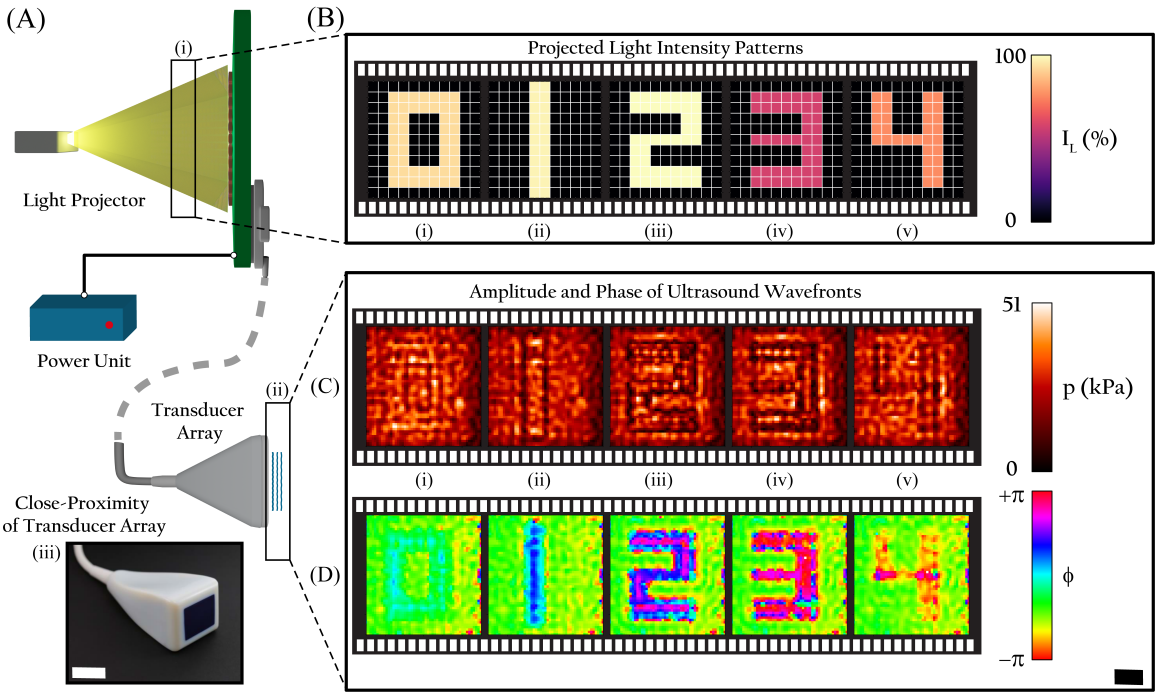

Figure 5.6: Phase mapping of ultrasound wavefront based on the light intensity pattern projected on the LAPSs. (A) Graphical representation of the OPATs which main components: light projection unit for illuminating defined intensity pattern (i), single power source unit, and transducer array for emitting ultrasound wavefront (ii). (iii) The photograph of the integrated transducer operated at the frequency of 0.75 MHz. A distance of 31 mm is symbolized by the white color scale bar. The measurement of the complex amplitude of pressure wave is performed through hydrophone at the close-proximity of the transducer array. The scanning plane is approximately 1.5 mm from the surface of transducer array. (B) The projected light intensity pattern represented by (A) (i) which are spatially structured to describe the formation of numerical digits (i) "0", (ii) "1", (iii) "2", (iv) "3", (v) "4". The maximum and minimum projected intensities are 65.7 mW cm^{-2} and 0.1 µW cm^{-2} respectively. (C) and (D) (i) - (v) The distribution of amplitude and phase-shift in the pressure wave recorded by the hydrophone at the close-proximity ((A) (ii)) of the transducer surface, which corresponds to the projected light patterns of (B) (i) - (v) respectively. The approximate area for the scan is 31 mm×31 mm. The black color scale bar represents a length of 7.5 mm

5.6 Fast Switching of Ultrasound Foci

We selected multifocal beam formation as the first ultrasonic function to experimentally demonstrate the dynamic reconfigurability of OPATs. We show that modulating the light intensity pattern generates multifocal ultrasound wavefronts as shown in Fig. 5.7 where N_f denotes the number of focal points, which otherwise require a complex electrical architecture.

Three steps are necessary to compute the light intensity pattern required to generate a desired ultrasound pressure wavefront at a given distance from the transducer. First, from the desired ultrasound pressure wavefront, the phase-shifts at the individual transducer elements are computed. This step is done iteratively using an opti-

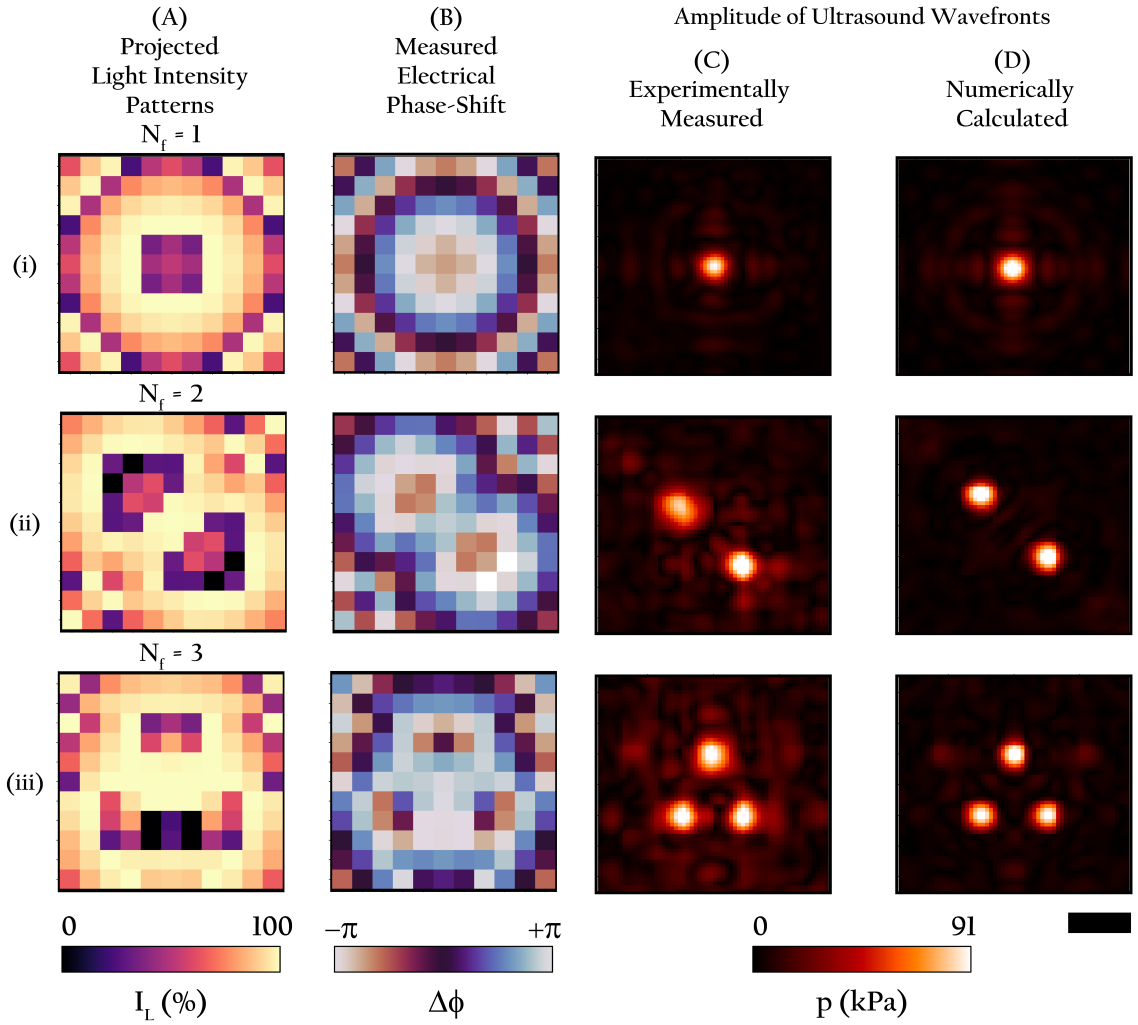

Figure 5.7: Light addressable ultrasound wavefront generation with variable number (N_f) of equivalent focus. (A) The spatially modulated light intensity pattern projected on the photoresistive elements to demonstrate ultrasound wavefront of variable focal points, which is categorized as (i), (ii), and (iii) for $N_f = 1$, $N_f = 2$, and $N_f = 3$ respectively. (B) The electrical phase-shift ($\Delta\phi$) measured with respect to the input signal (V_i) addressing transducer elements individually controlled by the projected light intensity (I_L). (C) The experimental results for the measured amplitude of ultrasound field at the target focal plane which is situated 50mm from the surface of transducer array. (D) The amplitude of ultrasound field calculated numerically based on the mapped electrical phase-shift feeding the transducer elements for $N_f = 1$, $N_f = 2$, and $N_f = 3$. The scale bar is 5mm

.

mization algorithm. Then, from the phase of the different transducer elements, the resistance values of the photoresistive elements are calculated considering the electrical characteristics of the back-end circuit. It should be noted that amplitude constraint on the terminal voltage of the transducer resulted from programmed phase-shift is considered in the calculation. The target light intensity patterns as shown in Fig. 5.7 (A), are then finally calculated based on optical characteristics of the photoresistive element. These 3 steps are illustrated for different examples with $N_f = 1$, $N_f = 2$,

and $N_f = 3$. The light projector is turned ON and corresponding to the illuminated pattern, as can be observed in Fig. 5.7 (A) (i), (ii), and (iii). Phase-shifts of electrical signal powering the transducer elements are mapped and represented as shown in Fig. 5.7 (B). The propagated ultrasound waves are locally phase-shifted by the transducer elements which interfere at the focal plane to produce the desired target intensity pattern. The projected ultrasound wavefronts have been mapped with a two-dimensional hydrophone scan which is schematically presented in the Fig. 5.3 (B) of the experimental systems. The experimentally measured ultrasound pressure distributions are in good agreement with the numerical results as shown in the Fig. 5.7 (C) and (D) respectively. These far-field results confirm that the designed OPATs demonstrate good performance as a multifocal beam generator. The numerical ultrasound wavefronts for $N_f = 1$, $N_f = 2$, and $N_f = 3$ are determined by considering the examined electrical phase-shift actuating the transducer elements. Moreover, it should be noted that the amplitude constraint on the terminal voltage is considered in the calculation of the optimizing ultrasound wavefront.

It has been mentioned in chapter 4 that the proposed LAPSs are capable of switching the phase of ultrasound waves at the maximum refresh rate of 100 Hz. Hence, we measured the performance of the OPATs to generate a "Movie of Ultrasound Wavefronts". The motion picture is constructed from the frames containing information about the light intensities as grayscale coded pixels; where "white" and "black" pixel correspond to the light intensities of 65.7 mW cm^{-2}, and 0.1 µW cm^{-2} respectively. The light intensity patterns are determined to generate focused ultrasound wavefront in the observation plane. The magnitude of the light intensity distributions that are encoded in the motion picture format are presented in the Fig. 5.8 (A) (i), (ii), and (iii), which corresponds to focus point/s F^-, F^+, and $F^- \wedge F^+$ respectively, where $F^- \wedge F^+$ denotes dual focused wavefront of ultrasound. Firstly, we measured the phase-shift in the electrical signal feeding individual elements of the transducer array. The results are plotted in the Fig. 5.8 (B) (i), (ii), and (iii) for the respective light intensity distributions. Secondly, we mapped the amplitude of ultrasound wavefront to locate the approximate position of the focal points namely; F^- and F^+. The surface distribution of pressure amplitude for the optical wavefront corresponding to Fig. 5.8 (B) (i), (ii), and (iii) are shown in Fig. 5.8 (C) (i), (ii), and (iii) respectively.

The fast-switchable operation of OPATs is recorded by simultaneous mounting of multiple hydrophones at the positions configured for the focal points at x = −10 mm, and x = +10 mm. The graphical implementation of the experimental system is presented in Fig. 5.3 (C). Generally, commercially available projector units have update rate between 30 − 50 Frames Per Second (FPS). The light projection hardware used in the measurements is capable of displaying graphics at the speed of 50 FPS. The frames representing the wavefront corresponding to focal points left (L, x = −10 mm), right

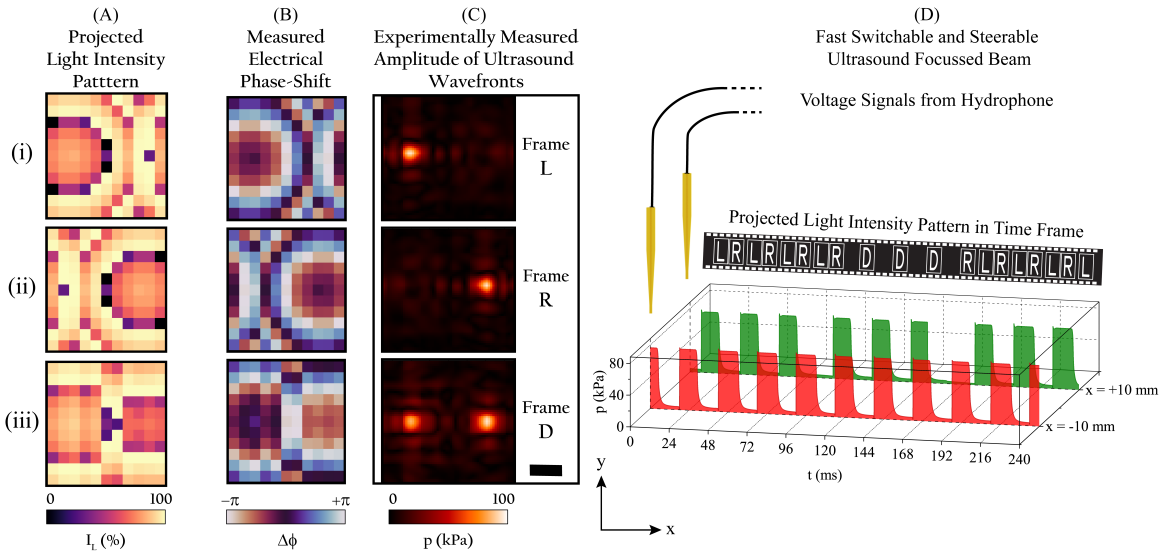

Figure 5.8: Movie of Ultrasound Wavefronts. A fast-switchable multi-focus ultrasound wavefront is generated with the OPAT system. (A) (i), (ii), (iii) The spatial modulated light intensity distributions for constructing focused ultrasound at the points x = −10 mm, x = +10 mm, and x = ±10 mm respectively. (B) The phase shift of mapped electrical signal actuating individual transducer elements independently corresponding to the light patterns of (i),(ii), and (iii). (C) (i),(ii), and (iii) The amplitude of ultrasound wavefronts recorded at the focal plane for light intensity pattern denoted by the frames L, R, and D, respectively, located at the distance of approximately 50 mm from the transducer surface. (D) The scale bar is 5 mm.

(R, x = +10 mm) or double focus (D, x = ±10 mm) are denoted by the alphabets "L", "R", and "D" respectively. The time frame representation of projected light patterns contain 4 instances of alternatively displayed "L" and "R" frames, and 3 instances of "D" frame projected in a regular pattern. The motion picture is presented in the form of "moviestrips" as shown in the Fig. 5.8 (D). The light intensity patterns are projected continuously and pressure is recorded simultaneously in a continuous and synchronous manner. It should be noted that ON time for the frames "L", "R", and "D" is identical and is approximately equal to 17.5 m sec. The results of the 100 points averaged pressure recorded by the positioned hydrophones is presented in Fig. 5.8 (D). We clearly observe a variation in pressure which is analogous and correlated to the time-framed projected motion picture. The measurement results indicate the generation of equifocal ultrasound beams with focal points switched at a refresh rate which is consistent with the property of motion picture.

5.7 Ultrasound Phase Gradient and Divergent Beam Wavefront

Many applications require the ability to modify the amplitude of the ultrasonic field, but influencing a wave's phase is just as crucial. An excellent illustration of the

significance of phase is an acoustic vortex beam, which is produced by a helical phase distribution. It is particularly helpful for underwater communication [144] and particle manipulation [145]. The traditional techniques for creating an acoustic vortex beam include structured transducers [146] and static phase masks [147]. Realizing dynamic and quickly reconfigurable vortex fields is still difficult, though. Here, we demonstrate that the OPATs can also create helical phase distributions to create vortex beams, where patterns of light intensity result in electrical phase shifts that create an acoustic vortex beam, as shown in Fig. 5.9 (A). The projected light intensity pattern was first computed to generate the target phase gradient as shown in Fig. 5.9 (B) (i). The electrical phase-shifts are then controlled by the corresponding light intensity. The mapped distribution of electrical phase-shift is shown in Fig. 5.9 (B) (ii). The hydrophone scan shows the experimental results which is shown in Fig. 5.9 (B) (iii) and the numerical simulations predict the acoustic vortex fields depicted in Fig. 5.9 (B) (iv). The amplitude distribution and the phase gradient are in good agreement with the results from numerical simulation, demonstrating the capability of the presented system, OPATs. The electrical phase map can be optically switched in milliseconds which enables fast transitions between different ultrasound wavefronts.

2D phased-arrays are used for conventional real-time 3D ultrasound imaging [148] or for more advanced 3D ultra-fast ultrasound imaging [149]. The field of view (FOV) for ultrasound imaging is proportional to the size of the transducer array which leads to the challenge of engineering large FOV devices [150]. However, the programmable OPATs could potentially be used to develop dynamic functionalities for ultrasound. OPATS can also generate diverging wavefront to increase the field of view as it is routinely done in 3D ultra-fast ultrasound imaging [149]. The illustration in Fig. 5.9 shows the increase of the FOV from a plane wavefront (A) to a diverging wavefront (B). A virtual focus, whose position is behind the plane of the array, allows the beam to diverge as illustrated in Fig. 5.10 (B). The spatial distribution of light intensity and the resultant map of phase-shifted input electrical signal is presented in Fig. 5.10 (C) (i) and (ii) respectively. The amplitude and phase distributions of the acoustic pressure measured at a plane located at a distance of 50 mm from the transducer surface are plotted in Fig. 5.10 (C) (iii).

5.8 Summary

This chapter has demonstrated a new solid state technology for ultrasound that introduces the idea of optically programmable ultrasound fields. The concept has been demonstrated with compact OPATs that consist of 121 LAPSs, each of which independently controls 121 transducer elements by a single power source unit. Therefore, it introduces the foundation for a scalable ultrasonic transducer array. The presented

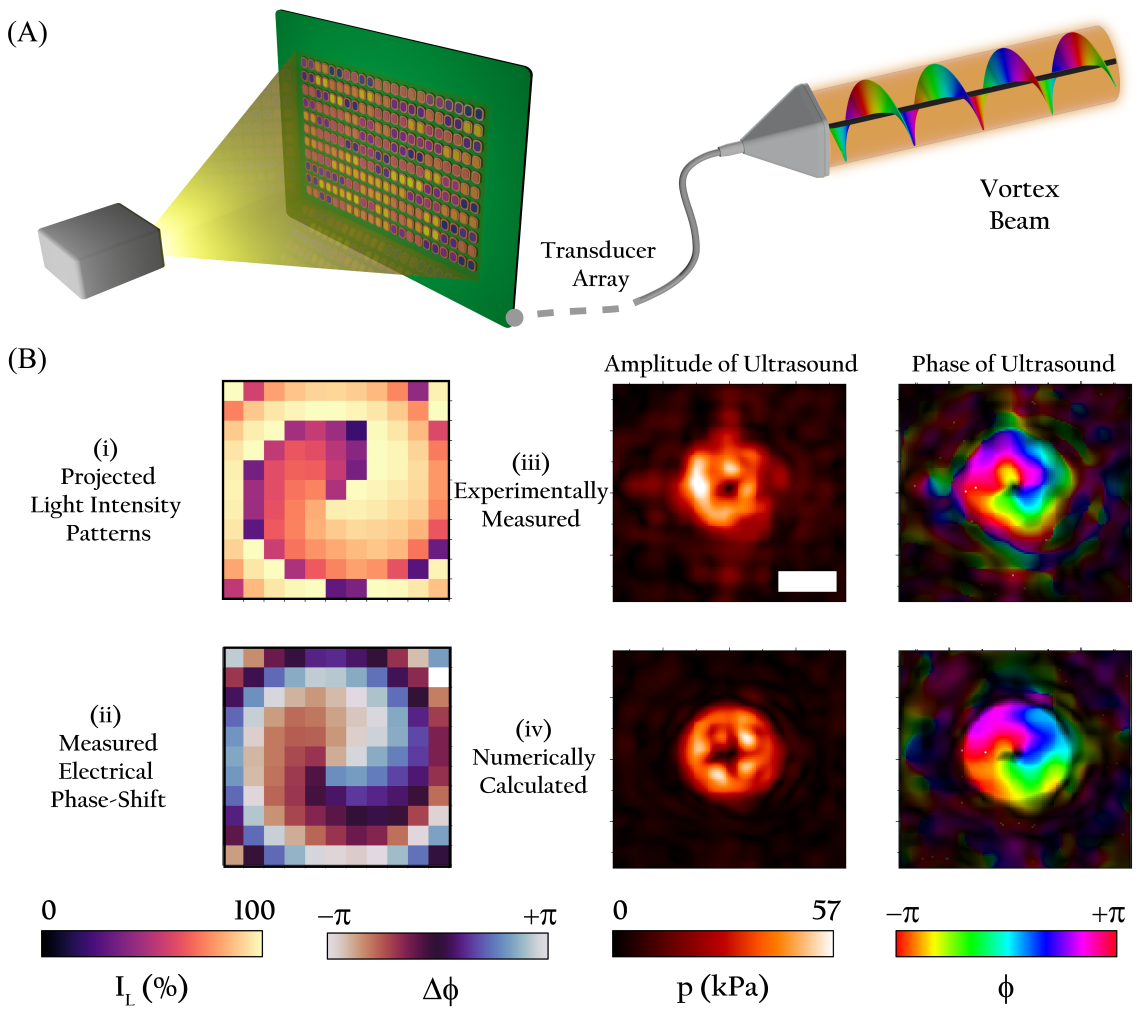

Figure 5.9: Generation of ultrasound phase gradient in the vortex beam wavefront. (A) Schematic representation of vortex beam generation by projecting the corresponding spatial light intensity distribution (B) (i) The spatially modulated light intensity which resulted in the (ii) electrical phase shift mapped for the transducer array. The experimental (iii) and numerically (iv) obtained amplitude and phase maps of the acoustic pressure pattern which is measured in a plane located at a distance of 60 mm from the transducer surface. The measured maps are consistent with the theoretical calculations. The scale bar is 7.5 mm.

system is fast with the light-triggered phase switching time of 100 ms. Further, the system is versatile as their distribution is simply controlled by the projection of a low-intensity optical images (66 mW cm^{-2}), and easily scalable to large sizes for generation of complex wavefronts. By varying the illumination intensity, each transducer element can achieve around 2π phase difference across a wide frequency range (bandwidth). After receiving different light patterns wirelessly, the OPATs can generate phase patterns to generate desired ultrasound wavefronts. We used spherical diverging wavefronts, locally addressable complex phase wavefronts, and multifocal ultrasound to illustrate the capabilities of our method. A fast-switchable focal point was also used to experimentally confirm the anticipated frame rate. The programmable OPATs that are being presented combine ultrasonic tunability and optical control. With > 1000

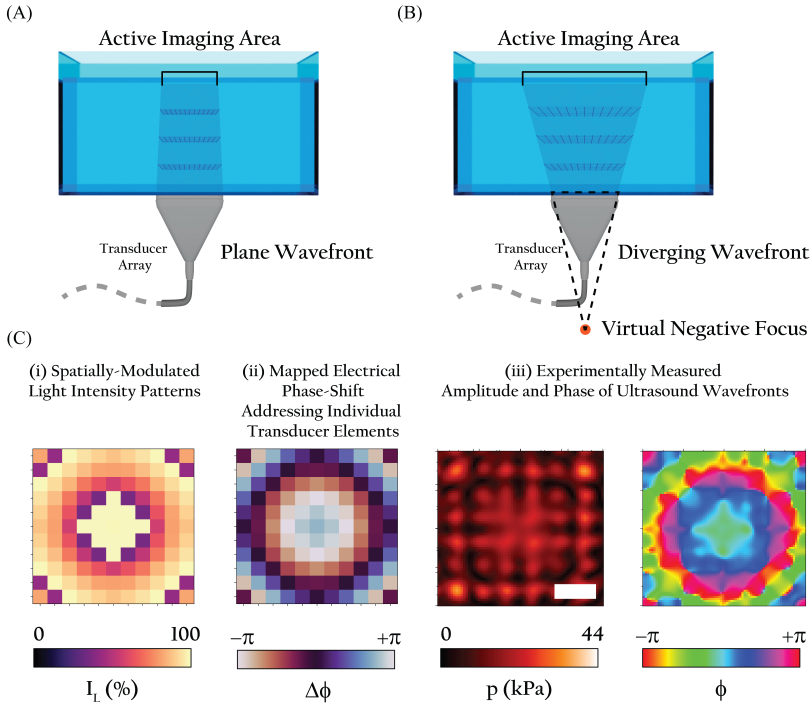

Figure 5.10: Experimental demonstration of spherical diverging wavefront. The field of view increases from a plane wavefront (A) to a diverging wavefront. (C) (i) The spatially modulated light intensity which resulted in the (ii) electrical phase-shift mapped for the transducer array. The amplitude (iii) and phase (iv) maps of the acoustic pressure are measured in a plane located at a distance of 50 mm from the transducer surface. The measure maps are consistent with the properties of spherical diverging wavefront. The scale bar is 7.5 mm

.

transducer elements, it might be utilized to create extremely large phased transducer arrays. The next chapter of this thesis presents a material systems-based approach for dynamic modulation of ultrasound, further it discusses the method through which a ultrasound modulator device could be realized for practical applications.

6 Material Systems to Dynamically Modulate Ultrasound

The results presented in this chapter have been submitted as a patent application "Thermal Spatial Sound Modulator for Ultrasound" under the inventor names of Rahul Goyal, Athanasios Athanassiadis, Oscar Demeulenaere and Peer Fischer. The work presented in this chapter is also being prepared for publication in scientific journals.

6.1 Dynamic Modulation of Ultrasound

The majority of metasurface-based acoustic holograms have the drawback of being static, which implies that for a given hologram, only one static acoustic field can be produced at a target plane [151, 152]. Nonetheless, there are numerous uses for dynamic acoustic field updating in tissue engineering, 3D printing, and therapeutic ultrasound [153, 154].

According to the previous chapter, PATs can produce reconfigurable acoustic fields in principle, where numerous ultrasonic devices are individually actuated with different phase/amplitudes [155–159]. Nevertheless, the spatial resolution at which PATs can produce complex wavefront manipulation is constrained by the aperture size of each individual pixel element. [160] This limits the use of PATs in acoustic holography, particularly for high-frequency actuation and complex patterns, which would necessitate tens of thousands of individually addressable, microscale transducers to produce high-resolution acoustic fields at frequencies and scales similar to those of static metasurface plates. [161–164] However, the majority of PATs are limited to a few hundred elements.

A programmable modulator to control the ultrasound wavefront can be conceptually generated in a quasi planar device. Thus, allowing for the modulation of the amplitude, phase and, or a combination of these parameters. This can be enabled through a local change of the path length, density or elasticity of the ultrasound propagation medium. The primary requirement of such ultrasound modulator is a

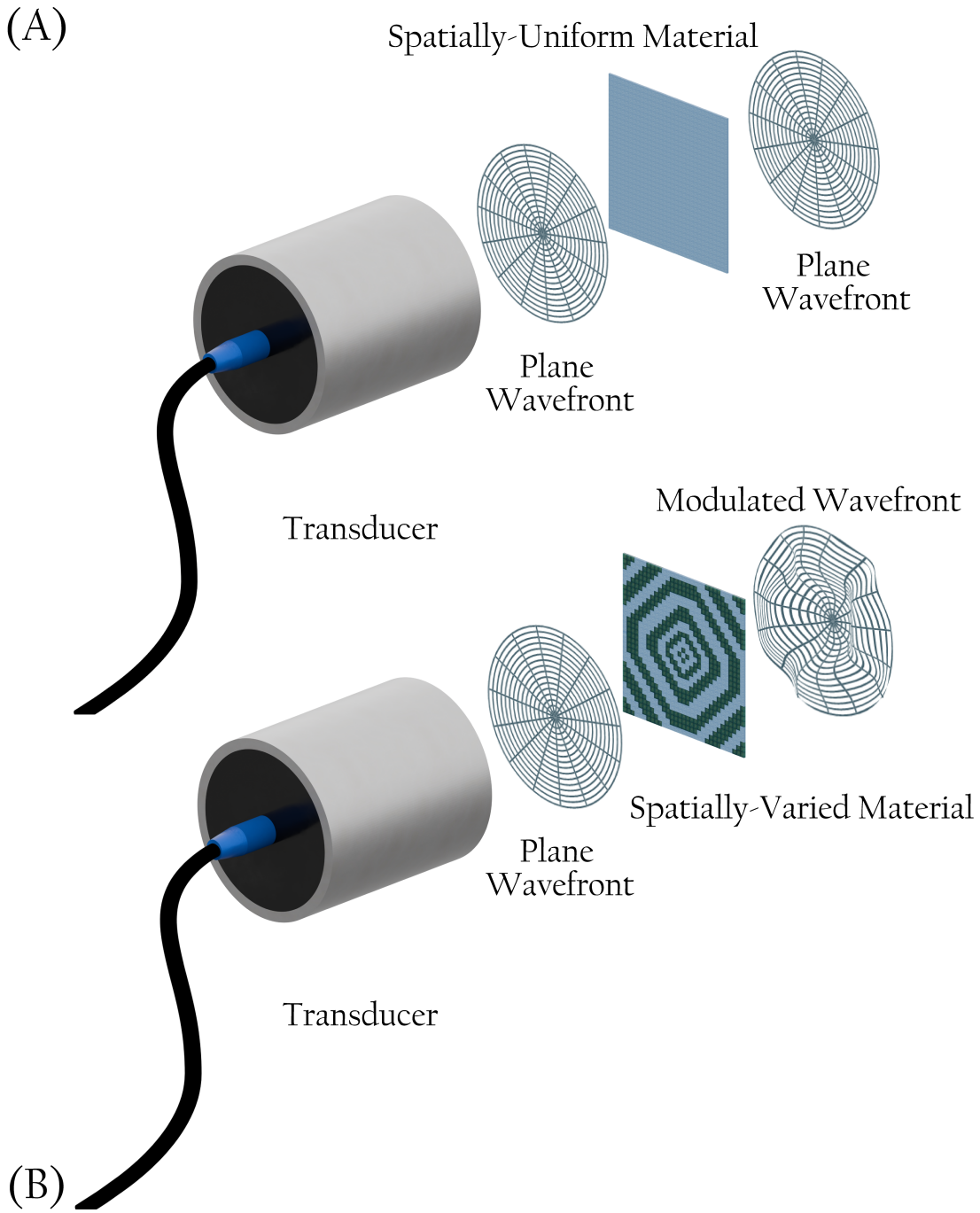

Figure 6.1: Concept demonstration for modulation of ultrasound wavefront. (A) Plane wavefront is emitted through a spatially-uniform material incident by a plane wavefront whereas a (B) wavefront modulation takes place in the output when the material is spatially different which happens due to the interference of locally modified phase of ultrasound waves.

dynamic material whose physical properties absorption or speed of sound can be tuned through external control fields. A schematic demonstration of the concept for ultrasound modulation is shown in Fig. 6.1. The transducer produces a plane wavefront which remains planar when transmitted through a spatially-uniform material as shown in Fig. 6.1 (A). Whereas the plane wavefront is (Fig. 6.1 (B)) modulated when transmitted through a spatially-modified material. The external control fields

are generally organized into four categories based on the technologies used to generate the local stimulus; (i) Electric Fields (ii) Magnetic Fields (iii) Optical Fields (iv) Thermal Fields. This chapter will discuss potential material systems with the aim to develop an integrated ultrasound modulator.

6.2 The Bulk Photovoltaic Effect and Acoustoelectric Effect

$BiFeO_3$ (BFO) is considerably one of the most less researched piezoelectric material due to relatively low piezoelectric coefficient, d_{33} of approximately $15-60\ \mathrm{pmV^{-1}}$ [165]. Ferroelectricity and piezoelectricity of bulk BFO are important functional properties for device implementation concerning to ultrasound. BFO has a great advantage that it exhibits the largest switchable remnant polarization ($100\,\mu\mathrm{C}\cdot\mathrm{cm}^{-2}$). The key to solve the problem of low piezoelectricity is to apply external stimuli which can be rather simple and effective and hence modify the speed of ultrasound propagating through the material. An article [165] was published recently where the authors generated interface piezoelectric and pyroelectricity effects using the local fields within Schottky barriers in centrosymmetric materials. The authors proved that the electric fields can be applied to manipulate the piezoelectric properties of the BFO crystal, offering an approach which is simple in implementation.

The main purpose to explore the possibilities with BFO was to modulate the speed of sound in the crystal using light. It has been reported [166] that the light can be used as a control parameter to enhance the peizoelectricity of single crystals. The authors used a 0.5 mm thick crystal and a laser light source of 405 nm wavelength was used to change the conductivity of BFO crystal by generating free carriers. The charge carriers can be generated optically in the BFO which can affect the polarization properties of the crystal [167, 168]. The experimental results reported by the authors suggested that light can potential be used as the control parameter to enhance piezoelectricity of BFO single crystals. Generally, the quantitative measure of piezoelectricity is the piezoelectric charge coefficient denoted by the term d_{33}. The expression of d_{33} goes as follows:

$$d_{33} = k_{33}\sqrt{\epsilon_0 K_3^T s_{33}^E} \tag{6.1}$$

where K_3^T is the relative dielectric constant and s_{33}^E is the charge compliance which is given by, $s_{33}^E = s_{33}^D/(1-k_{33}^2)$. s_{33}^D is the charge compliance measured with open circuit and hence is dependent on the sonic velocity (ς) in the crystal ($1/\rho\varsigma^2$). It should be noted that substituting the charge compliance s_{33}^E in Eq. 6.2 clearly shows a dependence of sonic velocity on the piezoelectric charge coefficient. However, after further research and careful consideration of the BFO as the dynamic material for

ultrasound modulation, we concluded that it is not a practical solution for the problem due to two important reasons. First, the Bulk Photovoltaic Effect functions only for a perfectly constructed crystal which has no defect states in the bandgap. This constraints the experimental feasibility and cost effective solution to the problem of ultrasound modulation. Secondly, the speed of sound in crystal is much higher as compared to water which affects the transmission coefficient of ultrasound waves as discussed in Chapter 1 of the thesis. We moved ahead in the research of materials that can acts as a suitable candidate for ultrasound modulator and hence, we explored an effect called as Acoustoelectric effect.

When a sound wave travels through a substance that contains conduction electrons, its momentum is altered. The momentum of acoustic wave and/or energy are attenuated by electrons. The electrons drift in the direction of force where the force is the result of the momentum attenuation of acoustic wave. Direct current is produced when there is a closed circuit in this direction. Since momentum attenuation is proportional to sound intensity, the generated current, also known as acoustoelectric current, is proportional to sound intensity. On the other hand, when there is an open circuit, the drifting electrons produce a space charge whose electric field cancels the DC force because of the attenuation in the momentum of sound waves. The electric field generated by the space charge is called as the acoustoelectric field [169]. The attenuation coefficient and the velocity of acoustic waves propagating through the piezoelectric semiconductors depend on the conductivity of the crystal [170]. The phenomenon can be applied to modulate the acoustic flux that travels through the material. By analyzing how the velocity changes with different levels of illumination, we can identify key material parameters that describe how acoustic waves interact with conduction electrons. Specifically, this includes assessing the light-dependent electrical conductivity and the elements of the piezoelectric tensor matrix. The attenuation coefficient can be expressed by the relation [170, 171],

$$\alpha = \frac{K^2}{2\,\nu} \times \frac{\omega_C}{1 + (\omega_C/\omega + \omega/\omega_D)^2}, \tag{6.2}$$

where ω is the angular frequency of the ultrasonic wave, $\omega_D = \nu^2 e/(\mu k T)$, $\omega_C = \sigma/\epsilon$, $K^2 = e_{33}^2/(\epsilon c_{33})$, ν is the velocity of ultrasonic wave, ϵ the permittivity, μ the mobility of electrons, σ the electrical conductivity, e_{33} the component of piezoelectric tensor, c_{33} the component of elastic tensor, T the temperature of the material, and k the Boltzmann constant. It should be noted that the term ω/ω_D can be neglected [171] and the formula can be approximately given by the relation [171],

$$\alpha = \frac{K^2}{2\nu} \times \frac{\omega_C}{1 + (\omega_C/\omega)^2}, \tag{6.3}$$

The relation can then be used to obtain a differential form such that the changes in the velocity can be calculated from the corresponding variation in the conductivity. The expression can be writtten as [170–172]

$$\frac{\Delta\nu}{\nu} = -\frac{K^2}{2}\frac{(\omega_C/\omega)^2}{1+(\omega_C/\omega)^2}, \tag{6.4}$$

The formulation presented in the Eq. 6.4 shows that the conductivity of the piezoelectric semiconductor can manipulate the speed of sound. Cadmium Sulphide (CdS) is the most promising acoustoelectric material that has been researched for almost 100 years due to its higher sensitivity to the visible wavelength [170, 172, 173]. However, further research leads us to the fact that this effect generally functions at higher frequencies with time periods smaller than the electron relaxation time (ns) [173]. The ultrasound frequency range that we are interested in is 3 orders of magnitude smaller and hence the estimated change in speed of sound with the conductivity is around 2% [170, 172] which is relatively very low and will require a crystal of thickness 10 mm to achieve a phase-shift of 2π at 1 MHz of operational ultrasound frequency. This amount of thick crystal is very ineffective solution to the problem of ultrasound modulation. The discussed disadvantages related to crystal properties and weak effect on the sound speed motivated us to move forward and explore further interesting concepts for material systems that can benefit the realization of integrated ultrasound modulator.

6.3 Electrostatic Particle Jamming for Tunable Elasticity

Externally applied electric field can be used to change the rheological properties of Electrorheological (ER) materials. This has resulted in promising applications in actuators, dampers, torque transducers, artificial muscle, and many more [174–177]. The ER materials can be composed by suspending dielectric particles in a nonconducting liquid. [178–183] The primary benefit of electrorheological (ER) fluids lies in their ability to rapidly and reversibly alter their rheological properties—such as viscosity and modulus—in response to an applied electric field, typically within a millisecond. However, despite their impressive ER effects, these fluids are not without limitations. Challenges such as particle aggregation and liquid medium leakage can lead to instability in their performance. [184, 185] However, these impediments can be resolved through selecting a viscous density-matched fluid such that the particles in ER fluids do not sediment. The tunable viscoelastic properties of ER fluids have been extensively studied in recent years. [186–188] The storage modulus influenced by an electric field, which refers to the overall change in this modulus when an electric field

is applied, is a key factor in assessing ER elastomers. This adjustable storage modulus feature can be harnessed for modulating ultrasound. The speed of ultrasound (c) depends on the storage modulus which is given by the following equation [189, 190],

$$c = \sqrt{\frac{K_S}{\rho}} \tag{6.5}$$

where K_S is the coefficient of stiffness and ρ is the density of medium. The primary requirement of modulating ultrasound is the manipulation of the phase and/or amplitude of the wave and through the sound speed modulation we can manipulate the phase of transmitted ultrasound.

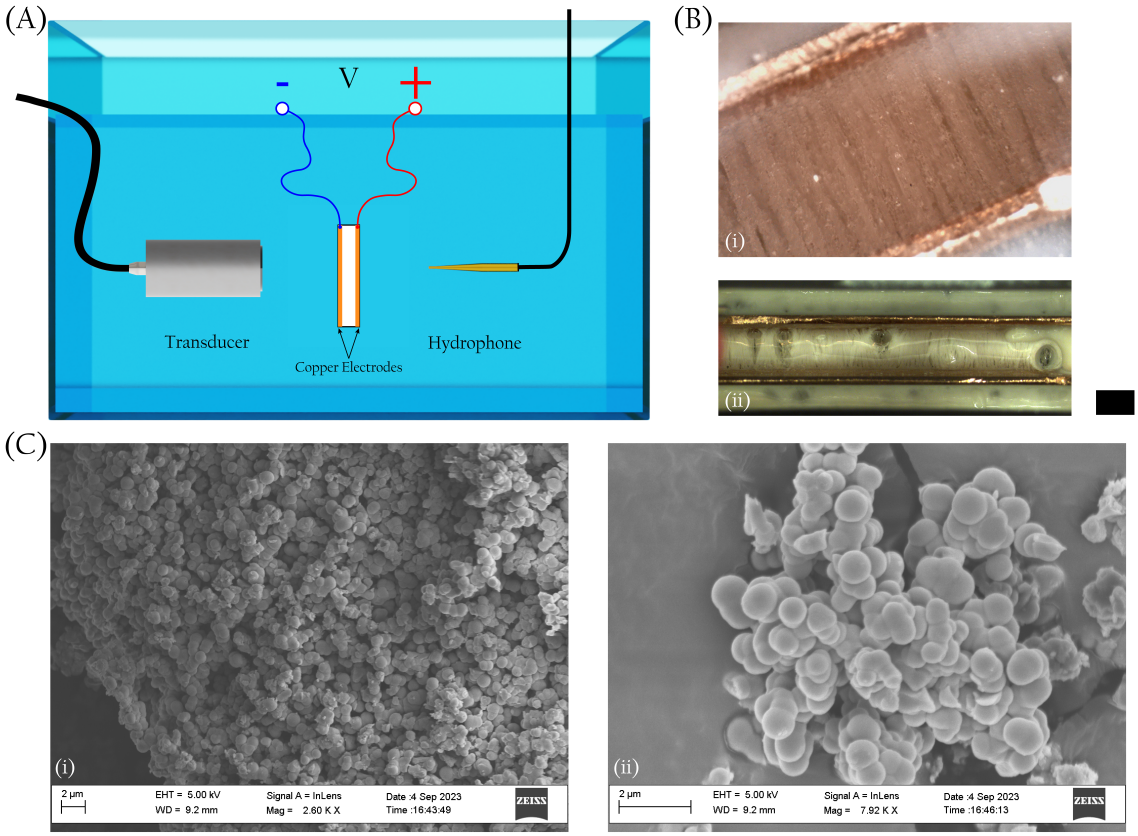

Figure 6.2: Experimental system and particle jamming under DC electric field. (A) Schematics of the experimental setup implemented to study the effect of particle jamming on ultrasound transmission. (B) Chain-like formation of (i) TiO_2 and (ii) $BaTiO_3$ under the application of DC electric field. The scale bar represents the length of 1 mm. (C) (i) and (ii) Scanning Electron Microscopy (SEM) images of fabricated TiO_2 particles using hydrolysis method.

A material with a higher weight fractions of particles generally shows stronger ER effect [191]. Therefore, we have investigated the possibility to dynamically program the material properties for practical applications in ultrasound devices. Although the properties of electrorheological (ER) materials are significantly influenced by the elastic modulus of the polymer matrix, the role of the suspended particles is equally

crucial. The polarity of these particles enhances the ER activities within the fluid, thereby expanding the range of tunability for the elastic modulus. The experimental system is shown schematically in Fig. 6.2 (A). A high voltage is applied using an amplifier (Trek 609D-6) which can provide up to 2 kV. The high voltage amplifier is connected with a function generator (Tektronix AFG1022). We have performed experiments with the following dielectric particles

Description of Particles	
Material	Dimensions
TiO_2-Urea	750 nm to 1000 nm
Aerosil 200	5 nm to 50 nm
SiO_2	100 µm
$BaTiO_3$	1 µm to 2 µm

Table 6.1: Description of particles utilized in the electrostatic jamming experiment.

The particles listed in table 6.1 have been suspended in silicon oil of viscosity $1\,Pa \cdot s$ with weight percentage varying between 100% to 200% with reference to the weight of silicon oil. We have implemented several experiments with the listed particles but could not observe any practical phase change in the transmitted ultrasound except with the $BaTiO_3$ particles. The formation of TiO_2 and $BaTiO_3$ particles assembly arranged into aligned chains paralleling to the direction of applied electric field are shown in Fig. 6.2 (B) (i) and (ii) respectively. The urea-coated titanium dioxide (TiO_2/urea) particles with complete core–shell structure are fabricated with a hydrolysis method [192] whereas the other particles are purchased from Sigma-Aldrich Gmbh. We synthesized TiO_2-urea particles because it has been observed that polar molecule-coated core-shell particles provide high electrorheological performance [192] compared with the bare TiO_2 particles filled elastomer. The TiO_2-urea particles filled elastomer presents higher dielectric constant [192] which indicates the enhanced polarizability of the particles.

The composition of fabricated TiO_2 particles as well as the microstructure is evident in the SEM images shown in the Fig. 6.2 (C) (i) and (ii). The influence of electrostatically controlled viscoelastic properties of the ER material on the transmitted ultrasound waves is experimentally determined and the results of the experiments are shown in Fig. 6.3. We have categorized the experimental results in two sections, first is the effect of DC voltage and second is the effect of frequency of the electric field in the case of an AC voltage. The observations of the transmitted ultrasound waves through a jammed-particle assembly for various |DC voltages are shown in Fig. 6.3 (A) (i), (ii), and (iii). It is evident from the results that there is in fact a phase change in the transmitted ultrasound waves for non-zero applied voltage with respect to the non-biased copper electrodes. However, the phase change is almost identical for the

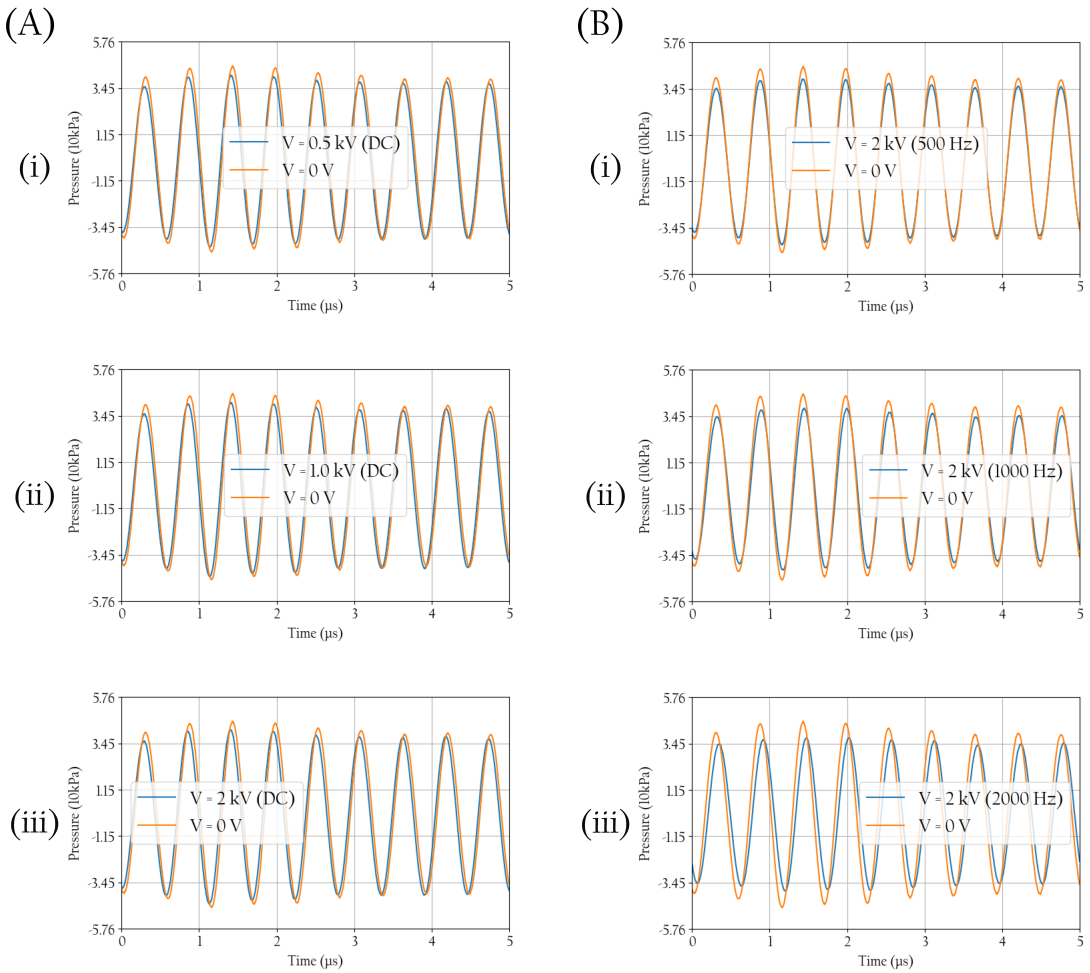

Figure 6.3: Experimental results for transmitted ultrasound waves through particle assemblies jammed with electrostatic fields. (A) Transmitted ultrasound waves plotted for various DC voltages in the suspension of $BaTiO_3$ particles (i) V = 0.5 kV, (ii) V = 1.0 kV, and (iii) V = 2.0 kV. (B) Transmitted ultrasound waves plotted for various frequencies of 2.0 kV AC voltage in the suspension of $BaTiO_3$ particles (i) V = 500 Hz, (ii) V = 1000 Hz, and (iii) V = 2000 Hz.

applied voltage of 0.5 kV, 1.0 kV, and 2.0 kV and simultaneously the phase is shifted by a very small quantity which approximately corresponds to 10°. Next, we experimented with the frequency of AC voltage while keeping the peak voltage amplitude constant at 2.0 kV. The results are presented in Fig. 6.3 (B) (i), (ii), and (iii) for the frequency of 500 Hz, 1000 Hz, and 2000 Hz respectively. The dependence of phase on frequency can be understood through the dielectric properties of the particles involved. In the case of ER elastomers, the electrorheological (ER) effect is linked to the polarization of the filler particles, a process that varies with frequency [193]. Although, we have observed a larger phase change for higher operational frequency of AC voltage, we found difficulties in reproducing the exact phase change with the experiments repeated with the identical experimental parameters. The non-repeatability of the phase-shift points towards variabilities in sample preparation including particle sedimentation. This may

result in changes in the particle number participating in the ultrasound propagation path. We further experimented with higher viscosity silicon oil to counter the problem of particle sedimentation. However, increase in the viscosity translated to a further smaller phase change in the ultrasound at an identical applied voltage. This can be explained due to increase in the resisting elastic force of the silicon oil with higher viscosity, indicating less prominent ER activities. Therefore, we concluded that the reversible particle-jammed assembly method is not suitable for scalable operations for ultrasound modulation.

6.4 Liquid Metal as Phase Change Material for Sound Modulation

In this section, we delve into the exploration of phase change materials for their potential in ultrasound modulation. A crucial aspect in identifying effective dynamic materials for this purpose is analyzing the speed of sound within the material. The most reliable method for measuring sound speed in water involves determining the time-of-flight (TOF) of an ultrasonic signal traveling through a specific path [194]. Typically, the TOF technique employs a piezoelectric transducer to transmit sound signals, while a hydrophone positioned on the other side of the sample captures the received signals. This part of the chapter aims to detail an experimental setup designed to accurately measure the speed of sound in phase change materials under ambient pressure conditions. Notably, this setup measures the path length directly, eliminating issues with acoustic reflections, making it ideal for profiling sound velocity in various materials of interest for dynamic ultrasound modulation.

The time difference method is utilized in the experimental results outlined in this section. The fundamental idea is to gauge the time-of-flight of an ultrasonic signal traveling through a precisely known distance in pure water. We assume that the sound signal propagates as a plane wave, allowing us to determine the speed of sound based on the measured time-of-flight and the acoustic path length [194]. The process unfolds as follows: first, we measure the time-of-flight in water; next, we alter the path length by integrating the phase change material into the acoustic path, and the time-of-flight is measured with phase 1 of the material, and finally the time-of-flight is measured again with the material in phase 2. The difference in the time-of-flight Δt_{TOF} [194] with respect to water of the two measurements for the two phases (for example the solid and liquid phase of the material) can be calculated. The sound waves are assumed to be planar. The path length affected due to the introduction of the material under observation is denoted by L as shown in the Fig. 6.4. The Δt_{TOF}

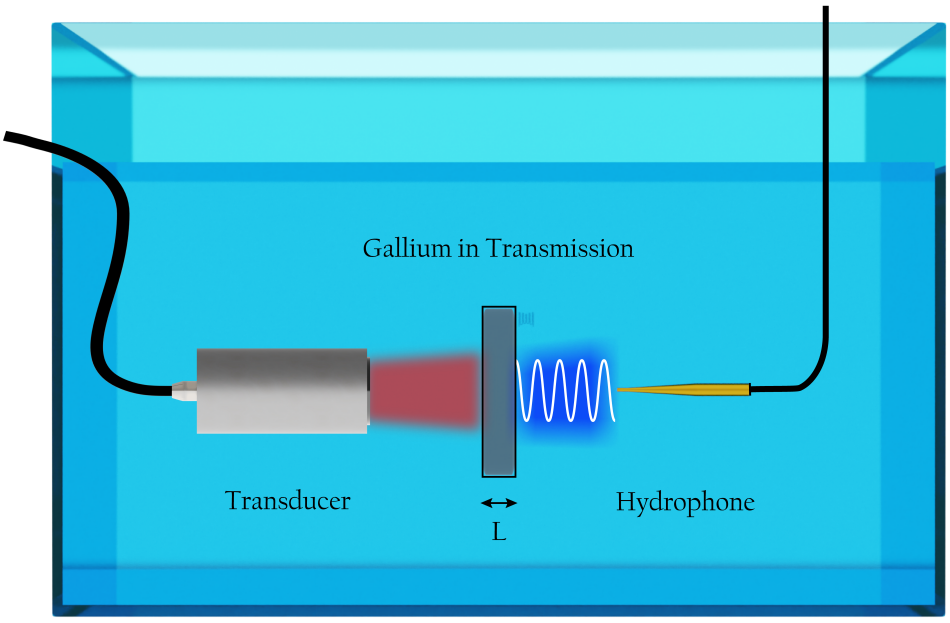

Figure 6.4: Experimental configuration of sound speed measurement of Ga in transmission.

can be written as follows:

$$\Delta t_{TOF} = \frac{L}{S_W} - \left[\frac{L-2W}{S_G} + \frac{2W}{S_P}\right] \tag{6.6}$$

Thus, the speed of sound in the material after rearrangement of the above equation can be written explicitly as follows,

$$S_G = \frac{S_W \times (L-2W)S_P}{S_P L - \Delta t_{TOF} S_W S_P - 2S_W W} \tag{6.7}$$

where S_W, S_P denote the speed of sound in water and Veroclear respectively, S_G represents the speed of the sound in phase change material and W denotes the thickness of the container walls which is 3D printed for the storage of the phase change material. The speed of sound in distinct phase of the material can be sequentially calculated from the Eq. 6.7 where the speed of sound of sound in water and Veroclear are considered as the reference for the measurements.

A Neslab RE 221 bath thermostat is employed to ensure a stable temperature environment, maintaining the temperature wit the stability of 10 mK throughout its full operating range. To achieve this, the system utilizes a heater/cooler feedback loop and features a motor that continuously circulates water between the reservoir and the experimental tank, effectively eliminating any temperature gradients.

Temperature readings are taken using two K-type resistance thermometers (Fluke, model SPRT 5683), strategically positioned at the center of the bath thermostat, as close to the transducer as possible. The transmitting transducer is securely mounted

on an emitter bracket, while the receiving hydrophone is attached to a sensor bracket that's connected to a motorized linear stage (Thorlabs Gmbh, XR25C/M). A rigid mechanical connection ensures stability between the motorized linear stage and the bracket.

The emitter and sensor brackets are specially designed to meet the specific experimental needs and are manufactured using 3D printing with Veroclear material from Stratasys Gmbh. This setup allows the receiving hydrophone to move linearly along the same axis as the transmitting transducer, ensuring that the centers of both the hydrophone and transducer are perfectly aligned. The broadband ultrasonic transducers (Sonoscan IK-5-10) made of a piezoelectric crystal is employed in the experiments which is illustrated schematically in Fig. 6.4. The transducer is operated at the frequency of 6 MHz and is fixed on the sensor mounting brackets face-to-face with the hydrophone. The pressure amplitude and phase output of the transmitted ultrasound waves are scanned in a water tank using a 0.4 mm-diameter hydrophone (HGL0400, Onda Corporation). The voltage signal from the hydrophone is digitized and stored in the computer for further analysis using a USB oscilloscope (Picoscope 5000 Series, Pico Technology). The values of the parameters that are measured experimentally and have been used in the experiments related to the phase change material are tabulated in Table 6.2. In view of the accuracy and design requirements, high accuracy time interval measurements are performed which is described in this section. The oscilloscope digitizes the signal from the hydrophone and enables measurement of short time intervals. We have sampled the hydrophone signal at a rate of 25 MHz. A frequency-sweep generator (Tektronix AFG1022) is employed to generate a pulse signal for triggering the function generator (Tektronix AFG1022), to measure the ultrasonic time-of-flight. An arbitrary function generator generates a the signal of 50 cycles to drive the transmitting transducer. The active diameter is 10 mm, and coaxial cables with an impedance of 50 Ω are used to connect the signal generator, transducers, and digital oscilloscope.

Values of Parameters	
Parameter	Value
S_W	1486 m/s
S_P	1413 m/s
L	7 mm
W	1 mm

Table 6.2: Tabular representation for the values of the parameters employed in the experimental measurements.

The measurements are carried out in the temperature range from 27 °C to 34 °C at ambient pressure. This is because, the melting temperature of Gallium is 29.7° as shown in Fig. 6.5 (yellow dotted line). At every state, the sound pulse is recorded

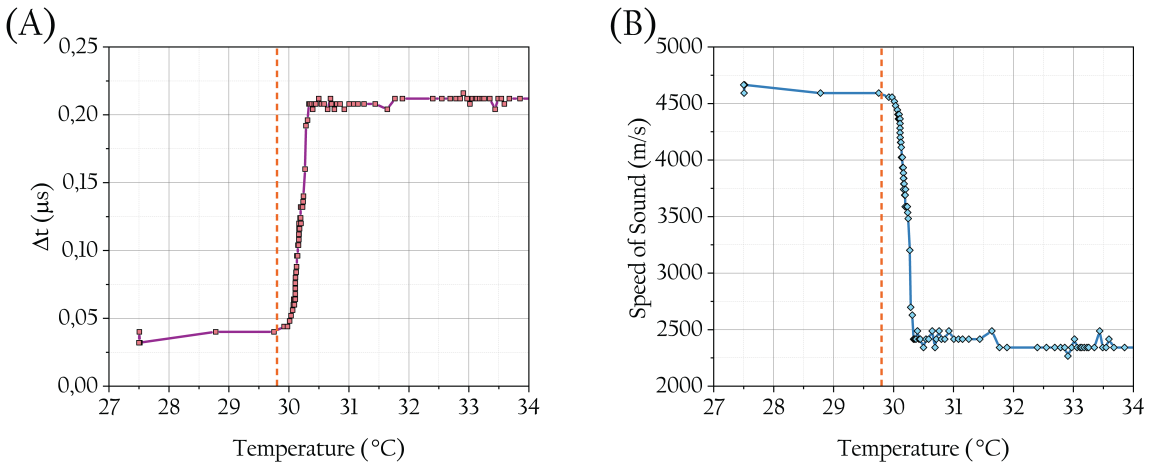

Figure 6.5: Experimental results for sound speed measurements in Ga as a function of temperature. (A) Magnitude of difference in Time-of-flight measured for Ga with respect to the arrival time of sound waves in water. (B) Sound speed calculated from the time-of-flight measurements as a function of temperature.

100 times using the digital oscilloscope and the time-of-flight measurement is deduced sequentially. Before the measurements are carried out, the apparatus is allowed to equilibrate for at least 1 h. In the bath thermostat, two temperature sensors (k-type) are added alongside the Ga chamber. We have performed repeated measurements to validate the reproducibility of the data, and the speed of sound in Ga for solid and liquid phases are 4665 m/s ± 3.6 m/s and 2341 m/s ± 2.1 m/s, respectively. The experimental measurements for different physical property of Ga are presented in Table 6.3. The experimental results for the time-of-flight measurements followed by the calculation of the sound speed in Ga as a function of temperature are shown in Fig. 6.5, (A) and (B) respectively. The relatively larger change in sound speed indicates the feasibility of using Ga as a promising dynamic material for ultrasound modulation. The density of gallium in solid and liquid states is almost identical, which results in a relatively large acoustic impedance mismatch between its solid and liquid states. In the steep phase transition process as shown in Fig. 6.5 (A) and (B), The initial melting process is clearly visible in the recorded behavior of sound speed, leading to a stable liquid medium as validated by the constant time-of-flight measurements. In the frequency range of 1 MHz to 10 MHz, the attenuation in Ga is insignificant.

6.4.1 Gallium as Reflective Metasurface Element

Unlike traditional materials whose properties are fixed after fabrication, phase change materials enable agile tuning of their functions to dynamically adapt to different needs. Active acoustic metasurfaces is a new avenue for creating potentially compact, high-performance reconfigurable acoustic devices that can be controlled externally without

Properties of Gallium in Different Phase		
Property	Phase	
	Solid	Liquid
Density (ρ)	6095 kg/m^3	5910 kg/m^3
Longitudinal Speed of Sound (C)	4665 m/s	2341 kg/m^3
Characteristic Acoustic Impedance (Z_0)	28 433 175 kg/m^{2}s	13 835 310 kg/m^{2}s

Table 6.3: Material properties of Ga in different phase [3].

the need for mechanical moving components. This can lead to the development of dynamically modulated complex ultrasound wavefronts. Reflective acoustic metasurfaces analogous to Digital Micromirror Device (DMD), could be used for shaping wavefronts. This section explores gallium as a metasurface element by firstly numerically calculating the amplitude and phase of the reflected and transmitted pressure waves from an incident acoustic wave at different angles (θ_I) and then experimentally demonstrates and validates the results predicted by the numerical calculations. The operation of gallium as a metasurface element requires the phase transformation which is discussed in chapter 6.

The reconfigurable or static metasurfaces introduced thus far for acoustic fields are limited to operating in the low frequency region [195] ranging from few kHz to few 10 kHz. The reason for the focus on low acoustic frequency is the size requirement of the metaelement which depends on the wavelength: smaller frequencies require large elements which are easier to fabricate. The MHz frequency region constraints the element size to be less than a mm, which makes it more challenging to engineer a metaelement. The schematics of the experimental system and the numerical framework are shown in Fig. 6.9 (A) and (B), respectively. The wave propagation diagram at the interface of water-gallium as shown in Fig. 6.9 (B), demonstrates mode-shift that occurs when a plane-wave reflects off an interface at a non-normal incidence. The notation in Fig. 6.9 (B) is as follows,

PP_I - Incident Primary Pressure Wave

PS_R - Reflected Shear Wave

PP_R - Reflected Pressure Wave

PS_T - Transmitted Shear Wave

PP_T - Reflected Pressure Wave

θ_I - Angle of Incidence for Primary Pressure Wave

θ_T - Angle of Transmission for Transmitted Pressure Wave

The numerical calculations for ultrasound waves incident at non-normal angles of incidence on the water-gallium interface are categorized into two parts: First, the boundary is considered as a liquid-liquid interface and the reflected and transmission coefficients are calculated based on the respective medium properties. Second, the coefficients are determined for the case of a liquid-solid interface. The categorization of the interface properties is performed to account for the liquid and solid phase of gallium, separately. The reflection and transmission coefficients of the P-wave (primary wave or pressure wave) for the case of liquid-liquid interface are defined as follows,

$$R_P^{L-L} = \frac{Z_T^{L-L} - Z_R^{L-L}}{Z_T^{L-L} + Z_R^{L-L}} \tag{6.8}$$

$$T_P^{L-L} = 1 + R_P^{L-L} \tag{6.9}$$

where Z_T^{L-L} and Z_R^{L-L} are the acoustic impedances for transmitted and reflected P-waves for liquid-liquid interface. The value of acoustic impedances can be determined from the following equations [196, 197],

$$\begin{aligned} Z_R^{L-L} &= \frac{\rho_W C_W}{\cos\theta_I} \\ Z_T^{L-L} &= \frac{\rho_{G/L} C_{G/L}}{\cos\theta_T} \end{aligned} \tag{6.10}$$

where $\rho_W = 1\,\mathrm{g/cm^3}$, $\rho_{G/L} = 5.91\,\mathrm{g/cm^3}$, $C_W = 1507\,\mathrm{m/s}$, and $C_{G/L} = 2341\,\mathrm{m/s}$ (The subscripts G/L and W represent liquid state of gallium and water medium respectively). The angle of transmission for pressure wave is represented by θ_T which is defined as follows,

$$\theta_T = \sin^{-1}\left[\frac{C_{G/L}}{C_W} \times \sin\theta_I\right] \tag{6.11}$$

The energy transfer coefficients E_R^{L-L} and E_T^{L-L} can be calculated from the amplitude coefficients in the following way [196, 197],

$$\begin{aligned} E_R^{L-L} &= [R_P^{L-L}]^2 \\ E_T^{L-L} &= [T_P^{L-L}]^2 \times \frac{Z_R^{L-L}}{Z_T^{L-L}} \end{aligned} \tag{6.12}$$

The equations governing the case for liquid-solid interface takes into account the partitioning of wave energy at the interface due to mode-shift. Zoeppritz equations [197] are used to numerically analyze the mode-conversion at the water-gallium interface. The Zoeppritz equations describe how the amplitude of an incoming pressure wave (P-wave) at a flat interface relates to the amplitudes of the reflected and refracted P-waves, as well as the shear waves (S-waves), depending on the angle of incidence. These equations serve as the cornerstone for exploring how different factors impact the

amplitude of reflected waves when the angle of incidence changes, a process commonly referred to as amplitude versus offset analysis. [198]. The Zoeppritz equations are generally consisting of four equations with four unknowns namely R_P, R_S, T_P, and T_S which represent the reflected P, reflected S, transmitted P, and transmitted S-wave amplitude coefficients, respectively. These parameters define the fundamental characteristics of reflected and transmitted waves. The Zoeppritz equations are reduced to three variables for the case of a water-gallium interface due to non-propagation of reflected S-waves in water. The equations are denoted in matrix representation as follows [196, 197],

$$\begin{bmatrix} R_P^{L-S} \\ T_P^{L-S} \\ T_S^{L-S} \end{bmatrix} = \begin{bmatrix} \cos\theta_I & \cos\theta_T & \sin\delta_T \\ Z_R^{L-S} & -Z_T^{L-S}\cos(2\delta_T) & W_T^{L-S}\sin(2\delta_T) \\ 0 & \frac{V_{G/S}}{C_{G/S}}\sin(2\theta_T) & -\cos(2\delta_T) \end{bmatrix}^{-1} \times \begin{bmatrix} \cos\theta_I \\ -Z_R^{L-S} \\ 0 \end{bmatrix}^T \tag{6.13}$$

where δ_T is the angle of the transmitted S-wave, Z_R^{L-S} is the acoustic impedance of reflected P-wave, Z_T^{L-S} is the acoustic impedance of the transmitted P-wave, and W_T^{L-S} is the acoustic impedance of the transmitted S-wave. The notations $C_{G/S} = 4665\,\mathrm{m/s}$ and $V_{G/S} = 2663\,\mathrm{m/s}$ represent sound speed of P-wave and S-wave for solid gallium respectively. The amplitude coefficients as a function of incident angle are determined from Eq. 6.13 by taking the inverse of the matrix. The acoustic impedances for liquid-solid interface defined numerically as follows [196, 197],

$$\begin{aligned} Z_R^{L-S} &= \rho_W \times C_W \\ Z_T^{L-S} &= \rho_{G/S} \times C_{G/S} \\ W_T^{L-S} &= \rho_{G/S} \times V_{G/S} \end{aligned} \tag{6.14}$$

The energy transfer coefficients for the liquid-solid interface can be calculated in the similar manner as that of liquid-liquid interface, which are defined as follows [196, 197],

$$\begin{aligned} E_R^{L-S} &= [R_P^{L-S}]^2 \\ E_{TP}^{L-S} &= [T_P^{L-S}]^2 \times \left[\frac{Z_T^{L-S}\cos\theta_T}{Z_R^{L-S}\cos\theta_I}\right] \end{aligned} \tag{6.15}$$

The results of the numerically determined magnitude of reflection and transmission coefficients are shown in Fig. 6.6. The phase of the reflection and transmission coefficients are shown in Fig. 6.7 where a region with identical angles of incidence is highlighted in Fig. 6.6 and Fig. 6.7. The highlighted section in Fig. 6.7 represents angles of incidence for the reflected ultrasound wave that have approximately a phase difference of π when the gallium undergoes a phase transition from solid to liquid or vice versa. It should be noted that the amplitude of the reflected ultrasound waves

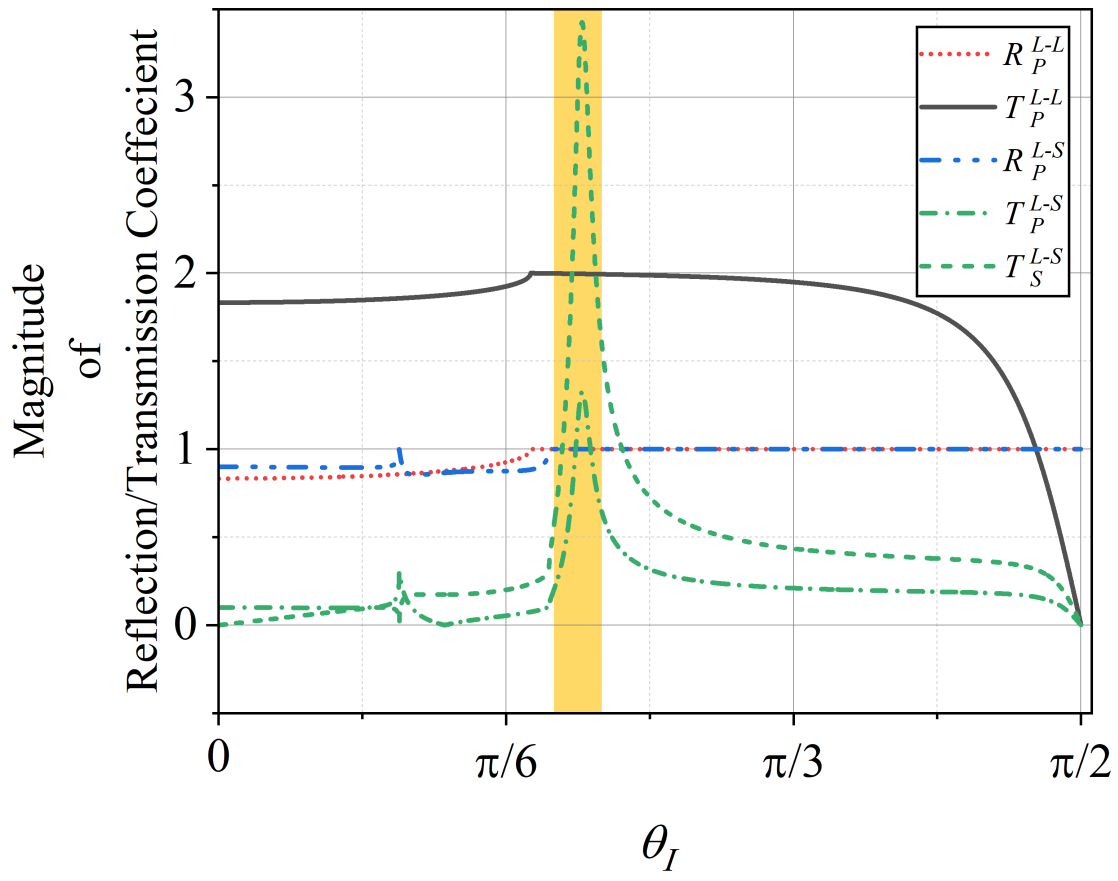

Figure 6.6: Plot of the magnitude of reflection and transmission coefficients for a water-Ga liquid-liquid interface and a water-Ga liquid-solid interface as a function of angle of incidence.

does not vary with respect to the incident waves in the highlighted range of θ_I as can be observed from Fig. 6.6. The magnitude of the reflection coefficient in solid and liquid state of gallium is unity which symbolizes that the magnitude of reflected wave is independent of the phase-shift happening for the highlighted region of incident angle. We further validated the phenomenon by plotting energy transfer coefficients corresponding to Eq. 6.12 and Eq. 6.15 as a function of θ_I. The results for the energy transfer coefficients are shown in Fig. 6.8. It can be observed that the energy transfer coefficients for the reflected waves are the same for the liquid and solid state of gallium. The numerical results in Fig. 6.6, Fig. 6.7, and Fig. 6.8 show that the phase-transition in gallium leads to a modulation of the reflected ultrasound waves. In addition, we identified the optimum angle of incidence to be 38° that contributes to the π phase-shifted reflected waves tupon the phase-transition in gallium at the water-gallium interface.

We experimentally validated the numerically calculated results. The experimental system is shown in Fig. 6.9 (A) which consists of a broadband ultrasound transducer (Sonoscan IK-5-10) mounted on an adjustable angle mounting system so that the angle

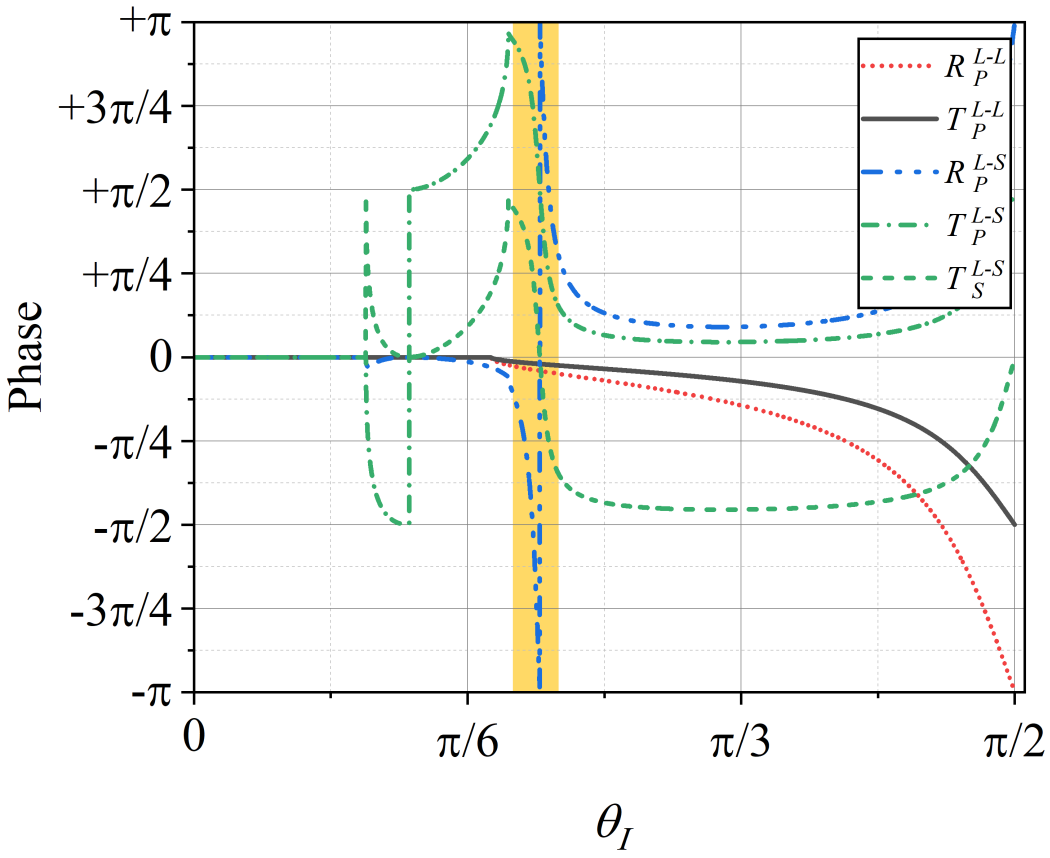

Figure 6.7: Plot of the phase of the reflection and transmission coefficients for a water-Ga liquid-liquid interface and a water-Ga liquid-solid interface as a function of angle of incidence.

of incidence (θ_I) for the ultrasound waves can be manipulated in a controlled manner. The angular position of the hydrophone is kept constant for the experiments. The pressure amplitude and phase output of the reflected ultrasound waves are scanned in a water tank using a 0.4 mm-diameter hydrophone (HGL0400, Onda Corporation). Pressure waves produce a voltage in the hydrophone, which was digitized using a USB oscilloscope (Picoscope 5000 Series, Pico Technology) and saved on the computer. The time-domain voltage data was converted to a pressure using the manufacturer-provided calibration. For accurate measurements, a 100-cycle sinusoidal pulse was used to incident on the water-gallium interface. The hydrophone correspondingly recorded a pulse, which was converted to amplitude and phase data at the center driving frequency using a Fast Fourier Transform.

The experimental results of Ga as a reflective metasurface element are shown in Fig. 6.10. The experimental system for the observation presented in Fig. 6.10 is analogous to angle-resolved measurements using a goniometer [199].

Ga has been stored in a 3D printed container made from Veroclear and the top exposed surface of Ga is spin coated with PDMS to maintain a smooth topology of the

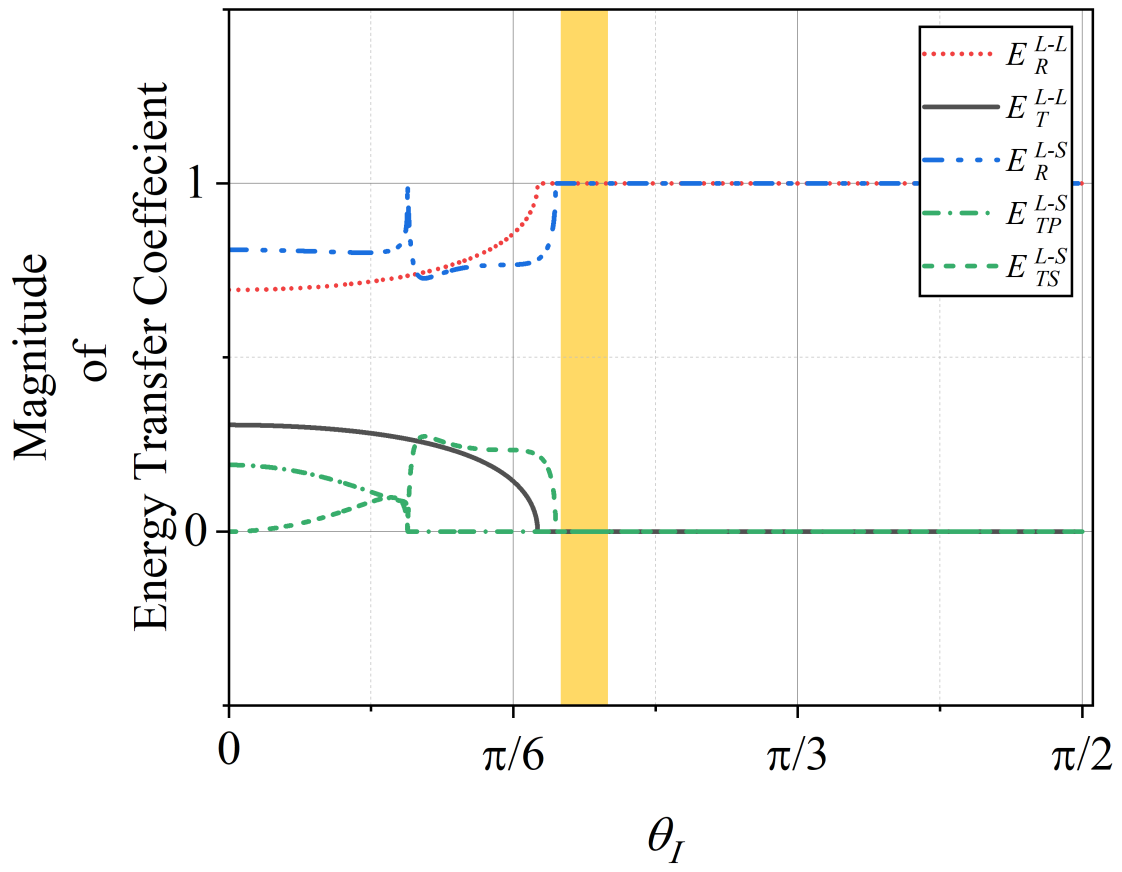

Figure 6.8: Plot of the magnitude of energy transfer coefficients for a water-Ga liquid-liquid interface and water-Ga liquid-solid interface as a function of angle of incidence. See text for details.

surface. The topology of the surface plays a critical role in the reflection experiments. We have optimized the spin coating parameters to deposit a 1 mm thick PDMS layer on the Ga surface. The PDMS is cured at room temperature for 24 h so that the physical state of Ga is solid during the curing process. The results of the experiments are shown as a function of amplitude (Fig. 6.10 (A)) and phase (Fig. 6.10 (B)) of the reflected pressure wave. It should be noted that in the control experiments we have performed measurements without a reflective surface of Ga and made sure that the hydrophone does not receive any pressure waves. This validates that the source of pressure waves received from hydrophone is the reflection from the surface of Ga when Ga is introduced in the path of the pressure waves. The experiments are performed for various angles of incidence to experimentally optimize the incident angle to obtain a π phase-shifted reflected wave. Based on the continuous pressure measurements from the hydrophone, we acquired an optimal incidence angle of approximately 48° which provides a π phase-shift of the reflected wave with respect to the incident wave. It can be inferred from Fig. 6.10 (A) that with the incident angle of 48° the amplitude of reflected wave remains unaffected from the solid-to-liquid phase-transition of Ga

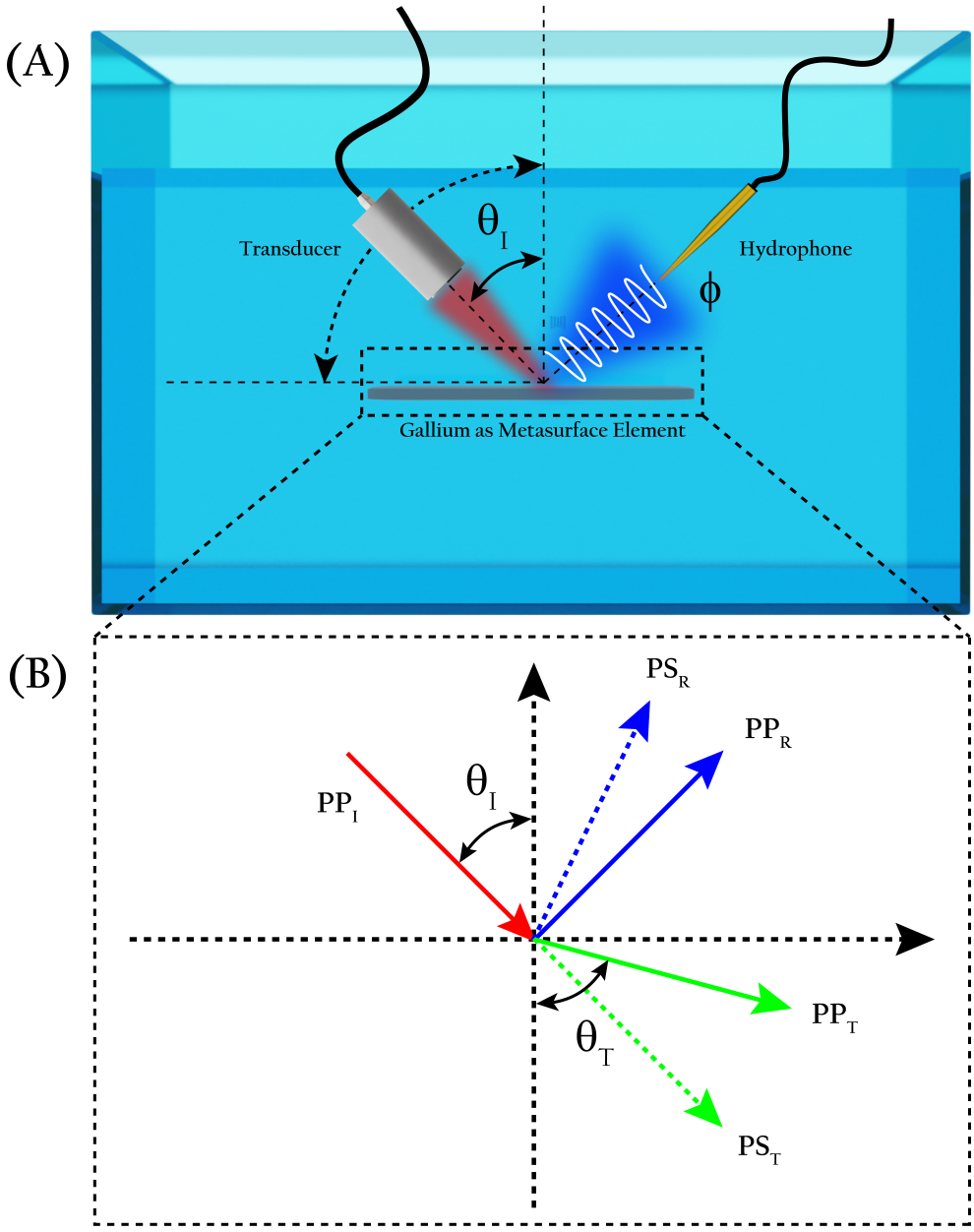

Figure 6.9: Experimental configuration of Ga as a reflective metasurface element. (A) Schematic representation of experimental system employed to measure the properties of water-gallium interface for different incident angles (θ_I). (B) Wave diagram at the interface of water-gallium where the notations denote the parameters computed to simulate the behavior of Ga as metasurface element.

which is around 31 °C but at the same time the phase of the reflected wave is shifted by π when measured with respect to the phase of the reflected wave from the solid state of Ga. This clearly validates the theoretical predicted results presented in Fig. 6.6, Fig. 6.7, and Fig. 6.8. We have compared the wave characteristics of π phase-shifted reflected wave with the pressure wave received by the hydrophone when the wave is incident with an angle of 37°. The amplitude of the reflected wave attenuates by a factor of 2 and the phase remains almost similar in the solid and liquid states of Ga.

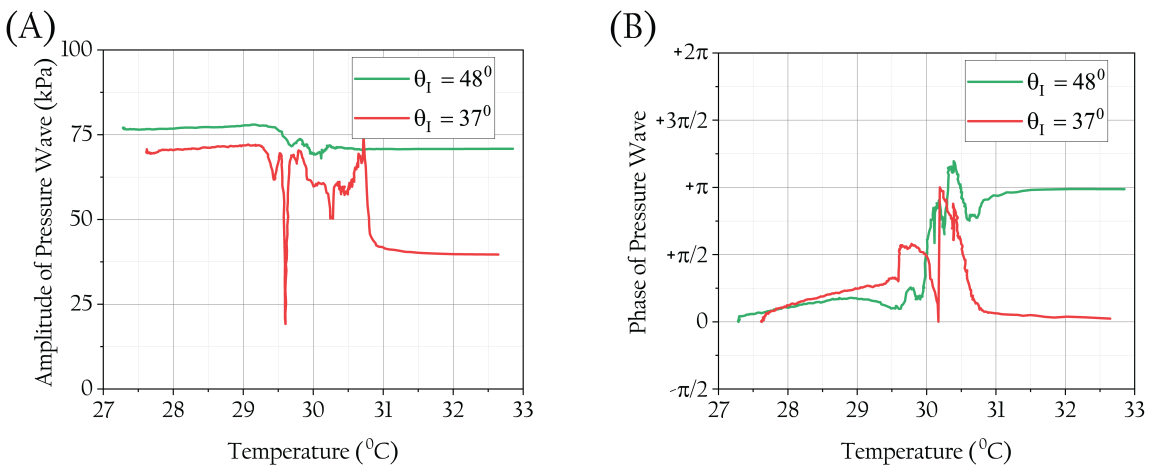

Figure 6.10: Experimental results for Ga as a reflective metasurface element. (A) Amplitude and (B) phase of the reflected pressure wave as a function of Ga temperature for different angles of incidence (θ_I).

The comparison of the reflected wave characteristics for incident angles of $\theta_I = 48°$ and $\theta_I = 37°$ demonstrates the phase-shift dependency on the incident angle.

In summary, the acoustic metasurface is composed of liquid metal material and by changing its phase from liquid to solid or vice versa, we can dynamically change the properties of reflected acoustic waves. Reflective metasurfaces can achieve large degree of tunability in wavefronts through reversible phase transformation analogous to phenomena such as the thermo-optic or electro-optic effect [200] for optical fields. The function of metasurface starts with a metaelement which manipulates the properties of reflected acoustic waves at local level through phenomenons of wave propagation.

6.5 Dynamic 1-D Phononic Metasurface Stack

6.5.1 1D Phononic Crystal

This section of the chapter focuses on the propagation of longitudinal elastic waves that travel perpendicular to the laminations in a periodically layered system [201]. The research examines how to achieve a tunable pass band within this framework. The system involves alternating thin layers of phase change materials, and comparisons have been made with numerical simulations of these periodically structured systems. Moreover, we present experimental evidence of an omnidirectional band gap that arises when longitudinal waves [201] interact with a finite multilayer composed of two different materials. Additionally, unique transmission peaks that appear within the gap region of a specifically designed one-dimensional phononic crystal [201] serve as a proof-of-concept. This demonstrates the potential for dynamic functionality in ultrasound-based devices that utilize phase change materials.

6.5.2 Phononic Gallium Stacks

Temperature tunable gallium shows a large change in sound speed variation induced by its phase transformation. The phase transformation of gallium does not affect the density of gallium which makes it a promising material for dynamic wavefront modulation. Wave transmission in solids and liquids differs because of the physical properties. A gallium-based phononic crystal is introduced to realize a reversible liquid–solid phase transition by heating/cooling, which is utilized to tune a high-frequency (2 MHz to 8 MHz) transmission band gap. A 1D phononic crystal is considered, which consists of a 1D stack of plates filled with either gallium or copper. We selected copper because of its acoustic properties which are very similar to the solid phase of gallium. Numerical simulations are conducted to substantiate the experimental results and to develop a platform to explore the geometric parameters to obtain a functional phononic crystal at MHz frequencies.

This section of the chapter describes the periodic multilayered stack and experimental details as well as finite element simulations using k-wave [202]. The plane wave expansion (PWE) method is utilized to obtain the band structure. The results shown in this chapter prove that the frequencies of the pass band can be tuned by controlling the temperature.

6.5.3 Numerical Model and Simulation

The wave propagation in a periodic multilayered structure composed of alternative arrangement of A and B layers is studied. The symbols d_A, d_B represent the thicknesses of the A, and B layers, respectively, as shown in Fig 6.11. It is assumed that transverse waves cannot be excited at normal longitudinal wave incidence, therefore only the propagation of longitudinal waves are considered in the periodic system. For this superlattice featuring a straightforward 1D structure, the transmission characteristics of the fundamental wave can be readily anticipated using the dispersion relationship of the linear band structure, as detailed below: [203, 204]:

$$\cos K(d_A + d_B) = \cos(\omega d_A/c_A)\cos(\omega d_B/c_B) - \cosh(\eta\omega d_A/c_A)\sin(\omega d_B/c_B) \quad (6.16)$$

where K is a Bloch vector, and $\eta = \ln(\rho_A c_A)/(\rho_B c_B)$. It can be observed from the Eq. 6.16 that pass bands and band gaps are produced in the frequency spectrum which is represented by the segments of curves inside and outside of the region bounded by $\cos K(d_A + d_B) = \pm 1$, respectively. In the superlattice shown in Fig. 6.11, acoustic waves are able to travel freely within the pass bands, while those caught in the band gaps experience exponential attenuation as they move forward. This fundamental property of the superlattice is essential to the phononic stack model. The general

band structure can be obtained by solving the Eq. 6.16. We have utilized the solutions of Eq. 6.16 to obtain a general band structure before performing a detailed numerical simulation in two-dimensions space [204]. Typically, numerical simulation

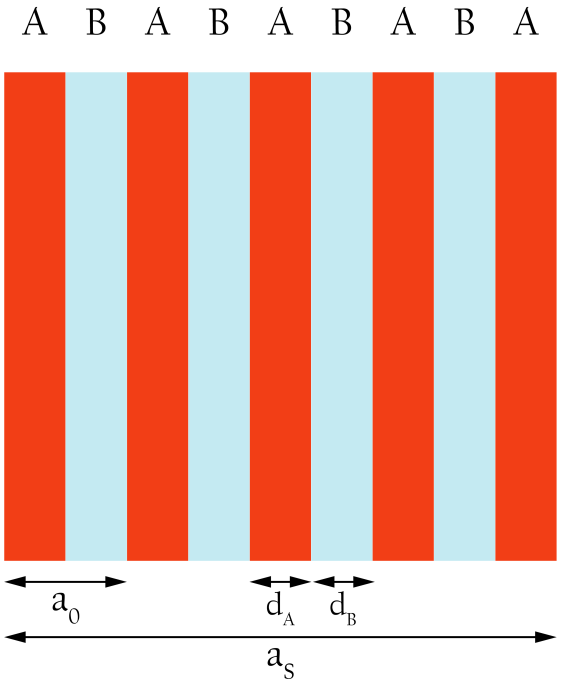

Figure 6.11: A 1-D phononic crystal of the multilayered system consisting of a state of material A, and B. a_0 is the length of one unit cell composed of material A and B, and a_S is the size of the entire stack.

plays an important role in the development of acoustic metamaterials because it can provide valuable information for understanding the wave dynamics and optimizing the technical parameters for specific applications.

We developed our computational framework using k-wave, an open-source acoustic simulation toolbox based on MATLAB. Initially created for biomedical photoacoustic tomography, k-wave serves as a numerical tool for realistic wave simulation and image reconstruction. Over time, its capabilities were expanded to include models for nonlinear ultrasound propagation and elastic wave propagation in absorbing media. Currently, k-wave is capable of simulating wave propagation in both homogeneous and heterogeneous media, across one, two, and three dimensions, and operates in both forward and reverse time [205].

The first step in running a k-wave simulation involves setting up the computational grid properties that will define other aspects of the simulation [205]. To assist with this, k-wave includes a predefined function called **makeGrid**. This function requires two input parameters: the number of grid points in the x, y, and z directions (N_X, N_Y, N_Z) and the spacing between those grid points (d_X, d_Y, d_Z) for each of the Cartesian axes. It is important to remember that during the simulation, the x and y directions

are considered lateral, while the z direction is axial with respect to the ultrasound transducer.

The grid points represent specific locations within the computational space where the governing equations will be resolved [205]. Within the **makeGrid** function, these grid points and spacings help create matrices that include wavenumbers and Cartesian grid coordinates. After this setup, an instance of the **kWaveGrid** class is created, which houses crucial parameters such as directional wavenumbers, total grid points, grid spacings, grid coordinates, spatial dimensions, and spatial frequencies that are used by the utility functions in k-wave [205].

Additionally, a specialized type of anisotropic absorbing boundary layer, referred to as the perfectly matched layer (PML), is implemented to effectively prevent wave reflections from the boundary back into the medium.

Simulation Parameters		
Medium	Physical Property	
	Sound Speed	Mass Density
Water	1483 m/s	998 kg/m^3
Copper	4699 m/s	8960 kg/m^3
Gallium (Solid)	4665 m/s	6110 kg/m^3
Gallium (Liquid)	2341 m/s	5990 kg/m^3

Table 6.4: Material properties of media used in the k-wave simulations [4].

Defining the Computational Grid

We utilized a two-dimensional grid featuring 1536 points in both the lateral and elevation directions, incorporating a perfectly matched layer (PML). The spatial step size was set at 39 µm (yielding over 10 grid points per wavelength at the maximum frequency) to ensure precise resolution of the acoustic field. The overall grid dimensions are 60 mm × 60 mm across both lateral and elevation directions. To effectively model the three-phase medium, which includes water, gallium, and copper as illustrated in Fig. 6.13, we referenced the material properties detailed in Table 6.4. Additionally, a 10-point PML was applied around the entire computational domain [205].

We utilized the function **kWaveGrid** to set up the simulation space. The time array for the simulation duration can be created with the built-in function **makeTime** [205]. This time array is a one-dimensional matrix that contains time values starting at zero and extending to the simulation's end time. The increments between these time values are determined by the simulation's bandwidth. This function takes into account both the total simulation time and the longitudinal wave speed of the medium. The time step for the simulation is automatically calculated based on the inputs provided to the **makeTime** function. We selected a total simulation time of 750 µs, resulting in an

automatically computed time step of approximately 4 ns. The four input parameters that define the k-wave simulation are

- Grid
- Media
- Source
- Sensor

The simulation process begins with the implementation of the function **kspaceFirstOrder2D** [205], which is preceded by detailing the necessary input parameters. This function effectively simulates the propagation of compressional waves within a two-dimensional domain. It is built upon a first-order k-space model [205], enabling the exploration of wave interactions with various structures or boundaries, as defined by four specific input configurations. On a setup featuring an Intel(R) Xeon(R) Gold 5215 CPU running at 2.50 GHz with two parallel processors, our simulations typically take around 19 hours. The workstation utilized is equipped with a Nvidia RTX A6000 that features 47.5 GB of GPU memory and 384 GB of RAM. After each simulation run, we save the specified acoustic field parameters at the grid points defined by the sensor mask for each time step.

To enhance computational efficiency for larger-scale 2D simulations, we also optimized versions of the functions **kspaceFirstOrder2D** which are implemented in Windows Power shell and compatible with 64-bit Windows systems. Depending on the unique characteristics of the simulation domain and system sizes involved, these optimized codes can significantly outperform the Matlab implementation by several folds.

6.5.4 Experimental Results and Discussion

The 1D phononic crystal stack is composed of alternate gallium (Ga) and copper (Cu) layers, where $\rho_C = 8.96\,\mathrm{g/cm^3}$, $\rho_{G/S} = 6.09\,\mathrm{g/cm^3}$, $\rho_{G/L} = 5.91\,\mathrm{g/cm^3}$, $C_C = 4699\,\mathrm{m/s}$, $C_{G/S} = 4665\,\mathrm{m/s}$, and $C_{G/L} = 2341\,\mathrm{m/s}$ where G/S and G/L represent solid state gallium and liquid state gallium respectively. The thickness of Ga and Cu are identical and the experiments only considered the longitudinal wave propagation in the phononic crystal. The schematic representation is shown in Fig. 6.13 which is composed of Cu (material A) and Ga (material B) layers. We explored the dynamic effect of phononic bandgaps from the liquid–solid phase transitions by performing wave transmission. We conducted tests on 1D low-amplitude wave transmission utilizing our custom testing system, as illustrated in Fig. 6.13.

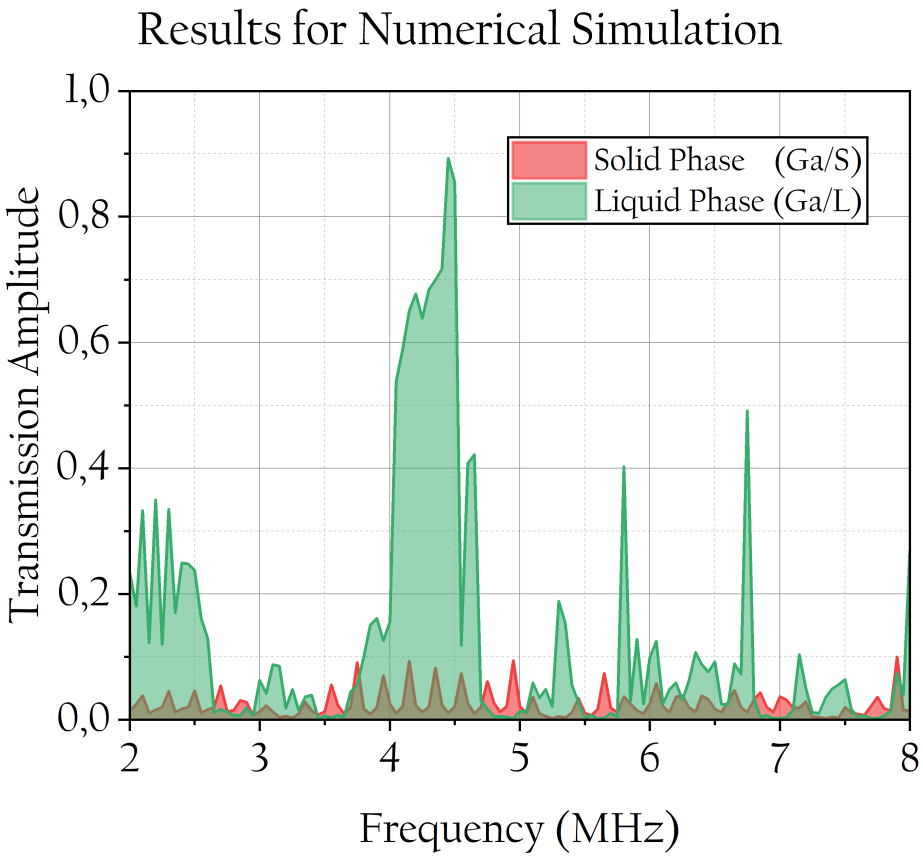

Figure 6.12: Simulation results of the multilayered phononic crystal consisting of Cu and Ga where the computational framework is architectured in k-wave and Matlab.

The experimental measurement setup consists of a frequency generator (Tektronix AFG1022), a broadband ultrasound transducer (Sonoscan IK-5-10 EN), a 3D-printed sample holder for the alternate panels of copper and gallium, a DC power supply, a water tank, a water circulating chiller (Neslab RTE211) and a digital oscilloscope (5242D PC Picoscope, Pico Technology) to record signals from hydrophone. The water circulation chiller system maintains the temperature of water inside the tank holding the phononic crystal. The DC power supply is connected to a preamplifier which amplifies the voltage signal from the hydrophone. The thermal flux from the water causes Ga to undergo a phase transition from solid to liquid. A k-type temperature sensor is introduced to monitor the temperature of the water. The generator produces harmonic signals ranging from 2 MHz to 8 MHz through the ultrasonic transducer. To secure the transducer's head at the left end of the 3D-printed specimen, vacuum grease is used. At the right end, a hydrophone is positioned to capture the transmitted output waves. The ultrasonic wave generation and recording are synchronized with an external trigger signal, enabling accurate time measurements.

The results of the experimental demonstration of dynamic phononic crystal is

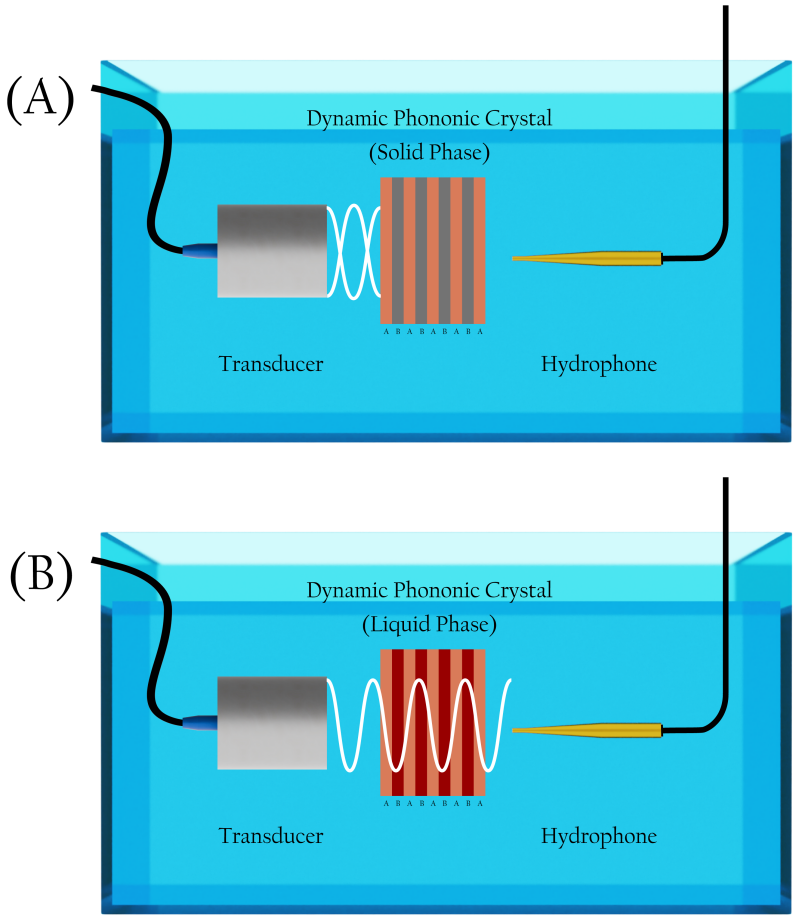

Figure 6.13: Schematic showing the experimental measurement system of the multilayer phononic Cu and Ga crystal stack. The ultrasound transducer has an operational range from 2 MHz to 8 MHz and the hydrophone measures the transmitted ultrasound wave. The phononic crystal works as a (A) bandstop filter when Ga is in solid phase and as (B) bandpass filter for the liquid phase of Ga.

shown in Fig. 6.14. Experimental results verify the position of the first-order bandpass in Fig. 6.14 (A), with a pass-band frequency ranging from 4.45 MHz to 4.75 MHz. The results of the numerical simulations are shown in Fig. 6.12. The first-order pass band is located between 4.15 MHz and 4.65 MHz of the numerical simulation which agrees well with the experimental results. We have tested a phononic stack with five layers. It is important to note that the number of layers in the phononic crystal only affects the amplitude of the pass band, not its frequency. In addition, the phase transition from solid to liquid induces a tunable phononic passband. The numerically simulated frequency characteristics of the solid-state medium is shown in Fig. 6.12 (with red colored curve) and it is clearly seen that the stack functions as a stopband in the complete frequency range from 2 MHz to 8 MHz. The experimental results of solid-solid lattice support the predictions from the numerical simulations.

This work demonstrates the potential of a liquid metal gallium-based metasurface

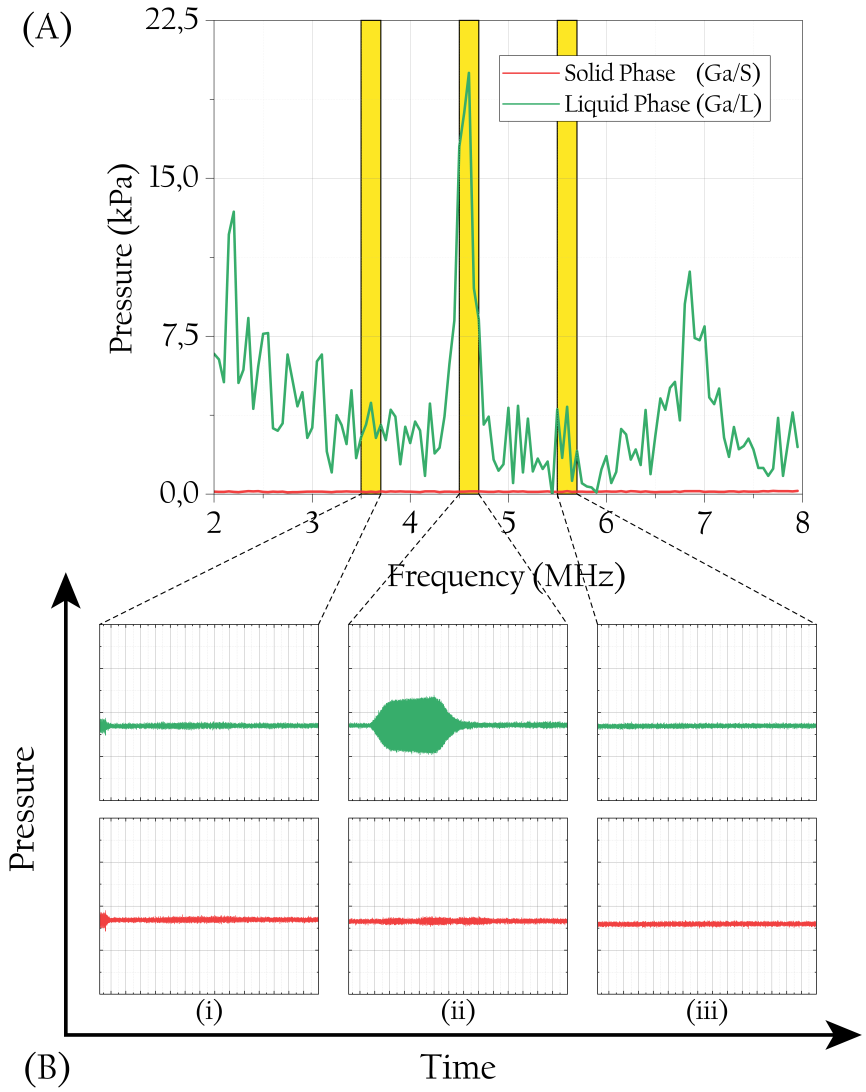

Figure 6.14: Results of the dynamic phononic crystal measurement. (A) The transmission spectrum of the waves transmitted through the phononic crystal where the frequency ranges from 2 MHz to 8 MHz. (B) The time domain characteristics at frequencies (i) 3.6 MHz, (ii) 4.6 MHz, and (iii) 5.6 MHz, which have been Fourier transformed to plot the frequency spectrum of the phononic crystal (A).

element that can reversibly change the transmission from stop pass ultrasound in the MHz regime. The experiments successfully demonstrate reversible switching of a non-mechanical ultrasound filter using pressure pulses of 250 cycles over an effective switching area of 25 mm × 25 mm. We have also demonstrated a reflected metasurface element via an angle specific response to the ultrasound waves. To the best of our knowledge, this is the first demonstration of a metasurface element with reliable and potentially scalable switching. In addition, through a detailed device characterization, we identified the parameters that contribute to device functionality and validated experimentally.

6.6 Towards an Integrated Ultrasound Modulator

To construct a modulator that can shape ultrasound waves it becomes necessary to realize a spatially controllable phase change of Ga. For this we now consider a heater array. The heater devices published thus far, however, have individual heating element on a millimeter length scale [206]. However, the engineering of ultrasound wavefronts in the frequency range of 1 MHz to 5 MHz for underwater and biomedical applications will require elements to be < millimeter (range of 100's of µm). Therefore, independently controlled and spatially micro heaters in 2D arrays are crucial for facilitating the advancement of next-generation active ultrasound metasurface devices or modulators based on the phase change of Ga. The aim is to integrate such a modulator into the beam path of the singular ultrasound transducer which will be highly cost effective with less operational complexity. The material used to generate heat in microheater elements should ideally possess a high melting point, high resistivity, commendable thermal conductivity, and a minimal coefficient of thermal expansion. Common choices for heat-generating materials include Platinum, Tungsten, Molybdenum, and Titanium. Each of these materials has distinct advantages and limitations, which can vary based on their intended application.

Among these, Platinum stands out as a popular option for resistive heating elements due to its high melting point, excellent electrical conductivity, stable chemical properties, and remarkable mechanical characteristics. However, Platinum does not provide an energy efficient solution due to high current requirements. Titanium has a 10× higher resistivity than Platinum which makes it a better candidate for the design of a microheater array. Therefore, Titanium is chosen as the material for the heat-generators. The other important parameters for a microheater are its uniformity, i.e. the constancy of the generated temperature field and the efficiency of the microheater, which directly related to its power consumption. The power consumption of the microheater is directly related to its complex impedance (Z_C) given by,

$$Z_C = R + \iota X \tag{6.17}$$

where the real part R translates to the thermal energy and the imaginary part X to the stored energy. Hence, for maximum power efficieny in a microheater it is important to have a very small imaginary component of the effective impedance. We have selected the architecture of microheater as a double-helix structure which ensures zero contribution of inductance or capacitance to the effective impedance due to opposite direction current flow in adjacent current lines. The double-helix structure further ensures temperature uniformity. The width of the wire in the double-helix structure is 3 µm which is constrained for two reasons; first due to micro fabrication process to con-

struct repeatable and identical devices and second to increase the effective resistance of the microheater which is proportional with the length of double-helix structure. We have fabricated the microheater on silicon dioxide layer due to its insulating properties and relatively poor thermal conductivity.

6.7 Fabrication Protocol

This section of the chapter provides a detailed description of the fabrication process adapted to realize an array of microheaters. The description is supported with schematics that illustrates the fabrication process. The 225 µm × 225 µm heater elements with minimum feature size of 1.5 µm were placed at an intervals of 400 µm in a 32 × 32 matrix structure on the substrate. The substrate is a p-type Silicon (Si) wafer with a thermally grown Silicon Dioxide (SiO_2) (Siegert Wafer Gmbh) with layer thickness of 1 µm to 5 µm thickness. The actual thickness of SiO_2 depends on the method employed for the thermal growth mechanism. The thickness of SiO_2 for wet thermal oxidation mechanism is 5 µm ± 0.5 µm whereas dry thermal oxidation provides a thickness of 1 µm ± 0.1 µm. The width of the heater element with double spiral architecture is 7.5 µm, the width of the power lines is 70 µm, and the dimension of the insulator is 115 µm × 85 µm.

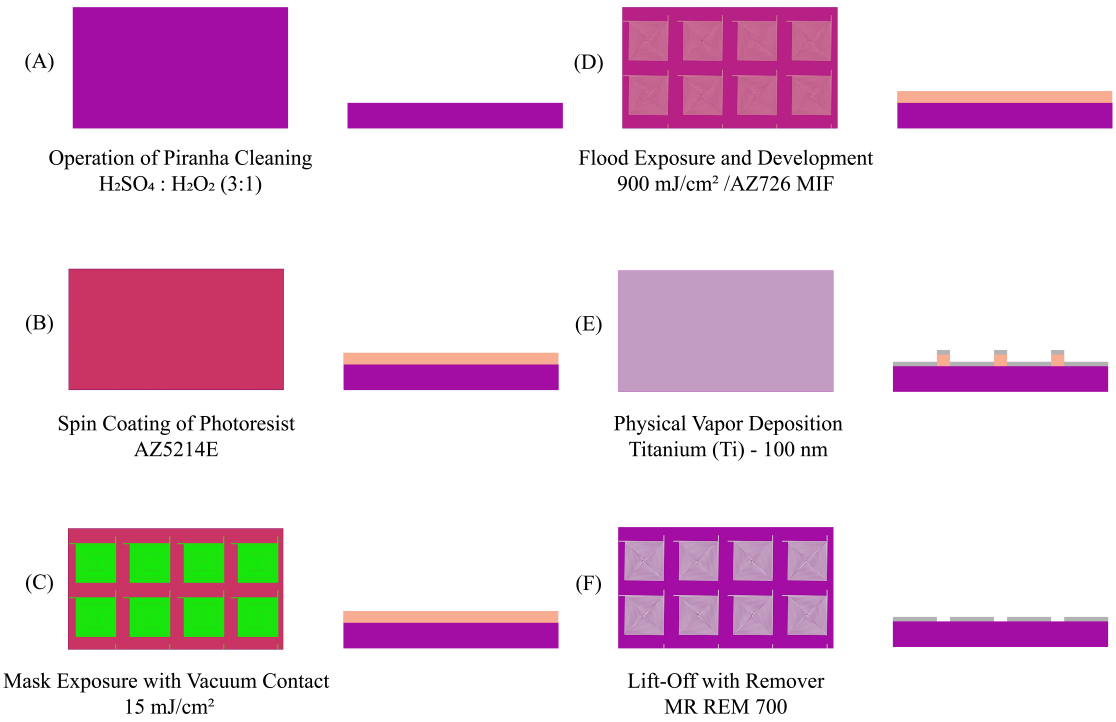

Figure 6.15: Fabrication process flow for 1st layer of the heater array. Left side of the panel shows the top view and right side represents the side view of the device fabrication stage. See text for further details.

The process for addressing individual heater elements is based on row-column indexing architecture. The fabrication of the micro heater device is performed in 4 layers. The complete fabrication process flow is shown in Fig. 6.15, Fig. 6.16, Fig. 6.17, and Fig. 6.18 for the 1st layer, 2nd layer, 3rd layer, and 4th layer, respectively. We have optimized the fabrication parameters of every layer individually to construct the complete device. The 1st layer consists of double spiral heater elements with extended input and output lines, where firstly the operation of piranha cleaning is performed to remove the organic and inorganic impurities as shown in Fig. 6.15 (A). We have used the AZ5214E (Micro Chemicals Gmbh) image reversal photoresist. The photoresist is spin coated at the speed of 6000 revolutions per minute (rpm) for 30 seconds with an acceleration of 500 rpm as shown in Fig. 6.15 (B), which is followed by a pre-exposure bake at 90 °C for 4 min. The photoresist coated substrate is then subjected to ultraviolet (UV) exposure in the MA/BA6 GEN 4 mask aligner (Suss Microtec Gmbh), where the vacuum contact mode has been employed to the chrome mask designed to pattern the array of heater elements. The optimal exposure energy determined to be 15 mJ/cm^2. The substrate is then immediately post-baked at 125 °C for 1 min which is followed by flood exposure at 900 mJ/cm^2. The flood exposure is performed to operate the photoresist in image reversal mode. The main application for this is to cleanly remove the resist structures. In the image reversal baking step, a small improvement of the thermal as well as chemical resistance of the photoresist can be attained which reduces the undercut.

The substrate is then transferred to an electron beam evaporation system (Thermionics) for depositing a thin layer of Titanium (Ti) with a thickness of 100 nm. The Thermionics electron beam evaporation system is a physical vapor deposition technique which utilizes an electron beam to vaporize a source material under high vacuum. This technique of physical vapor deposition is employed because of its compatibility with a wide variety of source materials and well-controlled deposition rates. The deposition is performed at a constant voltage of 8 kV with the filament current stabilized at around 30 mA. We have deposited Ti at an average rate of 0.03 nm/s. It should be noted that the substrate holder is rotated continuously around its normal to ensure uniform deposition on the substrate. The deposition is followed by the lift-off process with MR REM 700; a solvent-based remover for photoresists. The schematic representation of the resultant substrate after the lift-off process is shown in Fig. 6.15 (F). The first layer has provided the double spiral architectured heater elements which is fabricated from Ti, the heater elements are still isolated and not connected to the input and output power lines for electrical and thermal characterization.

The substrate is subsequently ready for the fabrication process of the 2nd layer which is shown in Fig. 6.16. The substrate is firstly cleaned with Iso-Propanol (IPA) in an ultrasound sonicator for 30 minutes. This is an important step to remove the

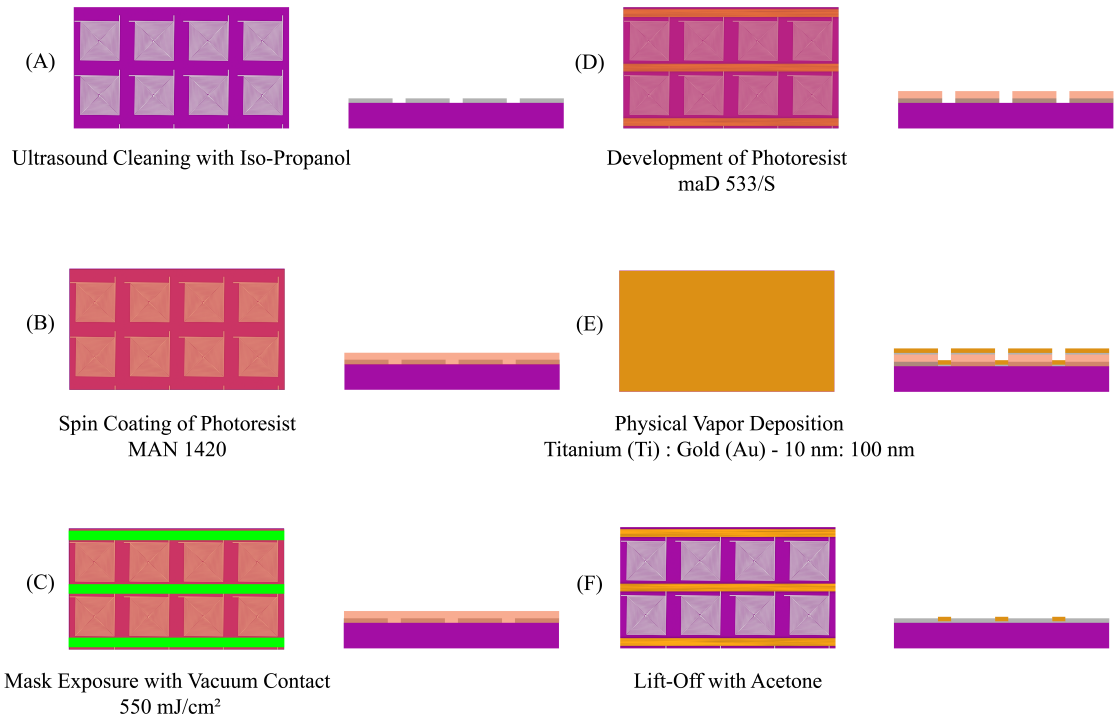

Figure 6.16: Fabrication process flow for 2nd layer of the heater array.

residue of the photoresist and other organic/inorganic impurities from the substrate. The photoresist MAN 1420 (Micro Resist Technology Gmbh) has been employed for the 2nd layer, which is used for the construction of the input power lines to the individual heater elements. Spin coating of MAN 1420 is performed at 3000 rpm for 30 s with an average acceleration of 500 rpm/s. The photoresist coated substrate goes through pre-exposure bake at the temperature of 90 °C for 60 s. The corresponding photomask for pattering the input power lines is irradiated with 550 mJ/cm^2 (Fig. 6.16 (C)). The substrate is vacuum contacted with the mask to provide a good quality alignment and features for photolithography. The development is performed with maD 533/S for 60 s and then subsequently the substrate is transferred for the physical vapor deposition of Ti and Gold (Au) with thicknesses of 10 nm and 100 nm, respectively (Fig. 6.16 (F)). The thin layer of Ti acts as an adhesion layer between SiO_2 and Au. It should be noted that the input power lines are patterned such the the gold lines make contact with the extended input terminal of the heater elements as shown in Fig. 6.16 (F). The lift-off procedure for the photoresist is performed with Acetone and the resulting structure is schematically shown in Fig. 6.16 (F). The photoresist MAN1420 is selected for 2nd layer fabrication due to its higher spin coated thickness of around 2 µm. This thickness is important to uniformly cover the substrate and any sharp features of the 1st layer of fabrication.

The next step in the fabrication process flow is the construction of insulation structures between the input and output power lines. The fabrication process flow for

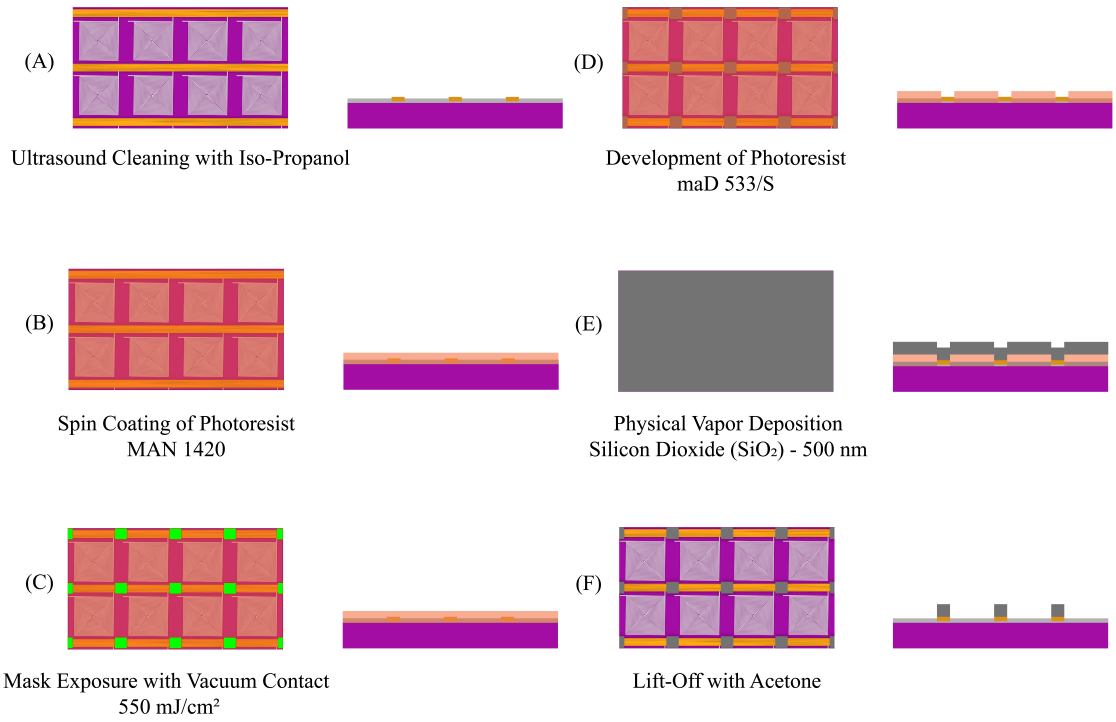

Figure 6.17: Fabrication process flow for 3rd layer of the heater array.

3rd layer is shown in Fig. 6.17. The parameters employed for photolithography process in 3rd layer is identical to the 2nd layer, except the chrome mask which is designed for patterning the photoresist with rectangular shaped isolation structures as shown in Fig. 6.17 (C). The developed sample, as shown in Fig. 6.17 (D), is then subjected to physical vapor deposition of SiO_2. We have deposited 500 nm of SiO_2 to construct isolation crossover joints between the input and output power lines. A particular method of physical vapor deposition called as Glancing Angle Deposition (GLAD) is implemented for the evaporation of SiO_2 material. We have inclined the substrate during deposition at an angle of 45° with respect to the direction of the vapor flux. The inclination is performed to minimize the possibility of constructing sharp edges of SiO_2 across the overlapping regions of the input power line and the crossover joint. We have deposited 100 nm under the inclination to construct smooth angled edges which also reduces the occurrence of defects along the edge. The resulting architecture of the device after the lift-off process with Acetone is shown in Fig. 6.17 (F).

The final layer of the fabrication process flow is responsible to construct the output power lines. The fabrication process flow for the 4th layer is shown in Fig. 6.18. The final layer is patterned with a positive photoresist MAP 1215 (Micro Resist Technology Gmbh). The photoresist is spin coated at a speed of 3000 rpm for 30 s with an acceleration of 500 rpm/s as shown in Fig. 6.18 (B). The pre-exposure bake is performed at 100 °C for 30 s at 35 mJ/cm² where the chrome mask is vacuum contacted with the substrate for good quality alignment and features. The post exposure

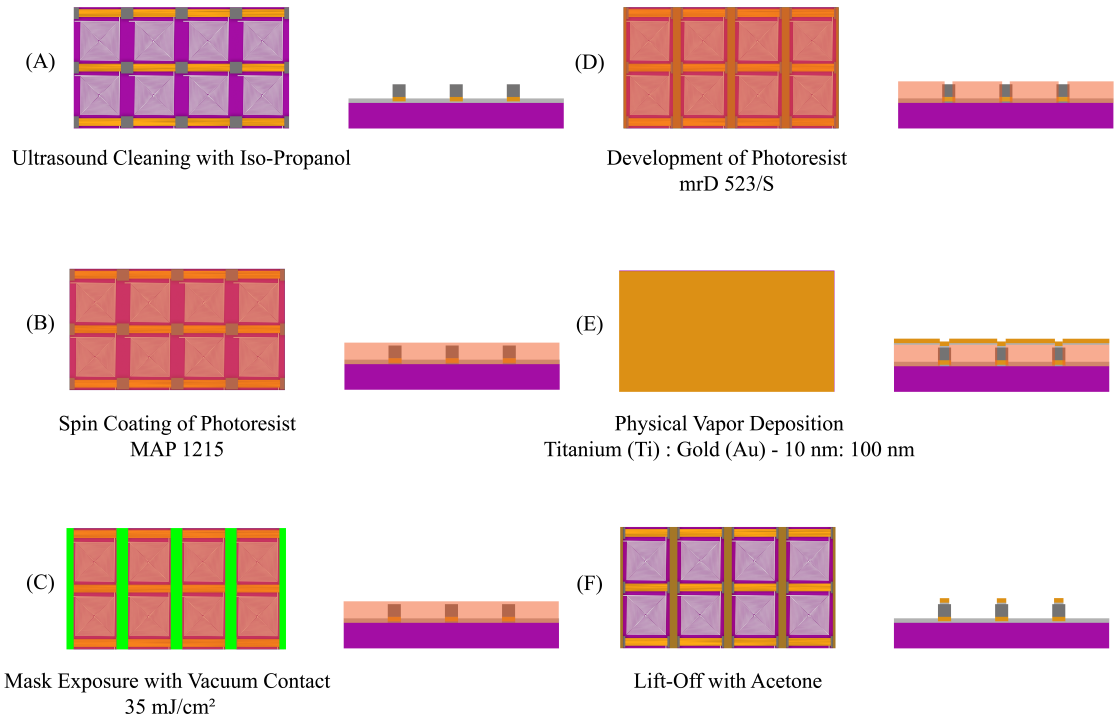

Figure 6.18: Fabrication process flow for 4th layer of the heater array.

substrate is developed with mrD 526/S for 60 s to efficiently remove the exposed photoresist from the substrate. The output power lines are constructed from Ti and Au with the thickness of 10 nm and 100 nm respectively. The substrate is inclined at 45° for the complete deposition to construct connected crossover output power lines over the insulation structures of SiO_2. The material evaporation is followed by the lift-off process which is performed in Acetone similar to MAN 1420 photoresist as shown in Fig. 6.18 (F).

The process flow described in the section has been tested multiple times to validate the repeatability and reliability of the fabrication process and parameters. It should be noted that we have utilized certain photoresists and developers depending on the availability, however the fabrication protocol is not restricted to these chemicals.

6.8 Experimental Results and Discussion

Images of the fabricated devices are shown in Fig. 6.20. Optical microscopy images of the device after the completion of 1st, 2nd, and 3rd layers are shown in Fig. 6.20 (A), (B), and (C), respectively. The magnified SEM images for some particular sections of the device are shown in Fig. 6.20 (D), (E), and (F) which show the double-spiral geometry of the microheater, contact pads, and the crossover junction area of the input and output power lines, respectively. The SEM image of the device is shown in Fig. 6.20 (G). The inset (H) shows the junction crossover area of the device. We have

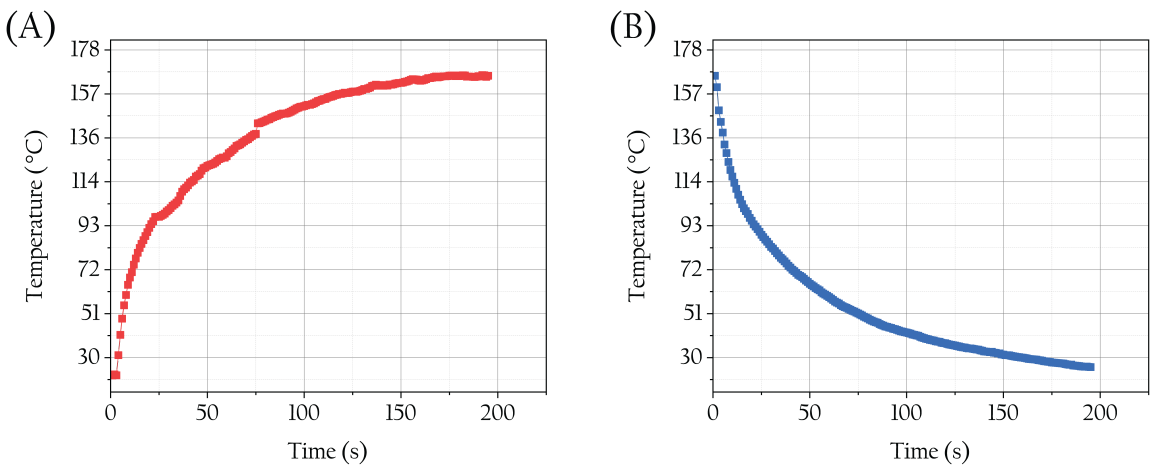

Figure 6.19: Temporal characteristics of a micro heater element when supplied with 130 V DC voltage. (A) Rise in the temperature under constant DC voltage of 130 V as determined by the k-type thermocouple and further verified by the FLIR IR thermal camera. (B) Fall in the temperature of monitored micro heater element when the applied voltage is turned off.

constructed a two-probe measurement system to characterize the electrical properties of the microheater. An image captured by a USB camera while measurements are performed is shown in Fig. 6.20 (I).

The profiles for the rise and fall in temperature as a function of time is presented in Fig. 6.19, for one element of the array with an applied voltage of 130 V DC for 200 s. The temperature initially rises steeply but then the heating rate decreases as the heater equilibrates with the surrounding air. It should be noted that the high temperature of 150 °C is not required for the intended application of ultrasound modulation with Ga. The experiments at such high temperature are performed to test the robustness and stability of the device in handling high electrical power. The experimental results clearly validate that the heater array is robust.

It is important that the response of the microheater element should principally depends on the applied voltage at the steady state but independent on the transient characteristics of the voltage. We have validated the voltage dependence by increasing the applied voltage from 20 V to 130 V with a step size of 10 V. We have provided the DC step voltage for around 300 s so that the temperature of the microheater element reaches a steady state as shown in Fig. 6.21 (A). The temperature stabilizes after about 100 seconds, resulting in a uniformly distributed temperature field with no specific hot spots. Figure 6.21 (B) illustrates the temperature scale relevant for ultrasound modulation, highlighted by a black rectangular outline in Figure 6.21 (A). Although some heat conduction towards the exterior occurs due to the temperature difference, the low thermal conductivity of the material mitigates thermal diffusion. To further investigate the uniform heating capability, we utilized a thermal camera (FLIR

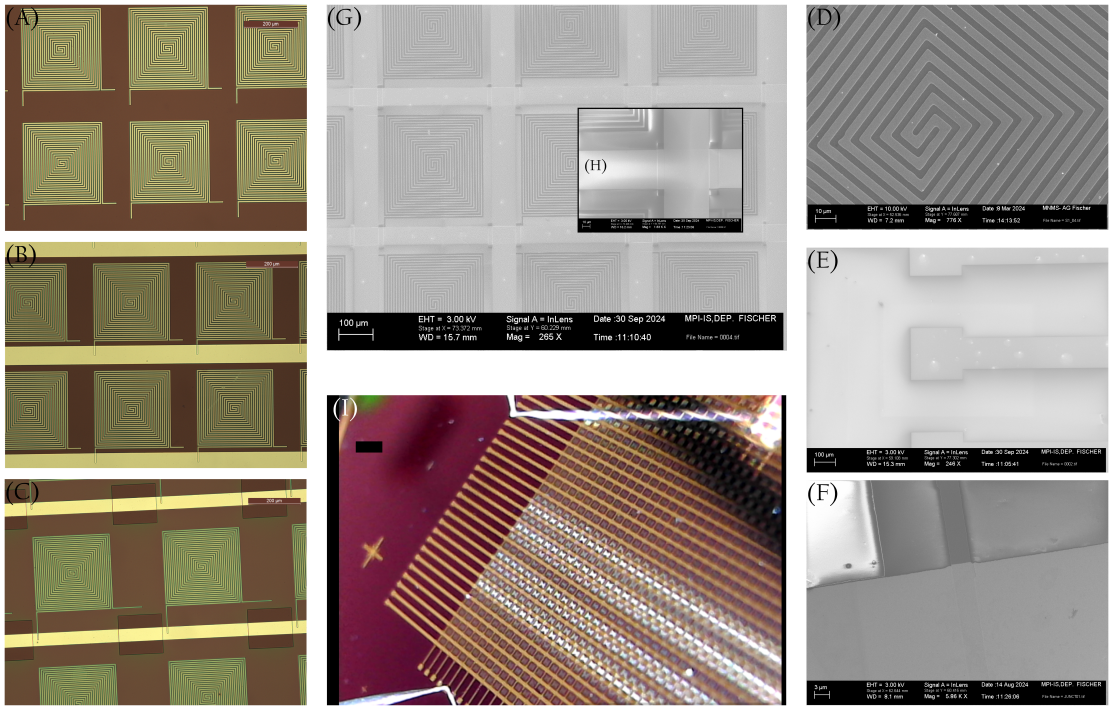

Figure 6.20: Optical and Scanning Electron Microscopy images of the micro heater array at different stages of the fabrication process. Optical microscopy images of the device after the completion of (A) 1st layer, (B) 2nd layer, and (C) 3rd layer. Magnified electron microscopy images of (D) double-spiral microheater (E) contact pads for external characterization and power supply (F) crossover junction of input and output power lines. (G) Electron microscopy image of the device after completion of the device fabrication process where inset (H) shows the crossover junction of input and output power lines. (I) Image captured by a camera during the electrical characterization of the device using a two-probe setup. The scale bar in (I) represents a length of 1 mm.

A65) capturing images at a rate of 30 frames per second. Snapshots taken at various time intervals are presented in Figure 6.22. Impressively, over 85% of the heated area sustains temperatures above 90% of the maximum temperature throughout the entire overlapping region. This suggests that the microheater can achieve a consistent temperature distribution across multiple target locations, supporting complex spatial heat distribution.

6.9 Design of Digitally Controlled Electronics Board

The microheater array is fabricated using a row-column addressing architecture. This section of the chapter introduces the electrical architecture of the board designed to individually address the microheater elements of the array. The schematic of the digitally controlled electronics board is shown in Fig. 6.23. The primary function of the board is to control the high voltage (V_{CC}) channel switch with a low voltage (V_{SS}) digital control. The board includes a demultiplexer, parallel-in/serial-out shift

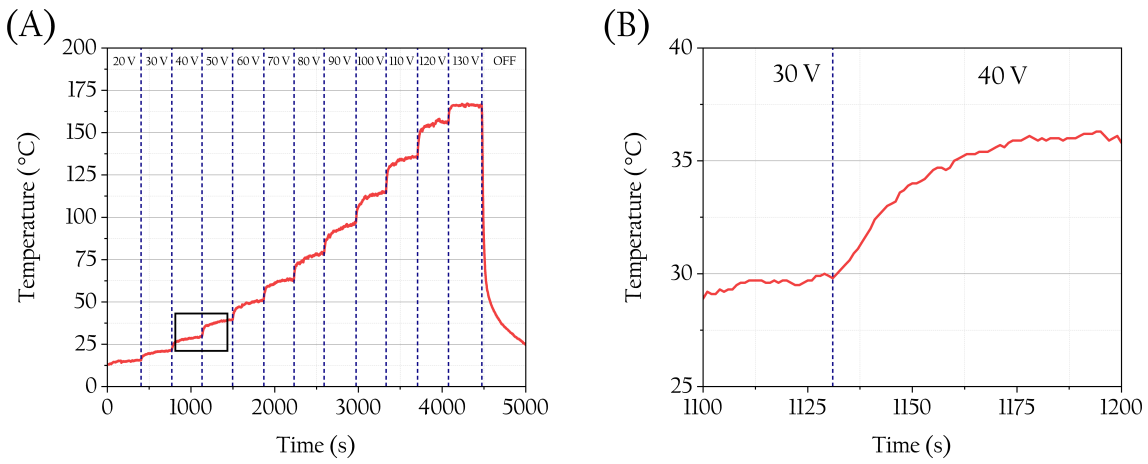

Figure 6.21: Temperature profile of the micro heater element operated under step voltage increment of 10 V. (A) Variation in temperature of the micro heater when the applied voltage increases from 20 V to 130 V with step size of 10 V. (B) The magnified section of (A) marked with black outlined box showing the temperature profile when the applied voltage increased from 30 V to 40 V which corresponds to the phase transition temperature of Ga.

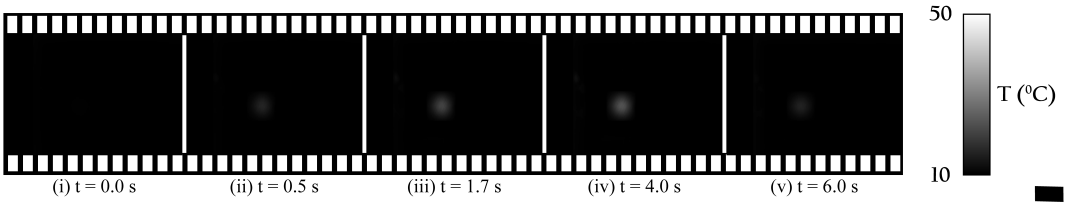

Figure 6.22: Images recorded by a FLIR IR thermal camera at different time instants. The temperature of a single microheater element was increased from 20 °C to 50 °C and then decreased to the initial temperature. The scale bar represents the length of 1 mm.

register and a serially addressed high voltage 1:1 channel switch. The schematics of Fig. 6.23 show the operation to control a 2×2 micro-heater array which is a scaled-down analogue of the actual 32×32 microheater array. The constructed board is then externally connected to the on-chip contact pads to drive the integrated microheater array.

The first component of the board is a 1:4 demultiplexer which operates via a four-stage combination logic function and reduces the number of terminals required to drive the array, from 4 to 2. The input control terminal shown in Fig. 6.23 takes the 2-bit code to switch the low-to-high state of the terminals D_0, D_1, D_2, and D_3. The truth table of the demultiplexer is shown in Table 6.5. The output of the demultiplexer is connected to the 4-bit shift-register which operates with a parallel-in/serial-out architecture. The shift register reads the input $D_3D_2D_1D_0$ in parallel and writes the bits in a serial manner at the output with the positive edge of the clock signal (CLK).

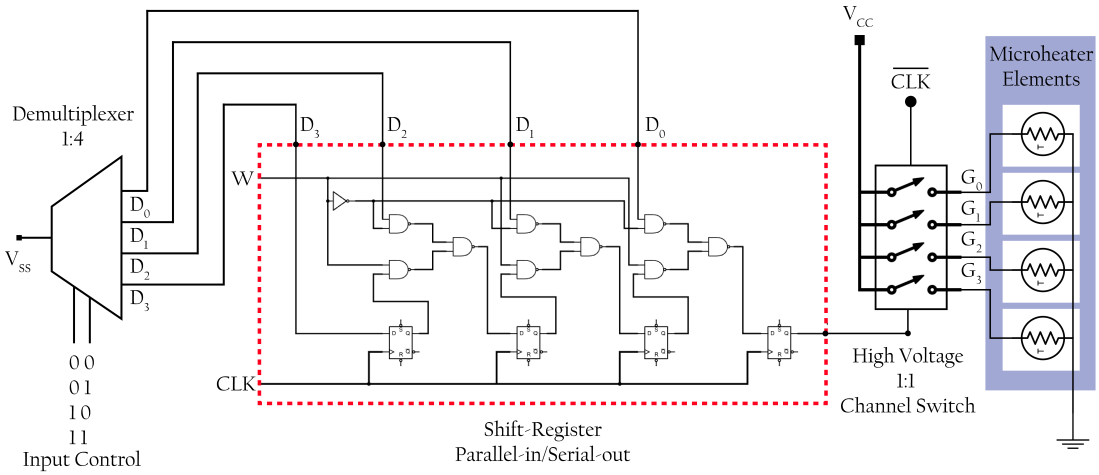

Figure 6.23: Schematic diagram of the electrical circuit designed for independent row-column addressing of the heater array.

The write input signal (W) should be high for the operation of the shift-register. The shift register takes N clock cycles to shift and write the N-bit data at the output. The output of the shift-register drives the high voltage 1:1 coupled channel switch. The device has 4 independently selectable 1:1, single-pole, single throw (SPST) switch channels. It supports bidirectional analog and digital signals on the source (V_{CC}) and drain (G_X; $X = 0, 1, 2, 3$) terminals. The 4-channel switch operates at the negative edge of the clock cycle which is contrary to the shift register, but is important for the synchronous operation of the 4:1 shift register and 4-channel switch.

Input Control	Active Terminal ($V = V_{SS}$)	$D_3D_2D_1D_0$
00	D_0	0001
01	D_1	0010
10	D_2	0100
11	D_3	1000

Table 6.5: Truth table of the demultiplexer.

Serial Input	Switch Connect
0001	G_0
0010	G_1
0100	G_2
1000	G_3

Table 6.6: Truth table of the high voltage 4-channel switch.

The truth table of the 4-channel switch is shown in Table 6.6. The negative edge of the clock feeds the input of the switch to the integrated shift registers for controlling each of the 4 switches independently. It reads the 4 inputs and correspondingly opens the channel such that the V_{CC} connects directly to the on-chip microheater element

as shown in Fig. 6.6. The board therefore takes the input in 2-bit code and operate individually the 2×2 microheater array. Thus, the board takes a 32-bit code as the input for digital and individual addressing of elements in the 32×32 microheater array. The following electronics components are used in the construction of the board:

- Demultiplexer - CD74HC4067M (Texas Instruments)
- Shift-Register - SNLS674 (Texas Instruments)
- High Voltage Channel Switch - TMUX9616 (Texas Instruments)

The 32-bit demultiplexer takes a 5-bit code for the input control which then requires a 5-bit shift register for the operation. The commonly available shift-registers are in the order of 2^i bits (where i is an integer digit). Therefore, two 16:1 demultiplexers are selected for the operation (CD74HC4067M from Texas Instruments). The demultiplexer has a low ON resistance and low OFF leakages. In addition, these devices have an "enable" control that, when high, disables all switches (OFF state). A 16-bit shift register SNLS674 from Texas Instruments is selected to serially write the parallel input at the output. The storage register is connected in a parallel data loop with the shift-register and may be asynchronously cleared by taking the store-clear (STRCLR) input low. It provides a provision of chip-select (CS) input which disables both the shift-register clock and the storage register clock and places the output (Q15) in the high impedance state which prevents the high throughput current to the microheater elements.

The TMUX9616 from Texas Instruments is a 16-channel low resistance, low capacitance high-voltage analog switch integrated circuit with latch-up immunity. Each device has 16 independently selectable switch channels. The device is rated to operate safely with dual supplies up to $\pm 110\,\mathrm{V}$ which can belong either to the category of digital or analog signals. This provides the capability of the board to operate the microheater elements with AC or DC voltages. The maximum clock speed of the entire board is $4.5\,\mathrm{MHz}$ which is calculated based on the clock speed of individual components of the board. The architecture of the printed circuit board is designed in the software KiCAD 6.1 which is shown in the Fig. 6.24 (A). The layout is based on a 4-layer design. The board is fabricated by Eurocircuits Gmbh and the components have been assembled in the laboratory using soldering tools. A schematic of the assembled board is shown in the Fig. 6.24 (B) where the placement of the components namely, CD74HC4067M, SNLS674, and TMUX9616 are presented in a box with white boundary. The input control terminals are also shown which are connected externally with a programmable multichannel digital output supply. The digital inputs can be provided through Arduino microcontrollers or National Instruments devices. We have used Arduino Mega 256 microcontrollers for the operation of the electronics board,

but the DC power supply for the integrated circuit are supplied separately from the power connectors shown in Fig. 6.24 (B). We have soldered a LPC 6/3-ST-7.62 PCB connector (Phoenix Contact) on the board for supplying DC voltage to the individual components of the board which also includes the high voltage power supply for the microheater array.

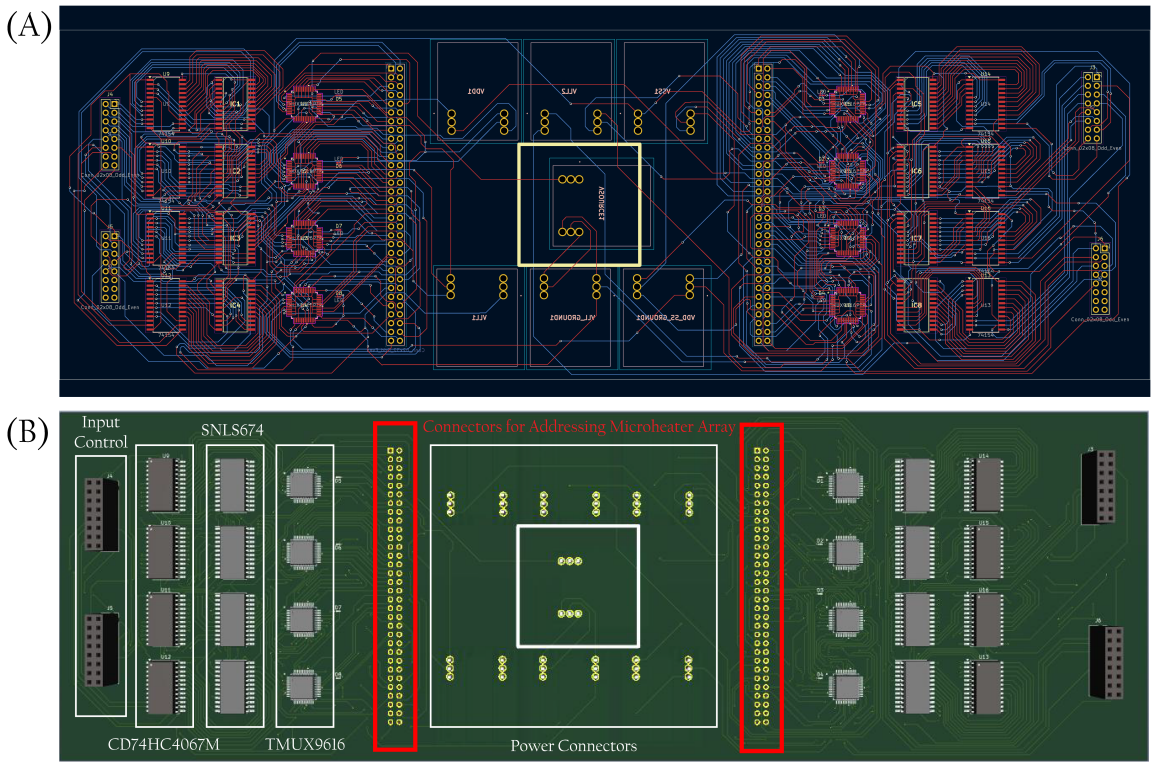

Figure 6.24: Schematic diagram of the electrical circuit designed for independent row-column addressing of a 32×32 heater array.

6.10 Operation of Microheater Array

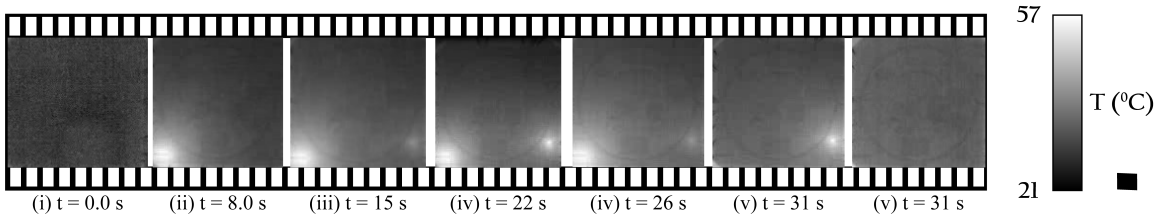

Figure 6.25: Images recorded by a FLIR IR thermal camera at different time instants. The temperature at multiple locations of the microheater array was independently set from 23 °C to 55 °C and 40 °C and then decreased to the initial temperature. The scale bar represents the length of 3 mm.

The spatially modulated thermal functionality includes localized heat generation and the operation of a pixelated array which is designed to generate complex thermal

outputs. The capability to generate thermal patterns through row/column addressing using the controller is demonstrated in Fig. 6.25. The demonstration shows the infrared images of the independent operation of two regions in the microheater array. The first region 'I' consists of a 2×5 sub-array of microheater elements and the size of the second region 'II' is 2×2. The target temperature for the 'I' and 'II' region is 55 °C and 40 °C respectively. The time-indexed frames clearly present the controlled temperature operation in region 'I' and 'II'. The method to generate the target pattern is achieved through the control of the total number of clock cycles and the duration of operation. The input control code is repeatedly executed in a continuous manner to activate the target temperature in the region. The control process is already described in detail in the previous section. The high voltage channel switch in the controller has been supplied with a constant voltage (V_{CC}) of 75 V and the board is operated with a 100 Hz clock (CLK). The pixel elements in region 'I' and 'II' are applied with 8 and 5 clock cycles, respectively, for one second of operation. The optimization of the number of applied clock cycles and the frequency of the clock has been carried out for the target spatial distribution of the temperature. The microheater array operated with precision, as each pixel was activated only when the voltage (V_{CC}) was sent to the horizontal electrodes via the driving signal line. Concurrently, the vertical electrodes were linked through the ground signal line. This setup created a notable temperature difference of over 25 °C between the activated and inactive pixels, attributed to minimal thermal diffusion and concentrated heating. As a result, distinct and clear thermal patterns emerged as shown in Fig. 6.25. The independent operation has been

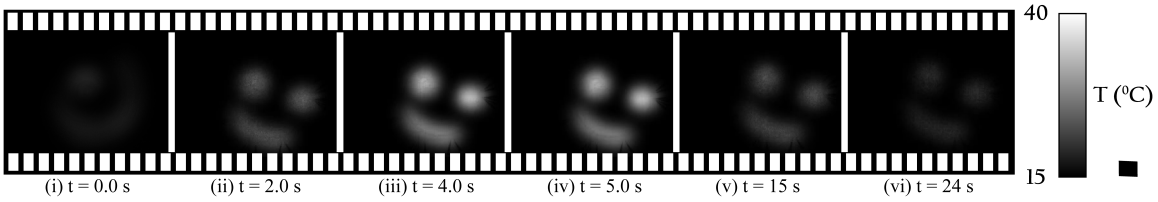

Figure 6.26: Images recorded by a FLIR IR thermal camera at different time instants. The spatial thermal profile shaped in the pattern of 'smiley face' where the temperature is increased from 21 °C to 38 °C and then decreased to the initial temperature. The scale bar represents the length of 3 mm.

demonstrated but it is also important to achieve 2D spatial distribution of constant temperature in a complex profile. The 2D spatial distribution is necessary for the ultrasound modulation using phase change material which was the primary motivation to build the integrated microheater array. Hence, a 2D thermal pattern in the shape of 'smiley face' has been programmed and demonstrated in the Fig. 6.26. A voltage of 50 V is applied to the driving signal line of the high voltage channel switch for the described operation. The frequency of the clock signal is 1 kHz which sequentially applies the voltage to the programmed pixel element. The temperature difference

between the activated and deactivated pixels is around 20 °C where the lower temperature of the FLIR camera has been set to 15 °C for a clear observation of the thermal pattern. The IR images recorded with the FLIR camera are shown at different time instants in Fig. 6.26 and clearly show the spatially modulated thermal pattern. The experimental results shown for the functioning of microheater array evidently proves that even for localized heating at high temperature of 150 °C, the microheater array maintains its thermal function, permits localized heating and row/column addressing without any dielectric breakdown, so the constructed microheater array is suitable for its intended application as an ultrasound modulation device with high resolution.

6.11 Future Work and Outlook

This work introduced Ga due to its low temperature liquid to solid phase transition. A phononic 1-D stack constructed from Cu and Ga plates, demonstrates that the phase transition allows a stop band to be modulated in the MHz regime. A numerical simulation model was built using k-wave to calculate the attenuation and transmission zone in the frequency range from 2 MHz to 8 MHz. 1D amplitude wave transmission measurements were carried out to verify the tunability of the bandgaps. By combining numerical simulations, it is shown that the proposed phononic crystal stack switches from a bandpass to a bandstop device. The results indicate that the phase transition induces a neat 100% modulation of the transmitted wave. The underlying mechanism is that the local resonances in the solid-liquid interface generate a pass band for certain frequencies. The findings suggested a novel approach to realize tunable acoustic devices which may be of interest for wave suppression, wave guiding, or wave filtering. Specifically, we have fabricated a heater array that is designed for the spatial thermal modulation of ultrasound in combination with Ga. The heater array should now be combined with Ga to demonstrate the dynamic modulation of the ultrasound wavefront. We have presented the experimental results for the electrical and thermal characterization of the microheater array device. In future work, we will construct a circuit architecture for complex patterning of spatially distributed heating which would then allow the realization of an electrically controlled 32×32 modulation of ultrasound waves (amplitude/phase).

7 Conclusion and Outlook

This thesis describes several results in the field of physical acoustics. First, an approach to render acoustic manipulation more practical. Then, two new approaches to generate and control complex ultrasound fields are demonstrated. In this thesis we developed an approach of directed assembly and manipulation using secondary Bjerknes forces through multiple strongly-interacting bubble arrays. To the best knowledge of the author this is the first time that the secondary Bjerknes force has been considered for selective assembly in a pre-programmed manner. The derived analytic formula proved to be consistent with experimental results for the microbubbles array. Traditionally, the forces that scatter bubbles are relatively weak. However, the findings presented in Chapter 3 demonstrate that using arrays of bubbles can significantly enhance the interaction strength, achieving an increase of up to 25× compared to the interactions of individual bubble pairs. The advantages of bubble arrays stem from the long-range interactions that the Bjerknes force facilitates, which enables greater force generation in macroscale systems and in some cases can even exceed that found in similar magnetic systems. The method was used to demonstrate the manipulation of centimeter scale objects on a wafer surface triggered by the µN-scale forces generated by 11×11 microbubbles arrays embedded in the objects. The assemblies develop almost instantly when an external sound field is applied, and they continue to exist as long as that sound field is present. This demonstrates the switchable nature of the proposed technique. The theoretical predictions about the forces and motion dynamics correlate well with experiment results. We anticipate that the dynamic acoustic radiation forces technique could be scaled up for larger systems, though it may exhibit slower dynamics due to increased drag. Limits on size will be determined by the buoyancy of the floating structure. While our current demonstrations focus on larger structures measured in centimeters, we believe that reducing the size of bubbles and arrays will enable the assembly of structures in the millimeter range. This all-acoustic method, which employs bubble arrays for manipulating and assembling macrostructures, can be enhanced with position-sensitive optical observations for con-

tactless manipulation and control. This approach opens up exciting possibilities for applications in manufacturing, soft robotics, and microfluidics. Future research could delve into the behavior of sign reversal at close range and explore the use of 3D bubble structures.

The dynamic acoustic fields are important for many applications. Nobel laureate K.F. Braun first proposed the concept of a phased array in 1905 and since then phased arrays have become a powerful tool to shape waves. The field of ultrasound has been greatly benefited by this invention, however, most Phased Array Transducers (PATs) are restricted to a few hundred elements, which limits the ability to shape complex ultrasound beams. Thus far there is no scalable approach to power and control PATs. This thesis for the first time demonstrate a completely novel and potentially scalable technique which is based on control with light and termed: Optically Programmable Array of Transducers (OPATs). Light intensity is used to control the individual phases of transducer elements. This technique dramatically simplifies the driving circuitry where now a single power amplifier independently drives all the transducer elements. It is also demonstrated that the electrical architecture does not need a separate clock circuit, because the signal driving each transducer is inherently phase synchronized. The OPATs are controlled by an analog circuit for high frequency operation based on photoresistive elements coupled with passive electronic devices in a cascaded architecture. The electrical circuit converts an optical intensity into a precisely phase shifted electrical signal, and permits the phase to be continuously tuned achieving a phase shift of up to 2π. This is in contrast to current architectures, which do not provide a net phase shift of 2π and which further operate with low tuning resolution ($> 22.5°$). The optically controlled array of transducers provides a simple analog design which comes with optical addressability and superior phase control. This technique in future can pave the way for scalable transducer arrays and the generation of high-intensity, spatially-complex ultrasound fields dynamically. After receiving different light patterns wirelessly, the OPATs can generate phase patterns. We demonstrate a multifocal ultrasound wavefront, spherical diverging wavefronts, locally addressable complex phase wavefront and a phase gradient vortex beam with video rate (100 Hz) updating capability. In future, it will be of interest to demonstrate a very large array, however, it remains challenging to increase the number of transducer elements to more than several hundred that is why this thesis also considered a material-based modulator.

Lastly, the thesis presents the concept of ultrasound modulator which is inspired by the spatial light modulator which shapes optical wavefronts. Modulation of ultrasound is discussed to be enabled through a local change in the ultrasound wave properties. The thesis discussed various material systems which have been researched and, or experimented with the possibility to develop the ultrasound modulator. Addi-

tionally, the applications, possibilities and problems are presented to distinguish the materials to effectively modulate the local properties of ultrasound. However, ultrasound interact weakly with materials and so it is challenging to find materials that can be used to modulate the sound speed by much. A promising candidate is a phase change material based on gallium. The acoustic properties of Ga is discussed and measured experimentally.

A functioning of metasurface element for the MHz regime based on Ga is developed. A stack of Ga and Cu has been shown to pass or stop ultrasound as a function of temperature. This constitutes a proof-of-concept demonstration of a dynamic 1D phononic metamaterial. To extend the work such that a 2D modulator may be realized, a microheater array is fabricated. The heater array which is necessary to construct a modulator to shape ultrasound waves. The electrical characterization of the microheater is presented and the independent operation of individual elements of microheater array is accomplished through a row-column addressing architecture. The robustness of the microheater design is validated by operating the device at a high temperature (150 °C). The combination of a suitable holder for Ga and the microheater array should allow the realization of a functional ultrasound modulator device which would be able to create complex ultrasound wavefronts dynamically through local change in the phase of transmitted ultrasound waves. This will be the topic of future research.

Acknowledgements

Pursuing a doctorate (PhD) has been more than just an academic challenge for me; it has been a transformative journey that has fostered both my professional and philosophical growth. I owe a profound debt of gratitude to my mentor, Prof. Dr. Peer Fischer. His encouragement to explore innovative ideas (but I must say very difficult for brain cells) has been invaluable. Under his guidance, I have successfully navigated the complexities of research while sharpening my analytical skills. I was particularly inspired by an article in *Nature* by Prof. Gundula Bosch [207], who highlights the importance of reintroducing philosophy into the realm of doctoral studies. I genuinely believe that Prof. Dr. Peer Fischer embodies the philosophical foundation that young researchers should cultivate to become critical thinkers in the scientific community. He created an incredibly supportive and intellectually invigorating environment where discussions went far beyond just science. The fresh insights and perspectives he shared were vital not only to my thesis but also to my life journey. From the instant I encountered him, it was clear that I was with someone truly remarkable. Over time, he evolved into not just a dependable mentor but also a cherished friend, standing by me during countless moments of stress throughout my studies. I want to take this opportunity to sincerely apologize for all those countless times/ for all the troubles/ for all the schwachsinnig Dinge but I think the patient needed the medicine and who is a better doctor than him!. He truly embodies the spirit of his name, "Peer". I'm so grateful to him for inviting me to be a part of the MNMS group—what an opportunity it has been!

I also want to extend my sincere thanks to the rest of my thesis committee for their invaluable comments and guidance. I am **very**$^{\infty}$ thankful to Dr. Kai Melde for million reasons but lets keep the context constrained to this thesis. It is hard to believe but I must say that he was the only person in the lab who could teach me Angular Spectrum method. I tried to get lesson from many colleagues but somehow I was not following the intricacies of the method. Thank you Kai! Thank you very much!

because without me understanding Angular Spectrum method this thesis would not have existed!.

It's time to acknowledge a great philosopher and a brilliant scientist with whom I had the privilege to work; Prof. Dr. Zhichao Ma, who was then a fellow postdoctoral researcher, was a constant source of encouragement. He provided me with the space to explore and evaluate some of my early ideas, which ultimately paved the way for this work. I will always remember and appreciate the support I received throughout this process! I am very thankful to my collaborator Dr. Marc Fournelle for providing the transducer array for the experiments discussed in this thesis. Thank you! Marc.

I am also deeply thankful to Dr. Athanasios Athanassiadis, who taught me the experimentation related to ultrasound and always answered my naive questions in the field which kept my interest in ultrasound engineering. I want to take a moment to acknowledge the invaluable contributions of him to my overall knowledge, especially in the field of ultrasonics. His unwavering support and belief in my academic endeavors have been crucial to my achievements. I am very grateful to Dr. Athanasios Athanassiadis for teaching me k-wave simulations with patience. The research presented in this dissertation represents not only my efforts but also the collective encouragement from everyone who has influenced my academic and personal journey. Through this experience, I've learned the significance of asking questions and embracing diverse perspectives to deepen our understanding of complex scientific and engineering challenges.

I express my profound gratitude to the present and past administrations of Max Planck Institute for Intelligent Systems, Stuttgart, Max Planck Institute for Medical Research, Heidelberg and Heidelberg University, Heidelberg. I want to thank the entire MNMS group for making me whom I am today. My time at the Max Planck Institute would not be enjoyable at all without all my brilliant, beautiful and handsome co-workers. Thank you all for the support, laughter, and memories! Thank you , Alejandro Pasoda, Alexander Song, Björn Miksch, Cornelia Miksch, Dandan Li, Eran Oren, Eunjin Choi, Florian Peter, Hannah Barad, Hyunah Kwon, Ida Saskia Bochert, Jan-Philipp Gunther, Johannes Sachs, Kai Melde, Lovish Gulati, Lucie Motyckova, Mariana Alarcon-Correa, Minghui Shi, Moon-Kwang Jeong, Nicolas Moreno Gomez, Nikhilesh Murty, Prof. Dr. Tian Qiu, Prof. Dr. Xiaolong Lu, Dr. Oscar Demeulenaere, Dr. Jianfeng Li and anyone I might have forgotten!! I don't know whether it would be possible in future but Dr. Oscar Demeulenaere should receive an OSCAR for BEST WRITER (Lab Manuals).

Thank you Lucie Motyckova, Mariana Alarcon-Correa, Corina Scalet, Nikhilesh Murty, Stephie Casale, and Simone Tsoneva for deep conservations about life. Your support means a lot to me and I could not have done it without you! ALL because you guys were there when I needed someone the most. Thank you Moonkwang Jeong

for taking me to vacations in different parts of Europe with different people everytime. Thank you Mariana Alarcon-Correa for trusting me with your beautiful and handsome kids namely; Victoria and Federicho respectively. Thank you Victoria and Federicho for reminding me the things that I should always remember in life. Thank you Dr. Alexander Song for coming with me to uuuhmami many times in the evening.

Thank you Helen Jade, Tine Limberg, Sadena Aguilas Gonzalez, and Danique Nakken for accompanying me to lunch so that I don't eat alone. I will never forget this kind gesture and I wish you guys the best from the bottom of my heart. I was taught an important lesson of my life which I will try to remember; "work is not my identity" by three most beautiful human beings, namely; Dr. Anuradha Jain, Dr. Daniel Scholch, and Dr. Gudrun Maria Henemann. Thank you!! I am very fortunate to have people like you around me during the course of my PhD. The acknowledgment section of this thesis would be incomplete without sincerely thanking Corina Scalet once more!!, so Thank you Corina Scalet. Thank you ALL for everything! and I am very sorry for somethings.

Bibliography

[1] C. Kittel, *Introduction to Solid State Physics*. John Wiley and Sons, 1976.

[2] N. W. Ashcroft, N. D. Mermin, *et al.*, *Solid State Physics*. Holt, Rinehart and Winston, New York, 1976.

[3] T. Yang, Y. Jin, B. Squires, T.-Y. Choi, N. B. Dahotre, and A. Neogi, "In-situ monitoring and ex-situ elasticity mapping of laser induced metal melting pool using ultrasound: Numerical and experimental approaches," *Journal of Manufacturing Processes*, vol. 71, pp. 178–186, 11 2021.

[4] A. Buch and A. International, *Pure Metals Properties: A Scientific-technical Handbook*. ASM International, 1999.

[5] K. G. Kshetri and N. Nama, *Basic Theories and Physics of Acoustic Technologies*, pp. 37–66. Wiley, 12 2023.

[6] T. Freegarde, *Introduction to the Physics of Waves*. Cambridge University Press, 11 2012.

[7] M. Mehta, J. Johnson, and J. Rocafort, *Architectural Acoustics: Principles and Design*. Prentice Hall, 1999.

[8] X. Lurton, *An Introduction to Underwater Acoustics: Principles and Applications*. Geophysical Sciences Series, Springer, 2002.

[9] D. T. Blackstock and A. A. Atchley, "Fundamentals of physical acoustics," *The Journal of the Acoustical Society of America*, vol. 109, pp. 1274–1276, 4 2001.

[10] A. P. Sarvazyan, M. W. Urban, and J. F. Greenleaf, "Acoustic waves in medical imaging and diagnostics," *Ultrasound in Medicine & Biology*, vol. 39, pp. 1133–1146, 7 2013.

[11] Y. Muanenda, "Recent advances in distributed acoustic sensing based on phase-sensitive optical time domain reflectometry," *Journal of Sensors*, vol. 2018, pp. 1–16, 2018.

[12] T. Laurell and A. Lenshof, eds., *Microscale Acoustofluidics*. The Royal Society of Chemistry, 12 2014.

[13] S. Jiménez-Gambín, N. Jiménez, and F. Camarena, "Transcranial Focusing of Ultrasonic Vortices by Acoustic Holograms," *Physical Review Applied*, vol. 14, p. 054070, Nov. 2020.

[14] A. Lee, "The third decade of microfluidics," *Lab on a Chip*, vol. 13, p. 1660, 2013.

[15] R. Hajar, "The art of listening," *Heart Views*, vol. 13, p. 24, 2012.

[16] H. Bruus, J. Dual, J. Hawkes, M. Hill, T. Laurell, J. Nilsson, S. Radel, S. Sadhal, and M. Wiklund, "Forthcoming lab on a chip tutorial series on acoustofluidics: Acoustofluidics—exploiting ultrasonic standing wave forces and acoustic streaming in microfluidic systems for cell and particle manipulation," *Lab on a Chip*, vol. 11, p. 3579, 2011.

[17] M. Wu, A. Ozcelik, J. Rufo, Z. Wang, R. Fang, and T. J. Huang, "Acoustofluidic separation of cells and particles," *Microsystems & Nanoengineering*, vol. 5, p. 32, 6 2019.

[18] F. Guo, P. Li, J. B. French, Z. Mao, H. Zhao, S. Li, N. Nama, J. R. Fick, S. J. Benkovic, and T. J. Huang, "Controlling cell–cell interactions using surface acoustic waves," *Proceedings of the National Academy of Sciences*, vol. 112, pp. 43–48, 1 2015.

[19] K. Melde, H. Kremer, M. Shi, S. Seneca, C. Frey, I. Platzman, C. Degel, D. Schmitt, B. Schölkopf, and P. Fischer, "Compact holographic sound fields enable rapid one-step assembly of matter in 3d," *Science Advances*, vol. 9, 2 2023.

[20] O. Jakobsson, C. Grenvall, M. Nordin, M. Evander, and T. Laurell, "Acoustic actuated fluorescence activated sorting of microparticles," *Lab Chip*, vol. 14, pp. 1943–1950, 2014.

[21] W. Qiu, J. H. Joergensen, E. Corato, H. Bruus, and P. Augustsson, "Fast microscale acoustic streaming driven by a temperature-gradient-induced nondissipative acoustic body force," *Physical Review Letters*, vol. 127, p. 064501, 8 2021.

[22] A. Salari, S. Appak-Baskoy, I. R. Coe, J. Abousawan, C. N. Antonescu, S. S. H. Tsai, and M. C. Kolios, "Dosage-controlled intracellular delivery mediated by acoustofluidics for lab on a chip applications," *Lab on a Chip*, vol. 21, pp. 1788–1797, 2021.

[23] *Physical Acoustics*. Elsevier, 1964.

[24] S. Sherrit, H. D. Wiederick, B. K. Mukherjee, and M. Sayer, "An accurate equivalent circuit for the unloaded piezoelectric vibrator in the thickness mode," *Journal of Physics D: Applied Physics*, vol. 30, pp. 2354–2363, 8 1997.

[25] "Ieee standard on piezoelectricity," 3 1987.

[26] D. A. BERLINCOURT, D. R. CURRAN, and H. JAFFE, *Piezoelectric and Piezomagnetic Materials and Their Function in Transducers*, pp. 169–270. Elsevier, 1964.

[27] T. Ikeda, *Fundamentals of Piezoelectricity*. Oxford science publications, Oxford University Press, 1996.

[28] X. Zeng and R. J. McGough, "Optimal simulations of ultrasonic fields produced by large thermal therapy arrays using the angular spectrum approach," *The Journal of the Acoustical Society of America*, vol. 125, pp. 2967–2977, 5 2009.

[29] K. Melde, A. G. Mark, T. Qiu, and P. Fischer, "Holograms for acoustics," vol. 537, no. 7621, pp. 518–522.

[30] J. W. Goodman, *Introduction to Fourier optics*. Roberts & Co, 3rd ed ed. OCLC: ocm56632414.

[31] D.-L. Liu and R. Waag, "Propagation and backpropagation for ultrasonic wavefront design," *IEEE Transactions on Ultrasonics, Ferroelectrics and Frequency Control*, vol. 44, pp. 1–13, 1 1997.

[32] P. R. Stepanishen and K. C. Benjamin, "Forward and backward projection of acoustic fields using fft methods," *The Journal of the Acoustical Society of America*, vol. 71, pp. 803–812, 4 1982.

[33] A. Pulkkinen, Y. Huang, J. Song, and K. Hynynen, "Simulations and measurements of transcranial low-frequency ultrasound therapy: skull-base heating and effective area of treatment," *Physics in Medicine and Biology*, vol. 56, pp. 4661–4683, 8 2011.

[34] R. Goyal, A. G. Athanassiadis, Z. Ma, and P. Fischer, "Amplification of acoustic forces using microbubble arrays enables manipulation of centimeter-scale objects," *Physical Review Letters*, vol. 128, p. 254502, 6 2022.

[35] *Physics of Sound in the Sea*. Washington, DC: The National Academies Press, 1949.

[36] M. Minnaert, "XVI. *On musical air-bubbles and the sounds of running water*," *The London, Edinburgh, and Dublin Philosophical Magazine and Journal of Science*, vol. 16, pp. 235–248, Aug. 1933.

[37] *Fundamentals of Acoustical Oceanography*. Elsevier, 1998.

[38] *The Acoustic Bubble*. Elsevier, 1994.

[39] E. L. Carstensen and L. L. Foldy, "Propagation of Sound Through a Liquid Containing Bubbles," *The Journal of the Acoustical Society of America*, vol. 19, pp. 481–501, May 1947.

[40] L. L. Foldy, "The Multiple Scattering of Waves. I. General Theory of Isotropic Scattering by Randomly Distributed Scatterers," *Physical Review*, vol. 67, pp. 107–119, Feb. 1945.

[41] C. Feuillade, "Scattering from collective modes of air bubbles in water and the physical mechanism of superresonances," *The Journal of the Acoustical Society of America*, vol. 98, pp. 1178–1190, Aug. 1995.

[42] H. Bruus, "Acoustofluidics 7: The acoustic radiation force on small particles," *Lab on a Chip*, vol. 12, no. 6, p. 1014, 2012.

[43] C. Feuillade and M. F. Werby, "Resonances of deformed gas bubbles in liquids," *The Journal of the Acoustical Society of America*, vol. 96, pp. 3684–3692, 12 1994.

[44] C. Feuillade, "The attenuation and dispersion of sound in water containing multiply interacting air bubbles," *The Journal of the Acoustical Society of America*, vol. 99, pp. 3412–3430, 6 1996.

[45] C. Feuillade, "Acoustically coupled gas bubbles in fluids: Time-domain phenomena," *The Journal of the Acoustical Society of America*, vol. 109, pp. 2606–2615, 6 2001.

[46] C. Devin, "Survey of Thermal, Radiation, and Viscous Damping of Pulsating Air Bubbles in Water," *The Journal of the Acoustical Society of America*, vol. 31, pp. 1654–1667, Dec. 1959.

[47] C. Feuillade, "Scattering from collective modes of air bubbles in water and the physical mechanism of superresonances," *The Journal of the Acoustical Society of America*, vol. 98, pp. 1178–1190, aug 1995.

[48] T. G. Leighton, *The Acoustic Bubble*. Elsevier, 1994.

[49] P. MARMOTTANT, J. P. RAVEN, H. GARDENIERS, J. G. BOMER, and S. HILGENFELDT, "Microfluidics with ultrasound-driven bubbles," *Journal of Fluid Mechanics*, vol. 568, p. 109, 12 2006.

[50] D. Rabaud, P. Thibault, M. Mathieu, and P. Marmottant, "Acoustically bound microfluidic bubble crystals," *Physical Review Letters*, vol. 106, p. 134501, 3 2011.

[51] A. Hashmi, G. Yu, M. Reilly-Collette, G. Heiman, and J. Xu, "Oscillating bubbles: a versatile tool for lab on a chip applications," *Lab on a Chip*, vol. 12, p. 4216, 2012.

[52] J. Xu and D. Attinger, *Piezoelectric Actuation in Multiphase Microfluidics*, pp. 2735–2743. Springer New York, 2015.

[53] N. Bertin, T. A. Spelman, T. Combriat, H. Hue, O. Stéphan, E. Lauga, and P. Marmottant, "Bubble-based acoustic micropropulsors: active surfaces and mixers," *Lab on a Chip*, vol. 17, pp. 1515–1528, 2017.

[54] A. Doinikov and S. Zavtrak, "On the mutual interaction of two gas bubbles in a sound field," *Physics of Fluids*, vol. 7, no. 8, pp. 1923–1930, 1995.

[55] Y. Chen, Z. Fang, B. Merritt, D. Strack, J. Xu, and S. Lee, "Onset of particle trapping and release via acoustic bubbles," *Lab on a Chip*, vol. 16, pp. 3024–3032, 2016.

[56] D. Rabaud, P. Thibault, J.-P. Raven, O. Hugon, E. Lacot, and P. Marmottant, "Manipulation of confined bubbles in a thin microchannel: Drag and acoustic bjerknes forces," *Physics of Fluids*, vol. 23, 4 2011.

[57] Y. Xu, A. Hashmi, G. Yu, X. Lu, H.-J. Kwon, X. Chen, and J. Xu, "Microbubble array for on-chip worm processing," *Applied Physics Letters*, vol. 102, 1 2013.

[58] D. Ahmed, A. Ozcelik, N. Bojanala, N. Nama, A. Upadhyay, Y. Chen, W. Hanna-Rose, and T. J. Huang, "Rotational manipulation of single cells and organisms using acoustic waves," *Nature Communications*, vol. 7, p. 11085, 3 2016.

[59] A. R. Tovar, M. V. Patel, and A. P. Lee, "Lateral air cavities for microfluidic pumping with the use of acoustic energy," *Microfluidics and Nanofluidics*, vol. 10, pp. 1269–1278, 6 2011.

[60] S. K. Chung and S. K. Cho, "On-chip manipulation of objects using mobile oscillating bubbles," *Journal of Micromechanics and Microengineering*, vol. 18, p. 125024, 12 2008.

[61] S. K. Chung and S. K. Cho, "3-d manipulation of millimeter- and micro-sized objects using an acoustically excited oscillating bubble," *Microfluidics and Nanofluidics*, vol. 6, pp. 261–265, 2 2009.

[62] J. O. Kwon, J. S. Yang, S. J. Lee, K. Rhee, and S. K. Chung, "Electromagnetically actuated micromanipulator using an acoustically oscillating bubble," *Journal of Micromechanics and Microengineering*, vol. 21, p. 115023, 11 2011.

[63] P. Rogers and A. Neild, "Selective particle trapping using an oscillating microbubble," *Lab on a Chip*, vol. 11, p. 3710, 2011.

[64] J. Kao, X. Wang, J. Warren, J. Xu, and D. Attinger, "A bubble-powered micro-rotor: conception, manufacturing, assembly and characterization," *Journal of Micromechanics and Microengineering*, vol. 17, pp. 2454–2460, 12 2007.

[65] A. D. Vellis, D. Gritsenko, Y. Lin, Z. Wu, X. Zhang, Y. Pan, W. Xue, and J. Xu, "Drastic sensing enhancement using acoustic bubbles for surface-based microfluidic sensors," *Sensors and Actuators B: Chemical*, vol. 243, pp. 298–302, 5 2017.

[66] N. Bertin, T. A. Spelman, O. Stephan, L. Gredy, M. Bouriau, E. Lauga, and P. Marmottant, "Propulsion of bubble-based acoustic microswimmers," *Physical Review Applied*, vol. 4, p. 064012, 12 2015.

[67] J. Feng, J. Yuan, and S. K. Cho, "2-d steering and propelling of acoustic bubble-powered microswimmers," *Lab on a Chip*, vol. 16, pp. 2317–2325, 2016.

[68] T. Segers and M. Versluis, "Acoustic bubble sorting for ultrasound contrast agent enrichment," *Lab Chip*, vol. 14, pp. 1705–1714, 2014.

[69] R. Thameem, B. Rallabandi, and S. Hilgenfeldt, "Particle migration and sorting in microbubble streaming flows," *Biomicrofluidics*, vol. 10, 1 2016.

[70] N. Garg, T. M. Westerhof, V. Liu, R. Liu, E. L. Nelson, and A. P. Lee, "Whole-blood sorting, enrichment and in situ immunolabeling of cellular subsets using acoustic microstreaming," *Microsystems & Nanoengineering*, vol. 4, p. 17085, 2 2018.

[71] M. Minnaert, "Xvi. on musical air-bubbles and the sounds of running water," *The London, Edinburgh, and Dublin Philosophical Magazine and Journal of Science*, vol. 16, pp. 235–248, 8 1933.

[72] L. Rayleigh, "Viii. on the pressure developed in a liquid during the collapse of a spherical cavity," *The London, Edinburgh, and Dublin Philosophical Magazine and Journal of Science*, vol. 34, pp. 94–98, 8 1917.

[73] M. S. Plesset, "Closure to "discussion of 'the dynamics of cavitation bubbles'" (1950, asme j. appl. mech., 17, pp. 100–101)," *Journal of Applied Mechanics*, vol. 17, pp. 101–101, 3 1950.

[74] O. Vincent and P. Marmottant, "On the statics and dynamics of fully confined bubbles," *Journal of Fluid Mechanics*, vol. 827, pp. 194–224, 9 2017.

[75] C. Wang, B. Rallabandi, and S. Hilgenfeldt, "Frequency dependence and frequency control of microbubble streaming flows," *Physics of Fluids*, vol. 25, 2 2013.

[76] B. Rallabandi, A. Marin, M. Rossi, C. Kähler, and S. Hilgenfeldt, "Three-dimensional streaming flow in confined geometries," *Journal of Fluid Mechanics*, vol. 777, pp. 408–429, 8 2015.

[77] C. Chindam, N. Nama, M. I. Lapsley, F. Costanzo, and T. J. Huang, "Theory and experiment on resonant frequencies of liquid-air interfaces trapped in microfluidic devices," *Journal of Applied Physics*, vol. 114, 11 2013.

[78] J. H. Wu, A. Q. Liu, and H. L. Chen, "Exact solutions for free-vibration analysis of rectangular plates using bessel functions," *Journal of Applied Mechanics*, vol. 74, pp. 1247–1251, 11 2007.

[79] A. Dmitriev, D. Gritsenko, and V. Mitrofanov, "Surface vibrational modes in disk-shaped resonators," *Ultrasonics*, vol. 54, pp. 905–913, 3 2014.

[80] D. Gritsenko, Y. Lin, V. Hovorka, Z. Zhang, A. Ahmadianyazdi, and J. Xu, "Vibrational modes prediction for water-air bubbles trapped in circular microcavities," *Physics of Fluids*, vol. 30, 8 2018.

[81] A. A. Doinikov and A. Bouakaz, "Microstreaming generated by two acoustically induced gas bubbles," *Journal of Fluid Mechanics*, vol. 796, pp. 318–339, 6 2016.

[82] X. Huang, Q.-X. Wang, A.-M. Zhang, and J. Su, "Dynamic behaviour of a two-microbubble system under ultrasonic wave excitation," *Ultrasonics Sonochemistry*, vol. 43, pp. 166–174, 5 2018.

[83] D. L. Miller and E. A. Neppiras, "On the oscillation mode of gas-filled micropores," *The Journal of the Acoustical Society of America*, vol. 77, pp. 946–953, 3 1985.

[84] D. L. Miller, "Frequency relationships for ultrasonic activation of free microbubbles, encapsulated microbubbles, and gas-filled micropores," *The Journal of the Acoustical Society of America*, vol. 104, pp. 2498–2505, 10 1998.

[85] H. Gelderblom, A. G. Zijlstra, L. van Wijngaarden, and A. Prosperetti, "Oscillations of a gas pocket on a liquid-covered solid surface," *Physics of Fluids*, vol. 24, 12 2012.

[86] C. Chindam, N. Nama, M. Ian Lapsley, F. Costanzo, and T. Jun Huang, "Theory and experiment on resonant frequencies of liquid-air interfaces trapped in microfluidic devices," *Journal of applied physics*, vol. 114, no. 19, p. 194503, 2013.

[87] L. Landau and E. Lifshitz, *Fluid Mechanics: Volume 6*. No. Bd. 6, Pergamon, 2013.

[88] D. D. JOSEPH, "Viscous potential flow," *Journal of Fluid Mechanics*, vol. 479, p. S0022112002003634, 3 2003.

[89] D. Gritsenko, Y. Lin, V. Hovorka, Z. Zhang, A. Ahmadianyazdi, and J. Xu, "Vibrational modes prediction for water-air bubbles trapped in circular microcavities," vol. 30, no. 8, p. 082001.

[90] D. Gritsenko, Y. Lin, V. Hovorka, Z. Zhang, A. Ahmadianyazdi, and J. Xu, "Vibrational modes prediction for water-air bubbles trapped in circular microcavities," *Physics of Fluids*, vol. 30, no. 8, p. 082001, 2018.

[91] V. Leroy, M. Devaud, T. Hocquet, and J. C. Bacri, "The bubble cloud as an N-degree of freedom harmonic oscillator," *The European Physical Journal E*, vol. 17, no. 2, pp. 189–198, 2005.

[92] A. Mata, A. J. Fleischman, and S. Roy, "Characterization of Polydimethylsiloxane (PDMS) Properties for Biomedical Micro/Nanosystems," *Biomedical Microdevices*, vol. 7, no. 4, pp. 281–293, 2005.

[93] E. Lifshitz and L. Landau, *Course of theoretical physics: fluid mechanics*. Butterworth-Heinemann, Oxford UK, 1987.

[94] F. L. Pedrotti, L. M. Pedrotti, and L. S. Pedrotti, *Introduction to Optics*. Cambridge University Press, 2017.

[95] A. Petrova-Mayor and S. Gimbal, "Advanced lab on fresnel equations," *American Journal of Physics*, vol. 83, pp. 935–941, 11 2015.

[96] D. Baresch and V. Garbin, "Acoustic trapping of microbubbles in complex environments and controlled payload release," *Proceedings of the National Academy of Sciences*, vol. 117, no. 27, pp. 15490–15496, 2020.

[97] V. Bjerknes, *Fields of Force*. Publication of the Ernest Kempton Adams Fund for Physical Research, Columbia University Press, 1906.

[98] N. A. Pelekasis and J. A. Tsamopoulos, "Bjerknes forces between two bubbles. part 1. response to a step change in pressure," *Journal of Fluid Mechanics*, vol. 254, pp. 467–499, 9 1993.

[99] N. A. Pelekasis and J. A. Tsamopoulos, "Bjerknes forces between two bubbles. part 2. response to an oscillatory pressure field," *Journal of Fluid Mechanics*, vol. 254, pp. 501–527, 9 1993.

[100] L. A. Crum, "Bjerknes forces on bubbles in a stationary sound field," *The Journal of the Acoustical Society of America*, vol. 57, pp. 1363–1370, jun 1975.

[101] Z. Ma, K. Melde, A. G. Athanassiadis, M. Schau, H. Richter, T. Qiu, and P. Fischer, "Spatial ultrasound modulation by digitally controlling microbubble arrays," *Nature Communications*, vol. 11, p. 4537, dec 2020.

[102] Z. Ma, A. W. Holle, K. Melde, T. Qiu, K. Poeppel, V. M. Kadiri, and P. Fischer, "Acoustic holographic cell patterning in a biocompatible hydrogel," *Advanced Materials*, vol. 32, p. 1904181, jan 2020.

[103] A. Marzo, S. A. Seah, B. W. Drinkwater, D. R. Sahoo, B. Long, and S. Subramanian, "Holographic acoustic elements for manipulation of levitated objects," *Nature Communications*, vol. 6, p. 8661, dec 2015.

[104] K. Melde, A. G. Mark, T. Qiu, and P. Fischer, "Holograms for acoustics," *Nature*, vol. 537, pp. 518–522, sep 2016.

[105] M. Caleap and B. W. Drinkwater, "Acoustically trapped colloidal crystals that are reconfigurable in real time," *Proceedings of the National Academy of Sciences*, vol. 111, pp. 6226–6230, apr 2014.

[106] D. Rabaud, P. Thibault, M. Mathieu, and P. Marmottant, "Acoustically bound microfluidic bubble crystals," *Physical Review Letters*, vol. 106, p. 134501, Mar. 2011.

[107] D. Rabaud, P. Thibault, J.-P. Raven, O. Hugon, E. Lacot, and P. Marmottant, "Manipulation of confined bubbles in a thin microchannel: Drag and acoustic bjerknes forces," *Physics of Fluids*, vol. 23, no. 4, p. 042003, 2011.

[108] G. Regnault, C. Mauger, P. Blanc-Benon, and C. Inserra, "Secondary radiation force between two closely spaced acoustic bubbles," *Physical Review E*, vol. 102, p. 031101, sep 2020.

[109] M. Lanoy, C. Derec, A. Tourin, and V. Leroy, "Manipulating bubbles with secondary bjerknes forces," *Applied Physics Letters*, vol. 107, p. 214101, nov 2015.

[110] J. G. S. Moo, C. C. Mayorga-Martinez, H. Wang, W. Z. Teo, B. H. Tan, T. D. Luong, S. R. Gonzalez-Avila, C.-D. Ohl, and M. Pumera, "Bjerknes forces in motion: Long-range translational motion and chiral directionality switching in bubble-propelled micromotors via an ultrasonic pathway," *Advanced Functional Materials*, vol. 28, p. 1702618, jun 2018.

[111] D. J. Griffiths, "Dipoles at rest," *American Journal of Physics*, vol. 60, no. 11, pp. 979–987, 1992.

[112] D. J. Griffiths, *Introduction to Electrodynamics*. Prentice-Hall of India, 2013.

[113] R. Goyal, A. G. Athanassiadis, Z. Ma, and P. Fischer, "Amplification of acoustic forces using microbubble arrays enables manipulation of centimeter-scale objects," vol. 128, no. 25, p. 254502.

[114] R. T. Pardasani and P. Pardasani, *Magnetic Properties of Paramagnetic Compounds, Magnetic Susceptibility Data, Volume 5*. Springer Berlin Heidelberg, 2022.

[115] D. Qin, Y. Xia, and G. M. Whitesides, "Soft lithography for micro- and nanoscale patterning," *Nature Protocols*, vol. 5, pp. 491–502, mar 2010.

[116] P. Li, E. Zahedi, Y. Shi, Y. Deng, and L. Liu, "Dynamically tuning and reconfiguring microwave bandpass filters using optical control of switching elements," *Microwave and Optical Technology Letters*, vol. 66, 2 2024.

[117] A. C. Guyette, "Intrinsically switched varactor-tuned filters and filter banks," *IEEE Transactions on Microwave Theory and Techniques*, vol. 60, pp. 1044–1056, 4 2012.

[118] F. Gentili, L. Urbani, G. Bianchi, L. Pelliccia, and R. Sorrentino, "p-i-n-diode-based four-channel switched filter bank with low-power ttl-compatible driver,"

IEEE Transactions on Microwave Theory and Techniques, vol. 62, pp. 3333–3340, 12 2014.

[119] J. Parke, R. Freitag, M. Torpey, R. S. Howell, E. J. Stewart, M. Snook, I. Wathuthanthri, S. Gupta, B. Nechay, M. King, P. Borodulin, K. Renaldo, and H. G. Henry, "High-performance slcfets for switched filter applications," in *2016 IEEE Compound Semiconductor Integrated Circuit Symposium (CSICS)*, pp. 1–4, IEEE, 10 2016.

[120] I. Reines, C. Goldsmith, C. Nordquist, C. Dyck, G. Kraus, T. Plut, P. Finnegan, F. Austin, and C. Sullivan, "A low loss rf mems ku-band integrated switched filter bank," *IEEE Microwave and Wireless Components Letters*, vol. 15, pp. 74–76, 2 2005.

[121] P. Grant, M. Denhoff, and R. Mansour, "A comparison between rf mems switches and semiconductor switches," in *2004 International Conference on MEMS, NANO and Smart Systems (ICMENS'04)*, pp. 515–521, IEEE.

[122] M. Derayatifar, M. Habibi, R. Bhat, and M. Packirisamy, "Holographic direct sound printing," *Nature Communications*, vol. 15, p. 6691, 8 2024.

[123] Z. Ma, A. W. Holle, K. Melde, T. Qiu, K. Poeppel, V. M. Kadiri, and P. Fischer, "Acoustic holographic cell patterning in a biocompatible hydrogel," *Advanced Materials*, vol. 32, 1 2020.

[124] K. Melde, E. Choi, Z. Wu, S. Palagi, T. Qiu, and P. Fischer, "Acoustic fabrication via the assembly and fusion of particles," *Advanced Materials*, vol. 30, 1 2018.

[125] L. Cox, K. Melde, A. Croxford, P. Fischer, and B. W. Drinkwater, "Acoustic hologram enhanced phased arrays for ultrasonic particle manipulation," *Physical Review Applied*, vol. 12, p. 064055, 12 2019.

[126] D. Andres, S. Jimenez-Gambin, N. Jimenez, and F. Camarena, "Multifocal acoustic holograms for deep-brain neuromodulation and bbb opening," in *2020 IEEE International Ultrasonics Symposium (IUS)*, pp. 1–3, IEEE, 9 2020.

[127] M. Xu, J. Wang, W. S. Harley, P. V. S. Lee, and D. J. Collins, "Programmable acoustic holography using medium-sound-speed modulation," *Advanced Science*, vol. 10, 8 2023.

[128] M. Xu, W. S. Harley, Z. Ma, P. V. S. Lee, and D. J. Collins, "Sound-speed modifying acoustic metasurfaces for acoustic holography," *Advanced Materials*, vol. 35, 4 2023.

[129] Z. Ma, H. Joh, D. E. Fan, and P. Fischer, "Dynamic ultrasound projector controlled by light," *Advanced Science*, vol. 9, 3 2022.

[130] A. G. Athanassiadis, L. Schlieder, K. Melde, V. Volchkov, B. Schölkopf, and P. Fischer, "Multiplane diffractive acoustic networks," *IEEE Transactions on Ultrasonics, Ferroelectrics, and Frequency Control*, vol. 70, pp. 441–448, 5 2023.

[131] X. G. Zhang, W. X. Jiang, H. L. Jiang, Q. Wang, H. W. Tian, L. Bai, Z. J. Luo, S. Sun, Y. Luo, C.-W. Qiu, and T. J. Cui, "An optically driven digital metasurface for programming electromagnetic functions," *Nature Electronics*, vol. 3, pp. 165–171, 3 2020.

[132] S. Rahimi, R. M. Jones, and K. Hynynen, "A high-frequency phased array system for transcranial ultrasound delivery in small animals," *IEEE Transactions on Ultrasonics, Ferroelectrics, and Frequency Control*, vol. 68, pp. 127–135, 1 2021.

[133] L. D. Marchi, "The blossoming of ultrasonic meta-transducers," *IEEE Transactions on Ultrasonics, Ferroelectrics, and Frequency Control*, pp. 1–1, 2024.

[134] P. L. M. J. van Neer, L. C. J. M. Peters, R. G. F. A. Verbeek, B. Peeters, G. de Haas, L. Hörchens, L. Fillinger, T. Schrama, E. J. W. Merks-Swolfs, K. Gijsbertse, A. E. C. M. Saris, M. Mozaffarzadeh, J. M. Menssen, C. L. de Korte, J.-L. P. J. van der Steen, A. W. F. Volker, and G. H. Gelinck, "Flexible large-area ultrasound arrays for medical applications made using embossed polymer structures," *Nature Communications*, vol. 15, p. 2802, 3 2024.

[135] P. Lu, T. Haddad, J. Tebart, C. Roeloffzen, and A. Stöhr, "Photonic integrated circuit for optical phase control of 1×4 terahertz phased arrays," *Photonics*, vol. 9, p. 902, 11 2022.

[136] Y. Zhang, A. W. Pang, and M. J. Cryan, "Optically controlled millimetre-wave switch with stepped-impedance lines," *IET Microwaves, Antennas & Propagation*, vol. 13, pp. 1737–1741, 8 2019.

[137] P. Y. Chiou, A. T. Ohta, and M. C. Wu, "Massively parallel manipulation of single cells and microparticles using optical images," *Nature*, vol. 436, pp. 370–372, 7 2005.

[138] P. Paulachan, R. Hammer, J. Siegert, I. Wiesler, and R. Brunner, "Fast inline failure analysis of sub-micron-sized cracks in 3d interconnect technologies utilizing acoustic interferometry," *Communications Engineering*, vol. 3, p. 100, 7 2024.

[139] G. Kook, Y. Jo, C. Oh, X. Liang, J. Kim, S.-M. Lee, S. Kim, J.-W. Choi, and H. J. Lee, "Multifocal skull-compensated transcranial focused ultrasound system for neuromodulation applications based on acoustic holography," *Microsystems & Nanoengineering*, vol. 9, p. 45, 4 2023.

[140] A. Jäger, "Airborne ultrasound phased arrays," 2018.

[141] H. J. Hewener, W. Bost, D. Speicher, M. Ehrhardt, M. Fournelle, and S. Tretbar, "Low-cost volumetric imaging with large footprint 11x11-element matrix array probe on a 128 channel ultrasound research scanner," p. 020008, 2019.

[142] D.-L. Liu and R. Waag, "Propagation and backpropagation for ultrasonic wavefront design," *IEEE Transactions on Ultrasonics, Ferroelectrics and Frequency Control*, vol. 44, pp. 1–13, 1 1997.

[143] K. Matsushima and T. Shimobaba, "Band-limited angular spectrum method for numerical simulation of free-space propagation in far and near fields," *Optics Express*, vol. 17, p. 19662, 10 2009.

[144] Z. Zou, R. Lirette, and L. Zhang, "Orbital angular momentum reversal and asymmetry in acoustic vortex beam reflection," *Physical Review Letters*, vol. 125, p. 074301, 8 2020.

[145] M. Baudoin, J.-L. Thomas, R. A. Sahely, J.-C. Gerbedoen, Z. Gong, A. Sivery, O. B. Matar, N. Smagin, P. Favreau, and A. Vlandas, "Spatially selective manipulation of cells with single-beam acoustical tweezers," *Nature Communications*, vol. 11, p. 4244, 8 2020.

[146] X. Chen, X. Qian, K. Lam, C. T. Chiu, R. Chen, Z. Chen, K. K. Shung, P. Yu, and Q. Zhou, "Helical-like 3d ultrathin piezoelectric element for complicated ultrasonic field," *Advanced Functional Materials*, vol. 29, 8 2019.

[147] Y. Jin, R. Kumar, O. Poncelet, O. Mondain-Monval, and T. Brunet, "Flat acoustics with soft gradient-index metasurfaces," *Nature Communications*, vol. 10, p. 143, 1 2019.

[148] Q. Huang and Z. Zeng, "A review on real-time 3d ultrasound imaging technology," vol. 2017, p. 6027029.

[149] J. Provost, C. Papadacci, J. E. Arango, M. Imbault, M. Fink, J.-L. Gennisson, M. Tanter, and M. Pernot, "3d ultrafast ultrasound imaging in vivo," vol. 59, no. 19, p. L1. Publisher: IOP Publishing.

[150] J. A. Jensen, M. Schou, L. T. Jorgensen, B. G. Tomov, M. B. Stuart, M. S. Traberg, I. Taghavi, S. H. Oygaard, M. L. Ommen, K. Steenberg, E. V. Thomsen, N. S. Panduro, M. B. Nielsen, and C. M. Sorensen, "Anatomic and functional imaging using row–column arrays," *IEEE Transactions on Ultrasonics, Ferroelectrics, and Frequency Control*, vol. 69, pp. 2722–2738, 10 2022.

[151] K. Kolesnik, M. Xu, P. V. S. Lee, V. Rajagopal, and D. J. Collins, "Unconventional acoustic approaches for localized and designed micromanipulation," *Lab on a Chip*, vol. 21, no. 15, pp. 2837–2856, 2021.

[152] Y. Tian, Q. Wei, Y. Cheng, and X. Liu, "Acoustic holography based on composite metasurface with decoupled modulation of phase and amplitude," *Applied Physics Letters*, vol. 110, p. 191901, May 2017.

[153] W. S. Harley, C. C. Li, J. Toombs, C. D. O'Connell, H. K. Taylor, D. E. Heath, and D. J. Collins, "Advances in biofabrication techniques towards functional bioprinted heterogeneous engineered tissues: A comprehensive review," *Bioprinting*, vol. 23, p. e00147, Aug. 2021.

[154] J. Cheng, R. Wang, Z. Sun, Q. Liu, X. He, H. Li, H. Ye, X. Yang, X. Wei, Z. Li, B. Jian, W. Deng, and Q. Ge, "Centrifugal multimaterial 3D printing of multifunctional heterogeneous objects," *Nature Communications*, vol. 13, p. 7931, Dec. 2022.

[155] L. Cox, K. Melde, A. Croxford, P. Fischer, and B. W. Drinkwater, "Acoustic Hologram Enhanced Phased Arrays for Ultrasonic Particle Manipulation," *Physical Review Applied*, vol. 12, p. 064055, Dec. 2019.

[156] B. Liu, Q. Wei, Z. Su, Y. Wang, and L. Huang, "Multifunctional acoustic holography based on compact acoustic geometric-phase meta-array," *Journal of Applied Physics*, vol. 131, p. 185108, May 2022.

[157] C. Zhong, Y. Jia, D. C. Jeong, Y. Guo, and S. Liu, "AcousNet: A Deep Learning Based Approach to Dynamic 3D Holographic Acoustic Field Generation From Phased Transducer Array," *IEEE Robotics and Automation Letters*, vol. 7, pp. 666–673, Apr. 2022.

[158] The PLOS ONE Staff, "Correction: Three-Dimensional Mid-Air Acoustic Manipulation by Ultrasonic Phased Arrays," *PLoS ONE*, vol. 9, p. e102525, July 2014.

[159] S. Harput and A. Bozkurt, "Ultrasonic Phased Array Device for Acoustic Imaging in Air," *IEEE Sensors Journal*, vol. 8, pp. 1755–1762, Nov. 2008.

[160] K. Y. Saleh and N. B. SMith, "Two-dimensional ultrasound phased array design for tissue ablation for treatment of benign prostatic hyperplasia," *International Journal of Hyperthermia*, vol. 20, pp. 7–31, Feb. 2004.

[161] M. Bakhtiari-Nejad, "Multi-focal transmission acoustic phase holograms in contactless ultrasonic power transfer systems," *Sensors and Actuators A: Physical*, vol. 340, p. 113551, June 2022.

[162] J. Li, P. Zhao, and Y. Pei, "Holographic Optimization Method of Acoustic Radiation Force for Continuously Manipulating a Mie Particle through a Fluid," *Physical Review Applied*, vol. 18, p. 064075, Dec. 2022.

[163] S. Jimenez-Gambin, N. Jimenez, A. Pouliopoulos, J. M. Benlloch, E. Konofagou, and F. Camarena, "Acoustic Holograms for Bilateral Blood-Brain Barrier Opening in a Mouse Model," *IEEE Transactions on Biomedical Engineering*, vol. 69, pp. 1359–1368, Apr. 2022.

[164] Y. Xie, C. Shen, W. Wang, J. Li, D. Suo, B.-I. Popa, Y. Jing, and S. A. Cummer, "Acoustic Holographic Rendering with Two-dimensional Metamaterial-based Passive Phased Array," *Scientific Reports*, vol. 6, p. 35437, Oct. 2016.

[165] M.-M. Yang, Z.-D. Luo, Z. Mi, J. Zhao, S. P. E, and M. Alexe, "Piezoelectric and pyroelectric effects induced by interface polar symmetry," *Nature*, vol. 584, pp. 377–381, 8 2020.

[166] Y. Heo and M. Alexe, "Boosting piezoelectricity under illumination via the bulk photovoltaic effect and the schottky barrier effect in bifeo 3," *Advanced Materials*, vol. 34, 2 2022.

[167] Y.-D. Liou, Y.-Y. Chiu, R. T. Hart, C.-Y. Kuo, Y.-L. Huang, Y.-C. Wu, R. V. Chopdekar, H.-J. Liu, A. Tanaka, C.-T. Chen, C.-F. Chang, L. H. Tjeng, Y. Cao, V. Nagarajan, Y.-H. Chu, Y.-C. Chen, and J.-C. Yang, "Deterministic optical control of room temperature multiferroicity in bifeo3 thin films," *Nature Materials*, vol. 18, pp. 580–587, 6 2019.

[168] B. Kundys, M. Viret, D. Colson, and D. O. Kundys, "Light-induced size changes in bifeo3 crystals," *Nature Materials*, vol. 9, pp. 803–805, 10 2010.

[169] H. D. Nine and R. Truell, "Photosensitive-ultrasonic properties of cadmium sulfide," *Physical Review*, vol. 123, pp. 799–803, 8 1961.

[170] D. L. White, "Amplification of ultrasonic waves in piezoelectric semiconductors," *Journal of Applied Physics*, vol. 33, pp. 2547–2554, 8 1962.

[171] I. Turek, "The illumination dependence of the velocity and attenuation of ultrasonic waves in gallium arsenide," *Physica Status Solidi (a)*, vol. 9, pp. 113–117, 1 1972.

[172] T. Ogawa, "Internal friction of cds crystal caused by photoconductivity," *Journal of the Physical Society of Japan*, vol. 17, pp. 400–401, 2 1962.

[173] M. N. Islam, "A study of electron transport processes in cadmium sulphide using the acoustoelectric effect," 1970.

[174] K. O. Havelka, *Novel Materials for Electrorheological Fluids*, pp. 43–54. Springer US, 1995.

[175] M. PARTHASARATHY and D. KLINGENBERG, "Electrorheology: Mechanisms and models," *Materials Science and Engineering: R: Reports*, vol. 17, pp. 57–103, 10 1996.

[176] T. Jordan and M. Shaw, "Electrorheology," *IEEE Transactions on Electrical Insulation*, vol. 24, pp. 849–878, 1989.

[177] W. M. Winslow, "Induced fibration of suspensions," *Journal of Applied Physics*, vol. 20, pp. 1137–1140, 12 1949.

[178] H. Block, J. P. Kelly, A. Qin, and T. Watson, "Materials and mechanisms in electrorheology," *Langmuir*, vol. 6, pp. 6–14, 1 1990.

[179] X. Liu, J. Guo, Y. Cheng, G. Xu, Y. Li, and P. Cui, "Synthesis and electrorheological properties of polar molecule-dominated tio 2 particles with high yield stress," *Rheologica Acta*, vol. 49, pp. 837–843, 8 2010.

[180] W. L. Zhang, Y. D. Liu, H. J. Choi, and S. G. Kim, "Electrorheology of graphene oxide," *ACS Applied Materials & Interfaces*, vol. 4, pp. 2267–2272, 4 2012.

[181] T. Plachy, M. Sedlacik, V. Pavlinek, M. Trchová, Z. Morávková, and J. Stejskal, "Carbonization of aniline oligomers to electrically polarizable particles and their use in electrorheology," *Chemical Engineering Journal*, vol. 256, pp. 398–406, 11 2014.

[182] T. Plachy, M. Mrlik, Z. Kozakova, P. Suly, M. Sedlacik, V. Pavlinek, and I. Kuritka, "The electrorheological behavior of suspensions based on molten-salt synthesized lithium titanate nanoparticles and their core–shell titanate/urea analogues," *ACS Applied Materials & Interfaces*, vol. 7, pp. 3725–3731, 2 2015.

[183] J. Yin, R. Chang, Y. Shui, and X. Zhao, "Preparation and enhanced electro-responsive characteristic of reduced graphene oxide/polypyrrole composite sheet suspensions," *Soft Matter*, vol. 9, p. 7468, 2013.

[184] X. P. Zhao and J. B. Yin, "Preparation and electrorheological characteristics of rare-earth-doped tio 2 suspensions," *Chemistry of Materials*, vol. 14, pp. 2258–2263, 5 2002.

[185] Y. Dong, J. Yin, and X. Zhao, "Microwave-synthesized poly(ionic liquid) particles: a new material with high electrorheological activity," *J. Mater. Chem. A*, vol. 2, pp. 9812–9819, 2014.

[186] T. Shiga, A. Okada, and T. Kurauchi, "Electroviscoelastic effect of polymer blends consisting of silicone elastomer and semiconducting polymer particles," *Macromolecules*, vol. 26, pp. 6958–6963, 12 1993.

[187] L. Gao and X. Zhao, "Electrorheological behaviors of barium titanate/gelatin composite hydrogel elastomers," *Journal of Applied Polymer Science*, vol. 94, pp. 2517–2521, 12 2004.

[188] L. Hao, Z. Shi, and X. Zhao, "Mechanical behavior of starch/silicone oil/silicone rubber hybrid electric elastomer," *Reactive and Functional Polymers*, vol. 69, pp. 165–169, 3 2009.

[189] A. A. Krokhin, J. Arriaga, and L. N. Gumen, "Speed of sound in periodic elastic composites," *Physical Review Letters*, vol. 91, p. 264302, 12 2003.

[190] V. Leroy, A. Bretagne, M. Fink, H. Willaime, P. Tabeling, and A. Tourin, "Design and characterization of bubble phononic crystals," *Applied Physics Letters*, vol. 95, 10 2009.

[191] R. Sakurai, H. See, T. Saito, and M. Sumita, "Effect of matrix viscoelasticity on the electrorheological properties of particle suspensions," *Journal of Non-Newtonian Fluid Mechanics*, vol. 81, pp. 235–250, 3 1999.

[192] C. Niu, X. Dong, and M. Qi, "Enhanced electrorheological properties of elastomers containing tio 2 /urea core–shell particles," *ACS Applied Materials & Interfaces*, vol. 7, pp. 24855–24863, 11 2015.

[193] J. Wu, G. Xu, Y. Cheng, F. Liu, J. Guo, and P. Cui, "The influence of high dielectric constant core on the activity of core–shell structure electrorheological fluid," *Journal of Colloid and Interface Science*, vol. 378, pp. 36–43, 7 2012.

[194] Z. Li, J. Zhu, T. Li, and B. Zhang, "An absolute instrument for determination of the speed of sound in water," *Review of Scientific Instruments*, vol. 87, 5 2016.

[195] S. A. Cummer, J. Christensen, and A. Alù, "Controlling sound with acoustic metamaterials," *Nature Reviews Materials*, vol. 1, p. 16001, 2 2016.

[196] R. E. Sheriff and L. P. Geldart, *Exploration Seismology*. Cambridge University Press, 8 1995.

[197] R. T. Shuey, "A simplification of the zoeppritz equations," *GEOPHYSICS*, vol. 50, pp. 609–614, 4 1985.

[198] S. Crampin, "Quantitative seismology: Theory and methods, volumes i and ii by keiiti aki and paul g. richards. w. h. freeman and co., san francisco. price: £41 · 40," *Geological Journal*, vol. 16, pp. 90–90, 1 1981.

[199] G. E. Hancock, T. Hepworth, and K. Wembridge, "Accuracy and reliability of knee goniometry methods," *Journal of Experimental Orthopaedics*, vol. 5, p. 46, 12 2018.

[200] Y. Zhang, C. Fowler, J. Liang, B. Azhar, M. Y. Shalaginov, S. Deckoff-Jones, S. An, J. B. Chou, C. M. Roberts, V. Liberman, M. Kang, C. Ríos, K. A. Richardson, C. Rivero-Baleine, T. Gu, H. Zhang, and J. Hu, "Electrically reconfigurable non-volatile metasurface using low-loss optical phase-change material," *Nature Nanotechnology*, vol. 16, pp. 661–666, 6 2021.

[201] L.-Y. Wu, M.-L. Wu, and L.-W. Chen, "The narrow pass band filter of tunable 1d phononic crystals with a dielectric elastomer layer," *Smart Materials and Structures*, vol. 18, p. 015011, 1 2009.

[202] S. Ghimire and F. Sabri, "K-wave modelling of ultrasound wave propagation in aerogels and the effect of physical parameters on attenuation and loss," *Applied Physics A*, vol. 129, p. 286, 4 2023.

[203] M. S. Kushwaha, P. Halevi, G. Martínez, L. Dobrzynski, and B. Djafari-Rouhani, "Theory of acoustic band structure of periodic elastic composites," *Physical Review B*, vol. 49, pp. 2313–2322, 1 1994.

[204] Y. Yun, G. Miao, P. Zhang, K. Huang, and R. Wei, "Nonlinear acoustic wave propagating in one-dimensional layered system," *Physics Letters A*, vol. 343, pp. 351–358, 8 2005.

[205] A. A. Masud and J. Liu, "Numerical simulation of impulse-induced surface acoustic waves for elastography purposes using k-wave simulation toolbox," *Journal of Applied Physics*, vol. 136, 10 2024.

[206] M. Kim, M. Cho, C. Chung, and K.-U. Kyung, "Stretchable, transparent and multifunctional pvc-gel heater: a novel approach to skin-mountable, wearable thermal devices," *npj Flexible Electronics*, vol. 8, p. 59, 9 2024.

[207] G. Bosch, "Train phd students to be thinkers not just specialists," *Nature*, vol. 554, pp. 277–277, 2 2018.